

Wannier-Orbital theory and ARPES for the quasi-1D conductor $\text{LiMo}_6\text{O}_{17}$. Part I: Six-band t_{2g} Hamiltonian.

L. Dudy

Randall Laboratory, University of Michigan, Ann Arbor, MI 48109, USA
Physikalisches Institut und Röntgen Center for Complex Material Systems,
Universität Würzburg, D-97074 Würzburg, Germany
and
Synchrotron SOLEIL, L'Orme des Merisiers, 91190 Saint-Aubin, France

J.W. Allen

Randall Laboratory, University of Michigan, Ann Arbor, MI 48109, USA

J.D. Denlinger

Advanced Light Source, Lawrence Berkeley National Laboratory, Berkeley, CA 94720, USA

J. He[†]

Department of Physics and Astronomy, Clemson University, Clemson, SC 29534, USA

M. Greenblatt

Department of Chemistry & Chemical Biology, Rutgers University, 123 Bevier Rd. Piscataway, NJ 08854, USA

M.W. Haverkort

Max-Planck-Institut für Festkörperforschung, Heisenbergstrasse 1, D-70569 Stuttgart, Germany
Max-Planck-Institut für Chemische Physik fester Stoffe,
Nöthnitzer Str. 40, D-01187 Dresden, Germany
and
Institut für Theoretische Physik, Universität Heidelberg,
Philosophenweg 16, D-69120 Heidelberg, Germany

Y. Nohara and O.K. Andersen

Max-Planck-Institut für Festkörperforschung, Heisenbergstrasse 1, D-70569 Stuttgart, Germany
 (Dated: May 16, 2023)

In this and the two following papers, we present the results of a combined study by density-functional (LDA) band theory and angle-resolved photoemission spectroscopy (ARPES) of lithium purple bronze, $\text{Li}_{1-x}\text{Mo}_6\text{O}_{17}$. This material is particularly notable for its unusually robust quasi-one-dimensional (quasi-1D) behavior. The band structure, in a large energy window around the Fermi energy, is basically 2D and formed by three Mo t_{2g} -like extended Wannier orbitals (WOs), each one giving rise to a 1D band running at a 120° angle to the two others. A structural "dimerization" from $\mathbf{c}/2$ to \mathbf{c} gaps the xz and yz bands while leaving the xy bands metallic in the gap but resonantly coupled to the gap edges and, hence, to the two other directions. The resulting complex shape of the quasi-1D Fermi surface (FS), verified by our ARPES, thus depends strongly on the Fermi energy position in the gap, implying a great sensitivity to Li stoichiometry of properties dependent on the FS, such as FS nesting or superconductivity. The theory is verified in detail by the recognition and application of an ARPES selection rule that enables, for the first time, the separation in ARPES spectra of the two barely split xy bands and the observation of their complex split FS. The strong resonances prevent either a two-band tight-binding (TB) model or a related real-space ladder picture from giving a valid description of the low-energy electronic structure. Down to a temperature of 6 K we find no evidence for a theoretically expected downward renormalization of perpendicular single particle hopping due to LL fluctuations in the quasi-1D chains. This paper I introduces the material, motivates our study, summarizes the Nth-order muffin-tin orbital (NMTO) method that we use, analyzes the crystal structure and the basic electronic structure, and presents our NMTO calculation of the t_{2g} low-energy WOs and the resulting tight-binding (TB) Hamiltonian for the six lowest energy bands, only the four lowest being occupied. Thus this paper sets the theoretical framework and nomenclature for the following two papers.

[†]deceased in 2021.

I. INTRODUCTION

The present paper (I) and its two companion papers (II and III) are devoted to a detailed study of the band structure of the lithium purple bronze (LiPB) $\text{LiMo}_6\text{O}_{17}$ ¹, combining angle-resolved photoemission spectroscopy (ARPES) and Wannier function band theory using the Nth-order muffin-tin orbital method (NMTO). Since its discovery [1] and structure determination [2] LiPB has been heavily studied as a quasi-1D material² [4–11]. Thus, it is notable as an unusually good and interesting example of the non-Fermi liquid (non-FL) properties exhibited by one-dimensional (1D) interacting electron systems, such as in the exactly solvable Tomonaga-Luttinger (TL) model [12, 13] or in the more generalized notion of the Luttinger Liquid (LL) [14]. A highly non-intuitive example of such non-FL properties is that the energy (E) dependence of the momentum (κ) integrated single-particle spectral function, which would give simply the one-electron density of states in a non-interacting system, goes to zero upon approaching the Fermi-energy (E_F) as a power law $(E_F - E)^\alpha$, with α interpreted as the anomalous exponent of the TL model.³

FIG. 1 reproduces angle-integrated data from a previous photoemission study [3], showing this unusual property for LiPB for the spectral function below E_F , as probed by ARPES. The spectra for κ -integration along the quasi-1D direction, for temperatures $T=4$ K and 30 K and resolution 5 meV, are well described by a power law with $\alpha=0.7$ over at least 40 meV, compared to the Fermi edge of a $T=4$ K gold reference spectrum. Also, scanning tunneling spectroscopy [15], which probes the spectral function on both sides of E_F , shows the power law "V-shape" down to 4 K⁴. It is then equally non-intuitive in the TL model that, nonetheless, the underlying band-structure Fermi momentum k_F and thus, the Fermi surface (FS) remains well-defined [16]. Paper III presents a detailed determination of the FS for LiPB.

The band structure and, in particular, the magnitude(s) of the transverse hoppings (t_\perp) between its 1D chains, and the resulting FS, are especially interesting and important for LiPB. The general theoretical expectation [14] is that, for T decreasing below a scale set by t_\perp , LL behavior is unstable against dimensional crossover from 1D to some sort of 3D Fermi-liquid (FL) behavior, typically by a phase transition to some 3D ordered state

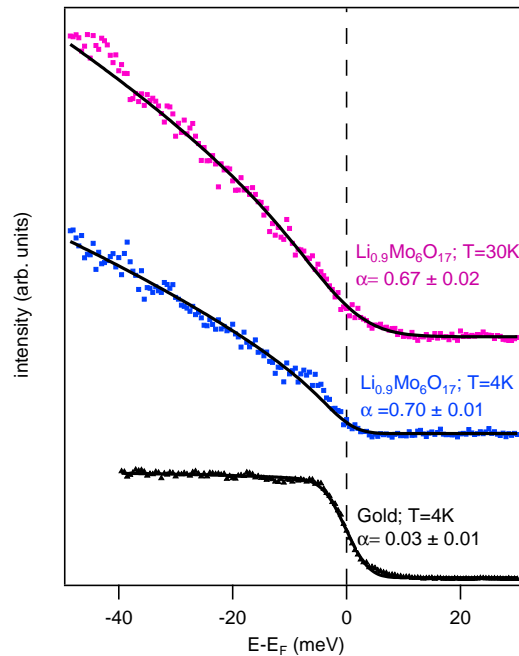


FIG. 1: Angle integrated photoemission spectra of lithium purple bronze for $T=4$ and 30 K taken with a resolution of 5 meV with photon energy $h\nu=8.4$ eV [3]. For reference, a gold spectrum with the same settings is also shown. All the spectra are generally well fitted by the TL-model lineshape, showing for $\text{LiMo}_6\text{O}_{17}$ a value of $\alpha \approx 0.7$. In Ref. 3, it was deemed ambiguous whether a very noisy feature around 5 meV in the fit residuals is intrinsic or arises from some systematic experimental error. The gold spectrum fits well with α essentially zero, corresponding mathematically to a Fermi edge.

like a charge or spin density wave (CDW or SDW). Band calculations to date suggest values of $t_\perp=20$ meV (232 K) and yet the data of FIG. 1 indicate that its non-FL 1D properties likely last until the material goes superconducting (SC) at $T_{SC}=1.9$ K. Indeed other properties of LiPB, albeit novel and interesting, exhibit no clear evidence for dimensional crossover above T_{SC} [3]. However, theory [14] also suggests that LL fluctuations on the chains can strongly suppress the single-particle hopping and consequently the crossover T . For example, in the case of one chain per primitive cell and hopping only to the nearest chain, the suppression of t_\perp is by the factor $(t_\perp/t)^{\alpha/(1-\alpha)}$, where $t \gg t_\perp$ is the hopping along the chains. For a typical band-theory value of $|t|=0.8$ eV [17] and the value of $\alpha=0.7$ cited above, one obtains $t_{\text{eff } \perp} = 4 \mu\text{eV}$ or 0.04 K, even smaller than T_{SC} .⁵ Such a small value might thus account for the exceptional stability of 1D physics in this material, and should be manifest in the

¹ We do not use the conventional name, $\text{Li}_{0.9}\text{Mo}_6\text{O}_{17}$, because the highly accurate ARPES bands to be described here are filled corresponding to the stoichiometry $\text{Li}_{1.02}\text{Mo}_6\text{O}_{17}$ (see Paper III)

² Ref.3 summarizes and references prior work dating back to Ref. 1.

³ The power law is valid for $T=0$. For nonzero T , the exact dependence evolves to be quantitatively more complicated but qualitatively similar.

⁴ In Ref. 3, it was deemed ambiguous whether a very noisy feature around 5 meV in the fit residuals is intrinsic or arises from some systematic experimental error.

⁵ Some measurements [18] have yielded a smaller $\alpha=0.6$, for which the effective t_\perp is larger, 80 μeV or 0.9 K, still smaller than T_{SC} .

low- T single-particle electronic structure. However, up to now, the transverse hopping and resulting FS have never been measured experimentally or characterized theoretically as fully as is needed and possible.

There is additional motivation for our study. As described in detail further below, LiPB is complex in having two approximately 1D bands associated with there being two equivalent chains (and two formula units) per primitive cell, each half filled for stoichiometric $\text{LiMo}_6\text{O}_{17}$. Thus most LiPB theories to date [4–7, 9–11, 17] have modeled the quasi-1D electrons as a lattice of pairs of chains regarded as ladders, with simple tight-binding (TB) t_\perp and t'_\perp parameters for nearest neighbor intra- and inter-ladder hopping, respectively. So it is of great interest to check the validity of the ladder picture, which involves the relative magnitudes of the perpendicular hoppings within and between primitive cells. These hoppings determine the perpendicular dispersion and splitting of the two bands forming the FS. Of particular interest is the normal state FS giving rise to SC. The FS also gives the clearest experimental access to the details of the transverse hoppings.

Another motivation is to demonstrate the use of the NMTO method for creating chemically meaningful Wannier functions –in the present case Wannier orbitals (WOs) centered on Mo1, the only octahedrally fully coordinated molybdenum (Sect. III A)– and their TB Hamiltonian, and to establish them as important tools for predicting and interpreting the ARPES data. As summarized in more detail below, like the study in Ref. 19, our theory uses the local density-functional approximation (DFT-LDA) to derive a set of localized Wannier functions, which, however, in our case, is complete in the sense that it contains all three $\text{Mo}1\,4d\,t_{2g}$ -like orbitals per formula unit, and thereby spans the occupied as well as the lowest empty bands. The two quasi-1D metallic bands are xy -like and situated in a 0.4 eV gap between valence bands formed by the xz and yz WOs, bonding between the ladder rungs, and conduction bands formed by the same WOs, but antibonding between rungs. After integrating out the xz and yz degrees of freedom (in Paper III), our theory leads to the conclusions, that the effective transverse couplings between the two quasi-1D bands cannot be described by a simple TB model, and also that they have very long range, making ladders ill-defined. In this respect all previous TB ladder models are very unrealistic.

The theory also leads to a new selection rule (in Paper II) that enables the two barely split quasi-1D bands to be separated in the ARPES spectra near E_F for the first time. The split and warped FS obtained thereby in ARPES at 6 K is in excellent agreement with the predicted FS, giving a detailed confirmation of the theory (Paper III). This means that the predicted LL renormalization of the perpendicular hoppings with decreased temperature does not occur, and so cannot be the origin of the robustness of the LiPB 1D behavior. We can also infer that the LDA FS is the normal state FS rele-

vant for theories [6, 7, 9, 20, 21] of the SC. We note that the occurrence of SC is sample dependent [22], and, in this context, that the details of the theoretical FS shape are extremely sensitive to the position of E_F , which is controlled by the Li-content (or the content of oxygen vacancies). For our samples, the E_F position indicates that they are very nearly stoichiometric, which is the circumstance found in theory to give the most 1D FS. Although we have not explicitly verified SC for our samples, these findings are consistent with the hypothesis that SC has a 1D origin⁶ and that the absence of SC in some samples may be linked to sample stoichiometry through the sensitivity of the FS. Finally, although T dependence was not a particular focus of the experiments, we find the *same* FS at 30K, implying that a mysterious resistivity upturn below $T_M \approx 25\text{K}$ is not likely to be associated with a gross change in electronic structure [3].

In the remainder of this introductory section, we give a more detailed overview of the new theory relative to previous work, and describe the division of content between the three papers.

The basic band structure in the vicinity of E_F has been known for many years from pioneering TB calculations based on the semi-empirical extended-Hückel method [24]. There are two approximately 1D-bands dispersing across E_F , associated with there being two equivalent chains of Mo atoms having a zigzag arrangement (zig-Mo1-zag-Mo4-zig), and two formula units per primitive cell. The two bands have Mo $4d_{xy}$ character and for stoichiometric $\text{LiMo}_6\text{O}_{17}$ they are half-filled. There are also two filled bands not far below E_F .

Quantitatively correct band structures require charge-self-consistent DFT calculations, not a small task for a transition-metal oxide with 48 atoms per cell, so it took nearly twenty years for the first self-consistent DFT (LDA) band structure to appear [25] and another six for the second [26]. Both calculations were performed with the linear muffin-tin orbital method (LMTO) in the atomic-spheres approximation. Such LDA-LMTO band structures provided guidance for the TB band-structure parameters used in early many-body models [4, 17]. Higher-resolution low-temperature ARPES data and more accurate NMTO calculations show agreement even on the details [27] of the filled bands.

An alternative TB model [19] has been derived by first using the highly accurate full-potential linear augmented-plane-wave (LAPW) method to perform a charge self-consistent DFT (LDA) calculation of the band structure over a wide energy range, and then projecting from it a set of four so-called maximally localized Wannier functions, which describe the two quasi-1D bands and the two valence bands. The Wannier functions of this model are

⁶ The SC upper critical field is much larger than the Pauli-limiting value[23], suggesting unconventional pairing arising from an essentially 1D normal state

therefore not atomic, but essentially the bonding linear combination of those on Mo1 and Mo4, and the integral for hopping between these xy -bond orbitals is only about half the one for hopping between the atomic orbitals considered in the TB models previously used [4, 17]. The study of Nuss and Aichhorn [19] also provides a simplified two-band TB Hamiltonian by folding the two occupied xz and yz bands down into the two xy bands, thereby becoming \widetilde{xy} bands, and fitting their hybridization such as to modify the t_{\perp} parameters. The result is said to be in good agreement with those discussed in Ref. 17.

For the new theory of the present paper and its two companion papers, early results of which were given in Ref. [27], we need and provide an improved 3D visualization of the crystal structure, with an associated wording (Sect. III of the present paper): ribbons containing Mo1, Mo2, Mo4, and Mo5 for zigzag chains and bi-ribbons for ladders, and an overview of the electronic structure (Sect. IV below). In the new theory, we perform an LDA Wannier-function calculation with the new full-potential version [28] of the NMTO method. We obtain the set of all three (per formula unit) Mo1 $4dt_{2g}$ WOs, not only the xy orbitals, but also the xz and yz orbitals. Also the latter form 1D bands, but with primitive translations $(\mathbf{c} \pm \mathbf{b})/2$ until the dimerization to $\mathbf{c} \pm \mathbf{b}$ gaps them around E_F . Indeed (Sect. III A below), the structural reason why LiPB is 1D while (most) other Mo bronzes are 2D [29–32] is exactly this $c/2$ to c dimerization of the ribbons (zigzag chains) into bi-ribbons (the two zigzag chains are not related by translation). Note that this dimerization of the xz and yz bands causing them to gap at $2k_F$ is distinct from the $b/2$ to b dimerization causing the xy bands to gap at $4k_F$ –and which we neglect, as did Nuss and Aichhorn (Sect. III B below). Hybridization between the resulting valence and conduction bands and the metallic xy bands⁷ induces striking $k_{\perp}=k_c$ -dependent features (FIG. 7 below, FIG.s II 20 and 24 (c2), and FIG. s III 27 and 32⁸). These features depend strongly on the energy position in the gap. Therefore the resulting FS warping and splitting also has features that depend strongly on the value of E_F , as set by the effective Li stoichiometry. Furthermore, this E_F dependence of the perpendicular dispersion cannot be captured with a Wannier basis which in addition the metallic xy orbitals contain only the *occupied* xz and yz orbitals [19]. We, therefore, include WOs which account not only for the valence but also for the conduction bands, leading to a very accurate and yet portable (i.e. analytical) t_{2g} six-band TB Hamiltonian. Subsequent analytical Löwdin downfolding to a two-band Hamiltonian, which has resonance- rather than TB form, enables a new and detailed understanding of all

the various microscopic contributions to the perpendicular dispersion, and their relation to the crystal structure and to the FS.

The details of the theoretical method including all six Mo1 t_{2g} WOs and their TB Hamiltonian are presented in Sect.s II, V, and VI of this Paper I. The theory of the ARPES intensity variations and its application to LiPB are presented in Sect. IX of the following Paper II, and the details of the downfolded two-band Hamiltonian and the resulting FS are presented in Paper III. The theory is validated in detail by new higher resolution ARPES experiments for two different samples, down to temperatures of 6 K and 30 K. The data and the analysis results are presented at appropriate places in the course of the presentation of the theory in the three papers. As found previously [19, 27] there is very good general agreement with LDA dispersions up to 150 meV below E_F . Refinement of the LDA-derived parameters of the six-band Hamiltonian yields an accurate and detailed description of the ARPES low-energy band structure (Sect. XI in Paper II), including the striking features of the xy -like bands and the associated distinctive FS features (FIG. 32 in Paper III). As mentioned already, the direct observation of these features, not identified in our previous ARPES studies, is enabled by the recognition and application of a selection rule (Sect. IX B 1 in Paper II) according to which the c -axis dimerization gaps the energy bands, but –for a range of photon energies– has negligible effects on the ARPES intensities.

II. NMTO METHOD

The electronic-structure calculations were performed for the stoichiometric crystal with the structure determined for $\text{LiMo}_6\text{O}_{17}$ [2]. Doping –which is small due to the opposing effects of Li intercalation and O deficiencies– was treated in the rigid-band approximation.

For the DFT-LDA [33] calculations, including the generation of Wannier functions and their TB Hamiltonian, we used the recently developed self consistent full-potential version [28] of the N th-order –also called 3rd-generation– muffin-tin orbital (NMTO) method [34, 35], a descendant [36] of the classical linear muffin-tin orbital (LMTO) method [37][38]. Since NMTOs were hitherto generated for overlapping MT potentials imported from self-consistent LMTO-ASA or linear augmented plane wave (LAPW) calculations [39–49] rather than self consistently in full-potential calculations, and since NMTO Wannier orbitals (WOs) are generated in a very different way than maximally localized Wannier functions [50], making them useful for many-body calculations also for d - and f -electron atoms at low-symmetry positions⁹, here

⁷ We call the xy band the metallic band and, like for semiconductors, call the gapped xz and yz bands valence and conduction bands.

⁸ I, II, and III refer to sections, figures, and equations in Paper I, II, and III, respectively.

⁹ For materials with d - or f -electron atoms exclusively at high-

follows a concise description of our method as applied to LiPB. More complete and pedagogical accounts of the formalism may be found e.g. in Ref.s [35, 36] and [51].

As illustrated in Chart (1) we first generate the full potential, $V(\mathbf{r})$, by charge self-consistent LDA calculation using a relatively large basis set, $\chi_{Rlm}^{\mathbf{k}}(\mathbf{r})$, consisting of the Bloch sums of the two Li 2s NMTOs per primitive cell, of all 60 Mo 4d NMTOs, of all 136 O 2s and 2p NMTOs, plus 138 1s NMTOs on the interstitial sites (E) with MT radii exceeding 1 Bohr radius. The resulting number of 336 NMTOs/cell is smaller than the number of LMTOs [25, 26] – and an order of magnitude smaller than the number of LAPWs [19] needed for LiPB.

Calculating $V(\mathbf{r})$ and $v_R(|\mathbf{r} - \mathbf{R}|)$ self-consistently using the LDA with the basis of 336 NMTOs/cell:

$$\begin{array}{ccc}
 H_{Rlm,R'l'm'}^{\mathbf{k}} \& O_{Rlm,R'l'm'}^{\mathbf{k}} & \rightarrow E_j^{\mathbf{k}} \& u_{Rlm,j}^{\mathbf{k}} \\
 \uparrow & Rlm & \downarrow \\
 E_{0,..,N} \& \chi_{Rlm}^{\mathbf{k}}(\mathbf{r}) & \in \rho(\mathbf{r}) \\
 \uparrow & 336 & \downarrow \\
 v_R(|\mathbf{r} - \mathbf{R}|) & \leftarrow & V(\mathbf{r}) \\
 \downarrow & & \downarrow \\
 (2) & & (2)
 \end{array} \quad (1)$$

After each iteration towards self-consistency, $V(\mathbf{r})$ is least-squares fitted to an *overlapping* MT potential (OMTP) [52], which is a constant, the MT zero, plus a superposition of spherically symmetric potential wells, $\sum_R v_R(|\mathbf{r} - \mathbf{R}|)$, centered at the atoms and larger interstitials. The ranges of the potential wells, the MT radii s_R , were chosen to overlap by 25%. Specifically: $s_{\text{Li}}=2.87$, $s_{\text{Mo}}=2.34-2.55$, $s_{\text{O}}=1.72-1.89$, and $s_{\text{E}}=1.03-2.48$ Bohr radii. The overlaps considerably improve the fit to the full potential and reduce the MT discontinuities of the potential and, hence, the curvatures of the basis functions¹⁰. The OMTP is used to generate the NMTO basis set for the next iteration towards charge self consistency and –this being reached– to generate the massively downfolded basis set consisting of the 6 Bloch sums of the Mo1 4d (t_{2g}) NMTOs which –after symmetrical orthonormalization and Fourier transformation (FT) (9) back to real space [see Chart (2)]– becomes the set of WOs de-

scribing the 6 bands around the Fermi level. The full potential, $V(\mathbf{r})$, enables us to accurately include in the 6-band TB Hamiltonian crystal-field terms, such as the one between the xy - and the xz - or the yz WOs which decisively influences the resonance peak in the metallic xy -like band [see Sect. XIV B 6 in Paper III].

Constructing the 6 WOs and their TB Hamiltonian:

$$\begin{array}{ccc}
 v_R(|\mathbf{r} - \mathbf{R}|) & \text{From (1) and Eq. (6)} & V(\mathbf{r}) \\
 \downarrow & \rightarrow & \downarrow \\
 E_{0,..,N} \& \chi_{Rlm}^{\mathbf{k}}(\mathbf{r}) & H_{Rlm,R'l'm'}^{\mathbf{k}} \& O_{Rlm,R'l'm'}^{\mathbf{k}} \\
 Rm \in 6 & & \downarrow \\
 w_{Rlm}(\mathbf{r} - \mathbf{R}) & \leftarrow \text{FT} & \chi^{\mathbf{k}}(\mathbf{r}) (O^{\mathbf{k}})^{-\frac{1}{2}} \\
 \tilde{H}_{Rlm,R'l'm'}^{TB} & \leftarrow \text{FT} & (O^{\mathbf{k}})^{-\frac{1}{2}} H^{\mathbf{k}} (O^{\mathbf{k}})^{-\frac{1}{2}}
 \end{array} \quad (2)$$

We now describe the construction (3) of the NMTOs which is more complex than that of e.g. LAPWs, but achieves order(s)-of-magnitude reduction in the size of the basis-set. Admittedly, some understanding of solid-state chemistry is required to use NMTOs efficiently to generate WO sets, but they can provide insights not usually obtained by use of plane-wave sets and projection of maximally localized Wannier functions [50].

Constructing the NMTO set:

$$\begin{array}{l}
 \text{Hard-sphere sites \& radii: } \mathbf{R}, a_R \\
 \text{OMTP wells \& radii: } v_R(r), s_R \approx 1.5a_R \\
 \text{Energy (E) mesh: } E_{0,..,N} \\
 \text{Radial wave functions: } \varphi_{Rl}(E, r) \\
 \text{Phase shifts: } \eta_{Rl}(E) \\
 \text{Partial waves: } [\varphi_{Rl}(E, r) - \varphi_{Rl}^o(E, r)] Y_{lm}(\hat{\mathbf{r}}) \\
 \text{Screened spherical waves: } \psi_{Rlm}(E, \mathbf{r}) \\
 \text{Screened structure (or slope) matrix: } S_{R'l'm', Rlm}(E) \\
 \text{Kinked partial waves: } \phi_{Rlm}(E, \mathbf{r}), \text{ Eq. (4)} \\
 \text{Kink matrix: } K_{R'l'm', Rlm}(E), \text{ Eq. (5)} \\
 \text{Downfolding from } K^{336}(E) \text{ to } K^6(E), \text{ Eq. (6)} \\
 \text{Green matrix: } G(E) = K(E)^{-1} \\
 \text{Lagrange matrix: } L_{Rlm,R'l'm'}(E_\nu) \\
 \text{NMTOs: } \chi_{Rlm}^{\mathbf{k}}(\mathbf{r}), \text{ Eq. (7)} \\
 \text{Overlap matrix: } \langle \chi_{Rlm}^{\mathbf{k}} | \chi_{R'l'm'}^{\mathbf{k}} \rangle \equiv O^{\mathbf{k}} \\
 \text{Hamiltonian matrix: } \langle \chi_{Rlm}^{\mathbf{k}} | -\Delta + V(\mathbf{r}) | \chi_{R'l'm'}^{\mathbf{k}} \rangle \equiv H^{\mathbf{k}}
 \end{array} \quad (3)$$

symmetry positions, maximally localized and NMTO Wannier functions (WFs) give similar results when settings are similar [42]. However, maximally localized WFs are usually not centered at low-symmetry sites, and if forced to, they generally do not transform according to the irreducible representations of the point group. As a consequence, crystal fields depend strongly on the settings. The software found on www.quanty.org interfaces several methods for generating WFs and allows users to compare results.

¹⁰ The LMTOs of Methfessel and Schilfgaarde [53] are defined for a conventional MT potential, but are modified in the interstitial near the MTs to avoid large discontinuities of the orbital curvatures. Also, the LMTOs of Wills et al. [54–56] are defined for MTs without overlap, but are not modified. As a consequence, multiple- κ sets are needed.

For each MT well, $v_R(r)$, and energy, E , on a $(N + 1)$ *point mesh*, the radial Schrödinger equations¹¹ for $l=0,..,l_{\text{Rmax}}$ are integrated outwards from the origin to the MT radius, s_R , thus yielding the radial functions, $\varphi_{Rl}(E, r)$, and their phase-shifts, $\eta_{Rl}(E)$, which due to the centrifugal term vanish for all $l \geq l_{\text{max}}(R)$. Continuing the integration smoothly inwards –this time over the MT zero– yields the phase-shifted free waves, $\varphi_{Rl}^o(E, r)$, which we truncate at and inside the so-called

¹¹ Actually, the scalar-relativistic Dirac equations.

hard sphere with radius, $a_R \approx 0.65s_R$. The differences, $\varphi_{Rl}(E, r) - \varphi_{Rl}^o(E, r)$, often referred to as *tongues*, tend smoothly to zero when going outside the MT sphere, and jump discontinuously to $\varphi_{Rl}(E, r)$ when going inside the hard sphere. After multiplication by the appropriate cubic harmonic, $Y_{lm}(\hat{\mathbf{r}})$, these *discontinuous and tongued partial waves* will be used together with the screened spherical waves (SSWs), $\psi_{Rlm}(E, \mathbf{r})$, to be defined below, to form a set of *kinked partial waves* (KPWs)¹², $\phi_{Rlm}(E, \mathbf{r})$, analogous to Slater's augmented plane waves (APWs), and –eventually– of smooth and energy-independent NMTOs [see Eq.s (4) and 7]. Partial waves with the same Rlm as one of the NMTOs in the basis set are called *active* (A) and the remaining partial waves with non-zero phase shifts *passive*. Since $l_{\max}(R) = 4, 3, 3$, and 2 for $R = \text{Mo, O, Li, and E}$, the vast majority of partial waves are passive.

In order to combine the many partial waves to the set of KPWs, we first form the set of *tail- or envelope* functions, $\psi_{Rlm}(E, \mathbf{r})$, also called *screened spherical waves* (SSWs): They are wave-equation solutions that satisfy the boundary conditions that any cubic-harmonic projection around any site, $\hat{P}_{R'l'm'}(r_{R'})\psi_{Rlm}(E, \mathbf{r})$, has a node at the hard-sphere radius if $R'l'm'$ is active and differs from Rlm , and has the proper phase shift, $\eta_{R'l'}(E)$, if $R'l'm'$ is passive. This node condition is what makes the SSW localized –and the more, the larger the basis set, i.e. the number of active channels. The input to a screening calculation (see Sect. 3.3 in Ref. [51] or II.B in Ref. [28]) is the energy, the hard-sphere structure, and the passive phase shifts. The output is the *screened structure- or slope matrix* whose element, $S_{R'l'm', Rlm}(E)$, gives the slope of $\psi_{Rlm}(E, \mathbf{r})$ at the hard sphere in the active $R'l'm'$ channel. The set of screened spherical waves is then augmented by the partial waves to become the basis set of KPWs (see e.g. FIG.s 4-6 in Ref. [51]):

$$\phi_{Rlm}(E, \mathbf{r}) = \psi_{Rlm}(E, \mathbf{r}) + [\varphi_{Rl}(E, r) - \varphi_{Rl}^o(E, r)] Y_{lm}(\hat{\mathbf{r}}). \quad (4)$$

The KPW, $\phi_{Rlm}(E, \mathbf{r})$, has a head formed by the active partial wave with the *same* Rlm , plus passive waves, and a tail which inside the other MT spheres is formed solely by passive partial waves. Hence, all active projections of $\phi_{Rlm}(E, \mathbf{r})$, except its own, vanish. Such a KPW is localized, everywhere continuous, and everywhere a solution of Schrödinger's equation for the MT potential –*except* at all hard spheres where it has *kinks* in the active channels. The kink, $K_{R'l'm', Rlm}(E)$, at the hard sphere in channel $R'l'm'$ is

$$S_{R'l'm', Rlm}(E) - \delta_{R'l'm', Rlm} \left. \frac{\partial \ln \varphi_{Rl}^o(E, r)}{\partial \ln r} \right|_{a_R}. \quad (5)$$

¹² KPWs are also called exact, energy-dependent MTOs (EMTOs)[57, 58].

This kink matrix also equals the MT Hamiltonian minus the energy, i.e. the kinetic energy, in the KPW representation: $K(E) = \langle \phi(E) | -\Delta + \sum_R v_R - E | \phi(E) \rangle$. Any linear combination of KPWs with the property that the kinks from all heads and tails cancel, is smooth and therefore, by construction, a solution with energy E of Schrödinger's equation for the OMTP –except for the tongues sticking into neighboring MT spheres and thereby causing errors of merely 2nd and higher order in the potential overlap. This kink-cancellation condition gives rise to the screened Korringa, Kohn, Rostoker (KKR) *secular* equations of band theory: $K(E)u = 0$.

Downfolding of a large to a small set of KPWs corresponds to changing the phase shifts in the channels to be downfolded (denoted I for "integrated out") from those of hard spheres, $\eta_A(E)$, to the proper phase shifts, $\eta_{Rl}(E)$, and is performed on the kink matrix (5). For example is the kink matrix for the set of 6 KPWs in terms of the blocks of the kink matrix for the 336 set:

$$K_{AA}^6(E) = K_{AA}^{336}(E) - K_{AI}^{336}(E) K_{II}^{336}(E)^{-1} K_{IA}^{336}(E). \quad (6)$$

Note, that this downfolding, which is done *prior* to N-ization (7) (see Chart (3)), makes the resulting NMTO set far better localized and far more accurate than the set obtained by standard Löwdin downfolding of a basis of energy-independent orbitals, e.g. LMTOs [59], Slater type orbitals [60], or NMTOs, followed by linearization of the energy dependence of the denominators (e.g. Eq. (95) in Paper III).

For a *Hamiltonian* formulation of the band-structure problem, we need a basis set of energy-independent *smooth* functions analogous to the well-known *linear* APWs (LAPWs) and MTOs (LMTOs) [37]. This set [34, 35][36] is arrived at by N th-order polynomial interpolation (Lagrange) in the Hilbert space of KPWs with energies at a chosen mesh of $N + 1$ energies, E_0, \dots, E_N :

$$\chi_{R'l'm'}(\mathbf{r}) = \sum_{\nu=0}^N \sum_{Rlm}^{\text{active}} \phi_{Rlm}(E_\nu, \mathbf{r}) L_{Rlm, R'l'm'}(E_\nu). \quad (7)$$

Here, $\chi_{R'l'm'}(\mathbf{r})$ is a member of the active set of NMTOs and $L(E_\nu)$ is the matrix of Lagrange coefficients, which is given by the kink matrix (5) evaluated at the points of the energy mesh. For an NMTO, the kinks at the hard spheres are reduced to discontinuities of the $(2N+1)$ st derivatives and for a quadratic ($N=2$) MTO (QMTO), as used for LiPB, this means that the 4 lowest radial derivatives are continuous, i.e. the QMTO is "supersmooth". Also the MT-Hamiltonian- and overlap matrices in the NMTO representation, $H = \langle \chi | -\Delta + \sum_R v_R | \chi \rangle$ and $O = \langle \chi | \chi \rangle$, are given by the kink matrix and its first energy derivative evaluated at the energy mesh –or more conveniently– as divided differences of its inverse, the Green matrix $G(E) \equiv K(E)^{-1}$ [see Eq.s (91), (94), and (95) in Ref. [36]].

The NMTO set may be arbitrarily small and, nevertheless, span the exact solutions at the $N+1$ chosen

energies of Schrödinger's equation for the MT potential to 1st order in the potential overlap. Specifically, a set with n NMTOs (per cell) yields n eigenfunctions and eigenvalues (energy bands), E , whose errors are proportional to respectively $(E - E_0) \dots (E - E_N)$ and $(E - E_0)^2 \dots (E - E_N)^2$. The choice of NMTO set, i.e. which orbitals to place on which atoms, merely determines the prefactors of these errors and the range of the orbitals. But only with chemically sound choices, will the delocalization of the KPWs, caused by the N-ization in Eq. (7), be negligible.

In order to explain this, we now consider the simple example of NaCl-structured NiO: Placing the three p -orbitals on every O, the five d -orbitals on every Ni, and letting the energy mesh span the 10 eV region of the pd -bands, generates a basis set of eight atomic-like NMTOs yielding the eight pd -bands and wave functions (see FIG.s 2 and 4 in Ref. [49] and FIG. 7 top in Ref. [51]). Placing merely the three p -orbitals on every O and letting the mesh span the 5 eV region of the O p -bands, generates a basis set, consisting of O p -like NMTOs with bonding d -like tails on the Ni neighbors, which yields accurate p -bands and wave functions (FIG. 7 bottom in Ref. [51]). Placing, instead, the five d -orbitals on every Ni and letting the mesh span the 4 eV region of the Ni d -bands, generates a basis set of Ni d -like NMTOs which have antibonding p -like tails on the O neighbors and yields accurate d -bands and wave functions (FIG. 7 center in Ref. [51]). With the five d -orbitals on Ni, *but* a mesh spanning the three O p -bands, we get three $d(t_{2g})$ -like Ni NMTOs, xy , xz , and yz , with large $pd\pi$ -bonding p -tails on the four O neighbors in the plane of the t_{2g} -orbital, plus the two $d(e_g)$ -like Ni NMTOs with huge $pd\sigma$ -bonding tails – on the two apical oxygens for $3z^2 - 1$, and on the four oxygens in the xy plane for $x^2 - y^2$. These fairly delocalized Ni d -NMTOs clearly exhibit the Ni-O bonding, but they form a schizophrenic basis set which yields the three O p -bands connected across the pd -gap to two of the five Ni d -bands by steep "ghost" bands.

This example indicates how the NMTO method can be used to explore covalent interactions in complex materials. Other examples may be found in Refs. [39–49]. Note that the fewer the bands to be picked out of a manifold, i.e. the more diluted the basis set, the more extended are its orbitals because the set is required to solve Schrödinger's equation in all space. The increased extent leads to an (exponentially) increased energy dependence of the KPWs and that requires using NMTOs with a finer energy mesh. As a consequence, the smaller the set, the more complicated its orbitals.

Generalized Wannier functions are finally obtained by orthonormalization of the corresponding NMTO set [see Chart (2)]. *Symmetrical orthonormalization* yields the set of Wannier functions, which we refer to as *Wannier orbitals* (WOs) because they are atom-centered with specific orbital characters. The localization of these WOs hinges on the fact that each KPW in the set vanishes (with a kink) inside the hard sphere of any other KPW

in the set. This condition essentially maximizes the on-site and minimizes the off-site Coulomb integrals and has the same spirit as the condition of minimizing the spread, $\langle \chi | |\mathbf{r} - \mathbf{R}|^2 | \chi \rangle$, used to define the maximally localized Wannier functions [50].

For LiPB, we used quadratic N(=2)MTOs and for the large-basis-set calculation chose the three energies $E_\nu = \pm 1$ and 0 Ry with respect to the MT zero, i.e. -22 , -8 and 6 eV with respect to the center of the gap, which is approximately the Fermi level (see FIG. 3). For the six-orbital calculation, we took $E_\nu = -0.8$, -0.4 , and 0.2 eV with respect to the center of the gap (see FIG. 22 in Paper II).

For the low-energy electronic structure of LiMo₆O₁₇ we need to pick from the sixty Mo 4d bands above the O 2p – Mo 4d gap (see FIG. 3) a conveniently small and yet separable set of bands around the Fermi level. In this case, where no visible gap separates such bands from the rest of an upwards-extending continuum, the NMTO method is uniquely suited for picking a subset of bands for which the Wannier set is intelligible and as localized as possible. This *direct generation* of WOs (through trial and error by inspecting the resulting bands like we discussed above for NiO) differs from the procedures for projecting localized Wannier functions from the Bloch functions of the computed band structure by judiciously choosing their phases [61, 62] or by minimizing the spread [50][19]. We shall return to it in Sect. V after the crystal structure and the basic electronic structure of LiPB has been discussed.

Since the resulting set of six NMTOs may have a fairly long range, all LDA calculations were performed in the representation of Bloch sums,

$$\chi_{Rm}(\mathbf{k}, \mathbf{r}) \equiv \sum_{\mathbf{T}} \chi_{Rm}(\mathbf{r} - \mathbf{T}) e^{2\pi i \mathbf{k} \cdot \mathbf{T}}, \quad (8)$$

of orbitals translated by the appropriate lattice vector, \mathbf{T} . Specifically, the screening of the structure matrix was done \mathbf{k} -by- \mathbf{k} . In order to obtain printable WOs – obtained by symmetrical orthonormalization of the NMTOs – and a portable Hamiltonian whose $H_{R'm', R+Tm}$ element is the integral for hopping between the WOs centered at respectively \mathbf{R}' and $\mathbf{R} + \mathbf{T}$, we need to Fourier transform back to real space:

$$H_{R'm', R+Tm} = |\mathbf{a} \cdot \mathbf{b} \times \mathbf{c}| \int_{\text{BZ}} d^3k e^{-2\pi i \mathbf{k} \cdot \mathbf{T}} H_{R'm', Rm}(\mathbf{k}). \quad (9)$$

Here, the integral with its prefactor is the average over the BZ, as is appropriate when the localized orbital is normalized to unity. Moreover, $H_{R'm', Rm}$ is the energy of the orbital when $m=m'$, and the crystal-field term when $m \neq m'$. The Hamiltonian (9), truncated after $|\mathbf{R} - \mathbf{R}' - \mathbf{T}|$ exceeds some distance, the lattice constant a for LiPB, we shall refer to as the *tight-binding* (TB) Hamiltonian (Sect. VI). This truncation makes its energy-band eigenvalues more smooth and wavy than those of $H_{R'm', Rm}(\mathbf{k})$.

To the MT Hamiltonian, we finally add the second-order correction for the tongue-overlap and the full-potential perturbation [36, 63]. Products of NMTOs –as needed for evaluation of matrix elements and the charge density– are evaluated as products of partial waves limited to their MT spheres plus products of screened spherical waves [36, 51]. The latter are smooth functions and are interpolated across the interstitial from their first three radial derivatives at the hard sphere [28]. In order to make it trivial to solve Poisson’s equation, this interpolation uses spherical waves which –in order to make the matching at the hard spheres explicitly– are screened to have all phase shifts with $l \leq 4$ equal to those of hard spheres.

The band structure obtained from our full-potential LDA calculation with the large NMTO basis set agrees well with LDA and GGA control calculations performed with the LAPW method. We did not include the spin-orbit coupling in the NMTO calculation, but did so with the LAPW method and show the result in Paper II FIG. 23 together with the LDA TB bands.

III. CRYSTAL STRUCTURE

The crystal structure of LiPB was determined at room temperature and described by Onoda et al [2]. As shown in FIG. 2, there are two $\text{LiMo}_6\text{O}_{17}$ units in the primitive cell spanned by the translations \mathbf{a} , \mathbf{b} , and \mathbf{c} shown in (a). Whereas \mathbf{b} is orthogonal to both \mathbf{c} and \mathbf{a} , the latter has a tiny component along \mathbf{c} . The relative lengths of the primitive translation vectors are: $a/b \approx 2.311$ and $c/b \approx 1.720$, with $b = 5.523 \text{ \AA}$. We note that in much of the literature, especially experimental papers, an alternate axis labeling [1] is used¹³ with the definitions of a and c interchanged. Here we follow Onoda et al. [2]. Since \mathbf{a} , \mathbf{b} , and \mathbf{c} are nearly orthogonal, so are the primitive translations, \mathbf{a}^* , \mathbf{b}^* , and \mathbf{c}^* , of the reciprocal lattice. They are defined by:

$$\begin{pmatrix} \mathbf{a} \cdot \mathbf{a}^* & \mathbf{a} \cdot \mathbf{b}^* & \mathbf{a} \cdot \mathbf{c}^* \\ \mathbf{b} \cdot \mathbf{a}^* & \mathbf{b} \cdot \mathbf{b}^* & \mathbf{b} \cdot \mathbf{c}^* \\ \mathbf{c} \cdot \mathbf{a}^* & \mathbf{c} \cdot \mathbf{b}^* & \mathbf{c} \cdot \mathbf{c}^* \end{pmatrix} \equiv \begin{pmatrix} 1 & 0 & 0 \\ 0 & 1 & 0 \\ 0 & 0 & 1 \end{pmatrix}, \quad (10)$$

where we use the *crystallographic* definition of the scale of reciprocal space without the factor 2π on the right-hand side used in the *solid-state* definition. The former is traditionally used in diffraction and the latter in spectroscopy. In this paper, we use the crystallographic definition unless otherwise stated. The top of FIG. 3 shows half the Brillouin-zone (BZ) with origin at Γ and spanned by $\pm \frac{\mathbf{a}^*}{2}$ (B), $\pm \frac{\mathbf{b}^*}{2}$ (Y), and $\pm \frac{\mathbf{c}^*}{2}$ (Z). The Bloch vector,

$$\mathbf{k} = k_a \mathbf{a}^* + k_b \mathbf{b}^* + k_c \mathbf{c}^*, \quad (11)$$

is specified by its dimensionless (k_a, k_b, k_c) -components which, according to Eq.s (10) and (11), are the projections of \mathbf{k} onto respectively \mathbf{a} , \mathbf{b} , and \mathbf{c} , or equivalently: they are the projections onto the respective *directions* in units of a^{-1} , b^{-1} , and c^{-1} . Occasionally, we shall use the solid-state definition where the k components are the same, but \mathbf{a}^* , \mathbf{b}^* , \mathbf{c}^* , and \mathbf{k} are 2π larger, e.g. the Fermi vector for stoichiometric LiPB has length $(\pi/2)b^{-1} = 0.2844 \text{ \AA}^{-1}$ instead of $(1/4)b^{-1}$.

The most relevant symmetry points have $k_a=0$, and are: $(k_b, k_c)=Z(0, \frac{1}{2})$, $Y(\frac{1}{2}, 0)$, $\Gamma(0, 0)$, $C(\frac{1}{2}, \frac{1}{2})$, $W(\frac{1}{2}, \frac{1}{4})$, $\Lambda(0, \frac{1}{4})$, plus their equivalents. Higher BZs are shifted by reciprocal lattice vectors, \mathbf{G} , which means that k_a , k_b , and k_c are shifted by integers, which we name respectively L , M , and N and shall use in Sect. VI, and in Sect.s IX B 1, and X C in Paper II.

A simplifying –hitherto overlooked– *approximate* view of the complicated structure in FIG. 2 is that all Mo atoms are on a lattice spanned by the primitive translations:

$$\frac{\mathbf{c} + \mathbf{a}}{6} \mp \frac{\mathbf{b}}{2} \equiv \frac{\mathbf{x}}{\mathbf{y}} \quad \text{and} \quad \frac{\mathbf{c}}{2} - \frac{\mathbf{c} + \mathbf{a}}{6} \equiv \mathbf{z}. \quad (12)$$

These are orthogonal to within a few degrees and their lengths, 3.82 \AA , are equal to within 0.3%. This means that all 12 Mo atoms approximately form a simple cubic lattice, 12 times finer than the proper lattice. In FIG. 2 (c), the structure is turned to have \mathbf{z} in the vertical direction, and \mathbf{x} and \mathbf{y} in the horizontal plane. This view is useful for understanding the structure, the computed Wannier orbitals and the measured ARPES, but should not be overstretched. Using for instance the inverse to the transformation (12),

$$\mathbf{a} = 2(\mathbf{x} + \mathbf{y} - \mathbf{z}), \quad \mathbf{b} = \mathbf{y} - \mathbf{x}, \quad \mathbf{c} = \mathbf{x} + \mathbf{y} + 2\mathbf{z}, \quad (13)$$

and assuming the *xyz* system to be orthonormal leads to: $a = 2\sqrt{3}$, $b = \sqrt{2}$, and $c = \sqrt{6}$ times 3.82 \AA , which are wrong by respectively +3.7, –2.2, and –2.1 per cent.

As specified in FIG. 2 (a), of the twelve Mo sites in the primitive cell, six are inequivalent. Four of these (dark-green Mo1 and Mo4, and green Mo2 and Mo5) are six-fold coordinated with oxygen (dark yellow and yellow) in the $\pm x$, $\pm y$, and $\pm z$ directions and form a network of *corner-sharing* MoO_6 *octahedra*. We shall call them octahedral molybdenums. The remaining two types of Mo (light-green Mo3 and Mo6) are four-fold coordinated with oxygen (yellow and light yellow). The latter, *tetrahedrally* coordinated Mo atoms (light green, set in parentheses in the following) form double layers, which separate the network of corner-sharing MoO_6 octahedra into *slabs*. The crystals cleave between slabs.

Such a slab has the form of a *staircase* with steps of *bi-ribbons* stacked with period \mathbf{c} as seen in FIG. 2 (c).

¹³ It is, therefore, essential to check any particular article for these definitions.

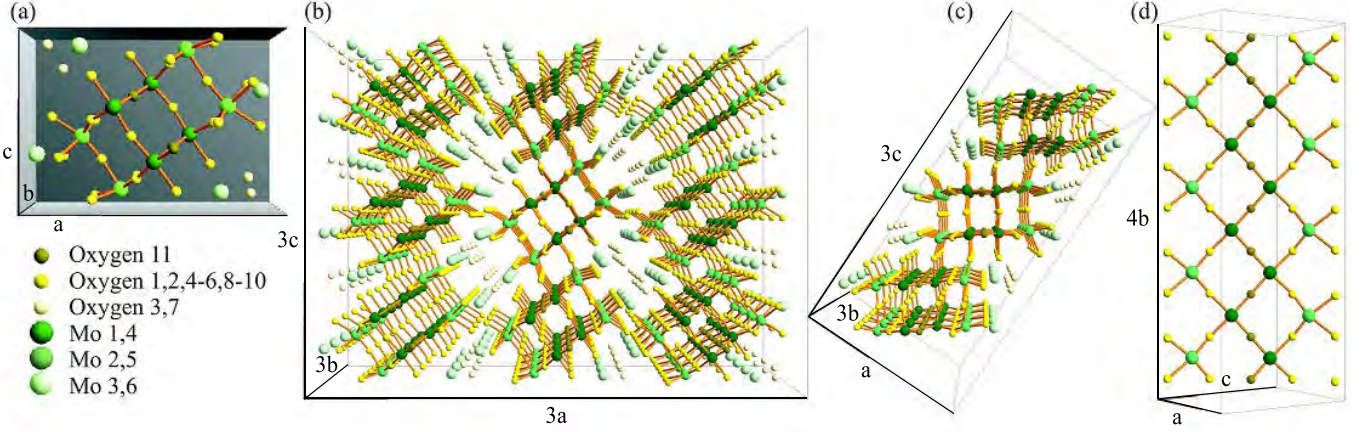


FIG. 2: Crystal structure of $\text{LiMo}_6\text{O}_{17}$. Li (not shown) is intercalated in the hollows near light-green Mo and light-yellow O atoms. (a) primitive cell spanned by the translation vectors \mathbf{a} , \mathbf{b} , and \mathbf{c} . Whereas \mathbf{b} is orthogonal to both \mathbf{c} and \mathbf{a} , the latter has a one-per-cent component along \mathbf{c} . The relative lengths of the translation vectors are: $a/b \approx 2.31$ and $c/b \approx \sqrt{3}$. The primitive cell contains two strings: (Mo3) - Mo2 - Mo1 - Mo4 - Mo5 - (Mo6) and the inverted one: (MO6) - MO5 - MO4 - MO1 - MO2 - (MO3). When we need to distinguish between two equivalent sites (related by inversion), we use upper-case letters for the one in the upper string. Together, the two strings form a bi-string. (b) a $3 \times 3 \times 3$ supercell showing bc -slabs translated by $\pm \mathbf{a}$. The slabs are separated by Mo3 and Mo6 (light green). (c) A single slab, rotated such that six-fold coordinated Mo (green and dark green) have their bonds to O in the vertical, z , and two horizontal, x and y , directions Eq. (12). Oriented this way, see also Chart (14), the slab forms a staircase running up the c -direction, i.e. with the steps translated by \mathbf{c} . A single step is a bi-ribbon formed by translating a bi-string infinitely many times by \mathbf{b} . The midpoint between Mo1 and a nearest MO1 in the same bi-ribbon is a center of inversion. The planes perpendicular to \mathbf{b} containing Mo1 and Mo5, as well as those containing Mo4 and Mo2, are mirror planes. The sequence along the vertical, almost straight lines along z is: (MO6) - Mo5 - MO2 - Mo1 - MO4 - (Mo3) and Li intercalates between the Mo_3O_4 tetrahedron and the MO_3O_4 tetrahedron right above it [2]. (d) 4 primitive cells along b of a single ribbon. Along its center runs the dark-green $\text{Mo1}/\text{Mo4}$ zigzag chain. Parallel herewith and shifted by \mathbf{z} [see (c) and Chart (15)] is the partner ribbon with its $\text{MO4}/\text{MO1}$ zigzag chain [see also FIG. 1 in Ref. [25]].

Schematically, this is:

$$\begin{array}{c}
 \mathbf{c} \nearrow \\
 \mathbf{a} \searrow \\
 \mathbf{z} \uparrow
 \end{array}
 \begin{array}{cccccc}
 \mathbf{2} & \mathbf{1} & \mathbf{4} & \mathbf{5} & & \mathbf{2} & \mathbf{1} & \mathbf{4} \\
 \mathbf{1} & \mathbf{2} & & & \mathbf{5} & \mathbf{4} & \mathbf{1} & \mathbf{2} \\
 \mathbf{4} & \mathbf{5} & & & \mathbf{2} & \mathbf{1} & \mathbf{4} & \mathbf{5} \\
 & & \mathbf{5} & \mathbf{4} & \mathbf{1} & \mathbf{2} & & \mathbf{5} \\
 & & \mathbf{2} & \mathbf{1} & \mathbf{4} & \mathbf{5} & & \mathbf{2} \\
 \mathbf{5} & \mathbf{4} & \mathbf{1} & \mathbf{2} & & \mathbf{5} & \mathbf{4} & \mathbf{1} \\
 \mathbf{2} & \mathbf{1} & \mathbf{4} & \mathbf{5} & & \mathbf{2} & \mathbf{1} & \mathbf{4}
 \end{array}, \quad (14)$$

where the octahedral molybdenums lying in the same ac -plane are either normal- or bold-faced. The distance between such ac -planes is $\frac{b}{2}$. A *single ribbon* is four octahedral molybdenums *wide* and, as seen here:

$$\begin{array}{c}
 \mathbf{b} \uparrow \\
 \mathbf{c} + \mathbf{a} \rightarrow \\
 \mathbf{y} \nearrow \\
 \mathbf{x} \searrow
 \end{array}
 \begin{array}{cc}
 \text{Mo :} & \text{MO :} \\
 \begin{array}{cc}
 \mathbf{2} & \mathbf{4} \\
 \mathbf{1} & \mathbf{5} \\
 \mathbf{2} & \mathbf{4} \\
 \mathbf{1} & \mathbf{5} \\
 \mathbf{2} & \mathbf{4} \\
 \mathbf{1} & \mathbf{5}
 \end{array} &
 \begin{array}{cc}
 \mathbf{5} & \mathbf{1} \\
 \mathbf{4} & \mathbf{2} \\
 \mathbf{5} & \mathbf{1} \\
 \mathbf{4} & \mathbf{2} \\
 \mathbf{5} & \mathbf{1} \\
 \mathbf{4} & \mathbf{2}
 \end{array}
 \end{array}, \quad (15)$$

and in FIG.s 2 (c) and (d), extends indefinitely in the b -direction and lies in the horizontal xy -plane containing the vectors $\mathbf{b} = \mathbf{y} - \mathbf{x}$ and $\mathbf{c} + \mathbf{a} = 3(\mathbf{x} + \mathbf{y})$. The

lower half of a bi-ribbon, seen in the left-hand panel of Chart (15), consist of (Mo3) - Mo2 - Mo1 - Mo4 - Mo5 - (Mo6) *strings* separated by \mathbf{b} and can be taken either as a zigzag line changing translation between \mathbf{y} and \mathbf{x} , and thus running along $\mathbf{c} + \mathbf{a}$, or as a nearly straight line running along \mathbf{x} , or as one running along \mathbf{y} [see (d) and (15)]. In the following, we shall refer to these as respectively $(\mathbf{c} + \mathbf{a})$ -zigzag, \mathbf{x} -, and \mathbf{y} strings.

The *upper* ribbon is shown to the right in Chart (15). Its Mo sequence, (MO6) - MO5 - MO4 - MO1 - MO2 - (MO3), is *inverted* such that e.g. MO4 is on top of Mo1. When we *need* to distinguish between two equivalent sites related by inversion in their midpoint – a center of inversion for the entire crystal – we use upper-case letters for the one in the upper ribbon.

Note that the $(\mathbf{c} + \mathbf{a})$ -zigzag string is different from – and perpendicular to – the $\text{Mo1}/\text{Mo4}$ zigzag chain along \mathbf{b} , the backbone of the electronic 1D xy -band shown in FIG.1 of Ref. [25] together with its partner $\text{MO4}/\text{MO1}$ in the upper ribbon.

A. c -dimerization

The vectors from Mo1 to its two nearest MO1 neighbors inside and outside the bi-ribbon are respectively

$\frac{\mathbf{c} \pm \mathbf{b}}{2} - \mathbf{d}$ and $-(\frac{\mathbf{c} \pm \mathbf{b}}{2} + \mathbf{d})$ where

$$\mathbf{d} = 0.012\mathbf{a} + 0.033\mathbf{c} \quad (16)$$

is the *displacement dimerization*. Hence, the distances measured along \mathbf{c} from a ribbon to its neighbors inside and outside the bi-ribbon are respectively 6.6% smaller and 6.6% larger than the average distance $\frac{\mathbf{c}}{2}$.

Due to the stacking (14) into a staircase of bi-ribbons, Mo4 differs from Mo1, and Mo5 differs from Mo2, in having *no* neighbor belonging to the next bi-ribbon, i.e., they have only *one* octahedral Mo neighbor along z . As seen in Charts (14) and (15), Mo1 has six, Mo4 five, Mo2 four, and Mo5 three nearest Mo neighbors which are octahedrally coordinated with oxygen.

In the next section, we shall explain –and later demonstrate by computation and experiment– that the six low-energy bands are described by the six *planar* t_{2g} Wannier orbitals (WOs), $w_m(\mathbf{r})$ and $W_m(\mathbf{r})$ ($m=xy, xz, yz$), centered¹⁴ on respectively Mo1 and on MO1. These sites, separated by $\frac{\mathbf{c} \pm \mathbf{b}}{2} - \mathbf{d}$, are *special* in having a *full* nearest-neighbor shell of octahedral molybdenums and therefore best preserve the t_{2g} symmetry of the WO and are least sensitive to the *steps* of the staircase, the second cause for the *dimerization*. Such a WO (FIG. 9) spreads substantially onto the four nearest Mo neighbors in the orbital's plane with amplitudes falling in the same order as the above-mentioned Mo coordination of those neighbors. As a result of this, and the smallness of the displacement dimerization (16), the two $t_{2g,m}$ WOs are *approximately* related by *half a lattice translation*:

$$W_m\left(\mathbf{r} - \frac{\mathbf{c} + \mathbf{b}}{2}\right) \approx w_m(\mathbf{r}). \quad (17)$$

However, the *exact* relation is:

$$W_m\left(\mathbf{r} - \frac{\mathbf{c} + \mathbf{b}}{2} + \mathbf{d}\right) = w_m(-\mathbf{r}), \quad (18)$$

and its differences, $W_m(\mathbf{r} - \frac{\mathbf{c} + \mathbf{b}}{2} + \mathbf{d}) - W_m(\mathbf{r} - \frac{\mathbf{c} + \mathbf{b}}{2})$ and $w_m(-\mathbf{r}) - w_m(\mathbf{r})$, to the approximate relation (17) will be referred to as respectively the *displacement-* and the *inversion dimerization*.

A consequence of the approximate translational equivalence (17), which may be seen to hold far better for the xy - than for the xz - and yz WOs, is that the low-energy band structure, $E_j(\mathbf{k})$ with $j=1-6$ (e.g. FIG. 6), approximately consists of 3 bands, $E_m(\mathbf{k})$, one with each m -character, and extending in a *double zone* of the *sparse* reciprocal sublattice spanned by

$$(\mathbf{a}^*, \mathbf{c}^* + \mathbf{b}^*, \mathbf{c}^* - \mathbf{b}^*). \quad (19)$$

This is the reciprocal of the *un-dimerized* lattice spanned by

$$\left(\mathbf{a}, \frac{\mathbf{c} + \mathbf{b}}{2}, \frac{\mathbf{c} - \mathbf{b}}{2}\right) = (\mathbf{a}, \mathbf{y} + \mathbf{z}, \mathbf{x} + \mathbf{z}) \quad (20)$$

with only *one* $\text{LiMo}_6\text{O}_{17}$ unit per primitive cell. The two last translations (20), we shall call *pseudo* translations. If expression (17) were true, the $E_m(\mathbf{k})$ band would be equivalent to the one translated by (any odd number times) $-\mathbf{c}^*$, e.g. with $E_m(\mathbf{k} + \mathbf{c}^*)$, but the presence of the inversion- and displacement dimerizations, (18) and (16), cause these two bands to gap where they cross, i.e. at the boundaries of the small zones. The resulting band structure is periodic in the proper (small) zone, corresponding to the proper primitive cell with *two* $\text{LiMo}_6\text{O}_{17}$ units, and has six continuous bands, two for each m , of which the lower is approximately $E_m(\mathbf{k})$ and the higher is approximately $E_m(\mathbf{k} + \mathbf{c}^*)$ in the odd-numbered zones; and the other way around in the even-numbered zones. As we shall see in Paper II, ARPES approximately sees only the $E_m(\mathbf{k})$ -like band, i.e. both bands, but separated in zones, and this will allow us to resolve the splitting and the perpendicular dispersion of the two quasi-1D bands in the gap.

The *un-dimerized* lattice has *one* $\text{LiMo}_6\text{O}_{17}$ unit per primitive cell and is spanned by the primitive translations (20) where, on the right-hand side, we have used the approximate relation (13). This shows that the un-dimerized lattice is 2D and hexagonal in the planes perpendicular to \mathbf{a} . This is the structure of the purple bronzes isoelectronic with LiPB, $\text{NaMo}_6\text{O}_{17}$ and $\text{KMo}_6\text{O}_{17}$, where CDW fluctuations with wavevector \mathbf{c}^* have been observed below 120 K and have been explained as driven by the simultaneous gapping of the 1D xz - and the yz Fermi-surface (FS) sheets by one and the same nesting vector, \mathbf{c}^* [30, 64]. The lattice reciprocal to the un-dimerized one is spanned by (19), and its BZ is the double zone of the dimerized structure, i.e. that of LiPB shown in FIG. 8. Hence, we may consider the structure of quasi-1D LiPB as the CDW dimerization of quasi-2D Na- or KPB, whose electronic structure consists of the 1D xy -, yz -, and xz -bands dispersing at 120° relatively to each other in the plane perpendicular to \mathbf{a} . The reason why not also the xy FS sheets gap away is that relation (17) holds much better for the xy WOs than for the xz and yz WOs.

For comparison with Charts (14) and (15), the un-dimerized slab is:

$$\begin{array}{c} \mathbf{c} \nearrow \\ \mathbf{a} \searrow \\ \mathbf{z} \uparrow \end{array} \begin{array}{|c|c|c|c|c|c|c|} \hline 4 & 1 & 2 & & 5 & 4 & 1 & 2 \\ \hline 1 & 2 & & & 5 & 4 & 1 & 2 \\ \hline 4 & & & & 5 & 4 & 1 & 2 \\ \hline & & & & 5 & 4 & 1 & 2 \\ \hline & & & & 5 & 4 & 1 & 2 \\ \hline 5 & 4 & 1 & 2 & & 5 & 4 & 1 \\ \hline 4 & 1 & 2 & & 5 & 4 & 1 & 2 \\ \hline \end{array}, \quad (21)$$

where the steps of the staircase are smoothed out to a

¹⁴ We use a notation according to which a function, e.g., $\phi_R(\mathbf{r})$, $w(\mathbf{r}) \equiv w_{\text{Mo1}}(\mathbf{r})$, or $W(\mathbf{r}) \equiv W_{\text{MO1}}(\mathbf{r})$, of the space vector \mathbf{r} is centered at $\mathbf{r} = \mathbf{R} \equiv \mathbf{R}_R$, whereas a function such as $\phi_R(r) Y_{lm}(\hat{\mathbf{r}})$ of $r \equiv |\mathbf{r}|$ and $\hat{\mathbf{r}} \equiv \mathbf{r}/|\mathbf{r}|$ is centered at the origin.

ramp, and the two ribbons are identical:

$$\begin{array}{c} \mathbf{b} \\ \mathbf{c} + \mathbf{a} \\ \mathbf{y} \\ \mathbf{x} \end{array} \begin{array}{c} \uparrow \\ \nearrow \\ \searrow \end{array} \begin{array}{|c|c|} \hline \text{Mo :} & \text{Mo :} \\ \hline 4 & 2 \\ 5 & 1 \\ 4 & 2 \\ 5 & 1 \\ 4 & 2 \\ 5 & 1 \\ \hline \end{array} \quad (22)$$

B. b-dimerization

An unrelated and different dimerization is the one known from the description of the 1D band structure as two, approximately 4 eV broad, $\frac{1}{4}$ -filled xy bands [FIG. 3 and Eq.s (23)-(24)] running on zigzag chains along \mathbf{b} [24,25] and with the nearest neighbor Mo1-Mo4 hopping integral $t \sim -1$ eV. In this view, Mo1 and Mo4 are inequivalent because of a dimerization from $\frac{b}{2}$ to \mathbf{b} . In reciprocal space, this dimerization is from $2\mathbf{b}^*$ to \mathbf{b}^* and causes gaps at $k_b = \pm\frac{1}{2} \approx \pm 2k_F$ which separate the broad xy bands into two lower $\frac{1}{2}$ -filled and two higher empty bands. The two latter bands will *not* be described by our set of six WOs, which are essentially Mo1-Mo4 bonding orbitals (FIG. 9), but would require the inclusion of also Mo1-Mo4 anti-bonding orbitals, thus leading to a basis set unpractically large for our purpose of understanding the photoemission from the occupied bands.

IV. BASIC ELECTRONIC STRUCTURE

Shortly after the structural determination, Whangbo and Canadell [24] used the extended Hückel method to calculate and explain the basic electronic structure, but it took almost twenty years before a charge-self-consistent calculation could be performed. This was done by Popović and Satpathy [25] who used the LDA-DFT and the LMTO method. In the following, we shall explain and expand on these works using the insights gained from the view of the structure given in the previous section and from the results of the WO calculations to be presented in Sect.s V and VI.

In FIG. 3, we show the LDA energy bands over a range of ± 9 eV around the Fermi level, together with their density of states projected onto O (green) and onto tetrahedrally- (blue) and octahedrally- (red) coordinated Mo. The bands between -8 and -2 eV have predominantly O $2p$ character and those extending upwards from $B \sim -0.7$ eV predominantly Mo $4d$ character and, above $+0.8$ eV, also Mo $5s$ and $5p$ characters. The states in the O $2p$ band are bonding linear combinations with Mo $5s$, $5p$, and $4d$ orbitals, the more bonding, the lower their energy. The states in the Mo $4d$ band are anti-bonding linear combinations with O $2s$ and $2p$ orbitals; the more anti-bonding, the higher their energy.

The 2 eV gap between the O $2p$ -like and Mo $4d$ -like bands is –for the purpose of counting– ionic with Li donating one and Mo six electrons to- and O acquiring two electrons from the Mo $4d$ -like bands above the gap, which thereby hold $2(1 + 6 \times 6 - 17 \times 2) = 6$ electrons per $2(\text{LiMo}_6\text{O}_{17})$. Had this charge been spread uniformly over all molybdenums, this would correspond to a Mo $d^{0.5}$ occupation.

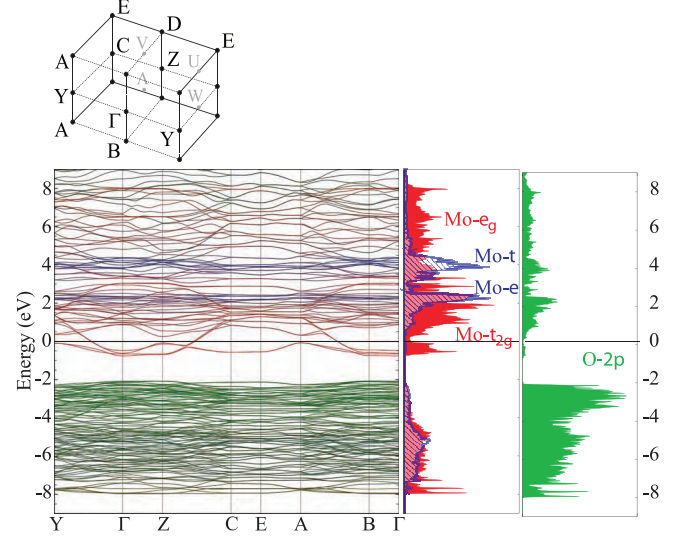


FIG. 3: The top shows half ($k_c \geq 0$) the (1st) Brillouin-zone of $\text{LiMo}_6\text{O}_{17}$ with the labeling of the symmetry points for $P2_1/m$ obtained from the Bilbao crystal server [65]. The most relevant symmetry points have $k_a=0$ and are: $(k_b, k_c)=\Gamma(0,0)$, $Y(\frac{1}{2},0)$, $W(\frac{1}{2},\frac{1}{4})$, $C(\frac{1}{2},\frac{1}{2})$, $Z(0,\frac{1}{2})$, $\Lambda(0,\frac{1}{4})$, and their equivalents. Below is the LDA band-structure calculated with the large basis set of 336 NMTOs (left) and its partial densities of states (right) over a wide energy range. The zero of energy is the Fermi level of the stoichiometric compound.

The $4d$ orbitals forming the most anti-bonding and bonding states with O are the e_g orbitals, $3z^2 - 1$ and $x^2 - y^2$, on the *octahedrally* coordinated Mo because their lobes point *towards* the two O neighbors along z and the four O neighbors in the xy plane, respectively, and thereby form $pd\sigma$ bonds and anti-bonds. Not only the e_g orbitals on the octahedrally coordinated Mo, but all $4d$ orbitals (t and e) on the *tetrahedrally* coordinated Mo form filled bonding and empty anti-bonding states with their O neighbors, and thereby contributing to the stability of the crystal. However, as seen from the projected densities of states in FIG. 3, none of them contribute to the LDA bands within an eV around the Fermi level, which are the ones of our primary interest. So as long as there are no additional perturbations or correlations with energies in excess of this, which is assumed in the $\frac{1}{2}$ -filled models, the Mo t and e orbitals are uninteresting for the low-energy electronics, and so are the Li $2s$ orbitals which contribute two bands several eV above the Fermi level and mix a bit with the oxygen states several eV below E_F .

Although the MoO_4 tetrahedra do not contribute any electrons near the Fermi level, their arrangement in double layers perpendicular to \mathbf{a} , separating the staircases of corner-sharing octahedra, has an important impact on the low-energy electronic structure: It suppresses the hopping between the low-energy orbitals across the double layer to the extent that we shall neglect it in our TB model for the six lowest bands ¹⁵.

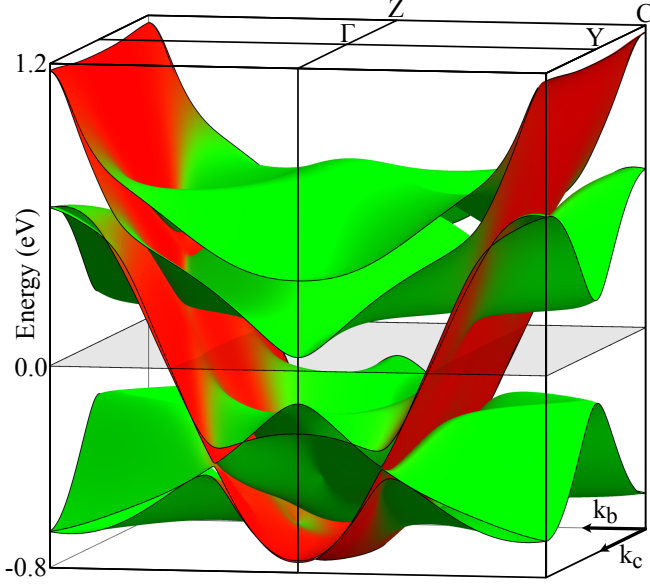


FIG. 4: LDA t_{2g} energy band structure and Fermi level of LiPB at half filling. Red and green colors indicate respectively xy and xz/yz characters. The energy region is from 0.8 eV below to 1.2 eV above E_F (see FIG. 3) and the \mathbf{k} -space region is the BZ (see FIG. 8). The LDA TB parameters listed in Tables (43)-(47) were used, like in FIG. 22 (a) in Paper II.

A. The t_{2g} bands

The remaining $4d$ orbitals on octahedrally coordinated Mo are the t_{2g} orbitals, xy , xz , and yz , whose lobes point *between* the four O neighbors in respectively the xy , xz , and yz planes and therefore form relatively weak $pd\pi$ bonds and antibonds, e.g. $\text{Mo}xy \pm \text{O}y$ on the $\frac{x}{2}$ bond. Whereas the bonds are dominated by oxygen and form bands that are part of the O $2p$ continuum below

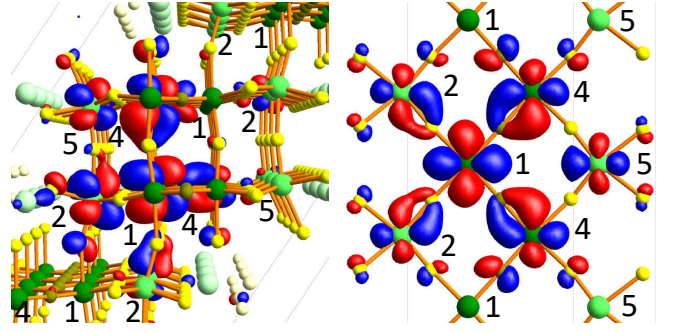


FIG. 5: *Left*: yz standing-wave state with $k_c + k_b = \pm \frac{1}{2}$ which behaves like $\cos 2\pi \frac{1}{2} (r_c + r_b)$. View along \mathbf{b} as in FIG. 2 (c) and Chart (14). *Right*: xy standing-wave state with $|k_b| = \frac{1}{4} \sim k_F$ which behaves like $\cos 2\pi \frac{1}{4} r_b$. View along $-\mathbf{z} \sim \mathbf{a} - \mathbf{c}$ as in (d) and Chart (15). The sign of a lobe is indicated by its color. See also FIG. 9 with caption.

about -4 eV, the *antibonds* are dominated by Mo and form $4 \times 2 \times 3 = 24$ bands which extend from $+3.0$ eV down to the bottom of the Mo $4d$ continuum at -0.7 eV. This spread in energy is *conventionally* described as due to hopping between *dressed* $\text{Mo}t_{2g}$ orbitals, where the dressing consists of the $pd\pi$ anti-bonding tails on the four oxygens in the plane of the orbital. Since the dressed orbitals are planar, the strongest hoppings are between *like* t_{2g} orbitals which are nearest neighbors in the same plane, e.g. as seen in the right-hand panel of FIG. 5 between the dressed xy orbital on Mo1_o and those on Mo4_x , Mo4_y , Mo2_{-x} , and Mo2_{-y} , or as seen in the left-hand panel between the dressed yz orbital on Mo1_o and those on Mo4_y , Mo4_z , Mo2_{-y} , and Mo2_{-z} . These hoppings are $dd\pi$ -like and of magnitude $t = -1$ eV.

The main dispersion of the xy band is, therefore, in the direction of the xy lobe pointing along $\mathbf{y} - \mathbf{x} = \mathbf{b}$, that of the yz band is in the direction of the yz lobe pointing along $\mathbf{y} + \mathbf{z} = \frac{\mathbf{c} + \mathbf{b}}{2}$ (see left-hand FIG. 5), and that of the xz band is in the direction of the xz lobe pointing along the $\mathbf{x} + \mathbf{z} = \frac{\mathbf{c} - \mathbf{b}}{2}$; see Charts (14) and (15)

1. The four xy bands.

The right-hand panel of FIG. 5 shows the xy standing-wave state with $|k_b| = \frac{1}{4} \sim k_F$ which behaves like $\cos 2\pi k_b \mathbf{b}^* \cdot \mathbf{b} r_b \equiv \cos 2\pi \frac{1}{4} r_b$, i.e. is even around the $\mathbf{c} + \mathbf{a}$ line through Mo1 and Mo5 and has nodes at the Mo1 - Mo5 lines translated by $\pm \mathbf{b}$. Here, the orientation is like in FIG. 2 (d) with the Mo numbering given in the left-hand panel of Chart (15). We see that the amplitudes of the dressed xy orbitals are largest at Mo1 and decrease in the order Mo4 , Mo2 , and Mo5 , thus following the decrease of the Mo coordination mentioned in Sect. III A. The dressed orbitals on the four nearest neighbors (Mo4 at x and y , and Mo2 at $-x$ and $-y$) anti-bond to the central orbital, i.e. nearest-neighbor lobes have different colors. This is the reason why the overlap from the

¹⁵ As seen in FIG. 2 (b) and Chart (14), the shortest path for hopping of low-energy electrons across the double layer of tetrahedrally coordinated molybdenums is $\text{Mo5} - (\text{MO6}) - \text{MO5}$, i.e. from Mo5 in a bottom ribbon, along $-\mathbf{z}$ to (MO6) in the top ribbon of the neighboring staircase, and then along $-\mathbf{x}$ or $+\mathbf{y}$ to MO5 in that top ribbon. This zigzag path thus passes via merely *one* tetrahedrally coordinated Mo atom and gives rise to the slight k_a -dispersion of the two nearly degenerate xy bands seen most clearly in FIG. 3 along CE and 1 eV above the Fermi level.

neighboring dressed xy orbital weakens the O y (or x) amplitude on the common oxygen such that its contour merges with that of the weaker Mo neighbor. Hence, O p is $pd\pi$ anti-bonding with Mo1 xy and bonding with Mo4 xy and Mo2 xy . The net result is $pd\pi$ non-bonding, essentially.

The xy band disperses almost exclusively in the \mathbf{b} direction, and now, we imagine going to the xy state with $|k_b| = \frac{3}{4} = \frac{1}{4} [\text{mod } \frac{1}{2}]$ and energy ~ 2.8 eV above E_F , i.e. to the state in the *next* xy band. Here, the signs (colors) of the dressed xy orbitals on the four nearest neighbors (Mo4 and Mo2) will have changed, whereby the overlaps on the common oxygens shared with Mo1 will have their amplitudes enhanced and the O y (or x) contour will be separated by a node, not only from the stronger Mo1- xy contour, but also from the weaker Mo4- xy (or Mo2- xy) contour. In the following, we shall refer to the xy band with the lower/higher energy as the Mo1-Mo4 bonding/anti-bonding band, although both of these bands are $pd\pi$ non- or anti-bonding; but the one with the lower energy has fewer $pd\pi$ nodes.

The dressed xy orbitals lie in the plane of a ribbon, and those along the infinite zigzag chain, $\overset{\times}{\rightarrow}$ Mo1 $\overset{\times}{\rightarrow}$ Mo4 $\overset{\times}{\rightarrow}$, with *pseudo* translation $\frac{\mathbf{y}-\mathbf{x}}{2} = \frac{\mathbf{b}}{2}$ form the well-known [24][25][17] quasi-1D band with dispersion¹⁶:

$$\varepsilon_{xy}(\mathbf{k}) \sim 2t \cos \left(2\pi \mathbf{k} \cdot \frac{\mathbf{b}}{2} \right) = 2t \cos \pi k_b, \quad (23)$$

where $t \sim -1$ eV. Since \mathbf{b} , and not $\frac{\mathbf{b}}{2}$, is the proper lattice translation because Mo1 and Mo4 are not equivalent, the band must be folded from the large BZ bound by the midplanes ($k_b = \pm 1$) of the reciprocal-lattice vectors $\pm 2\mathbf{b}^*$, into the proper, small BZ bound by the midplanes ($k_b = \pm \frac{1}{2}$) of $\pm \mathbf{b}^*$ whereby it becomes $-2t \cos \pi k_b$. An equivalent prescription –more useful than BZ-folding, as we shall see below for the bonding yz and xz bands,– is to say that if \mathbf{k} must be limited to the proper, small BZ, then we must also consider the band,

$$\varepsilon_{xy}(\mathbf{k} + \mathbf{b}^*) \sim 2t \cos [\pi (k_b + 1)] = -2t \cos \pi k_b, \quad (24)$$

translated by the proper reciprocal lattice vector, $-\mathbf{b}^*$. Finally, the *inequivalence* of –or “dimerization into”– Mo1 and Mo4, couples the $xy(\mathbf{k})$ and $xy(\mathbf{k} + \mathbf{b}^*)$ bands, and where they are degenerate –which is for $|k_b| = \frac{1}{2}$, i.e. at the boundaries of the proper BZ (YC)– they are gapped by ± 0.3 eV. Since this gap is relatively large, the $xy(\mathbf{k})$ band is bonding and the $xy(\mathbf{k} + \mathbf{b}^*)$ band anti-bonding between Mo1 and Mo4 for \mathbf{k} inside the proper BZ. The latter, empty xy band, which extends from approximately 1.7 to 3.4 eV above E_F , we shall neglect in the bulk of the present papers, as was already mentioned in Sect. III B.

Degenerate and parallel with the Mo1-Mo4 bonding and anti-bonding xy bands running along the lower ribbon are MO4-MO1 bonding and anti-bonding XY bands running along the upper ribbon [see FIG. 2 (d), Chart (14), and the right-hand panel of Chart (15)]. Their $|k_b| = \frac{1}{4} \sim k_F$ standing-wave state looks like the one shown on the right-hand side of FIG. 5, but has MO1 on top of Mo4 and vice versa. Viewed along \mathbf{b} , the appearance of the xy and XY states is like that of the xy and XY WOs in the first two columns on the top row of FIG. 9. From there, we realize that these flat, parallel states are well separated, each one on its own ribbon, with no contribution on the oxygens in between. The $dd\delta$ -like hops between the xy and XY orbitals inside the same bi-ribbon ($t_\perp \equiv t_1 + u_1 \sim -14$ meV) and between the XY and xy orbitals in different bi-ribbons ($t'_\perp \equiv t_1 - u_1 \sim -8$ meV), give the bands a *perpendicular* (k_c -) *dispersion*, which is two orders of magnitude smaller than the k_b -dispersion given by Eq. (23). If all ribbons were translationally equivalent, i.e. if the primitive translations (neglecting \mathbf{a}) were $\mathbf{x} + \mathbf{z} = \frac{\mathbf{c}-\mathbf{b}}{2}$ and $\mathbf{y} + \mathbf{z} = \frac{\mathbf{c}+\mathbf{b}}{2}$, with reciprocal-lattice translations $\mathbf{c}^* - \mathbf{b}^*$ and $\mathbf{c}^* + \mathbf{b}^*$, the $dd\delta$ hopping would add

$$2t_1 [\cos \pi (k_c - k_b) + \cos \pi (k_c + k_b)] = 4t_1 \cos \pi k_b \cos \pi k_c$$

to Eq. (23). But since the primitive translations are really \mathbf{b} and \mathbf{c} , we must –if we want to confine \mathbf{k} to the proper BZ– also add the equivalent term translated by the proper reciprocal lattice vector¹⁷, $-\mathbf{c}^*$. As a result, we get for the two $\frac{1}{2}$ -filled xy bands:

$$\varepsilon_{xy} \left(\frac{\mathbf{k}}{\mathbf{k} + \mathbf{c}^*} \right) \sim 2t [1 \pm (2t_1/t) \cos \pi k_c] \cos \pi k_b, \quad (25)$$

where the distortion caused by the gap extending upwards from ~ 1.1 eV above E_F has been neglected. As long as \mathbf{k} is inside the 1st BZ ($|k_c| \leq \frac{1}{2}$), the $xy(\mathbf{k})$ band is bonding and the $xy(\mathbf{k} + \mathbf{c}^*)$ band anti-bonding between ribbons, i.e. between xy and XY . In the 2nd BZ ($|k_c - 1| \leq \frac{1}{2}$), the opposite is true (see FIG. 6). The translational *inequivalence* of the two ribbons –i.e. the dimerization into bi-ribbons– finally splits the degeneracy of the $xy(\mathbf{k})$ and $xy(\mathbf{k} + \mathbf{c}^*)$ bands at the BZ boundaries $|k_c| = \frac{1}{2}$ (the ZCED planes) by $\pm 2\sqrt{2}u_1 \cos \pi k_b$, which for $k_b = \frac{1}{4} \sim k_F$ is a mere ± 8 meV.

2. The two yz and the two xz bands.

In the planes perpendicular to the bi-ribbons [FIG. 2 (c) and Chart (14)] and cutting them along the \mathbf{y} -strings [FIG. 2 (d) and Chart (15)], lie the dressed yz

¹⁶ We denote energy bands $E(\mathbf{k}) = \varepsilon(\mathbf{k}) + E_0$, and their dispersions $\varepsilon(\mathbf{k})$. Here, E_0 is the center of the band.

¹⁷ Substituting \mathbf{c}^* by $-\mathbf{c}^*$ gives the same result because their difference, $2\mathbf{c}^*$, is a translation of the reciprocal lattice spanned by $\mathbf{c}^* - \mathbf{b}^*$ and $\mathbf{c}^* + \mathbf{b}^*$.

orbitals, and in the planes cutting along the \mathbf{x} -strings, lie the dressed xz orbitals. The left-hand panel of FIG. 5 shows that $|k_c + k_b| = \frac{1}{2}$ standing-wave state of the yz band which behaves like $\cos 2\pi \frac{1}{2} (r_c + r_b)$, i.e. is even around the Mo1-containing planes which are perpendicular to $\mathbf{c}^* + \mathbf{b}^*$ and has nodes in the MO1-containing planes. Like for xy state in the right-hand panel, the dressed yz orbitals on the four nearest neighbors in the plane of the orbital (MO4 at \mathbf{z} , Mo4 at \mathbf{y} , Mo2 at $-\mathbf{y}$, and MO2 at $-\mathbf{z}$) are $dd\pi$ anti-bonding with the dressed yz on the central Mo1, which means $pd\pi$ non-bonding with the oxygen. Here again, the amplitudes of the dressed yz orbitals decrease like the Mo coordination.

Whereas in the plane of the xy orbital, Mo4 –like Mo1– has four nearest neighbors of molybdenums coordinated octahedrally with oxygen, in the plane of the yz orbital, Mo4 has only three neighbors, and so does Mo2, while Mo5 has merely two. As noted in Sect. III A, this is due to the stacking into a staircase of bi-ribbons (14). As a result, the yz orbitals on the Mo1- and MO1-sharing zigzag double chain,

$$\begin{array}{c} \mathbf{c} \nearrow \\ \mathbf{a} \searrow \\ \mathbf{z} \uparrow \end{array} \left[\begin{array}{ccccccc} & & & \mathbf{5} & \rightarrow & \mathbf{4} & \uparrow \mathbf{1} \rightarrow \mathbf{2} \uparrow \\ & & & \rightarrow \mathbf{2} & \uparrow \mathbf{1} \rightarrow & \uparrow \mathbf{4} & \mathbf{5} \\ \mathbf{5} & \rightarrow & \mathbf{4} & \uparrow \mathbf{1} \rightarrow & \mathbf{2} \uparrow & & \\ \rightarrow \mathbf{2} & \uparrow \mathbf{1} \rightarrow & \mathbf{4} \uparrow & & \mathbf{5} & & \end{array} \right], \quad (26)$$

running up the staircase with pseudo translation $\mathbf{z} + \mathbf{y} = \frac{\mathbf{c} + \mathbf{b}}{2}$, form a quasi-1D band dispersing like

$$\varepsilon_{yz}(\mathbf{k}) = 2A_1 \cos \left(2\pi \mathbf{k} \cdot \frac{\mathbf{c} + \mathbf{b}}{2} \right) = 2A_1 \cos \pi (k_c + k_b), \quad (27)$$

with an effective hopping integral, $A_1 \sim -0.3$ eV and bandwidth $4|A_1| \sim 1.2$ eV. Because the hopping between ribbons proceeds via Mo4 inside the bi-ribbon, but via Mo2 between bi-ribbons, and because the former distance is shorter than the latter, the hopping integrals are different, respectively $A_1 + G_1 \sim -0.3 - 0.1 \sim -0.4$ eV and $A_1 - G_1 \sim -0.2$ eV. This dimerization into bi-ribbons causes \mathbf{c} , rather than $\frac{\mathbf{c} + \mathbf{b}}{2}$, to be a primitive lattice translation whereby the $yz(\mathbf{k} + \mathbf{c}^*)$ band with dispersion

$$\varepsilon_{yz}(\mathbf{k} + \mathbf{c}^*) = -2A_1 \cos \pi (k_c + k_b) \quad (28)$$

is equivalent to the $yz(\mathbf{k})$ band (27). Where these bands are degenerate, i.e. for $|k_c + k_b| = \frac{1}{2}$, they gap by $\pm 2|G_1| \sim \pm 0.2$ eV whereby they become:

$$\varepsilon_{yz} = \pm \sqrt{[2A_1 \cos \pi (k_c + k_b)]^2 + [2G_1 \sin \pi (k_c + k_b)]^2}. \quad (29)$$

For \mathbf{k} between the $|k_c + k_b| = \frac{1}{2}$ planes, the $yz(\mathbf{k})$ and $yz(\mathbf{k} + \mathbf{c}^*)$ bands are respectively bonding and anti-bonding between neighboring ribbons. The two yz bands, decorated by the \mathbf{k} -character (27), are shown in green in FIG. 6.

It should be noted that the gapping takes place for $|k_c + k_b| = \frac{1}{2}$, which is *not* at the boundary of the conventional BZ, $|k_b| = \frac{1}{2}$ and $|k_c| = \frac{1}{2}$ shown in FIG.s 3 and

8, but where the $\varepsilon_{yz}(\mathbf{k})$ and $\varepsilon_{yz}(\mathbf{k} + \mathbf{c}^*)$ bands are degenerate. Nevertheless, the zone centered at $\Gamma(0,0)$ and bound by the planes $|k_b| = \frac{1}{2}$ and $|k_c + k_b| = \frac{1}{2}$ (ZYAD) is a primitive cell of the reciprocal lattice, and we call it a *physical zone*, useful for understanding properties of the yz bands.

With the substitution: $\mathbf{b} \rightarrow -\mathbf{b}$, everything said about the yz bands holds for the xz bands (shown in blue in FIG. 6).

As regards choices of zones, we can either take:

$$|k_b| \leq \frac{1}{2} \text{ and } |k_c| \leq \frac{1}{2}, \quad (30)$$

$$|k_b| \leq \frac{1}{2} \text{ and } |k_c + k_b| \leq \frac{1}{2}, \quad (31)$$

$$\text{or } |k_b| \leq \frac{1}{2} \text{ and } |k_c - k_b| \leq \frac{1}{2}, \quad (32)$$

but *not* $|k_c + k_b| \leq \frac{1}{2}$ and $|k_c - k_b| \leq \frac{1}{2}$ whose volume (area) is only *half* the BZ volume (see FIG. 8). Expressions (30)-(32) thus define the *physical zones* for respectively the xy , the yz , and the xz bands.

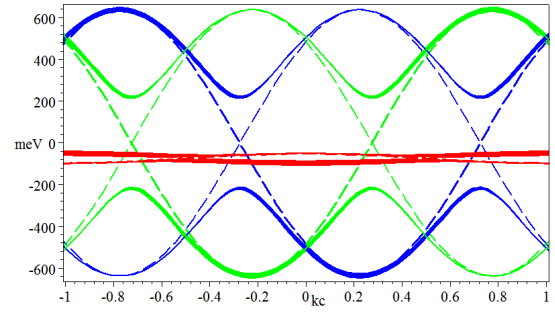


FIG. 6: The six pure- m t_{2g} bands ($m = yz$ green, xz blue, and xy red) as functions of k_c in the double zone ($-1 < k_c \leq 1$) and for $k_b = 0.225$, i.e. along the brown dot-dashed line containing P and Q in FIG. 8. 10% hole doping will place the Fermi level inside the red bands. The $m(\mathbf{k})$ and $m(\mathbf{k} + \mathbf{c}^*)$ bands, whose dispersions are described in Sect. IV A, have period $\Delta k_c = 2$ and are shown in respectively fat- and normal dashed lines. The $\{m(\mathbf{k}), m(\mathbf{k} + \mathbf{c}^*)\}$ -hybridized bands have period 1 and are shown in full lines. Their *additional* (vertical) fatness is proportional to the $|\mathbf{k}|$ -character and has period 2. The ARPES-refined TB parameters listed in Tables (43), (44), (45), and (49) were used and, accordingly, the zero of energy is the center of the gap, i.e., the common energy of the xz , XZ , yz , and YZ WOs. The Fermi level of samples G and H is at +75 meV.

3. Line-up of the six lowest t_{2g} bands

The bottoms of the xz and yz bands and those of the degenerate xy bands are *all* at $\Gamma(\mathbf{k} = \mathbf{0})$ and at the energy of that linear combination of the dressed xz , yz , or

xy orbitals which is the least anti-bonding between all octahedral molybdenums (FIG. 3). According to the LDA, these energies are: $B_{xz/yz} \sim E_F - 0.6$ eV and $B_{xy} \sim E_F - 0.7$ eV. Since the $4|A_1|$ width of the xz and yz bands is only about one third the $4|t|$ -width of the xy bands, the $4|G_1|$ -gap halfway up in the xz and yz bands extends between the energies $B_{xz/yz} + 2|A_1 \pm G_1| \sim \pm 0.2$ eV with respect to the Fermi level set by the $\frac{1}{2}$ -filled, lower xy bands. In the following Paper II (e.g. FIG. 22), we shall see that agreement with ARPES requires a 0.1 eV downward shift of the xz/yz bands with respect to the xy bands, whereby $B_{xz/yz} \sim E_F - 0.7$ eV $\sim B_{xy} \equiv B$. This low-energy t_{2g} band structure is shown in FIG. 6 along the line $k_b=0.225$ perpendicular to \mathbf{b} , the direction of quasi 1D conductivity.

In summary, since the 6 lowest bands are t_{2g} like, the 6 electrons would half fill them in case of weak Coulomb correlations, thus corresponding to a t_{2g}^3 configuration. Covalency between the xz and XZ orbitals, as well as between the yz and YZ orbitals, together with the availability of one xz and one yz electron per string, result in the covalent bonds which dimerize the ribbons into bi-ribbons and thereby gap the xz and yz bands into filled bonding and empty anti-bonding bands. The remaining one xy electron per string finally half fills the quasi-1D band dispersing strongly along \mathbf{b} .

The six t_{2g} bands are illustrated in FIG. 4, from where it is seen that the gaps in the green xz and yz bands are around the center of the red, metallic xy bands and, hence, around the grey, transparent Fermi level.

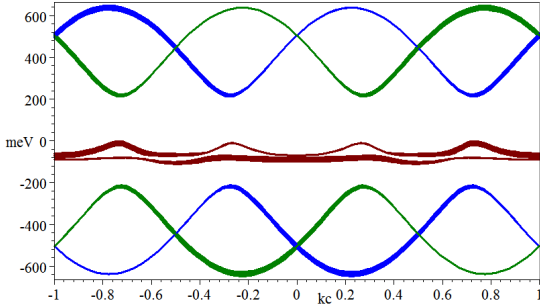


FIG. 7: As FIG. 6 ($k_b=0.225$), but including the hybridization of the \widetilde{xy} band (dark red) with the xz (blue) and yz (green) valence and conduction bands via Löwdin downfolding as explained in Paper III. This hybridization brings in the parameters $\alpha_n \pm \gamma_n$ and $a_n \pm g_n$ [Eq.s (39) and (46)]. Not included in this figure are the xy -hybridizations of the blue xz and the green yz bands, as well as the hybridization between the xz and yz bands.

4. Constant energy contours (CECs)

FIG. 8 shows the double zone, $|k_b| \leq \frac{1}{2}$ and $|k_c| \leq 1$, and –schematically and in weak lines– constant-energy contours (CECs) for the $xz(\mathbf{k})$ bands in blue, the $yz(\mathbf{k})$ bands in green, and the (almost) degenerate, $\frac{1}{2}$ -filled $xy(\mathbf{k})$ and $xy(\mathbf{k} + \mathbf{c}^*)$ bands (25) in red. The bottoms of these four bands are along respectively the blue, green, and red lines passing through $\Gamma(0,0)$. The tops of the $xz(\mathbf{k})$ and $yz(\mathbf{k})$ bands are along the blue and green lines passing through $\Gamma'(0, \pm 1)$. The top of the degenerate xy bands (which is a cusp because Eq. (25) neglects the Mo1-Mo4 gap) is along the red, vertical BZ boundary $|k_b| = \frac{1}{2}$.

For the degenerate xy bands, we also show the CECs for three energies close to the Fermi level corresponding to half-filling (red dot-dash), 10% hole- (brown dot-dash), and 10% electron (olive dot-dash) doping. For the gapped $xz(\mathbf{k})$ and $xz(\mathbf{k} + \mathbf{c}^*)$ bands we show the coinciding CECs for the valence- and conduction-band edges (blue solid lines), and similarly for the yz -band edges (green solid lines). The CECs for the $xz(\mathbf{k} + \mathbf{c}^*)$ and $yz(\mathbf{k} + \mathbf{c}^*)$ bands of course equal those for respectively the $xz(\mathbf{k})$ and $yz(\mathbf{k})$ bands, but translated along k_c by an odd integer.

As seen in FIG. 7 for $k_b=0.225$, corresponding to 10% hole-doping, the xz and yz valence-band edges running along $|k_c \mp k_b| = \frac{1}{2}$ (YZY') and merely 0.2 eV below the xy bands push *resonance peaks* up at $|k_c|=0.725$ and 0.275 in the upper xy band. This gives rise to “notches” pointing towards Z (FIG. 8) in the inner sheets of xy CECs with energies in the lower half of the gap. Near $k_c=0$ (FY) and $k_c=\pm 1$ (F'Y'), hybridization with the xz and yz valence and conduction bands, which are now 0.5 eV away (FIG. 7), reduces the $dd\delta$ -like splitting (25) between the two xy bands seen FIG. 6 to become almost a *contact* between the two xy bands and CECs. Near the BZ boundaries, $|k_c| = \frac{1}{2}$ (FC), mixing of the $xy(\mathbf{k})$ and $xy(\mathbf{k} + \mathbf{c}^*)$ bands and hybridization of the lower with the xz and yz conduction bands 0.5 eV above, pushes down *bulges* in the lower xy band, thus causing the outer CEC sheets to bulge outwards. We shall search for these features – predicted here for the first time – using new ARPES measurements in Paper III, devoted to the detailed study and explanation of the splitting and perpendicular dispersion of the quasi-1D metallic bands in the gap.

V. LOW-ENERGY WANNIER ORBITALS

In the previous section, our view moved from the energy scale of the Li 2s, Mo 5sp4d, and O 2p atomic shells to the decreasing energy scales of the Li^+ , Mo^{6+} , and O^{2-} ions, to the covalently bonded MoO_4 tetrahedra and MoO_6 octahedra and, finally, to the low-energy bands of the MoO_6 octahedra condensed into strings, ribbons, and staircases of bi-ribbons by sharing of the $pd\pi$ -bonded O corners. This change of focus from large

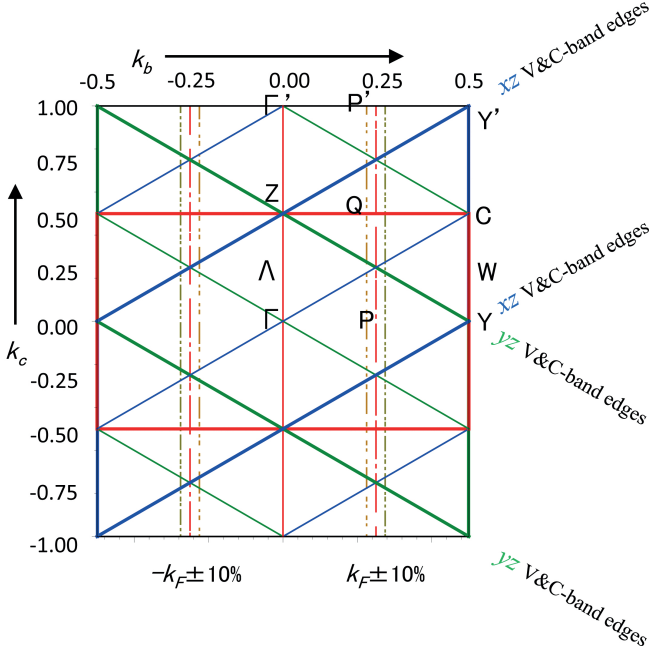


FIG. 8: Double zone: $-0.5 < k_b \leq 0.5$ and $-1 < k_c \leq 1$. The red, blue, and green solid lines show the *physical* zones for respectively the xy , xz , and yz pure bands; see Eq.s (30), (32), and (31). The red zone is the BZ, and its irreducible part is the one with $0 \leq k_c \leq 0.5$. The reciprocal-lattice points are: $\mathbf{G} = M\mathbf{b}^* + N\mathbf{c}^*$, i.e. $(k_b, k_c) = (M, N)$, with M and N integers. Those (19) with $M + N$ even, form the lattice reciprocal of the un-dimerized lattice (20) whose BZ is the double zone. Shifting this even reciprocal lattice by \mathbf{c}^* yields the *odd* reciprocal lattice; see Sect. VIB. Weak lines indicate the positions of pure-band maxima and minima (see FIG. 6). The red dot-dashed lines indicate the positions of the left and the right, doubly degenerate Fermi-surface sheets for stoichiometric $2(\text{LiMo}_6\text{O}_{17})$. The brown and olive dot-dashed lines correspond to 10%, respectively, hole and electron doping. Because $c/b = 1.720 \approx \sqrt{3}$, the $\Gamma\text{CT}'$ triangles are almost equilateral, and since this is so in the present figure, it is to scale. The k_b axis, has been turned by $\sim 90^\circ$ w.r.t. \mathbf{b} in the real-space FIG.s 2 (d), and 5 right.

to small energy scales and, concomitantly, from small to large spatial scales, we have followed computationally with the NMTD method in the LDA by using increasingly narrow and fine energy meshes and increasingly sparse basis sets as was described in Sect. II.

The *six lowest Mo 4d bands*, i.e. those within ± 0.75 eV around the Fermi level (see FIG.s 3 and 4), we found to be completely described by the basis set consisting of the three xy , xz , and yz NMTOs centered on Mo1 plus the three equivalent ones (18) centered on MO1, that is of *one t_{2g} -set per string*, which is per $\text{LiMo}_6\text{O}_{17}$. Symmetrical orthonormalization yielded the corresponding set of WOs whose xy and yz orbitals are what was actually shown in FIG. 5. The centers of the t_{2g} WOs were chosen at Mo1 and MO1 because those are the only octahedral molybdenums whose 6 nearest molybdenum neighbors are also octahedrally surrounded by O.

Each WO spreads out to the 4 nearest octahedral molybdenums in the plane of the orbital and, as explained in the previous sections, this leads to almost half the WO charge being on Mo1, slightly less on Mo4, considerably less on Mo2, and much less on Mo5. There is no discrepancy between the t_{2g}^3 configuration and the Mo $d^{0.5}$ occupancy mentioned at the beginning of Sect. IV: The latter is an average over all 6 molybdenums in a string of which only 4 carry t_{2g} partial waves, which are combined into *one* set of t_{2g} WOs, each one being effectively spread onto 3 molybdenums. So the occupation is perhaps more like Mo d^1 .

What *localizes* a $t_{2g,m}$ WO in the set of all three t_{2g} WOs on all Mo1 and MO1 atoms, is the condition that its projections onto all t_{2g} partial waves on all Mo1 and MO1 atoms, *except* the $t_{2g,m}$ partial wave on the own site, must *vanish*¹⁸. On the other hand, the WO spreads onto any *other* site and partial wave in the crystal in such a way that the WO set spans the solutions of Schrödinger's equation at the $N+1=3$ chosen energies. For the view (14), this is schematically:

$$\begin{array}{c} \mathbf{c} \nearrow \\ \mathbf{a} \searrow \\ \mathbf{z} \uparrow \end{array} \begin{array}{|c|c|c|c|c|} \hline 4 & 5 & & 2 & \circ & 4 \\ \hline & 5 & 4 & \circ & 2 & \\ \hline & 2 & \otimes & 4 & 5 & \\ \hline 5 & 4 & \circ & 2 & & 5 \\ \hline 2 & \circ & 4 & 5 & & 2 \\ \hline \end{array}, \quad (33)$$

with \otimes indicating the site (here Mo1) of the WO, and \circ the sites where all t_{2g} characters are required to vanish, i.e. the sites of the other WOs in the t_{2g} set. For the view (15), the Mo1-centered WO is:

$$\begin{array}{c} \mathbf{b} \uparrow \\ \mathbf{c} + \mathbf{a} \rightarrow \\ \mathbf{x} \searrow \\ \mathbf{y} \nearrow \end{array} \begin{array}{|c|c|c|} \hline \text{Mo :} & & \\ \hline \circ & 5 & \\ \hline 2 & 4 & \\ \hline \otimes & 5 & \\ \hline 2 & 4 & \\ \hline \circ & 5 & \\ \hline \end{array} \begin{array}{|c|c|} \hline \text{MO :} & \\ \hline 4 & 2 \\ \hline 5 & \circ \\ \hline 4 & 2 \\ \hline 5 & \circ \\ \hline 4 & 2 \\ \hline \end{array}. \quad (34)$$

Our t_{2g} WOs are insensitive to the exact orientation chosen for the xyz system –we took the one given by Eq. (12)– because they have all partial waves *other than* xy , xz , and yz on Mo1 and MO1 downfolded¹⁹. The contents of these partial waves are thus determined uniquely by the requirement that the WO basis set solves Schrödinger's equation exactly at the chosen energies for

¹⁸ Strictly speaking, this holds for the set of KPWs rather than of NMTOs and of WOs (see Sect. II)

¹⁹ For the XYZ system located on MO1 in the upper ribbon, we merely translate the xyz system from Mo1 to MO1. These two parallel, local coordinate systems do *not* follow the space-group symmetry, specifically the center of inversion between the nearest Mo1-MO1 neighbors. But the t_{2g} projections on the Mo1 and MO1 hard spheres do, because they are even, and this is all that matters for the WOs.

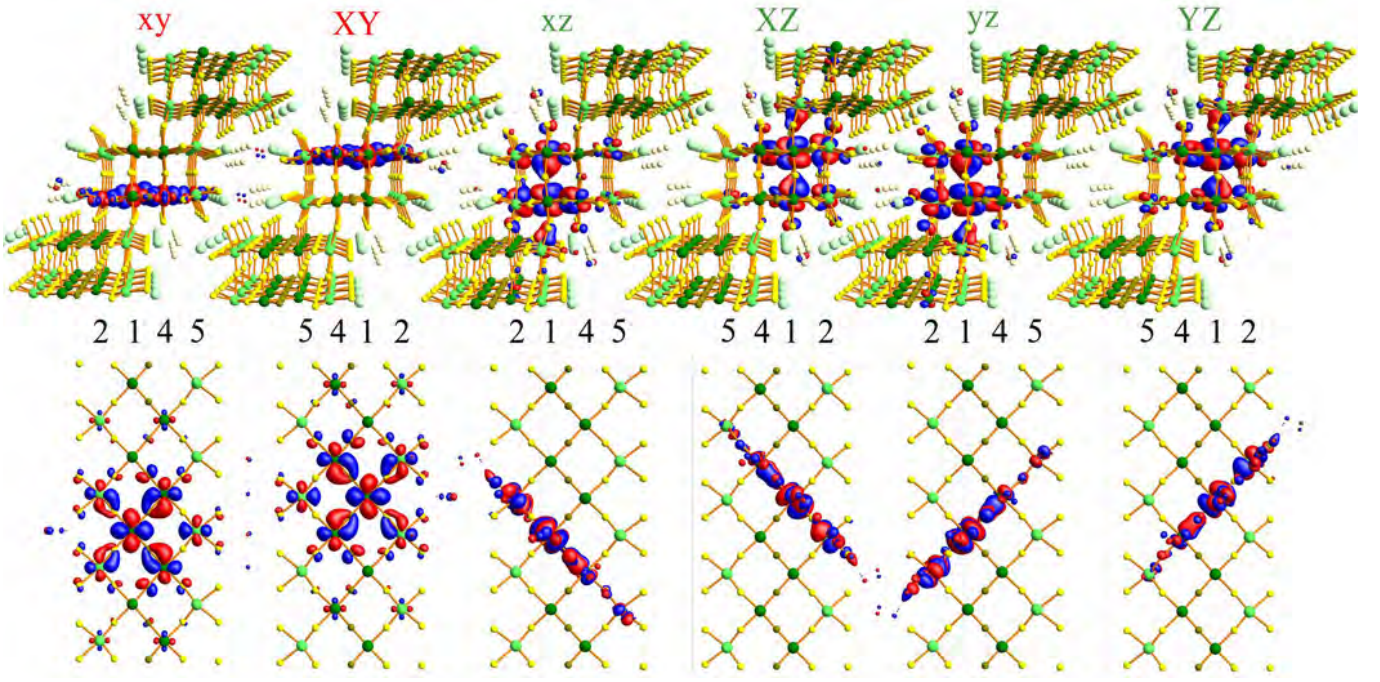


FIG. 9: The six Mo1- and MO1-centered t_{2g} WOs spanning the six lowest energy bands of $2(\text{LiMo}_6\text{O}_{17})$ shown in FIG. 4. The orientation is as in FIG. 2 (c) and (d), with the numbering of the octahedrally-coordinated molybdenums given in respectively Charts (14) and (15). Shown are the WO's constant-density surfaces containing 70% of the WO's charge with the color giving the sign of the lobe. With the usual 90% cut-off, as e.g. used for the t_{2g} WOs in NiO [49]), the overlaps would have been obscurely large. This more diffuse character of the LiPB WOs is needed in order that they accurately describe bands that are not visibly separated from the higher, more anti-bonding bands [see FIG. 3, and the long-range of the hopping integrals in (43), (46), and (47)]. The slices shown in FIG. 5 of standing-wave yz and xy states equal the corresponding WO, because for the values of $|\mathbf{k}|$ chosen, the overlap from the neighbor WOs in (52) is invisible.

the LDA potential used to construct the WOs. In this way, the downfolding procedure ensures that the shape of t_{2g} orbitals is given by the *chemistry* rather than by the choice of directions. Specifically, the downfolded content of partial waves with e_g character rotates the directions of the t_{2g} lobes into the proper "chemical" directions [39]. Moreover, the downfolded partial-wave contents on the remaining Mo2, Mo4, and Mo5 atoms in the string ensure that their relative phases are the proper ones for the energies chosen. Also, a WO on the upper string is correctly inverted with respect to the one on the lower string [see Eq. (18)]. Similarly, the downfolded partial waves on all oxygens give the proper O $2p$ dressing.

The WOs are obtained by symmetrical orthonormalization of the NMTO set and this causes a delocalization which, however, for our t_{2g} set is small and invisible in FIG. 5. What we do see, and noted in the previous section, is that each t_{2g} WO has tails with the same t_{2g} character as that of the head on the 4 nearest molybdenums in the plane of the orbital. These tails are connected to the head via $pd\pi$ tails on the 4 connecting oxygens such that the sign is anti-bonding with the t_{2g} head and bonding with the t_{2g} tail. In effect, this results in a $dd\pi$ anti-bond between the oxygen-dressed t_{2g} orbitals forming the WO head and tail.

Since the xy WO lies *in* the plane of its ribbon, it only

spreads onto a neighboring ribbon via a weak covalent interaction of symmetry $dd\delta$ causing no visible tails in the upper rows of FIG. 9. This is in contrast to the strong inter-ribbon $dd\pi$ -spread of the xz and yz WOs. The consequence for the six-band Hamiltonian to be presented in the next section is that the xy -XY inter-ribbon hopping integral t_1 in Eq. (25) and its dimerization u_1 , are about 30 times smaller than the respective xz -XZ and yz -YZ inter-ribbon integrals A_1 and G_1 in Eq. (29). For the same reason, the selection rule derived in Sect. IX B of Paper II that ARPES sees the lower band in the 1st and the higher band in the 2nd zone is better obeyed for the xy bands than for the (occupied) lower xz and yz bands (compare FIG.s 12 and 13 in Paper II).

With the knowledge that the right-hand panel of FIG. 5 shows the WO, $xy(\mathbf{r})$, let us now imagine building the 1D Bloch sum $xy(k_b\mathbf{b}^*, \mathbf{r})$ of WOs (8) through integer translations by $n\mathbf{b}$, multiplication with $e^{2\pi i n k_b}$, and superposition: Around Mo1 and Mo5, only $xy(\mathbf{r})$ contributes (neglecting the tail outside the 70% contour), but around Mo2 and Mo4, also $xy(\mathbf{r} + \mathbf{b})e^{-2\pi i k_b}$ and $xy(\mathbf{r} - \mathbf{b})e^{2\pi i k_b}$ contribute. As a result, at the bottom of the band ($k_b=0$) the amplitudes around Mo1 and Mo4 are nearly equal, and anti-bonding between Mo1 and Mo4, whereas the amplitude around Mo2 is smaller, but also anti-bonding to Mo1 so that the $p\pi$ character on all 4 oxy-

gens vanishes. At the Fermi level, $|k_b|=\frac{1}{4}$, whereby the *sum* of the Bloch waves with positive and negative k_b has the same shape as $xy(\mathbf{r})$ near Mo1 and Mo5, and a node at the neighboring Mo1 and Mo5 (i.e., those translated by $\pm\mathbf{b}$). This is the standing-wave state described in the previous section. The shape of the *difference* between the waves with k_b positive and negative is the same, but shifted by \mathbf{b} . At the top of the band, $|k_b|=\frac{1}{2}$, whereby the Bloch waves change sign upon translation by \mathbf{b} so that there is a node through Mo2 and Mo4 for one of the linear combinations, and through Mo1 and Mo5 for the other. If we finally build the Bloch sums with $|k_b|=\frac{3}{4}$, we find that they are *identical* with those for $|k_b|=\frac{1}{4}$, because in order to form both the low-energy Mo1-Mo4 bonding and the high-energy anti-bonding states, we would need a set containing *two* xy WOs, one centered at Mo1 and the other at Mo4. In order for a *single* WO to describe the lower, bonding part of a 4 eV wide band, gapped in the middle by merely 0.6 eV, it must in order to reproduce the strong curvature at the top of the lower band at $|k_b|=\frac{1}{2}$ have the ZB here (rather than at 1), as well as long-range in the direction (b) of the dispersion. That the latter is not seen in the first panel on the bottom row of FIG. 9 is due to our contour cut-off at 70%. But in the Hamiltonian [Eq.s (35), (37), and (43)], it gives rise to xy - xy hopping integrals, τ_n , which we need to carry as far as to $n=12$.

For future first-principles studies enabling Mott localization onto Mo1 or Mo4, WO sets larger than the one of six used in the present papers will be needed.

In a similar way, we can imagine building the states of the two 1D yz bands (27)-(29) from pseudo Bloch sums of the yz and YZ WOs (FIG.s 5 and 9) through pseudo translations by $n\frac{\mathbf{c}+\mathbf{b}}{2}$, multiplication with $e^{\pi i n(k_c+k_b)}$, and superposition. These WOs have their proper positions, i.e. at respectively Mo1 and MO1¹⁴, and we use $yz(\mathbf{r}-n\frac{\mathbf{c}+\mathbf{b}}{2})$ for n even and $YZ(\mathbf{r}-(n-1)\frac{\mathbf{c}+\mathbf{b}}{2})$ for n odd; see Eq. (17) and also Eq. (52) to which we shall return. These WOs are so localized that each one spills over only to its neighboring \mathbf{y} -string. The integrals for intra and inter bi-ribbon hops, $A_1 \pm G_1$, whose complicated hopping paths between elementary, dressed yz orbitals were shown in (27), are simply those between nearest-neighbor yz and YZ WOs. All farther-ranged hopping integrals, $A_{n>1}$ and $G_{n>1}$, are negligible.

The square of a WO, summed over all lattice translations yields the charge density obtained by filling that band, provided that we neglect its hybridization with the other bands. Summing this charge density over all six WOs yields the charge density obtained by filling all six t_{2g} bands, hybridizations now included. As an example: Squaring the xy WO in FIG. 5 will remove the colors and enhance the density on Mo1 with respect to that on the two Mo4 atoms, and even more with respect to that on the two Mo2 atoms, and mostly with respect to that on Mo5. Translating this charge density by $\pm\mathbf{b}$ and summing, doubles the charge density on Mo4 and on Mo2 due to overlap. As a result, the charge density on Mo1

and Mo4 will be nearly equal and larger than that on Mo2, while the one on Mo5 will be the smallest.

This charge density compares well with the one obtained by Popovic and Satpathy [25] for the quasi-1D band by filling it in a narrow range around the Fermi level and shown in the plane of the lower ribbon in their FIG. 5.²⁰

Nuss and Aichhorn [19] described the *four* lowest bands, i.e. the two valence bands and the two metallic bands, with a set of maximally localized Wannier functions obtained numerically by minimizing the spread $\langle \chi | |\mathbf{r} - \mathcal{R}|^2 | \chi \rangle$. Their WFs are bond centered and are essentially our $yz(\mathbf{r}) + YZ(\mathbf{r})$, our $xz(\mathbf{r}) + XZ(\mathbf{r})$, and a WF along each $\backslash_{\text{Mo1}}/\text{Mo4}\backslash_{\text{Mo1}}/\text{Mo4}\backslash$ chain with xy -like, similar-sized contours on all four sites, smaller contours on the Mo2 and Mo5 sites closest to the bond, and even smaller contours on the next Mo2 and Mo5 sites. This WF is extended along the chain, but appears from their FIG. 4 to have about the same degree of localization as our disc-shaped WO seen in the first column of FIG. 9.

VI. SIX-BAND t_{2g} TIGHT-BINDING HAMILTONIAN

Since our TB Hamiltonian is considerably more detailed than those previously published [25, 26][4, 17], we have been forced to change *notation*. The relation between the earlier notation and ours is, first of all: $t_{\perp} = t_1 + u_1$ and $t'_{\perp} = t_1 - u_1$. The integral $t \sim -1$ eV for the Mo1-Mo4 hopping used in the earlier work – as well as in the previous sections – is the coefficient to $\cos \pi k_b$, whereas τ_n to be used in Eq. (36) and in the following is the coefficient to $\cos 2\pi n k_b$. The symbol t will from *now* on – unless with explicit reference to Eq. (23) – denote the *function* of k_b and k_c which is defined in terms of the *perpendicular* 1st and 2nd nearest hopping integrals t_1 and t_2 in Eq. (37).

A. Sublattice $\{w, W\}$ -representation

In the representation of the six Bloch sums (8) of the three Mo1-centered t_{2g} WOs¹⁴, $w_m(\mathbf{k}, \mathbf{r}) = xy(\mathbf{k}, \mathbf{r})$, $xz(\mathbf{k}, \mathbf{r})$, and $yz(\mathbf{k}, \mathbf{r})$, as well as of the three MO1-centered WOs times a common phase factor, $W_m(\mathbf{k}, \mathbf{r}) e^{\pi i(k_c+k_b)} = XY(\mathbf{k}, \mathbf{r}) e^{\pi i(k_c+k_b)}$, $XZ(\mathbf{k}, \mathbf{r}) e^{\pi i(k_c+k_b)}$, and $YZ(\mathbf{k}, \mathbf{r}) e^{\pi i(k_c+k_b)}$, the TB

²⁰ That their [25] density on Mo2 is smaller than the one on Mo5 is presumably due to an erroneous exchange of the labels Mo1 and Mo4.

Hamiltonian (9) is:

H	xy	XY	xz	XZ	yz	YZ
xy	τ	$t - iu$	$\alpha + i\gamma$	$a - ig$	$\bar{\alpha} + i\bar{\gamma}$	$\bar{a} - i\bar{g}$
XY	$t + iu$	τ	$a + ig$	$\alpha - i\gamma$	$\bar{a} + i\bar{g}$	$\bar{\alpha} - i\bar{\gamma}$
xz	$\alpha - i\gamma$	$a - ig$	0	$A - iG$	$\lambda - i\mu$	$l - im$
XZ	$a + ig$	$\alpha + i\gamma$	$A + iG$	0	$l + im$	$\lambda + i\mu$
yz	$\bar{\alpha} - i\bar{\gamma}$	$\bar{a} - i\bar{g}$	$\lambda + i\mu$	$l - im$	0	$\bar{A} - i\bar{G}$
YZ	$\bar{a} + i\bar{g}$	$\bar{\alpha} + i\bar{\gamma}$	$l + im$	$\lambda - i\mu$	$\bar{A} + i\bar{G}$	0

(35)

using simplified labeling of the rows and columns. The six WOs are real-valued and shown in FIG. 9. The common \mathbf{k} -dependent phase factor, $e^{\pi i(k_c + k_b)}$, multiplying the Bloch sums of the upper-string WOs, has been included in order that matrix-elements between the two different sublattices take the simple form (35) where the asymmetry between integrals for hopping in- and outside a bi-ribbon (electronic dimerization) is given by the imaginary part.

The zero of energy is chosen as the common energy of the xz , XZ , yz , and YZ WOs.

The quantities in (35) named by Greek and Latin letters are real-valued *functions* of the Bloch vector (11). Specifically:

$$\tau(k_b) = \tau_0 + \sum_{n=1}^{12} 2\tau_n \cos 2\pi n k_b, \quad (36)$$

$$t(\mathbf{k}) = (2t_1 \cos \pi k_b + 2t_2 \cos 3\pi k_b) 2 \cos \pi k_c, \quad (37)$$

$$u(\mathbf{k}) = (2u_1 \cos \pi k_b + 2u_2 \cos 3\pi k_b) 2 \sin \pi k_c,$$

describe the pure xy/XY bands,

$$A(\mathbf{k}) = 2A_1 \cos \pi(k_c - k_b), \quad (38)$$

$$G(\mathbf{k}) = 2G_1 \sin \pi(k_c - k_b),$$

describe the pure xz/XZ bands, and \bar{A} and \bar{G} describe the pure yz/YZ bands. An *overbar* is generally used when switching from an xz to a yz orbital and indicates the mirror operation $k_b \leftrightarrow -k_b$, e.g.: $\bar{a}(k_b, k_c) \equiv a(-k_b, k_c)$. The hybridizations between the xy/XY and the xz/XZ bands are given by the Bloch sums:

$$\alpha(\mathbf{k}) = \alpha_0 + 2\alpha_1 \cos 2\pi k_b + 2\alpha_2 \cos 2\pi k_c \quad (39)$$

$$+ 2\alpha_3 \cos 2\pi(k_c + k_b) + 2\alpha'_3 \cos 2\pi(k_c - k_b),$$

$$a(\mathbf{k}) = 2a_1 \cos \pi(k_c - k_b) + 2a'_1 \cos \pi(k_c + k_b) \\ + 2a_2 \cos \pi(k_c - 3k_b) + 2a'_2 \cos \pi(k_c + 3k_b),$$

$$\gamma(\mathbf{k}) = 2\gamma_1 \sin 2\pi k_b + 2\gamma_2 \sin 2\pi k_c \\ + 2\gamma_3 \sin 2\pi(k_c + k_b) + 2\gamma'_3 \sin 2\pi(k_c - k_b),$$

$$g(\mathbf{k}) = 2g_1 \sin \pi(k_c - k_b) + 2g'_1 \sin \pi(k_c + k_b) \\ + 2g_2 \sin \pi(k_c - 3k_b) + 2g'_2 \sin \pi(k_c + 3k_b),$$

and the hybridizations between the xz/XZ and yz/YZ bands by:

$$\lambda(\mathbf{k}) = \lambda_0 + 2\lambda_1 \cos 2\pi k_b + 2\lambda_2 \cos 2\pi k_c + 2\lambda_3 \cos 2\pi 2k_b,$$

$$l(\mathbf{k}) = (2l_1 \cos \pi k_b) 2 \cos \pi k_c,$$

$$\mu(\mathbf{k}) = 2\mu_1 \sin 2\pi k_b + 2\mu_3 \sin 2\pi 2k_b.$$

$$m(\mathbf{k}) = (2m_1 \cos \pi k_b) 2 \sin \pi k_c. \quad (40)$$

The dispersion along \mathbf{a}^* is neglected, and the Bloch sums are truncated for distances exceeding the lattice constant a , which means after the 3rd-nearest neighbors. The long-ranged $\tau(k_b)$ is an exception and will be discussed below. Due to the truncation of hops longer than a , the effective value of k_a is not 0, but the one for which $\cos 2\pi k_a = 0$, i.e. $\frac{1}{4}$. The truncation also means that our LDA TB bands are a bit more wavy and smoother than those obtained from the original LDA NMTO Hamiltonian downfolded in \mathbf{k} -space. The A and G sums (38) are converged already after 1st-nearest neighbors.

The Greek-lettered Bloch sums are over hops on the *same* sublattice whereby their \mathbf{k} dependence is periodic in the reciprocal lattice spanned by \mathbf{b}^* and \mathbf{c}^* , e.g.

$$\alpha(k_b, k_c) = \alpha(k_b + M, k_c + N) \quad (41)$$

with M and N any integer. The Latin-lettered Bloch sums are over hops *between* the Mo1- and MO1-centered sublattices and averaged such that these Bloch sums are periodic in the double zone spanned by $\mathbf{c}^* + \mathbf{b}^*$ and $\mathbf{c}^* - \mathbf{b}^*$ (see Sect. VIB), but change sign upon odd reciprocal-lattice translations, e.g.

$$a(k_b, k_c) = (-1)^{M+N} a(k_b + M, k_c + N). \quad (42)$$

Note the difference between α and a .

The number of parameters entering Eq.s (36)-(40) and whose values are given in Eq.s (43)-(47) below are far more numerous than those few (t , t_\perp , t'_\perp , A_1 , G_1 , and B) used in the simplified description given in Sect. IV; a description which, nevertheless, suffices to understand the CECs and bands measured by ARPES and shown in respectively FIG.s 20 and 21 in Paper II. The LDA low-energy TB bands shown in FIG. II 22 (a) together with the occupied bands measured by ARPES (grey circles and black dots) have much more detail, and the surprisingly good agreement between them proves this detail to be real. This is emphasized by the nearly perfect agreement seen in FIG. 22 (b) and obtained by shifting merely the on-site energy, τ_0 , of the degenerate xy and XY WOs upwards by 100 meV with respect to the energy of the degenerate xz , XZ , yz , and YZ WOs. In Sect. XE of Paper II we shall describe the details of the energy bands while the differences between LDA and ARPES will be in focus of Sect. XI of Paper II.

Below, we give the values in meV of the on-site energies and hopping integrals obtained from the first-principles LDA full-potential NMTO calculation (9) together with the (shifted) values and the [ARPES refined] values (see Sect.s XIA and XIB in Paper II), in those cases where they differ:

$\tau_0 = 47$ (147) [203]	$\tau_5 = -11$	$\tau_9 = -2$
$\tau_1 = -422$ [-477]	$\tau_6 = 8$	$\tau_{10} = 1$
$\tau_2 = 47$ [87]	$\tau_7 = -4$	$\tau_{11} = -1$
$\tau_3 = -31$	$\tau_8 = 3$	$\tau_{12} = 1$
$\tau_4 = 17$		

(43)

$$\begin{array}{cc} t_1 = -11 & u_1 = -3 \\ t_2 = -5 & u_2 = 1 \end{array} \quad (44)$$

$$A_1 = -319 \quad G_1 = -98 \quad [-109] \quad (45)$$

$$\begin{array}{cccc} \alpha_0 = 31 & & & \\ \alpha_1 = 20 & a_1 = -49 & \gamma_1 = 8 & g_1 = 1 \\ \alpha_2 = -5 & a'_1 = -8 & \gamma_2 = -6 & g'_1 = 5 \\ \alpha_3 = 10 & a_2 = -6 & \gamma_3 = 2 & g_2 = -3 \\ \alpha'_3 = -4 & a'_2 = -11 & \gamma'_3 = -4 & g'_2 = -11 \end{array} \quad (46)$$

$$\begin{array}{cc} \lambda_0 = -61 & \mu_1 = 7 \\ \lambda_1 = 7 & \mu_3 = -11 \\ \lambda_2 = 22 \quad [15] & l_1 = 20 \\ \lambda_3 = -11 \quad [-5] & m_1 = 12 \quad [6] \end{array} \quad (47)$$

Subscript 0 indicates an on-site energy, which is the energy of the WO in case the two WOs are identical, and an anisotropy energy in case they are different. Further subscripts indicate 1st, 2nd, and 3rd-nearest neighbor hops.

As mentioned above, the zero of energy is chosen as the common energy of the xz , XZ , yz , and YZ WOs. This is the center of the gap in the approximation that the hybridizations (40) between the xz/XZ and yz/YZ bands are neglected. In Sect. IV and in footnote 16 this energy was named $E_0 \sim B + 2|A_1|$. The common energy of the xy and XY WOs, i.e. the center of the unhybridized xy bands, is τ_0 with respect to that of the xz , XZ , yz , and YZ WOs.

For our basis containing merely one Mo1- and one MO1 WO, the Fourier series (36) for the dominating k_b dependence of the two $\frac{1}{2}$ -filled xy bands converges slowly as explained in Sect. V). For many purposes, it suffices to linearize $\tau(k_b)$ around $k_b = \frac{1}{4} \approx k_F$ or $-\frac{1}{4}$:

$$\begin{aligned} \tau(k_b) \approx & \tau_0 + 2 \sum_{n=1} (-1)^n \tau_{2n} \\ & - \left(|k_b| - \frac{1}{4} \right) 4\pi \sum_{n=0} (-1)^n (2n+1) \tau_{2n+1}. \end{aligned} \quad (48)$$

With the values given in (43), the upper line of Eq. (48) says that –neglecting FS warping and splitting, i.e. the perpendicular (44) and hybridization (46) integrals – the Fermi level at *half* filling is

$$E_F \approx \tau \left(\frac{1}{4} \right) = -23 \quad (77) \quad [53] \quad \text{meV} \quad (49)$$

above the center of the gap. According to Eq. (48), this differs from the on-site xy energy, $\tau_0 = 47 \quad (147) \quad [203]$, by the alternating sum $2(-\tau_2 + \tau_4 - \dots)$. Hence, the reason

why the ARPES-refined value of the Fermi level for half-filling is 150 meV below τ_0 –and thereby closer to the center of the gap than the LDA value shifted by 100 meV– is caused by the refinement of the τ_2 value. In Sect. XV B of Paper III, the average k_{Fb} -value measured by ARPES at 33 eV is 0.254. The Fermi level is thus approximately $\tau(0.254) = 75$ meV rather than 53 meV above the center of the gap.

The value of the coefficient to $|k_b| - \frac{1}{4}$ in the lower line of Eq. (48), times b , yields the Fermi velocity at half filling:

$$v_F = 4.0 \quad (4.0) \quad [4.6] \quad \text{eV} \cdot \text{\AA}. \quad (50)$$

This LDA value is a bit larger than those of Satpathy and Popovic (3.72 eV \AA) [25] and of Nuss and Aichhorn (0.93 10^5 m/s = 3.8 eV \AA) [19]. Our ARPES-refined value, which is consistent with FIG. 24 (c2) in Paper II, exceeds the LDA value by 15%. Reasons for this velocity enhancement will be discussed in Sect. XV B 2 of Paper III. The dimensionless coupling constant used in Ref. [66] has the value

$$e^2 / (\pi \hbar v_F) = 1.14 \quad [0.99]. \quad (51)$$

The splitting-and-warping effects neglected above are considered in detail in Sect.s XIV A 2, XIV B and XV B, in Paper III.

Of the matrix elements, $\langle xy_0 | H | xz_n \rangle = \alpha_n \pm \gamma_n$, determining the xz and yz hybridization of the xy bands, α_0 is the crystal-field term and $\alpha_n \pm \gamma_n$ and $\bar{\alpha}_n \pm \bar{\gamma}_n$ are integrals for hopping between n th-nearest neighbors with the upper sign for forwards- and the lower for backward hopping. Although these Greek-lettered hops are between WOs on the same sublattice, forwards and backward hoppings differ because there is no inversion symmetry around Mo1. These energies, except α_0 and α_1 , are small but significant for the detailed k_c -dispersion of the xy band near the Fermi level, especially the resonance behavior. The same holds for the Latin-lettered hopping integrals, $\langle xy_0 | H | XZ_n \rangle = a_n \pm g_n$, between WOs on different sublattices, except for a_1 . In Paper III, Sect. XIV B 6 in particular, we shall see that the crystal-field term α_0 and the integral for hopping from xy to an XZ or YZ nearest-neighbor, a_1 , are of major importance.

The matrix elements $\langle xz_0 | H | yz_n \rangle = \lambda_n \pm \mu_n$ and $\langle xz_0 | H | YZ_n \rangle = l_n \pm m_n$ are larger than these, but of minor importance for the xy band near E_F , and we shall neglect them in the two-band Hamiltonian derived in Paper III Sect. XIV A 2. They are decisive for the levels near Z where the valence (V) and conduction (C) bands come closest. Since the Bloch sums (40) are badly converged, we found it necessary to truncate the sum and then refine the hopping values as shown in square brackets in Table 47. This refinement was enabled by the fact that the six-band Hamiltonian (35) simplifies at the points of high symmetry such as Z .

B. Reciprocal sublattice $\{\mathbf{k}, \mathbf{k} + \mathbf{c}^*\}$ -representation

In connection with Eqs (25) and (29), we noted that the numerical values of the most important inter-ribbon hoppings have smaller dimerizations than mean values, i.e. $t_1 \pm u_1 \sim -11 \mp 3$ meV for the xy band and $A_1 \pm G_1 \sim -0.3 \mp 0.1$ eV for the xz and yz bands. If such electronic c -axis dimerizations (Sect. III A) are neglected, the energy bands are the dashed bands in FIG. 6 and correspond to all strings being related by primitive translations $\frac{\mathbf{c}+\mathbf{b}}{2}$ and $\frac{\mathbf{c}-\mathbf{b}}{2}$, rather than there being 2 translationally inequivalent strings per primitive cell whose primitive translations are \mathbf{c} and \mathbf{b} . A natural way of describing the proper electronic structure is therefore in terms of basis functions which are *pseudo Bloch sums* of WOs with respect to this –too short– lattice periodicity. Specifically in LiPB, a pseudo-Bloch sum is:

$$|w; \mathbf{k}\rangle \equiv \frac{1}{\sqrt{2}} \sum_{\mathbf{T}} e^{2\pi i \mathbf{k} \cdot \mathbf{T}} \left[w(\mathbf{r} - \mathbf{T}) + e^{2\pi i \mathbf{k} \cdot \frac{\mathbf{c}+\mathbf{b}}{2}} W(\mathbf{r} - \mathbf{T}) \right], \quad (52)$$

where the \mathbf{T} -sum is over the proper lattice translations, $w(\mathbf{r})$ is the WO centered on Mo1, taken as the origin of the primitive cell, and $W(\mathbf{r})$ is the WO on MO1, which is at $\frac{\mathbf{c}+\mathbf{b}}{2} - \mathbf{d}$. Both $\sum_{\mathbf{T}} e^{2\pi i \mathbf{k} \cdot \mathbf{T}} w(\mathbf{r} - \mathbf{T})$ and $\sum_{\mathbf{T}} e^{2\pi i \mathbf{k} \cdot \mathbf{T}} W(\mathbf{r} - \mathbf{T})$ are proper Bloch sums (8) and, hence, periodic functions of \mathbf{k} in a single zone. However, the \mathbf{k} -dependent phase factor, $e^{\pi i(k_c + k_b)}$, multiplying the second Bloch sum makes this –and herewith the entire pseudo Bloch sum (52)– a function of \mathbf{k} which is merely *periodic in the double zone*, i.e. on the *sparse* reciprocal lattice spanned by $\mathbf{c}^* + \mathbf{b}^*$ and $\mathbf{c}^* - \mathbf{b}^*$, that is:

$$\begin{aligned} |w; \mathbf{k}\rangle &= |w; \mathbf{k} + M'(\mathbf{c}^* + \mathbf{b}^*) + N'(\mathbf{c}^* - \mathbf{b}^*)\rangle \\ &\equiv |w; \mathbf{k} + M\mathbf{b}^* + N\mathbf{c}^*\rangle, \end{aligned} \quad (53)$$

with M' and N' any integers, which means: with $M + N$ *even* (e). Had $W(\mathbf{r})$ not been displaced and inverted as described in Sect. III A, the pseudo Bloch sum (52) would have been a proper Bloch sum for the *undimerized* crystal. In FIG. 6, the energy bands of the even pseudo-

Bloch sums are the dashed blue, green, and red bands with bottoms near $k_c=0$.

The correct long periodicity in real space –and *single-zone* periodicity in reciprocal space– can now be described by including in the basis set the pseudo Bloch sum with \mathbf{k} translated to the *other* sparse sublattice (we may think of reciprocal space as a checkerboard consisting of 1st and 2nd zones). This second set of Bloch waves¹⁷ is thus $|w; \mathbf{k} + \mathbf{c}^*\rangle$, for which $M + N + 1$ is even, i.e. $M + N$ is *odd* (o). Their energy bands are the dashed ones with bottoms near $k_c=\pm 1$ (and tops near $k_c=0$) in FIG. 6. Finally, in order to diagonalize the Hamiltonian (56), the even and odd pseudo-Bloch sums with the same value of \mathbf{k} are allowed to mix and the bands to gap. In absence of dimerization, the even and odd pseudo-Bloch functions are identical, apart from a phase factor, and so are the even and odd energy bands which are merely separated by \mathbf{c}^* and cross without gapping (FIG. 6).

The basis set $(|w; \mathbf{k}\rangle, |w; \mathbf{k} + \mathbf{c}^*\rangle)$ of pseudo-Bloch sums is simply the unitary transformation:

$$\begin{aligned} |w; \mathbf{k}\rangle &= [w(\mathbf{k}, \mathbf{r}) + e^{\pi i(k_c + k_b)} W(\mathbf{k}, \mathbf{r})] / \sqrt{2} \\ |w; \mathbf{k} + \mathbf{c}^*\rangle &= [w(\mathbf{k}, \mathbf{r}) - e^{\pi i(k_c + k_b)} W(\mathbf{k}, \mathbf{r})] / \sqrt{2} \end{aligned} \quad (54)$$

of the set $(w(\mathbf{k}, \mathbf{r}), W(\mathbf{k}, \mathbf{r}))$ of proper Bloch sums (8) of the two WOs, $w(\mathbf{r})$ and $W(\mathbf{r})$. We may check that translation of \mathbf{k} by \mathbf{c}^* exchanges the functions on the left-hand side, leaves the proper Bloch functions on the right-hand side invariant, and –by adding 1 to k_c – changes sign for the second row of the matrix, which correctly exchanges its columns. With the common phase factor $e^{\pi i(k_c + k_b)}$ included in the definition of $W(\mathbf{k}, \mathbf{r})$ as done for the Hamiltonian (35) in the $\{w, W\}$ -representation, the transformation (54) is simply the bonding-anti-bonding transformation for each of the three t_{2g} Bloch orbitals, and the inverse transformation is:

$$\begin{aligned} w(\mathbf{k}, \mathbf{r}) &= [|w; \mathbf{k}\rangle + |w; \mathbf{k} + \mathbf{c}^*\rangle] / \sqrt{2} \\ e^{\pi i(k_c + k_b)} W(\mathbf{k}, \mathbf{r}) &= [|w; \mathbf{k}\rangle - |w; \mathbf{k} + \mathbf{c}^*\rangle] / \sqrt{2}. \end{aligned} \quad (55)$$

Transformed to this $\{\mathbf{k}, \mathbf{k} + \mathbf{c}^*\}$ -representation, the six-band Hamiltonian (35) becomes:

H	$ xy; \mathbf{k}\rangle$	$ xy; \mathbf{k} + \mathbf{c}^*\rangle$	$ xz; \mathbf{k}\rangle$	$ xz; \mathbf{k} + \mathbf{c}^*\rangle$	$ yz; \mathbf{k}\rangle$	$ yz; \mathbf{k} + \mathbf{c}^*\rangle$
$\langle xy; \mathbf{k} $	$\tau + t$	iu	$\alpha + a$	$i(\gamma + g)$	$\bar{\alpha} + \bar{a}$	$i(\bar{\gamma} + \bar{g})$
$\langle xy; \mathbf{k} + \mathbf{c}^* $	$-iu$	$\tau - t$	$i(\gamma - g)$	$\alpha - a$	$i(\bar{\gamma} - \bar{g})$	$\bar{\alpha} - \bar{a}$
$\langle xz; \mathbf{k} $	$\alpha + a$	$-i(\gamma - g)$	A	iG	$\lambda + l$	$-i(\mu - m)$
$\langle xz; \mathbf{k} + \mathbf{c}^* $	$-i(\gamma + g)$	$\alpha - a$	$-iG$	$-A$	$-i(\mu + m)$	$\lambda - l$
$\langle yz; \mathbf{k} $	$\bar{\alpha} + \bar{a}$	$-i(\bar{\gamma} - \bar{g})$	$\lambda + l$	$i(\mu + m)$	\bar{A}	$i\bar{G}$
$\langle yz; \mathbf{k} + \mathbf{c}^* $	$-i(\bar{\gamma} + \bar{g})$	$\bar{\alpha} - \bar{a}$	$i(\mu - m)$	$\lambda - l$	$-i\bar{G}$	$-\bar{A}$

(56)

where $|m; \mathbf{k}\rangle \equiv |w_m; \mathbf{k}\rangle$.

The 3×3 blocks $\langle \mathbf{k} | H | \mathbf{k} \rangle$ and $\langle \mathbf{k} + \mathbf{c}^* | H | \mathbf{k} + \mathbf{c}^* \rangle$

are real-valued, symmetric, and periodic in respectively the even and the odd sublattice. This means that $\langle \mathbf{k} + \mathbf{c}^* | H | \mathbf{k} + \mathbf{c}^* \rangle$ equals $\langle \mathbf{k} | H | \mathbf{k} \rangle$ with the sign in front of the Latin-lettered Bloch sum flipped [see Eq. (42)]. The off-diagonal blocks $\langle \mathbf{k} | H | \mathbf{k} + \mathbf{c}^* \rangle$ are caused by the c -axis dimerizations and are purely imaginary.

The band structure with the c -axis dimerizations neglected, consists of the 3 eigenvalues of the $\langle \mathbf{k} | H | \mathbf{k} \rangle$ block in the double zone ($|k_c| \leq 1$). The dimerization effects may be included by translating these 3 *undimerized* bands (dashed in FIG. 6) by -1 along k_c , whereby the 2nd BZ ($\frac{1}{2} \leq k_c \leq \frac{3}{2}$) falls on top of the 1st ($-\frac{1}{2} \leq k_c \leq \frac{1}{2}$), and finally split them by $\langle \mathbf{k} | H | \mathbf{k} + \mathbf{c}^* \rangle$.

In the following, we shall keep the c -axis dimerizations, but often neglect the mm' hybridizations.

C. Pure- m bands

The xy (red), xz (blue), and yz (green) bands drawn in full lines in FIG. 6 have the hybridizations between them neglected. They are the so-called *pure- m* bands, the eigenvalues of the three 2×2 blocks, H_m , along the diagonal in Eq. (35) or (56), with elements given as functions of k_b and k_c in Eq.s (36), (37), and (38), and numerical values in Eq.s (44) and (45). The pure- yz band we already met in Eq. (29). Note that t , A , and \bar{A} are negative in the 1st zone and that u , G , and \bar{G} are negative in the positive half of the first zone. After subtraction from H_{xy} of the diagonal $\tau(k_b)$ -term, all three blocks have the same form (traceless and Hermitian), and so do, therefore, their upper ($j=2$) and lower ($j=1$) eigenvalues:

$$\pm \sqrt{A^2 + G^2}, \pm \sqrt{\bar{A}^2 + \bar{G}^2}, \text{ and } \pm \sqrt{t^2 + u^2} \quad (57)$$

for $m=xz$, yz , and xy , respectively. Similarly for the orthonormal eigenfunctions expressed in terms of the WO Bloch sums used as a basis in Eq. (35) or the WO pseudo Bloch sums used in Eq. (56):

$$\begin{aligned} w_2(\mathbf{k}, \mathbf{r}) &= \frac{1}{\sqrt{2}} \left[w(\mathbf{k}, \mathbf{r}) e^{-i\phi(\mathbf{k})} \pm W(\mathbf{k}, \mathbf{r}) e^{\pi i(k_c + k_b)} \right] \\ &= \frac{1}{2} \left[|w; \mathbf{k}\rangle (e^{-i\phi(\mathbf{k})} \pm 1) + |w; \mathbf{k} + \mathbf{c}^*\rangle (e^{-i\phi(\mathbf{k})} \mp 1) \right], \end{aligned} \quad (58, 59)$$

where

$$e^{i\phi} \equiv \frac{A + iG}{\sqrt{A^2 + G^2}}, \frac{\bar{A} + i\bar{G}}{\sqrt{\bar{A}^2 + \bar{G}^2}}, \text{ and } \frac{t + iu}{\sqrt{t^2 + iu^2}}. \quad (60)$$

From Eq. (59) we see that the $|\mathbf{k}\rangle$ characters of the upper and lower m bands –shown in FIG. 6 as *fatness* added to the respective band dispersions and computed by perturbing the $\langle m; \mathbf{k} | H | m; \mathbf{k} \rangle$ element in the matrix (56) by a small constant energy– are:

$$\left| \frac{e^{-i\phi(\mathbf{k})} \pm 1}{2} \right|^2 = \frac{1 \pm \cos \phi(\mathbf{k})}{2}, \quad (61)$$

and these are the same as the $|\mathbf{k} + \mathbf{c}^*\rangle$ characters of respectively the lower and upper bands. In FIG. 10, the solid dark and light curves give the $|\mathbf{k}\rangle$ -character of respectively the lower and upper xy bands as function of k_c in the double zone and along the same line ($k_b=0.225$) as in FIG. 6. We see the dominant $|\mathbf{k}\rangle$ character switch from the lower band in the 1st zone to the upper band in the 2nd zone over a range of k_c around the zone boundary (ZB), $|k_c|=\frac{1}{2}$. On ϕ -scale (60), the switching behavior is independent of m and given by Eq. 61), which says that the interval around the ZB, $|\phi|=\frac{\pi}{2}$, where the $|\mathbf{k}\rangle$ character of *both* bands exceeds e.g. $\frac{1}{7} \approx 14\%$, is: $\phi = (0.5 \pm 0.253)\pi$. For the two xy bands and $k_b=0.225$, this "overlap interval" obtained from the 3rd Eq. (60) with Eq.s (37) and (44) is: $k_c = (0.35|0.65)$. Had there been no electronic dimerization, i.e. if u or $G=0$, the switching curves (FIG. 10) would have had steps at the zone boundaries where the two m bands would have crossed without gapping.

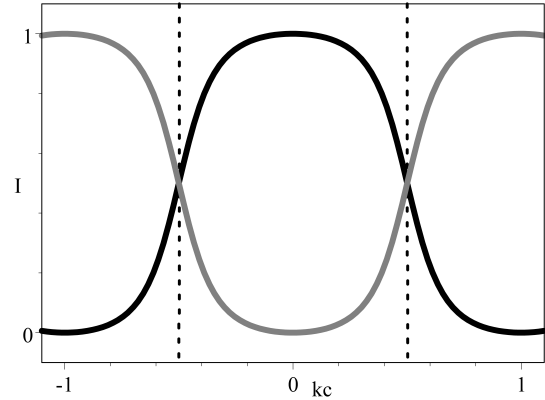


FIG. 10: $|\mathbf{k}\rangle$ character (or relative intensity), $[1 \pm \cos \phi(\mathbf{k})]/2$, of the upper (light) and lower (dark) pure xy bands as functions of k_c for $k_b=0.225$ in the double zone (FIG. 8); from Eq.s (59), (61), (37), and (44). The dominant (or most intensive) $|\mathbf{k}\rangle$ character switches from the lower band in the odd-numbered zones, $|k_c - 2n| < \frac{1}{2}$, to the upper band in the even-numbered zones, $|k_c - (2n + 1)| < \frac{1}{2}$. Whereas the gapped bands (57) have single-zone periodicity, their $|\mathbf{k}\rangle$ characters are periodic in the double zone. In FIG.s 6 and 7 the $|\mathbf{k}\rangle$ character is shown as fatness added to (i.e. decorating) the band.

In contrast to the complementarity of the $|\mathbf{k}\rangle$ and $|\mathbf{k} + \mathbf{c}^*\rangle$ characters exhibited by Eq. (59), the w and W characters are 50% for both bands and all \mathbf{k} , as seen from Eq. (58).

Bands with *different* m do hybridize with each other: the $xy(\mathbf{k})$ band with the $xz(\mathbf{k})$ and $yz(\mathbf{k})$ bands due to the α and a hops, and with the $xz(\mathbf{k} + \mathbf{c}^*)$ and $yz(\mathbf{k} + \mathbf{c}^*)$ due to the γ and g hops. The $xz(\mathbf{k})$ band hybridizes with the $yz(\mathbf{k})$ band due to the λ and l hops, and with the $yz(\mathbf{k} + \mathbf{c}^*)$ band due to the μ and m hops.

When $|k_b| \sim \frac{1}{4} \approx k_F$, the xy bands are situated in the gap between the xz valence and conduction bands and between the yz valence and conduction bands. The hybridization caused by the (α, a) hops in the $|\mathbf{k}\rangle$ -conserving part and by the (γ, g) hops in the $|\mathbf{k}\rangle$ - $|\mathbf{k} + \mathbf{c}^*\rangle$ mixing part of the Hamiltonian (56) makes the difference between the red pure xy bands in FIG. 6 and the dark-red hybridized \widetilde{xy} bands in FIG. 7. The (γ, g) hops modify the shape of the \widetilde{xy} bands, but do not significantly extend the switching region around the BZ boundary, $|k_c| = \frac{1}{2}$, in which the $|\mathbf{k}\rangle$ - $|\mathbf{k} + \mathbf{c}^*\rangle$ mixing occurs.

D. Brillouin- and physical zones

Bloch functions are characterized by their translational symmetry in reciprocal space and the choice of the primitive cell (zone) is arbitrary as long as it contains each \mathbf{k} -point once and only once. As we mentioned after Eq.s (29) and (30)-(32), it may be possible and convenient to choose the zone compatible with the electronic structure, i.e. such that gaps occur at the zone boundaries.

For the familiar free-electron model, where $|\mathbf{k}\rangle \sim e^{2\pi i \mathbf{k} \cdot \mathbf{r}}$ and $\varepsilon(\mathbf{k})$ increases isotropically and monotonically with the distance, k , from $\Gamma(0,0,0)$, one chooses that zone which is closer to Γ than to any other point, \mathbf{G} , of the reciprocal lattice. This is the Brillouin zone (BZ). Application of a weak pseudopotential with crystalline symmetry will couple the basis functions $|\mathbf{k}\rangle$, $|\mathbf{k} - \mathbf{G}_1\rangle$, ..., and $|\mathbf{k} - \mathbf{G}_n\rangle$, where \mathbf{G}_1 , ..., \mathbf{G}_n are the reciprocal lattice points closest to Γ , and thereby gap bands where they cross, i.e. where $k = |\mathbf{k} - \mathbf{G}_n|$, which is at the boundaries of the BZ.

For LiPB, the situation is different: Rather than being isotropic, the low-energy electronic structure consists of three pairs of quasi-1D bands. For each, we have only two inequivalent pseudo-Bloch sums, $|w_m; \mathbf{k}\rangle$ and $|w_m; \mathbf{k} + \mathbf{c}^*\rangle$. As described in the previous subsection, and already in the introductory section IV A, and as seen in FIG.s 6-8, the lower (bonding) m band has $|\mathbf{k}\rangle$ character inside its zone and $|\mathbf{k} + \mathbf{c}^*\rangle$ character outside, while the upper (anti-bonding) band has $|\mathbf{k} + \mathbf{c}^*\rangle$ character inside and $|\mathbf{k}\rangle$ character outside. Here, "inside" means around a point, such as $\Gamma(k_b=0, k_c=0)$, of the *even* reciprocal sublattice (confusingly called an odd-numbered BZ), and "outside" means around a point, such as $\Gamma(0, 1)$ or $\Gamma(0, -1)$, of the *odd* reciprocal sublattice (called an even-numbered BZ).

The xz (blue) and yz (green) bands are functions with period 2 of respectively $k_c - k_b$ and $k_c + k_b$ whereby the \mathbf{k} and $\mathbf{k} + \mathbf{c}^*$ bands cross –and gap by $\pm 2G_1$ – along respectively $|k_c - k_b| = \frac{1}{2}$ and $|k_c + k_b| = \frac{1}{2}$, which are then "physical" zone boundaries of the xz and yz bands [Eq.s (32) and (31) and FIG. 8].

The xy bands (red) disperse strongly with k_b , which is normal to the plane of FIG. 6, but since the gap at $|k_b| = \frac{1}{2}$ caused by b -axis dimerization is far above E_F , we

merely consider the two lowest of the four xy bands (see Sect. III B) and their strong k_b -dependence is described merely by $\tau(k_b)$. The small, $\pm 2u$, gap near E_F is due to the c -axis dimerization (Sect. III A) and occurs at the $|k_c| = \frac{1}{2}$ zone boundary. Hence, the physical zone for the xy bands is the rectangular one, $[|k_b| \leq \frac{1}{2} \text{ and } |k_c| \leq \frac{1}{2}]$, Eq. (30) which is –actually– the Brillouin zone (BZ).

While the nearly degenerate, xy bands are half full (metallic), the lower xz and yz bands are full and the upper are empty.

For the purpose of *calculating* the electronic structure, i.e. when diagonalizing the 6×6 Hamiltonian or the Löwdin downfolded 2×2 Hamiltonian in Paper III, we normally use the rectangular BZ.

VII. SUMMARY

In this paper, we have developed the single-particle framework on the basis of which we shall discuss and refine the new ARPES measurements of the band structure and Fermi surface of LiPB to be presented in Papers II and III.

In the Introduction, we gave an overview of the properties and current theories of this intriguing quasi-1D metal and laid out the plan for –and gave the main results of– our three papers.

In Sect. II, the new DFT method for direct computation of Wannier functions and their TB Hamiltonian, the full-potential NMTO method, was explained. Its unique ability to produce physically and chemically meaningful Wannier *orbitals* (WOs) –multi-center Mo1 $4d_{t_{2g},m}$ orbitals in the present case– is crucial for our understanding of LiPB whose crystal structure (FIG. 2) consists of MoO₆ octahedra connected via corners into slabs perpendicular to \mathbf{a}^* . Each slab consists of *ribbons*, 4 molybdenums wide in the $\mathbf{a} + \mathbf{c}$ direction and extending indefinitely in the perpendicular direction, the direction of quasi-1D conductivity Chart (14). The well-known zigzag chains, $\backslash_{\text{Mo1}}/\text{Mo4}\backslash_{\text{Mo1}}/\text{Mo4}\backslash$, with primitive translation \mathbf{b} are the spines of the ribbons. The ribbons, with every second *displaced* from the position $\frac{\mathbf{c} + \mathbf{b}}{2}$ by a vector $-\mathbf{d}$ (16) and *inverted* [Eq. (18) and Chart (14)], are stacked on top of each other into *bi-ribbons*, whereby the slab forms a *staircase* with steps of bi-ribbons and primitive translations \mathbf{c} . Without this c -axis dimerization, the staircase would have been a smooth ramp [Charts (21)-(22)] with the undimerized crystal lattice spanned by $(\mathbf{a}, \frac{\mathbf{c} + \mathbf{b}}{2}, \frac{\mathbf{c} - \mathbf{b}}{2})$ and its reciprocal lattice spanned by $(\mathbf{a}^*, \mathbf{c}^* + \mathbf{b}^*, \mathbf{c}^* - \mathbf{b}^*)$, as compared with the primitive translations $(\mathbf{a}, \mathbf{b}, \mathbf{c})$ and $(\mathbf{a}^*, \mathbf{b}^*, \mathbf{c}^*)$ of real LiPB. The staircase is terminated by insulating MoO₄ tetrahedra and Li intercalates between staircases, which is also where the crystal cleaves. All 8 octahedral and 4 tetrahedral molybdenums approximately form a simple cubic lattice [Eq. (12)].

Anticipating the results of the more technical Sect.s V and VI –as well as the band structures and Fermi sur-

face in Papers II and III– in Sect. IV we gave an elementary description of the electronic structure inside the slab, from the 10 to the 0.1 eV scale around the Fermi level seen in respectively FIG.s 3, 4, and 6. The *double* zone, which is the BZ of the undimerized lattice, was shown in FIG. 8. The boundary between the 1st and 2nd *physical* zones, which is where in the absence of dimerization the $m(\mathbf{k})$ and $m(\mathbf{k} + \mathbf{c}^*)$ bands cross, is shown in solid red, blue, and green lines for $m=xy$, xz , and yz , respectively. The minimum and maximum of the pure- $m(\mathbf{k})$ band – as well as of the pure- $m(\mathbf{k} + \mathbf{c}^*)$ band– are at the weak lines. The brown dot-dashed line has $k_b=0.9k_F$, and is the one along which the pure- m bands in FIG. 6 were shown.

The DFT-LDA full-potential NMTO calculations in Sect. V showed that the six lowest energy bands –half of them occupied– are described by a *set of six* t_{2g} WOs per $2\text{LiMo}_6\text{O}_{17}$, namely $w_m(\mathbf{r})$ centered on Mo1 in the lower ribbon and $W_m(\mathbf{r})$ on the equivalent MO1 in the upper ribbon. These sites, separated by $\frac{\mathbf{c}+\mathbf{b}}{2} - \mathbf{d}$, are special in having a full nearest-neighbor shell of octahedral molybdenums and therefore best preserve the t_{2g} symmetry of the WO and are least sensitive to the steps of the staircase. As seen in FIG.s 5 and 9, the WOs have t_{2g} symmetry around Mo1 (or MO1), and spill over into neighboring atoms –such as Mo4– which carry *no* WO [see Charts (33) and (34)]. This spill-over is necessitated by the requirement that the six Mo1- and MO1 centered t_{2g} WOs completely span the wavefunctions of the six lowest bands.

The xy WOs lie inside their respective ribbon and have strong, long-ranged $dd\pi$ intra-ribbon hopping integrals, τ_n , along \mathbf{b} , very weak $dd\delta$ inter-ribbon xy - XY hopping integrals, $t_n + u_n$, between partner ribbons, and even weaker, $t_n - u_n$, between bi-ribbons [Eq.s (35)-(36), (37), and (43)-(44)]. Between slabs, the xy hopping is negligible¹⁵.

The equivalent xz and yz WOs stand perpendicular to the ribbons and the $dd\pi$ nearest-neighbor xz - XZ hopping integral, $A_1 + G_1$, between partner ribbons is as strong as the $dd\pi$ intra-ribbon hopping integral τ_1 between xy orbitals, twice as strong as the hopping integral $A_1 - G_1$ between bi-ribbons [Eq.s (35), (38) and (45)] and 30 times stronger than the $dd\delta$ integrals $t_1 \pm u_1$ for xy - XY hopping. The $A_1 \pm G_1$ integrals are for hopping up or down the staircase with steps $\frac{\mathbf{c}-\mathbf{b}}{2}$ for xz - XZ and $\frac{\mathbf{c}+\mathbf{b}}{2}$ for yz - YZ . The two xz bands are gapped by the hopping dimerization, $\pm 2G_1 \approx \pm 0.2$ eV, and so are the two yz bands (FIG.s 6 and 7).

The six-band TB Hamiltonian was given in Eq. (35) in terms of these and further hopping integrals, Bloch summed as in Eq. (8). The basis functions were the Bloch-summed WOs, $w_m(\mathbf{k}, \mathbf{r})$ and $e^{\pi i(k_c + k_b)} W_m(\mathbf{k}, \mathbf{r})$, on respectively the lower and the upper ribbon, and the \mathbf{k} -dependent phase factor in front of $W_m(\mathbf{k}, \mathbf{r})$ was included in order to make the electronic dimerizations purely imaginary. Further insight was gained in Sect. VIB by transforming from this basis set –which for

each m consists of two Bloch sums, one over the Mo1 positions and the other over the MO1 positions,– to one with two *pseudo* Bloch sums (52), $|m; \mathbf{k}\rangle \equiv |w_m, \mathbf{k}\rangle$ and $|m; \mathbf{k} + \mathbf{c}^*\rangle$, each of which is a Bloch sum over both Mo1 and MO1 with every second phase factor along \mathbf{c} chosen as $e^{2\pi i \mathbf{k} \cdot (\mathbf{T} + \frac{\mathbf{c}+\mathbf{b}}{2})}$, i.e. as if there were no displacement dimerization, $\mathbf{d}=\mathbf{0}$. The transformation is (54). Considered as a function of \mathbf{k} , the pseudo Bloch sum $|\mathbf{k}\rangle$ is a periodic function on the sparse, so-called *even*, reciprocal lattice spanned by $(\mathbf{a}^*, \mathbf{c}^* + \mathbf{b}^*, \mathbf{c}^* - \mathbf{b}^*)$ whose BZ is the *double* zone shown in FIG. 8. Together with the function $|\mathbf{k} + \mathbf{c}^*\rangle$, periodic on the *odd* reciprocal lattice, they form a complete, orthonormal basis set for the proper, dimerized crystal. In the absence of dimerization, $|\mathbf{k}\rangle$ and $|\mathbf{k} + \mathbf{c}^*\rangle$ are identical apart from a phase factor, but they become linearly *independent* in the presence of dimerization and will mix near the boundaries of the appropriate physical zone. The six-band TB Hamiltonian (56) in this so-called $\{\mathbf{k}, \mathbf{k} + \mathbf{c}^*\}$ -representation was used to visualize the $|\mathbf{k}\rangle$ characters of the band structures in FIG.s 6 and 7 (and in Paper II FIG. 14) as their (additional) *fatness* (61). FIG. (10) showed how the $|\mathbf{k}\rangle$ characters of the lower and upper m bands switch between 0 and 1, and back again, as the Bloch vector crosses the boundaries of the physical (m -dependent) zone.

In the following Paper II, we shall find the important result that this interesting $|\mathbf{k}\rangle$ -character variation is experimentally manifested as an ARPES intensity selection rule. As mentioned already in the Introduction, when this selection rule is combined with our new ARPES data, it enables the separation of the two bands that disperse to define the FS. In Paper III we will also use the selection rule to reveal the FS features that are peculiar to each of the two bands. Thereby our new ARPES results both confirm, and are greatly aided by, our new theory. But first, at the beginning of Paper II, we shall give the complete theory which includes the distortion of the ARPES intensity variations caused by the c -axis displacement- and inversion dimerizations. The latter depends on the photon energy which we have chosen such that they basically cancel.

Acknowledgments

We are indebted to Tanusri Saha-Dasgupta, Sashi Satpathy, and Zoran Popovic for their active participation at the initial stage of this project. JWA acknowledges past support of this work by the U.S. National Science Foundation (grant DMR-07-04480).

This research used resources of the Advanced Light Source, which is a DOE Office of Science User Facility under contract no. DE-AC02-05CH11231. MG acknowledges support by NSF-DMR-1507252 grant.

Wannier-Orbital theory and ARPES for the quasi-1D conductor $\text{LiMo}_6\text{O}_{17}$.

Part II: Intensity variations and the six t_{2g} -bands

L. Dudy

Randall Laboratory, University of Michigan, Ann Arbor, MI 48109, USA
Physikalisches Institut und Röntgen Center for Complex Material Systems,
Universität Würzburg, D-97074 Würzburg, Germany
and
Synchrotron SOLEIL, L'Orme des Merisiers, 91190 Saint-Aubin, France

J.W. Allen

Randall Laboratory, University of Michigan, Ann Arbor, MI 48109, USA

J.D. Denlinger

Advanced Light Source, Lawrence Berkeley National Laboratory, Berkeley, CA 94720, USA

J. He[†]

Department of Physics and Astronomy, Clemson University, Clemson, SC 29534, USA

M. Greenblatt

Department of Chemistry & Chemical Biology, Rutgers University, 123 Bevier Rd. Piscataway, NJ 08854, USA

M.W. Haverkort

Max-Planck-Institut für Festkörperforschung, Heisenbergstrasse 1, D-70569 Stuttgart, Germany
Max-Planck-Institut für Chemische Physik fester Stoffe,
Nöthnitzer Str. 40, D-01187 Dresden, Germany
and
Institut für Theoretische Physik, Universität Heidelberg,
Philosophenweg 16, D-69120 Heidelberg, Germany

Y. Nohara and O.K. Andersen

Max-Planck-Institut für Festkörperforschung, Heisenbergstrasse 1, D-70569 Stuttgart, Germany
(Dated: May 16, 2023)

This is the second paper of a series of three papers presenting a combined study by band theory and angle-resolved photoemission spectroscopy (ARPES) of lithium purple bronze. The t_{2g} Wannier Orbitals (WOs) and resulting six-band tight-binding (TB) Hamiltonian found in paper I are here used to develop a theory of the ARPES intensity variations, including a selection rule whose validity relies on cancellation between the displacement- and inversion-dimerizations of the zig-zag chains (ribbons) in regions of the final-state wavevector, κ . We then present the ARPES results for the band structure of the four occupied t_{2g} bands (gapped xz , yz , and split metallic xy). A detailed comparison to the theory validates the selection rule. We present the Fermi surface (FS) as seen directly in the raw ARPES data, both parallel and perpendicular (using photon-energy dependence) to the sample surface, and show that the selection rule can enable separation of the barely split and highly quasi-one-dimensional xy bands. We adjust the energy of the xy WO energy by 0.1 eV ($\approx \frac{1}{4}$ of the gap) with respect to that of the xz and yz WOs and fine-tune merely 7 out of the more than 40 TB parameters to achieve an excellent fit to the ARPES bands lying more than 0.15 eV below the Fermi level. So doing then also gives nearly perfect agreement closer to the Fermi level. The good agreement between the TB- and the ARPES bands implies a very small on-site Coulomb repulsion U with an estimated upper limit of 0.35 to 0.75 eV.

VIII. INTRODUCTION

This is the second paper in a series of three presenting a detailed study of the band structure of the quasi-1D lithium purple bronze (LiPB) combining LDA-

NMTO band theory and angle-resolved photoemission spectroscopy (ARPES).

In Paper I we explained the NMTO method (Sect. II) and used it to derive, for the occupied and lowest unoccupied bands of LiPB (Sect. IV), a chemically meaningful set of Wannier functions (Sect. V)–called Wannier orbitals (WO)– and their tight-binding (TB) Hamiltonian in portable, i.e. analytical, form (Sect. VI).

The monoclinic crystal structure of $\text{LiMo}_6\text{O}_{17}$

[†]deceased in 2021.

(Sect. III of Paper I) consists of MoO_6 octahedra connected by corners into slabs perpendicular to the reciprocal-lattice vector \mathbf{a}^* . Each slab consists of *bi-ribbons*, 4 molybdenums wide in the $\mathbf{a}+\mathbf{c}$ direction, $\text{Mo2} \backslash \text{Mo1} / \text{Mo4} \backslash \text{Mo5}$ and $\text{MO5} \backslash \text{MO4} / \text{MO1} \backslash \text{MO2}$ (using lower/upper-case letters for the lower/upper string), and extending indefinitely along the direction \mathbf{b} of quasi-1D conductivity [See Fig. I 2 together with Charts I (14) and (15)]. The spines of the ribbons are the well-known $\text{Mo1} \backslash \text{Mo4} \backslash \text{Mo1} / \text{Mo4}$ and $\text{MO4} \backslash \text{MO1} \backslash \text{MO4} / \text{MO1}$ zigzag chains along \mathbf{b} . The upper string is related to the lower by translation of Mo1 to MO1 by the vector $\frac{\mathbf{c}+\mathbf{b}}{2} - \mathbf{d}$, followed by *inversion* around their midpoint, $\frac{1}{2}(\frac{\mathbf{c}+\mathbf{b}}{2} - \mathbf{d})$. Had there been *no* displacement ($\mathbf{d}=0$) and no inversion, i.e. no *c*-axis dimerization (Sect. I III A), all ribbons would have been related by a primitive translation vector $\frac{\mathbf{c}+\mathbf{b}}{2}$, and thus stacked into a ramp [Chart I (21)]. *With* displacement- and inversion dimerization, the slab forms a *staircase* with steps of bi-ribbons and running up and down along $\pm\mathbf{c}$. A staircase is terminated by insulating MoO_4 tetrahedra, and Li intercalates between staircases which is also where the crystal cleaves.

We found that the six lowest energy bands (Figs. I 3 and I 4) –half occupied– are accurately described by the set of six, real-valued t_{2g} WOs,¹¹⁴ $w_m = xy, xz, yz$ centered on Mo1, and $W_m = XY, XZ, YZ$, centered on MO1, and with x, y , and z directions as indicated in Charts I (14) and (15). Such a t_{2g} WO has tails (haloes) with the same m on the nearest Mo neighbors in its plane (Fig. I 9).

The xy WOs lie well inside their respective ribbon and have strong, long-ranged $dd\pi$ xy - xy or XY - XY hopping integrals, τ_n , with Bloch sum $\tau(k_b)$ along the ribbon, very weak $dd\delta$ xy - XY hopping integrals, $t_n + u_n$, between partner ribbons, and even weaker hopping integrals, $t_n - u_n$, between bi-ribbons [Eq.s I (36), (37), (43), and (44)]. Between slabs, the hopping is negligible. The equivalent xz and yz WOs stand perpendicular to the ribbons and the $dd\pi$ nearest-neighbor hopping integral, $A_1 + G_1$, between partner ribbons –up or down the staircase with steps $\frac{\mathbf{c}-\mathbf{b}}{2}$ for xz - XZ and $\frac{\mathbf{c}+\mathbf{b}}{2}$ for yz - YZ – is twice as strong as the hopping integral, $A_1 - G_1$, between bi-ribbons. The two xz bands are gapped by the hopping dimerization, $\pm 2G_1 \sim \pm 0.2$ eV, and so are the two yz bands [Eq.s I (38) and (45)].

In our notation, greek-lettered Bloch sums, e.g. τ , are over hops on the ribbon, whereby they are real and single-zone periodic in \mathbf{k} . Latin-lettered Bloch sums, such as t, u, A , and G , are over hops between ribbons and are therefore real and double-zone periodic [Eq.s I (41) and (42)].

In Eq. I (35) we gave the six-band TB Hamiltonian in the representation of the Bloch-summed WOs, $w_m(\mathbf{r}, \mathbf{k}) \equiv \sum_{\mathbf{T}} e^{2\pi i \mathbf{k} \cdot \mathbf{T}} w_m(\mathbf{r} - \mathbf{T})$ and $W_m(\mathbf{r}, \mathbf{k}) \equiv \sum_{\mathbf{T}} e^{2\pi i \mathbf{k} \cdot \mathbf{T}} W_m(\mathbf{r} - \mathbf{T})$, with the latter multiplied by $e^{2\pi i \mathbf{k} \cdot \frac{\mathbf{c} \pm \mathbf{b}}{2}} = e^{\pi i (k_c \pm k_b)}$ so that the hopping dimerizations are purely imaginary; numerically, they are about 30% of the corresponding hopping integral. Further insight

was gained by transforming from this sublattice $\{w, W\}$ -representation (Sect. I VIA) to the reciprocal sublattice $\{\mathbf{k}, \mathbf{k} + \mathbf{c}^*\}$ -representation (Sect. I VIB), i.e. from a basis with two sets of Bloch sums, $w_m(\mathbf{r}, \mathbf{k})$ and $W_m(\mathbf{r}, \mathbf{k})$, each a periodic function of \mathbf{k} in the single zone, to a set of *pseudo* Bloch sums (Eq. I (52)),

$$\left| m; \begin{matrix} \mathbf{k} \\ \mathbf{k} + \mathbf{c}^* \end{matrix} \right\rangle = \frac{1}{\sqrt{2}} \sum_{\mathbf{T}} e^{2\pi i \mathbf{k} \cdot \mathbf{T}} \left[w_m(\mathbf{r} - \mathbf{T}) \pm e^{\pi i (k_c + k_b)} W_m(\mathbf{r} - \mathbf{T}) \right],$$

which are periodic functions of \mathbf{k} in the *double zone* (Fig. I 8), redrawn as Fig. 11 in this Paper II) and evaluated in two different single zones, i.e. at \mathbf{k} and $\mathbf{k} + \mathbf{c}^*$. Each pseudo-Bloch sum is over *both* ribbons with the phase factor multiplying $W(\mathbf{r} - \mathbf{T})$ chosen as if there were *no* displacement dimerization, \mathbf{d} [see Eq.s I (17) and (18)¹], i.e. as $e^{2\pi i \mathbf{k} \cdot \frac{\mathbf{c} \pm \mathbf{b}}{2}}$. It is now conceivable that the ARPES intensity of an occupied band in LiPB approximately follows its $|\mathbf{k}\rangle$ -character, i.e. what we called its fatness in Sect. I VIC and showed in Fig. I 10 for the two xy bands as functions of k_c for $k_b=0.225$. In the absence of dimerization, the two pseudo Bloch sums are linearly dependent, and the $|\mathbf{k}\rangle$ - and $|\mathbf{k} + \mathbf{c}^*\rangle$ -projected bands are double-zone periodic and translated by \mathbf{c}^* with respect to each other. With dimerization, the pseudo Bloch sums become linearly *independent* and will mix near the crossings of the *undimerized* \mathbf{k} - and $(\mathbf{k} + \mathbf{c}^*)$ -bands, where the dimerized bands will gap and thus restore the single-zone periodicity. Correspondingly, the $|\mathbf{k}\rangle$ projection follows the undimerized \mathbf{k} -band, except near its crossing with the undimerized $(\mathbf{k} + \mathbf{c}^*)$ -band, where it loses half its intensity to the $|\mathbf{k} + \mathbf{c}^*\rangle$ -projected band (see Figs. I 6-8).

The first task of the present Paper II is to derive an expression for the ARPES intensity which *includes* the distortion caused by *c*-axis dimerization. In order to do so, we neglect the coupling between t_{2g} WOs with different m , a good approximation near the FS ($|k_b| \approx \frac{1}{4}$), and in fact everywhere, except near the ΓZ -line ($k_b=0$). In this *pure m*-band approximation introduced in Sect. I VIC, the six-band Hamiltonian factorizes in three 2×2 Hamiltonians, H_m , with eigenvalues (Eq.s I (57)),

$$\pm \sqrt{A^2 + G^2}, \pm \sqrt{\bar{A}^2 + \bar{G}^2}, \text{ and } \tau \pm \sqrt{t^2 + u^2},$$

for $m=xz, yz$, or xy , respectively, and with \mathbf{k} dependencies given by Eq.s I (37) and (38). The crossings, I (32), (31) and (30), of these pure- m bands define the boundaries of the so-called *physical zones*. The eigenfunctions

¹ I, II, and III refer to sections, figures, and equations in Paper I, II, and III, respectively.

of the pure m bands were given by for instance Eq. I (58):

$$w_1^2(\mathbf{k}, \mathbf{r}) = \frac{1}{\sqrt{2}} \left[w(\mathbf{k}, \mathbf{r}) e^{-i\phi(\mathbf{k})} \pm W(\mathbf{k}, \mathbf{r}) e^{\pi i(k_c + k_b)} \right],$$

with the band-structure phase

$$e^{i\phi} \equiv \frac{A + iG}{\sqrt{A^2 + G^2}}, \frac{\bar{A} + i\bar{G}}{\sqrt{\bar{A}^2 + \bar{G}^2}}, \text{ and } \frac{t + iu}{\sqrt{t^2 + u^2}}.$$

According to Eq.s I (59) and (61), the fatness of the ^{upper}/_{lower} m band illustrated in Fig. I 10 is $\frac{1}{2} [1 \pm \cos \phi_m(\mathbf{k})]$. In Sect. IX B 1 we shall show that the intensity of photo-emission from the ^{upper}/_{lower} m band is simply $\frac{1}{2} [1 \pm \cos \{\phi_m(\mathbf{k}) - \eta_m(\boldsymbol{\kappa})\}]$, which means that it is shifted in phase by $\eta_m(\boldsymbol{\kappa})$, the difference (70) between the phase shifts due to the c -axis inversion and displacement.

On top of these fine-grained intensity variations caused by the near-translational equivalence Eq. I (20) of the WOs on the upper and lower ribbons, there are coarse-grained variations due to the approximate translational equivalence Eq. I (12) of the halos on the Mo neighbors in the plane of the WO and therefore described by the WO form factor (Sect. IX B 2).

The understanding of the ARPES intensity variations gained in Sect. IX enabled us to obtain the new, detailed ARPES results for the occupied part of the t_{2g} bands which we present in Sect. X, compare with the WO band theory (Sect.s X D and X E), and in Sect. XI use to adjust the parameters of the six-band TB Hamiltonian (derived in Sect. I VI A). Important information on the technical experimental details are given in Sect.s X A and X B. The ARPES FS measurements turned out to have a rather strong photon-energy dependence (Sect. X C) whose origin seems to be the narrowness along κ_c of the form factor for the \widetilde{xy} WO, i.e. the widening along \mathbf{c} of $w_{\widetilde{xy}}(\mathbf{r})$ caused by the hybridization with the valence band (see Sect. III XIV A 2).

IX. THEORY OF ARPES INTENSITY VARIATIONS IN LIPB

Our ARPES data to be presented in Sect. X show intensity variations between equivalent zones, similar to the BZ-selection effects observed in graphite and explained by Shirley et al. [67]. The primitive cell of LiPB, $\text{Li}_2\text{Mo}_{12}\text{O}_{34}$, is however much larger than that of graphite, C_2 , and its ARPES intensity exhibits not only fine-grained zone selection, but also coarse-grained structures in reciprocal space. On the other hand, like in graphite, there are only four occupied bands in LiPB, and this enables a simple description for LiPB in terms of WOs. As we shall explain, it is the tails of the Mo1 and MO1-centered t_{2g} WOs, $w_m(\mathbf{r})$ and $W_m(\mathbf{r})$ shown

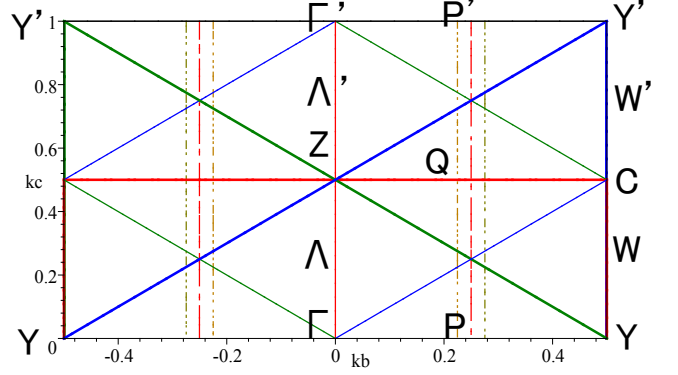


FIG. 11: Upper part ($|k_b| \leq \frac{1}{2}, 0 \leq k_c \leq 1$) of the double zone shown in FIG. I 8. The ^{1st}/_{2nd} physical zones for xy (red), xz (blue), and yz (green) are respectively: $|k_c| \leq \frac{1}{2}$, $|k_c + k_b| \leq \frac{1}{2}$, and $|k_c - k_b| \leq \frac{1}{2}$. See Sect. IIV A 4 and Sect. X D. This figure is to scale because the YZY' triangles are equilateral.

in Fig. I 9, which give rise to the coarse-grained structure², and it is the approximate equivalence I (17) by half a lattice translation which gives rise to the fine-grained structure. This zone-selection effect is simpler than the one found for the π band in graphite because it is due to the existence of a hypothetical, un-dimerized form ($\text{LiMo}_6\text{O}_{17}$) of LiPB, which cannot exist for C_2 where the two carbons are far from being separated by half a lattice vector.

A. Preliminaries

We shall follow the treatment of Shirley et al. [67], but in the next subsection switch from their representation of the initial-states in terms of atomic orbitals (AOs) to one in terms of WOs. Hence, we start from the one-step (Fermi's golden rule) expression:

$$I(\boldsymbol{\kappa}, \omega) \propto \theta(\omega) \sum_{j\mathbf{k}}^{\text{zone}} \delta[E_j(\mathbf{k}) + \omega] \times |\langle e^{2\pi i \boldsymbol{\kappa} \cdot \mathbf{r}} | \mathbf{p} \cdot \mathbf{E} | \psi_j(\mathbf{k}, \mathbf{r}) \rangle|^2, \quad (62)$$

for the photoemission intensity as functions of the electrons binding energy ω and momentum $(2\pi) \boldsymbol{\kappa}$ inside the sample. We have used the one-electron approximation with initial-state Bloch functions $\psi_j(\mathbf{k}, \mathbf{r})$ and energy bands $E_j(\mathbf{k})$ with respect to the Fermi level. The sum

² This effect is not included in the recent *experimentalist's guide to the matrix element in ARPES* [68] because the WOs used there did not extend over several atoms per primitive cell.

in (62) is over all occupied states $j\mathbf{k}$ with \mathbf{k} in a (single) zone and $\sum_{\mathbf{k}}$ denoting the average over this zone. For simplicity –and lack of knowledge– the final state inside the sample is taken as the plane wave $e^{2\pi i\boldsymbol{\kappa}\cdot\mathbf{r}}$, the least specific choice possible. For our purpose, it suffices to express the matrix element as:

$$\langle e^{2\pi i\boldsymbol{\kappa}\cdot\mathbf{r}} | \mathbf{p} \cdot \mathbf{E} | \psi_j(\mathbf{k}, \mathbf{r}) \rangle \propto (\boldsymbol{\kappa} \cdot \hat{\mathbf{e}}) \langle e^{2\pi i\boldsymbol{\kappa}\cdot\mathbf{r}} | \psi_j(\mathbf{k}, \mathbf{r}) \rangle \quad (63)$$

as obtained by, first of all, operating with the dipole operator $\mathbf{p} \cdot \mathbf{E}$ to the left, that is on the plane wave, and then by pulling the polarization-dependent factor from Eq. (84) outside the integral, exploiting the fact that the photon wavelength is long compared with inter-atomic distances. The proportionality constants in (62) and (63) are independent of the initial states.

Hence, photoemission at energy ω occurs for $\boldsymbol{\kappa}$ at the constant-energy contours $\omega = -E_j(\boldsymbol{\kappa} [\text{mod zone}])$ with an intensity which, contrary to $E_j(\mathbf{k})$, is aperiodic in the reciprocal lattice and depends on the polarization of the photons and on the initial states, $\psi_j(\mathbf{k}, \mathbf{r})$, of the electrons.

The initial states may be expanded in Bloch sums I (8) of localized orbitals $\chi_{RL}(\mathbf{r})$, e.g. AOs, NMTOs, or WOs:

$$\psi_j(\mathbf{k}, \mathbf{r}) = \sum_{RL}^{\text{cell}} \chi_{RL}(\mathbf{k}, \mathbf{r}) u_{RL,j}(\mathbf{k}) = \sum_{RL}^{\text{cell}} \sum_{\mathbf{T}} \chi_{RL}(\mathbf{r} - \mathbf{T}) e^{2\pi i\mathbf{k}\cdot\mathbf{T}} u_{RL,j}(\mathbf{k}). \quad (64)$$

Since for a Bloch sum I (8) of orbitals, $\chi_R(\mathbf{r})$ centered¹⁴ at $\mathbf{r}=\mathbf{R}$,

$$\begin{aligned} \langle e^{2\pi i\boldsymbol{\kappa}\cdot\mathbf{r}} | \chi_R(\mathbf{k}, \mathbf{r}) \rangle &= \\ e^{-2\pi i\boldsymbol{\kappa}\cdot\mathbf{R}} \int \chi_R(\mathbf{r}) e^{-2\pi i\boldsymbol{\kappa}\cdot(\mathbf{r}-\mathbf{R})} d^3r \sum_{\mathbf{T}} e^{-2\pi i(\boldsymbol{\kappa}-\mathbf{k})\cdot\mathbf{T}} \\ &= e^{-2\pi i\boldsymbol{\kappa}\cdot\mathbf{R}} \tilde{\chi}_R(\boldsymbol{\kappa}) \sum_{\mathbf{G}} \delta(\boldsymbol{\kappa} - \mathbf{k} - \mathbf{G}), \end{aligned} \quad (65)$$

where the sum is over all points, \mathbf{G} , of the reciprocal lattice and

$$\tilde{\chi}_R(\boldsymbol{\kappa}) \equiv \int \chi_R(\mathbf{r}) e^{-2\pi i\boldsymbol{\kappa}\cdot(\mathbf{r}-\mathbf{R})} d^3r \quad (66)$$

is the Fourier transform (FT)³ of $\chi_R(\mathbf{r})$. Note that we use a notation according to which real-space functions such as $\chi_R(\mathbf{r})$ are centered at $\mathbf{r}=\mathbf{R}$, but their Fourier transforms, $\tilde{\chi}_R(\boldsymbol{\kappa})$ defined by (66), only depend on their shape and not on where they are centered.

The second factor of the matrix element (63) thus factorizes as:

$$\begin{aligned} \langle e^{2\pi i\boldsymbol{\kappa}\cdot\mathbf{r}} | \psi_j(\mathbf{k}, \mathbf{r}) \rangle &= \sum_{RL}^{\text{cell}} e^{-2\pi i\boldsymbol{\kappa}\cdot\mathbf{R}} \tilde{\chi}_{RL}(\boldsymbol{\kappa}) u_{RL,j}(\mathbf{k}) \\ &\times \sum_{\mathbf{G}} \delta(\boldsymbol{\kappa} - \mathbf{k} - \mathbf{G}), \end{aligned}$$

whereby expression (62) for the photoemission intensity becomes:

$$I(\boldsymbol{\kappa}, \omega) \propto (\boldsymbol{\kappa} \cdot \hat{\mathbf{e}})^2 \theta(\omega) \sum_{j\mathbf{k}}^{\text{zone}} \delta[E_j(\mathbf{k}) + \omega] \times \left| \sum_{RL}^{\text{cell}} e^{-2\pi i\boldsymbol{\kappa}\cdot\mathbf{R}} \tilde{\chi}_{RL}(\boldsymbol{\kappa}) u_{RL,j}(\mathbf{k}) \sum_{\mathbf{G}} \delta(\boldsymbol{\kappa} - \mathbf{k} - \mathbf{G}) \right|^2, \quad (67)$$

which vanishes unless the wave-vector, $\boldsymbol{\kappa}$, of the final electronic state inside the sample (see Sect. X A) equals the Bloch vector, \mathbf{k} , of the initial electronic state, plus an arbitrary reciprocal lattice vector, \mathbf{G} . In (67), $\sum_{\mathbf{G}}$ is a periodic function of $\boldsymbol{\kappa} - \mathbf{k}$ in the \mathbf{G} -lattice, but the other factors are not.

An AO factorizes as: $\chi_{RL}(\mathbf{r}) \equiv Y_L(\widehat{\mathbf{r}}_R) \varphi_{RL}(r_R)$, whereby its FT (66), which depends on its shape, L , including its orientation, but *not* on its center, \mathbf{R} , can be taken outside the sum over translationally equivalent AOs:

$$\begin{aligned} \sum_{R \in \text{eq}}^{\text{cell}} e^{-2\pi i\boldsymbol{\kappa}\cdot\mathbf{R}} \tilde{\chi}_{RL}(\boldsymbol{\kappa}) u_{RL,j}(\mathbf{k}) &= \\ \tilde{Y}_L(\hat{\boldsymbol{\kappa}}) \int j_l(2\pi\kappa r) \varphi_{RL}(r) r^2 dr \sum_{R \in \text{eq}}^{\text{cell}} e^{-2\pi i\mathbf{k}\cdot\mathbf{R}} u_{RL,j}(\mathbf{k}), \end{aligned} \quad (68)$$

thus leaving the sums $\sum_{R \notin \text{eq}}^{\text{cell}}$ over the translationally *inequivalent* AOs to be performed later. Hence, the sum (68) over translationally equivalent AOs factorizes into a κ -dependent AO form factor, times a so-called (Ref. 69–71) photoemission structure factor (PSF). The latter is similar to the geometrical structure factor in x-ray diffraction, but depends on the initial-state wave function [via its LCAO coefficients, $u_{RL,j}(\mathbf{k})$]. This factorization holds for the π band in C_2 , because this band is singly degenerate and contains only one type of orbital, $Y_{10}=p_z$, so that the entire sum, $\sum_{RL}^{\text{cell}} e^{-2\pi i\boldsymbol{\kappa}\cdot\mathbf{R}} \tilde{\chi}_{RL}(\boldsymbol{\kappa}) u_{RL,j}(\mathbf{k})$, reduces to the factorized form (68). The PSF for the graphene π band thus depends merely on the \mathbf{k} -dependent phase between the p_z orbitals on the two atoms [67]. However, to the three σ bands in graphene *three* translationally inequivalent AOs on each of the two C atoms (s , p_x , and p_y , or the three equivalent sp^2 orbitals directed towards the three nearest neighbors) contribute, so that for the σ bands, $\sum_{RL}^{\text{cell}} e^{-2\pi i\boldsymbol{\kappa}\cdot\mathbf{R}} \tilde{\chi}_{RL}(\boldsymbol{\kappa}) u_{RL,j}(\mathbf{k})$ does *not* factorize into an orbital form factor and a geometrical structure factor.

Whereas 8 AOs are needed to describe the occupied bands in graphene, LiPB needs more than 300 atomically localized AOs (see Sect. I II), but merely the six t_{2g} WOs shown in Fig. I 9. Using those in expression (67) for the ARPES intensity leads to great simplification, as we shall now see:

³ The small tilde denoting the FT has nothing to do with the large tilde denoting the downfolding of the xz and yz characters into the $\bar{x}\bar{y}$ states in the gap.

B. Using the six t_{2g} WOs

For LiPB, we shall now predict, and in Sect. X E confirm, that the near-translational equivalence of the t_{2g} WOs $w_m(\mathbf{r})$ and $W_m(\mathbf{r})$ by half a lattice translation causes ARPES to have double-period fine-grained intensity variations which approximately follow the $|\mathbf{k}|$ -character I (61), shown in Figs I 6, 7, and 10, of the occupied bands. This implies that the m band with the lower energy appears in the 1st- and is extinguished near the centre of the 2nd physical zone, and conversely for the m band with the higher energy. On top of this, comes that the upper xz and yz bands are unoccupied and therefore cause no intensity in their respective 2nd physical zones. The metallic xy band with the lower energy should best be seen in the 1st- and the xy band with the higher energy in the 2nd BZ. This zone-selection effect will allow us to resolve the perpendicular dispersion and splitting of the quasi-1D \tilde{xy} bands predicted in the bottom panel of Fig. 14. The deviations from this translational equivalence of $w_m(\mathbf{r})$ and $W_m(\mathbf{r})$, i.e. the inversion- and displacement dimerizations I (18), will simply shift the ARPES intensity variation from that of the $|\mathbf{k}|$ character, $\frac{1}{2} [1 \pm \cos \phi(\mathbf{k})]$, to $\frac{1}{2} [1 \pm \cos \{\phi(\mathbf{k}) - \eta(\boldsymbol{\kappa})\}]$ where $\eta(\boldsymbol{\kappa})$ is the dimerization phase shift. This shift is negligible for the xy -, and may by suitable choice of κ_a via be so also for the occupied xz and yz bands.

In addition to the *fine-grained zone-selection* effect (Sect. IX B 1), well-known from the geometrical *struc-*

ture factor in x-ray crystallography, we shall predict (Sect. IX B 2) and find (Sect. X) that the *internal* structure of the $w_m(\mathbf{r})$ t_{2g} WO, spreading out to about the four nearest molybdenums in its plane, makes the *form factor* of the WO approximately factorize into a *coarse-grained structure factor* times the *form factor* of the *local* partial-wave projection, $Y_{2m}(\hat{\mathbf{r}}) \varphi_2(r)$, of the WO tail (halo).

1. Zone selection; the fine-grained structure

The DFT calculation resulting in the low-energy six-band t_{2g} TB Hamiltonian and in the band structures in Figs 20 (b) and 22 shows that –except near band crossings such as those below -0.5 eV and the ones near the top of the valence bands near Z– each band is dominated by *one* m -character. For describing the ARPES matrix elements, but not the bands, we shall neglect by-mixing of WOs with other m -values, i.e. use the pure- m approximation (Sect. I VI C). Therefore, in the general expression (64) for the the initial-state wave function, L takes *one* value (m), R takes two values (Mo1 and MO1), and expression (64) becomes Eq. I (58) which is repeated in the Introduction of the present paper.

Hence, the second factor of the matrix element (63) for photoemission from the upper ($j=2$) or lower ($j=1$) m -band state is the FT of the respective eigenfunction I (58):

$$\begin{aligned} \left\langle e^{2\pi i \boldsymbol{\kappa} \cdot \mathbf{r}} | w_2(\mathbf{k}, \mathbf{r}) \right\rangle &= \frac{1}{\sqrt{2}} \sum_{\mathbf{G}} \delta(\boldsymbol{\kappa} - \mathbf{k} - \mathbf{G}) \left[\tilde{w}(\boldsymbol{\kappa}) e^{-i\phi(\mathbf{k})} \pm \tilde{W}(\boldsymbol{\kappa}) e^{2\pi i \boldsymbol{\kappa} \cdot \mathbf{d}} \right] \\ &= \frac{1}{\sqrt{2}} \sum_{\mathbf{G}} \delta(\boldsymbol{\kappa} - \mathbf{k} - \mathbf{G}) \tilde{w}(\boldsymbol{\kappa}) \left[e^{-i\phi(\mathbf{k})} \pm e^{-i\eta(\boldsymbol{\kappa})} \right]. \end{aligned} \quad (69)$$

For the FTs of $w(\mathbf{k}, \mathbf{r})$ and $W(\mathbf{k}, \mathbf{r})$ we have used Eq. (65) with the sum being over all points \mathbf{G} of the reciprocal lattice⁴. Inside this sum, the product of the phase factors, $e^{\pi i(k_c + k_b)}$ and $e^{-2\pi i \boldsymbol{\kappa} \cdot (\frac{\mathbf{c} + \mathbf{b}}{2} - \mathbf{d})}$, from respectively Eq.s I (58) and (65), is simply $e^{2\pi i \boldsymbol{\kappa} \cdot \mathbf{d}}$ with \mathbf{d} being the displacement dimerization I (16). On the second line of Eq. (69) we have used that, due to the inversion dimerization I (18), $\tilde{W}(\boldsymbol{\kappa}) = \tilde{w}(-\boldsymbol{\kappa})$ and $\tilde{w}(-\boldsymbol{\kappa}) = \tilde{w}(\boldsymbol{\kappa})^* = |\tilde{w}(\boldsymbol{\kappa})| e^{-i \arg \tilde{w}(\boldsymbol{\kappa})}$, because $w(\mathbf{r})$ is a real-valued t_{2g} function. As a consequence, $e^{2\pi i \boldsymbol{\kappa} \cdot \mathbf{d}} \tilde{W}(\boldsymbol{\kappa}) / \tilde{w}(\boldsymbol{\kappa}) = e^{-i\eta(\boldsymbol{\kappa})}$,

where

$$\eta(\boldsymbol{\kappa}) \equiv 2 \arg \tilde{w}(\boldsymbol{\kappa}) - 2\pi \boldsymbol{\kappa} \cdot \mathbf{d}, \quad (70)$$

is the *dimerization phase shift* whose first term is due to the inversion- and the second to the displacement dimerization. We shall evaluate $\arg \tilde{w}(\boldsymbol{\kappa})$ in the next subsection IX B 2.

The intensity (67) of photoemission from two dimerized m bands ($j=1, 2$) in LiPB is thus:

$$\begin{aligned}
I(\boldsymbol{\kappa}, \omega) &\propto (\boldsymbol{\kappa} \cdot \hat{\mathbf{e}})^2 \theta(\omega) \sum_{j=1}^2 \sum_{\mathbf{k}}^{\text{zone}} \delta[E_j(\mathbf{k}) - E_F + \omega] \left| \sum_{\mathbf{G}} \delta(\boldsymbol{\kappa} - \mathbf{k} - \mathbf{G}) \tilde{w}(\boldsymbol{\kappa}) \left[e^{-i\phi(\mathbf{k})} \pm e^{-i\eta(\boldsymbol{\kappa})} \right] \right|^2 \propto \\
&\sim (\boldsymbol{\kappa} \cdot \hat{\mathbf{e}})^2 |\tilde{w}(\boldsymbol{\kappa})|^2 \theta(\omega) \sum_{j=1}^2 \sum_{\mathbf{k}}^{\text{zone}} \delta[E_j(\mathbf{k}) - E_F + \omega] \delta[\boldsymbol{\kappa} - (6, 0, 0) - \mathbf{k}] \frac{1 \pm \cos[\phi(\mathbf{k}) - \eta(\boldsymbol{\kappa})]}{2}, \quad (71)
\end{aligned}$$

where the second line holds when –hinging on the coarse-grained structure of $\tilde{w}(\boldsymbol{\kappa})$ and the experimental set up as seen in the following sections and figures– the \mathbf{G} -sum is *dominated by one term*, the one for $\mathbf{G} = (6, 0, 0)$ in our case. We can then use that $\frac{1}{2} |e^{-i\phi} \pm e^{-i\eta}|^2 = 1 \pm \cos(\phi - \eta)$, which is like in Eq. I(61) but shifted by η , and obtain the simple result that the intensity of photoemission from two dimerized m bands ($j=1, 2$) in LiPB follows the $|\mathbf{k}|$ character (fatness), *shifted* by the dimerization phase shift (70).

The band-structure phase $\phi(\mathbf{k})$ defined in Eq. I(60) –and repeated in the Introduction– depends on k_b and k_c , but negligibly on k_a due to the long paths for hopping between slabs^{I15}. The $\kappa_a = k_a + 6$ dependence therefore enters the last factor, $\sum_{j\mathbf{k}}$, of the intensity (71) only via the dimerization phase shift $\eta(\boldsymbol{\kappa})$ (70). For this, the inversion (dash) and displacement (dots) phase shifts *tend to cancel out* as seen in the 1st columns of Figs 12 and 13: For the xy bands, a zero of $\eta(\boldsymbol{\kappa})$ (full) decreases through the 1st zone ($-\frac{1}{2}|\frac{1}{2}$) for κ_a increasing from 6.4 to 7.2, and for the yz bands, it increases through the 1st zone for κ_a increasing from 4.8 to 5.8. In these intervals of κ_a , the c -axis dimerization hardly distorts the zone selection as is illustrated in the 2nd column. This distortion cancellation is surprising, in particular for the yz (and xz) WO whose $dd\pi$ coupling between $yz(\mathbf{r})$ and $YZ(\mathbf{r} - \frac{c+\mathbf{b}}{2} + \mathbf{d})$ is much larger than the $dd\delta$ coupling between the parallel $xy(\mathbf{r})$ and $XY(\mathbf{r} - \frac{c+\mathbf{b}}{2} + \mathbf{d})$ WOs.

In Sects. XB and XC we shall explain how κ_a is deduced and how it is controlled by the photon energy, $h\nu$.

In Paper III, we shall study the dispersion of the two quasi-1D bands in the gap and –as demonstrated by comparison of the red and dark-red bands in respectively the middle and bottom parts of Fig.14– this requires that we take the weak hybridization of these xy -like bands with the xz and yz valence and conduction bands into account. This we shall do by downfolding those characters into the tails of the xy WOs, which thereby attain longer range and become what we call \tilde{xy} WOs. The concomitant modification of the WO form factor –and, hence, dimerization phase shift– we shall neglect. The zone selection remains as described above because weak hybridization hardly changes the distribution in reciprocal space of the $|\mathbf{k}|$ characters (see Sect. I VID). What *does* change, is the energy-band *dispersion*. As mentioned before, a main goal of the present and the following Paper III is to detect with ARPES the predicted dispersion

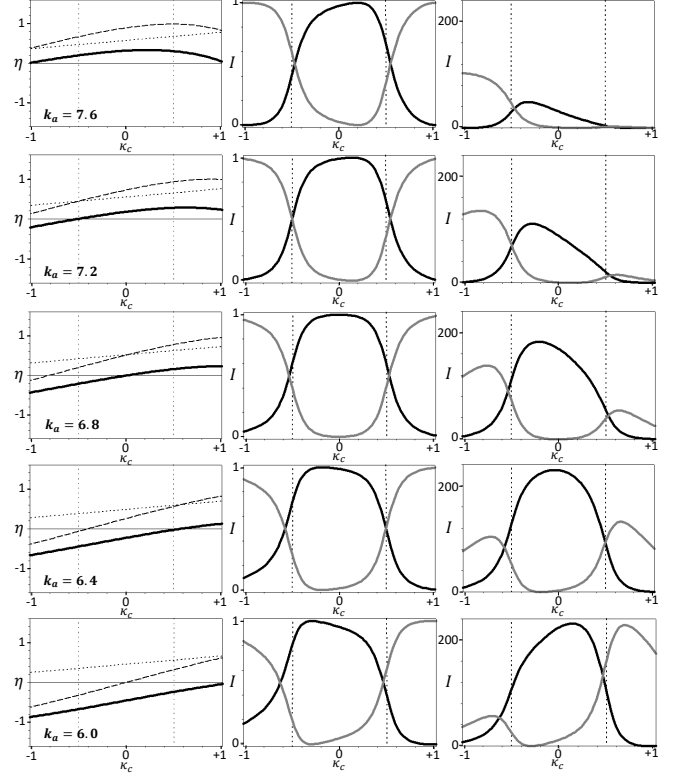


FIG. 12: Photoemission from the xy bands. *Column 1:* Inversion- ($2 \arg \tilde{w}(\boldsymbol{\kappa})$, dash), displacement- ($2\pi \boldsymbol{\kappa} \cdot \mathbf{d}$, dots), and total ($\eta(\boldsymbol{\kappa})$, full) dimerization phase shift for $\kappa_a = 6.0$ to 7.6, and $\kappa_b = 0.225$ as functions of κ_c in the interval $[-1|1]$. *Column 2:* Relative intensities of photoemission, $[1 \pm \cos\{\phi(\mathbf{k}) - \eta(\boldsymbol{\kappa})\}]/2$, from the upper (light) and lower (dark) bands for $\kappa_b = k_b = 0.225$ and as functions of $\kappa_c = k_c$ in the double zone. See also FIG. I10. *Column 3:* Absolute photoemission intensities, i.e. the relative intensities in column 2, times the polarization- and WO form factors, $(\boldsymbol{\kappa} \cdot \hat{\mathbf{e}})^2 |\tilde{w}(\boldsymbol{\kappa})|^2$, evaluated in Sect. IX B 2 and shown in the top panel of FIG. 14.

in the perpendicular (k_c) direction, most noticeably the resonance peak in the \tilde{xy} band caused by the xz band and expected to be seen near $\kappa_c=0.75$.

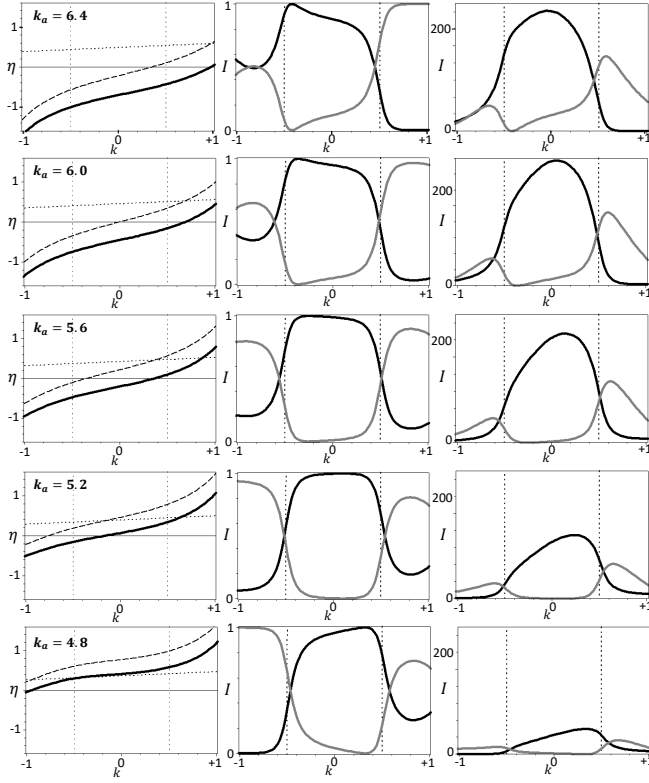


FIG. 13: As in FIG. 12, but for the yz bands along the $\kappa_b = \kappa_c$ line (CFC in FIG. 18) as functions of $k \equiv 2\kappa_b = 2\kappa_c$ in the interval $(-1|1)$. The mirror operation $k_b \rightarrow -k_b$ yields the figures for the xz bands. Note that the light curves should have been deleted because there is no emission from the upper xz and yz bands which are empty.

2. WO form factor, $\tilde{w}_m(\boldsymbol{\kappa})$, inversion dimerization, and the coarse-grained structure

A t_{2g} WO, $w_m(\mathbf{r})$, has tails (haloes) with essentially the same m character as that of its head on the Mo neighbors in the plane of this nearly 2D (flat) WO (see Fig. I 9). For the present purpose, we shall neglect the hybridization between WOs with different values of m , as well as the details of the oxygens which $pd\pi$ anti-bond with the WO head and bond with the tail. What is important, is that the head has a partial-wave shape, $Y_m(\hat{\mathbf{r}})\varphi_2(r)$, which is translated to the Mo n neighbors and multiplied by a factor, $c_n < 1$. This makes the FT, $\tilde{w}_m(\boldsymbol{\kappa})$, of the WO factorize approximately into an orbital-dependent structure factor, $\mathcal{S}_m(\boldsymbol{\kappa})$, times the FT of $Y_m(\hat{\mathbf{r}})\varphi_2(r)$:

$$\tilde{w}_m(\boldsymbol{\kappa}) \propto \mathcal{S}_m(\boldsymbol{\kappa}) \tilde{Y}_m(\hat{\boldsymbol{\kappa}}) \int_0^{0.55} j_2(2\pi\kappa r) \varphi_{\text{Mod}}(r) r^2 dr. \quad (72)$$

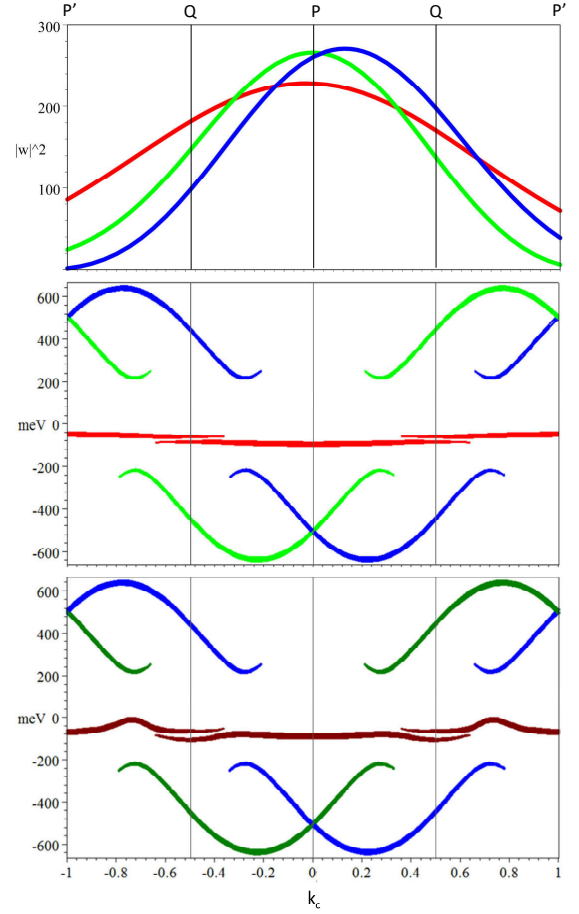


FIG. 14: *Top*: Polarization- and form factor intensities, $(\boldsymbol{\kappa} \cdot \hat{\mathbf{e}})^2 |\tilde{w}_m(\boldsymbol{\kappa})|^2$, for $m=xy$ red, xz blue, and yz green along the $P'QPQP'$ line, $\kappa_b=0.225$, in the double zone $-1 < \kappa_c \leq 1$. These aperiodic, coarse-grained intensities depend on κ_a – chosen here to be 6.4 – as explained in Sect. XB. *Middle and bottom*: Band-factor intensities according to Eq. (71) without dimerization, $\eta_m(\boldsymbol{\kappa}) = 0$. They are the $|\mathbf{k}|$ -projected bands [see Eq. I (61)] and give rise to the fine-grained intensity distributions with period 2 in κ_c . Their dependence on κ_a is negligible. Like in FIG.s I 6 and 7 the red xy band in the *middle* is pure, while the dark-red \tilde{xy} band at the *bottom* is perturbed by the xz and yz valence and conduction bands. The $(\mathbf{k}, \mathbf{k} + \mathbf{c}^*)$ -hybridization is seen to effectively extend over a κ_c -region of width 0.3 around the ZBs, $\kappa_c = \frac{1}{2} + \text{integer}$. The zero of energy is the center of the gap in the xz and yz bands, whereby $E_F=75$ meV (see Sect. I VI). The occupation factor, $\theta(\omega)$ in Eq. (71), will remove the intensity from the bands with $E > E_F$.

We have not computed the form factor by accurate, numerical FT of the WO,⁵ but shall use the factorization

⁵ It may be kept in mind [see text after Eq. I (34)] that our t_{2g} WOs are given by the exact crystal structure and are insensitive to the orientation of the xyz system I (12), which is only approximately

(72) together with the real-space figures to provide a qualitative *understanding* of the ARPES data to be presented in the following section.

Whereas the radial and angular factors, $\int_0^{0.55} j_2(2\pi\kappa r) \varphi_{\text{Mo}d}(r) r^2 dr$ and $\tilde{Y}_m(\hat{\kappa})$, are even, real functions of κ , the structure factor, $\mathcal{S}_m(\kappa)$, is a complex function whose real and imaginary parts, like those of $\tilde{w}_m(\kappa)$, are respectively even and odd. From the WO figures I 5 and 9, we estimate these structure factors to be:

$$\mathcal{S}_{xy}(\kappa) \sim \left[\begin{array}{ccc} +\frac{1}{4}e^{-2\pi i\kappa_x} & +\frac{1}{2}e^{2\pi i\kappa_y} & +\frac{1}{6}e^{2\pi i(\kappa_x+\kappa_y)} \\ & 1 & +\frac{1}{2}e^{2\pi i\kappa_x} \\ & +\frac{1}{4}e^{-2\pi i\kappa_y} & \end{array} \right] / \left(1 + \frac{1}{2} + \frac{1}{2} + \frac{1}{4} + \frac{1}{4} + \frac{1}{6} \right), \quad (73)$$

$$\mathcal{S}_{yz}(\kappa) \sim \left[\begin{array}{ccc} +\frac{1}{8}e^{2\pi i(\kappa_z-\kappa_y)} & +1e^{2\pi i\kappa_z} & 0 \\ +\frac{1}{3}e^{-2\pi i\kappa_y} & 1 & +\frac{1}{2}e^{2\pi i\kappa_y} \\ 0 & +\frac{1}{4}e^{-2\pi i\kappa_z} & 0 \end{array} \right] / \left(1 + 1 + \frac{1}{2} + \frac{1}{3} + \frac{1}{4} + \frac{1}{8} \right), \quad (74)$$

and $\mathcal{S}_{xz}[\kappa_x, \kappa_z] = \mathcal{S}_{yz}[\kappa_y, \kappa_z]$.

In Fig. I 5 we clearly see that the inversion symmetry of the xy WO around its center, Mo1, is far better preserved than that of the yz WO. The inversion dimerization I(18) is $w_m(-\mathbf{r}) = w_m(\mathbf{r})$, and the phase shift (70) due to inversion dimerization is $2\arg \tilde{w}(\kappa) = 2\arg S(\kappa)$. The latter function is easily found from Eq. (73) for xy and from (74) for yz , and was used to produce Figs 12 and 13. Since $\mathcal{S}_{xz}[\kappa_x, \kappa_z] = \mathcal{S}_{yz}[\kappa_y, \kappa_z]$, we have: $\eta_{xz}[\kappa_x, \kappa_z] = \eta_{yz}[\kappa_y, \kappa_z]$.

The structure factors, \mathcal{S}_{xy} , \mathcal{S}_{yz} , and \mathcal{S}_{xz} , peak – with value 1 if the normalizations are as above – along the respective lines: $[\kappa_x, \kappa_y, \kappa_z] = [L, M, \kappa_z]$, $[\kappa_x, M, N]$, and $[L, \kappa_y, N]$, passing through the respective points, $L\mathbf{x}^* + M\mathbf{y}^* + N\mathbf{z}^*$, of the lattice reciprocal to the lattice I(12) with 1 Mo per primitive cell. In other words: $|\mathcal{S}_{xy}|^2$, $|\mathcal{S}_{yz}|^2$, and $|\mathcal{S}_{xz}|^2$ form 2D square lattices of "beams" running in respectively the κ_z , κ_x , and κ_y directions. This gives rise to intensity patterns that are coarser than the zone-selection patterns ($M+N$ even or odd) whose origin is the smallness of the dimerization that increases the size of the primitive cell from 6 to 12 molybdenums.

The relation between the $[\kappa_x, \kappa_y, \kappa_z]$ - and the $(\kappa_a, \kappa_b, \kappa_c)$ -components –used to describe respectively the WO and the band structure and, hence, respectively the coarse and the fine-grained structure– is:

$$\frac{\kappa_x}{\kappa_y} = \frac{\kappa_a + \kappa_c}{6} \mp \frac{\kappa_b}{2} \text{ and } -\kappa_z = \frac{\kappa_a + \kappa_c}{6} - \frac{\kappa_c}{2}, \quad (75)$$

which is the same as the transformation I (12) between the primitive translations of the approximately cubic Mo1- and the exact Mo12-lattice [see also Charts I (14) and I (15)]. The inverse transformation –the same as I (13)– is:

$$\begin{aligned} \kappa_a &= 2(\kappa_x + \kappa_y - \kappa_z), \\ \kappa_b &= \kappa_y - \kappa_x, \text{ and } \kappa_c = \kappa_x + \kappa_y + 2\kappa_z. \end{aligned} \quad (76)$$

Since exchange of κ_x and κ_y merely causes κ_b to change sign, $\mathcal{S}_{xz}(\kappa_a, \kappa_b, \kappa_c) = \mathcal{S}_{yz}(\kappa_a, -\kappa_b, \kappa_c)$.

The angular factors $\tilde{Y}_m(\kappa)$ in expression (72) have the same orientation with respect to the $a^*b^*c^*$ system as $Y_m(\hat{\mathbf{r}})$ has with respect to the abc system seen in Fig. I 5 and Charts I (14)-(15). This is so because the abc system is (almost) orthogonal (Sect. I III), whereby \mathbf{a} is parallel with \mathbf{a}^* , \mathbf{b} with \mathbf{b}^* , and \mathbf{c} with \mathbf{c}^* . As a result:

$$\tilde{Y}_{xy} \propto -\frac{\kappa_x \kappa_y}{\kappa^2} = \left(\frac{\kappa_b}{2\kappa} \right)^2 - \left(\frac{\kappa_c + \kappa_a}{6\kappa} \right)^2, \quad (77)$$

where:

$$\kappa^2 \equiv \kappa_x^2 + \kappa_y^2 + \kappa_z^2 = \frac{1}{12}\kappa_a^2 + \frac{1}{2}\kappa_b^2 + \frac{1}{6}\kappa_c^2, \quad (78)$$

and similarly for \tilde{Y}_{yz} and \tilde{Y}_{xz} . The angular factor extinguishes the intensity around the $[0, 0, \kappa_z]$ -, $[\kappa_x, 0, 0]$ -, or $[0, \kappa_y, 0]$ -lines, as is clearly seen when proceeding from the 1st to the 2nd column in Fig. 15.

The last, radial factor in Eq. (72) is independent of m and merely gives the overall shape of the ARPES intensity. We found it sufficient to mimic the main part of the Mo 4d radial function, continued for $r > 0.5$ (in units of 3.82Å) as the $t_{2g,m}$ -average of the neighboring $pd\pi$ anti-bonds, by $\varphi_2(r) \propto (e^{-14r} - e^{-7})r^2$. This function peaks at $r \approx 0.14$, has a node at 0.5, and is truncated at 0.55. The negative part mimics the contribution from the $pd\pi$ antibonds. The last factor in (72) thus raises quadratically from $\kappa=0$ and peaks at $\kappa \approx \sqrt{3}$, which is at the sphere passing through $[1, 1, -1]$. For larger values of κ , the radial factor decreases monotonically and for $\kappa \gtrsim 3$, i.e. outside the sphere passing through $[1, 2, -2]$ and $[2, 1, -2]$, it has fallen to below one third its value at the peak. The radial factor has been included in the two last columns of Fig. 15.

We thus realize that the angular and radial factors leave intensity in only small parts of reciprocal space.

The xy form-factor intensity, $|\tilde{w}_{xy}(\kappa)|^2$, shown in the 1st row and 3rd column in Fig. 15, has *one dominant peak*; its position is at $[\kappa_x, \kappa_y] = (1 + \frac{\epsilon}{6})[1, 1]$, where the small shift away from $[1, 1]$, proportional to $\epsilon \sim 0.4$, is mainly due to the angular factor. In 3D, and according to Eq. (76), this peak becomes a beam centered on the line given by:

$$\kappa_a + \kappa_c = 6 + \epsilon \text{ and } \kappa_b = 0. \quad (79)$$

This holds as long as the κ_z dependence from the radial factor can be neglected. There are two, less intensive

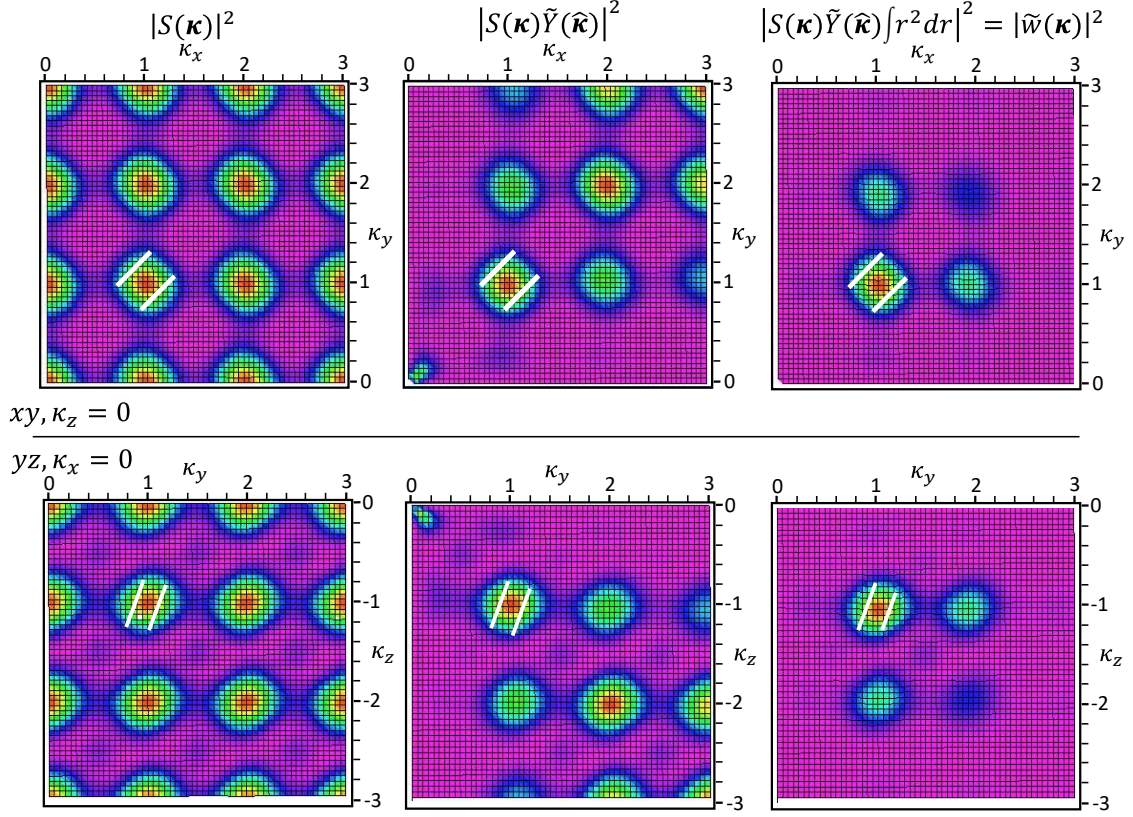


FIG. 15: Form-factor intensities, $|\tilde{w}_m(\boldsymbol{\kappa})|^2$. *Top row:* xy form-factor intensities in the $\kappa_z=0$ plane. *Bottom row:* yz form-factor intensities in the $\kappa_x=0$ plane. $\tilde{w}_{xz}(\kappa_x, \kappa_y, \kappa_z) = \tilde{w}_{yz}(\kappa_y, \kappa_x, \kappa_z)$. *Columns 1-3:* Turning on factors following Eq. (72) with $\mathcal{S}_m(\boldsymbol{\kappa})$ given by Eqs (73) and (74). The little white lines are the projections onto the $\kappa_z=0$ plane or the $\kappa_x=0$ plane of the near-FS lines $|\kappa_b| \sim \frac{1}{4}$, limited to the double zone $-1 \leq \kappa_c \leq 1$, along which the bands and intensities for $\kappa_a=6.4$ were plotted in FIG. 14. The κ_a , κ_b , and κ_c directions are those of respectively $\kappa_x + \kappa_y - \kappa_z$, $\kappa_y - \kappa_x$, and $\kappa_x + \kappa_y + 2\kappa_z$; see Eq. (76).

peaks near $[\kappa_x, \kappa_y]=[1, 2]$ and $[2, 1]$, which in 3D become beams around the lines given by:

$$\kappa_a + \kappa_c = 9 \text{ and } \kappa_b = \pm 1. \quad (80)$$

In Fig. 16 we show the intensity distributions⁶, $\kappa_a^2 |\tilde{w}_m(\boldsymbol{\kappa})|^2$, in the planes with $\kappa_a=6.0$ and 6.8 in the region $-0.5 \leq (\kappa_b, \kappa_c) \leq 1.5$. In the left-hand panel, we see the xy beam (79) form spots around the points $(\kappa_b, \kappa_c) = (0, \epsilon)$ and $(0, \epsilon - 0.8)$ when hitting the $\kappa_a=6.0$ and 6.8 planes. In the latter plane, the less intensive spot centered near $(\kappa_b, \kappa_c)=(1, 2.2)$ and formed by the positive- κ_b beam (80) can be barely seen.

The yz form-factor intensity of zone selection, shown in the 2nd row and 3rd column in Fig. 15, has its *dominant peak* near $[\kappa_y, \kappa_z]=[1, -1]$. In 3D, this peak becomes a

beam centered on the line given by:

$$\kappa_a - 2\kappa_c = 6 \text{ and } \kappa_b + \kappa_c = 0. \quad (81)$$

There are two weaker peaks at $[\kappa_y, \kappa_z]=[2, -1]$ and $[1, -2]$, which in 3D become beams centered along the lines given by respectively:

$$\kappa_a - 2\kappa_c = 6 \text{ and } \kappa_b + \kappa_c = 2, \quad (82)$$

and

$$\kappa_a - 2\kappa_c = 12 \text{ and } \kappa_b + \kappa_c = -2 \quad (83)$$

In the right-hand panel of Fig. 16 we see the yz beam (81) form spots around $(\kappa_b, \kappa_c)=(0, 0)$ and $(-0.4, 0.4)$ upon hitting the $\kappa_a=6.0$ and 6.8 planes, as well as the beam (82) hitting these two planes at respectively $(\kappa_b, \kappa_c)=(2, 0)$ and $(1.6, 0.4)$.

The vertical and diagonal black lines, periodically repeated, but limited to the regions where the intensity exceeds 40 in the units used in Fig. 14, indicate the CECs with binding energy 0.1 eV for xy and 0.5 eV for yz . The CECs will be discussed in the experimental section XD.

⁶ We take the polarization factor $\boldsymbol{\kappa} \cdot \hat{\mathbf{e}}$ as κ_a because this is about six times larger than κ_b and κ_c , and because the e_a component of the polarization (84) is much larger than e_b and e_c .

Since the xz form-factor intensity is related to the one shown for yz in Fig. 16 by a sign change of κ_b , we can see that only for $\kappa_a \sim 6.4$ do the xz and yz intensities along e.g. the P'QPQP' (0.225, κ_c)-line reach roughly the same maximum value. This is the maximum at ~ 250 seen in the top part of Fig. 14 and in the 3rd column of Fig. 13.

Our ARPES measurements, to be presented and discussed in the following section, were mainly performed in the neighborhood of the point $[\kappa_x, \kappa_y, \kappa_z] = [1, 1, -1]$ which is close to the peaks of all three form factors and which is the Γ point ($\kappa_a, \kappa_b, \kappa_c$) = (6, 0, 0). It may be noted that upon going from the 1st to the 2nd column in the 1st row of Fig. 15, the angular factor sharpens up the [1,1] peak of the xy intensity. The traces of the two FS sheets, $|\kappa_b| = \frac{1}{4}$, on the $\kappa_a = 6.4$ plane and bound between the $\kappa_c = \pm 1$ planes are the little white lines in Fig. 15, when projected onto the $\kappa_z = 0$ plane in the 1st row and onto the $\kappa_x = 0$ plane in 2nd row. These are the P'QPQP' lines along which the intensity distributions were shown in Fig. 14. Since the xy band disperses in the direction of the κ_b -lobe of its WO, this direction is perpendicular to the little white lines.

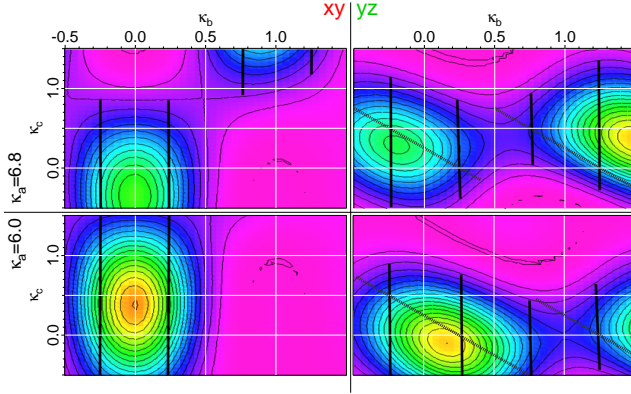


FIG. 16: Theoretical xy (left) and yz (right) coarse-grained ARPES intensity distributions, $\kappa_a^2 |\tilde{w}_m(\kappa)|^2$, in the $\kappa_b\kappa_c$ planes with $\kappa_a = 6.0$ (bottom) and 6.8 (top) planes. The xz intensities equal the yz ones mirrored around $\kappa_b = 0$. See top part of FIG. 14 and Eq.s (71) and (79)-(83). The contours go from 0 to 400 in steps of 20. The black lines extending where the intensity exceeds 40 indicate xy and yz CECs with energy respectively 0.1 and 0.5 eV below the Fermi level (see FIG. 20) and in the periodic zone scheme.

At the end of this long section IX, we emphasize the following two points:

Whereas the k_a -dependence of the $|\mathbf{k}\rangle$ -projected bands, i.e. of the fine-grained structure, is negligible compared with the k_b - and k_c -dependencies, the κ_a -dependence of the aperiodic form factors, $|\tilde{w}_m(\kappa)|^2$, i.e. of the coarse-grained structure, is strong, as strong as the dependence on κ_c for xy , and half as strong for yz/xz ; see Eq.s (79)-(81). This is due to the form factors being 2D, $\propto \kappa_x\kappa_y$, $\kappa_y\kappa_z$, or $\kappa_x\kappa_z$, and to the orientation of the t_{2g} orbitals with respect to the crystallographic axes I (13).

Since the low-energy WOs in LiPB are relatively ex-

tended (covering several atoms), the radial part of the WO form factors make the beams narrow and thus cause the ARPES intensity to depend rather strongly on the photon energy $h\nu$, as we shall see in Sect. XC.

X. PRESENTATION AND DISCUSSION OF THE ARPES DATA

From the basics of the electronic structure in Sect. IIV we expect the two \widetilde{xy} bands crossing the Fermi level to have by far the largest dispersion with k_b , i.e. along the ribbon, weak dispersion with k_c , i.e. up and down the staircase, weak k_c -dependent splitting caused by direct inter-ribbon hopping and by hybridization with the gapped xz and yz bands, and essentially no dispersion with k_a due to the lack of hopping between the staircases. In the following, we want to demonstrate that this strong one-dimensionality is indeed confirmed by our ARPES experiment. We also pay attention to the aperiodic variations of the ARPES intensity between equivalent zones and compare them with the coarse-grained intensity variations predicted in the preceding Sect. IX B 2. The fine-grained intensity variations (zone selection) predicted in Sect. IX B 1 will be observed in Sects. XD and XE where, most importantly, we also compare the band dispersions in detail with those predicted by the LDA as parametrized by the t_{2g} TB Hamiltonian (Sect. I VI).

Intensity variations and one-dimensionality are also features of the ARPES yz and xz bands, but of course not near the Fermi level where they are gapped. Moreover, their one-dimensionality is with $k_c + k_b$ or $k_c - k_b$, rather than with k_b .

A. ARPES method

We measured several samples for the conclusions presented in this work. The samples came from two different crystal growers and were all prepared by a temperature gradient flux growth technique [72]. In the text, we refer to two samples G (M. Greenblatt) and H (J. He) representing the variation detectable in our experiments.

Photoemission measurements were performed at the MERLIN endstation (BL 4.0.3) of the Advanced Light Source with a Scienta R4000 electron detector. The polarization was set to linear vertical, i.e. in Fig. 20 the vector of the electric field horizontal. The temperature was set to $T = 26$ K for sample G and $T = 6$ K for sample H and the samples were cleaved while attached to the cold manipulator at $p \approx 4 \times 10^{-11}$ torr. The overall energy resolution was set to around 16 meV at photon energy $h\nu = 30$ eV going up to around 40 meV at $h\nu = 100$ eV. At $h\nu = 30$ eV, the momentum resolution in the \mathbf{b}^* -direction is 2% of k_{FB} at half-filling (i.e. at nominal Li_1 stoichiometry), i.e. 0.005. With the solid-state definition of reciprocal space [see Sect. I III below Eq. (11)], this is 0.006

\AA^{-1} . The polarization vector in sample coordinates is:

$$\frac{\mathbf{E}}{|\mathbf{E}|} = \begin{pmatrix} e_a \\ e_b \\ e_c \end{pmatrix} = \begin{pmatrix} \sin(65^\circ - \phi) \cos \theta \\ \sin(65^\circ - \phi) \sin \theta \\ \cos(65^\circ - \phi) \end{pmatrix}. \quad (84)$$

Here, ϕ is the polar rotation, and the θ the tilt angle. In our measurements, $|\phi| \lesssim 5^\circ$ and $|\theta| \lesssim 5^\circ$ resulting overall in a strong component along the **a**-axis, normal to the cleavage plane, a weak component along the **c**-axis, and a very weak component along the **b**-axis.

$\text{LiMo}_6\text{O}_{17}$ is susceptible to oxygen loss caused by intense ultraviolet light where the desorption is due to the Knotek-Feibelman mechanism including a core level excited resonant Auger decay [73]. It shares this behavior with, i.e. $\text{NaMo}_6\text{O}_{17}$ [74], $\text{K}_{0.3}\text{MoO}_3$ [32], or oxides like TiO_2 [75] and SrTiO_3 [76]. We were not able to prevent this damage by oxygen dosing, as i.e. possible for SrTiO_3 [77]. The reason might be the existence of both, tetrahedral and octahedral coordinated molybdenums. A small oxygen loss causes a slight electron doping, but, as time progresses, the ARPES signal eventually blurs. In order to prevent the loss, one concept might be to keep the photon energy below that of the lowest energy core level resonance. However, often there is higher-order light that still causes a slow degradation (with the timescale in the hours instead of minutes) and therefore our concept is to use a large homogenous area and slightly alter the position of the beam spot when the sample degradation begins.

Even though the ARPES lineshapes have the general 1D holon-peak and spinon-edge features [3], they were analyzed by a model-free method described in detail in Paper III Sect. XV. This procedure was necessitated because the low- T ARPES lineshape is not sharp enough to agree in detail with the low- T TL lineshape [78]. If the TL lineshape is broadened ad hoc it can be made to fit [3], but we did not want to use that ad hoc procedure in the current work.

B. Ansatz for deducing κ_a

We repeat here some basics of ARPES, cf. [79, 80] As in Sect. IX A we use a notation according to which \mathbf{k} denotes the Bloch vector in a (periodically repeated) single zone of an initial-state, and $\boldsymbol{\kappa}$ is the momentum of the final, plane-wave state *inside* the crystal. According to Eq. (71), $\boldsymbol{\kappa} [\text{mod zone}] = \mathbf{k}$. Upon leaving the crystal, the photoelectron is diffracted in the direction away from the surface, whereby the normal momentum component, $\boldsymbol{\kappa}_\perp = \kappa_a \mathbf{a}^*$, jumps discontinuously to a smaller value, $\boldsymbol{\kappa}_{\perp o}$. Parallel to the surface, the momentum is conserved:

$$\boldsymbol{\kappa}_\parallel \equiv \kappa_b \mathbf{b}^* + \kappa_c \mathbf{c}^* = \boldsymbol{\kappa}_{\parallel o}.$$

What is measured in ARPES is, for a given photon energy $h\nu$, the yield, I , the angle of exit, θ , and the kinetic energy, $T = \frac{h^2}{2m} |\boldsymbol{\kappa}_o|^2$, of the photoelectrons in the

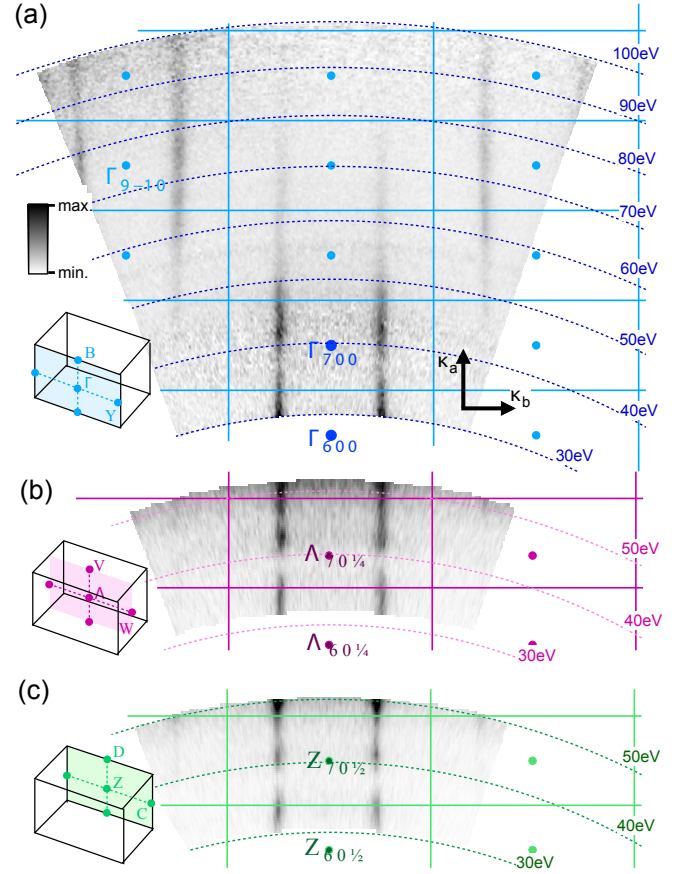


FIG. 17: Photon energy scan of sample H at $T=6$ K for $\boldsymbol{\kappa}$ in three $\mathbf{a}^*\mathbf{b}^*$ -planes: (a) FS map through $\kappa_c=0$ (GBY) (b) $\kappa_c=\frac{1}{4}$ (AWV), and (c) $\kappa_c=\frac{1}{2}$ (ZDC). The colored full lines along \mathbf{a}^* and \mathbf{b}^* are the intersections with the BZs. The blue dotted lines intersect at the reciprocal lattice points Γ_{LMN} . The high-intensity traces represent the 1D FS showing no dispersion in the \mathbf{a}^* -direction. There are coarse-grained intensity variations whose origin is the structure factor of the form factor for the xy WOs; see Sect. IX B 2 and FIG. 18. This figure and the following are approximately to scale, i.e. consistent with $a/b = 2.31$.

analyzer *outside* the crystal. The value of κ_a inside the sample is deduced from the two latter quantities by assuming that inside the crystal, the energy of the final state is $V + \frac{h^2}{2m} |\boldsymbol{\kappa}|^2$, i.e. the energy of an electron, free with respect to a potential floor, V , and that outside the crystal, the momentum is:

$$\boldsymbol{\kappa}_o = (\boldsymbol{\kappa}_{\perp o}, \boldsymbol{\kappa}_\parallel) = \frac{\sqrt{2mT}}{h} (\cos \theta, \sin \theta), \quad (85)$$

and the energy is $\Phi + T$. Here, Φ is the work function of the sample. It should not be confused with $\Delta\Phi$ which is a constant given by the apparatus and is essentially the difference between work function of sample and analyzer. $\Delta\Phi$ allows to relate the measured kinetic energy to the binding energy ω within the sample

$$\omega \equiv -E_j(\mathbf{k}) = h\nu - (\Delta\Phi + T). \quad (86)$$

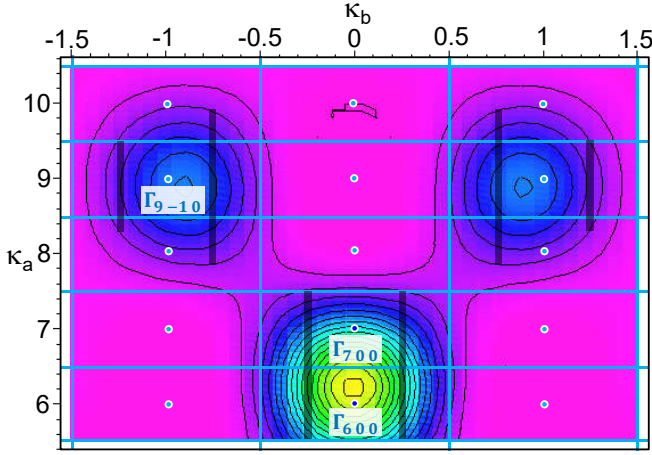


FIG. 18: Theoretical ARPES intensity distribution $\kappa_a^2 |\tilde{w}_{xy}(\kappa_a, \kappa_b, \kappa_c=0)|^2$ to be compared with the coarse-grained part of the experimental intensity distribution in FIG. 17. The contours go from 0 to 400 in steps of 20. The black lines indicate the traces of the near-FS sheets, $|\kappa_b| \sim \frac{1}{4}$, in the periodic zone scheme and extend where the intensity exceeds 40.

Equating the inside and outside energies, yields the desired relation for κ_a :

$$\frac{\kappa_a}{a} = |\kappa_\perp| = \frac{\sqrt{2m}}{h} \sqrt{T \cos^2 \theta + V_0}, \quad (87)$$

where $V_0 \equiv \Phi - V$ is the so-called *inner potential*. Taking V and Φ with respect to the Fermi level, which is common for the crystal and the analyzer, V is negative and Φ is positive, whereby V_0 is positive. Its value is determined empirically.

C. Photon energy dependence

1. FS intersection with $\mathbf{a}^*\mathbf{b}^*$ planes

We begin by showing ARPES for photoelectrons coming from slightly below the Fermi level, i.e. from the \tilde{xy} electrons. Fig. 17 shows for sample H at $T=6$ K the photoelectron yield as a grey-scale intensity, a so-called FS map, in the three $\kappa_a\kappa_b$ planes with $\kappa_c=0$, $\frac{1}{4}$, and $\frac{1}{2}$, colored respectively blue, red, and green. In the $\kappa_c=0$ plane, the scan covers many BZs. We see the traces of the two FS sheets separating the occupied states, $|k_b| < k_F$, between the sheets from the empty states, $|k_b| > k_F$, outside the sheets. These traces appear as straight lines and are thus consistent with being the intersections with a $\kappa_a\kappa_b$ plane of a 1D, nearly half-filled FS, $|k_b| = k_F \sim \frac{1}{4}$. This FS is seen to be periodic in the $\mathbf{a}^*\mathbf{b}^*\mathbf{c}^*$ lattice and to have aperiodic, coarse-grained intensity variations.

Since the κ_a direction is perpendicular to the plane of the sample, it must be accessed by variation of the photon energy. For presenting these measurements, we have

converted our raw yield (I) and kinetic-energy (T) data as functions of angle (θ) and photon energy ($h\nu$) as explained above to binding-energy (ω) and momentum vector (κ), using the value $V_0=11$ eV for the inner potential. With the work function of the analyzer being $\Phi=4$ eV, the potential floor is thus 7 eV below the Fermi level, i.e. $V=-7$ eV. The dotted constant- $h\nu$ circles in Fig. 17 are the cross-sections of the sphere $V + \frac{h^2}{2m} |\kappa|^2 = h\nu$ with the constant- κ_c planes. For a given $h\nu$, normal emission ($\theta=0=\kappa_b=\kappa_c$) from the Fermi level⁷ thus has the κ_a value:

$$\kappa_a(0, 0, h\nu) = \frac{a\sqrt{2m}}{h} \sqrt{h\nu - V} \approx 7.0 \sqrt{\frac{h\nu + 7 \text{ eV}}{40 + 7 \text{ eV}}}, \quad (88)$$

which, as expressed on the right-hand side, is 7.0 for $h\nu=40$ eV.

Fig. 17 (a) shows intensity variations in central ($\kappa_c=0$) plane: Strong intensity in the region $(\kappa_a, \kappa_b) = (5.5-7.5, \pm k_F)$ and weak intensity in the regions $(8.0-10.5, \pm (1 \pm k_F))$. In the former, we see an intensity variation with minimum at the zone boundary ($\kappa_a=6.5$). In the last-mentioned regions, the intensity along the FS is weak and fairly constant. In Fig. (b), the $\kappa_c=\frac{1}{4}$ plane, which contains the resonance peak (see bottom part of Fig. 14), the intensity variation seems to be shifted a bit, and again in (c) to be in register with the variation in (a).

The qualitative theory of the coarse-grained intensity variations presented in Sect. IX B 2 associate them with the form factor of the xy WO in the present case. The theory yields the result shown in Fig. 18 which compares quite well with the experimental Fig. 17 (a). We thus realize that the region of strong intensity is due to the beam (79) whose center hits the $\kappa_c=0$ plane at $(\kappa_a, \kappa_b)=(6.4, 0)$, and that the two regions of weak intensity are due to the beams (80) causing the spots at $(\kappa_a, \kappa_b) = (9, \pm 1)$.

Apart from the observed coarse-grained intensity variations, we confirm that slightly below the Fermi level there is no dispersion along κ_a , i.e. there is strongly reduced dimensionality in the \mathbf{a}^* -direction¹⁵. The intensity variation seen as a function of κ_a in Fig. 17 has period 1 in κ_a and is, therefore, *not* the fine-grained intensity variation (zone selection) described in Sect. IX B 1, which has period 2 in κ_c and is due to emission from *one* of the two xy bands. The intensity seen could, in principle, be due to k_a dispersion¹⁵, but this, we judge, is far too weak; so we currently have no explanation.

In the \mathbf{c}^* -direction, i.e. from figure (a) to (b) to (c), the dispersion is very weak. That there are two bands at the Fermi level and the FS therefore has two close-lying Fermi vectors, $k_{Fu}=k_{F2}$ and $k_{Fl}=k_{F1}$ along κ_b , cannot

⁷ For finite binding energy, $h\nu$ should be substituted by $h\nu - \omega$ in Eq. (88). But even going to the bottom of the band, where $\omega=0.7$ eV, this lowers κ_a by merely ≈ 0.06 .

be seen in these figures, but might, in principle, be resolved because the resolution is 16 meV when $h\nu=30$ eV (and decreases to 40 meV when $h\nu=100$ eV).

2. FS intersection with $\mathbf{b}^*\mathbf{c}^*$ planes; $h\nu=30, 33$, and 37 eV

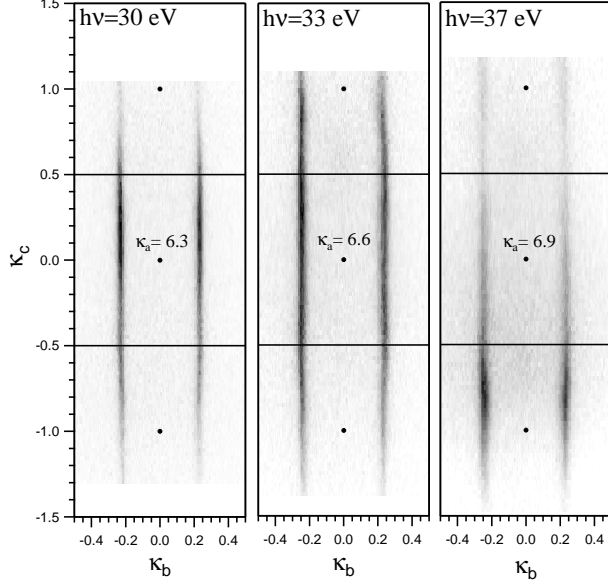


FIG. 19: FS map at different photon energies $h\nu = 30, 33, 37$ eV. For $\kappa_b = \kappa_c = 0$, this is at $\kappa_a = 6.3, 6.6$, and 6.9 as indicated. These figures have been stretched along κ_c by a factor 1.7 (compare with FIG.s 11 and 20 (b), which are to scale).

Like in Fig. 17, the intensity for photoelectrons coming from slightly below the Fermi level is shown in Fig. 19, but now in the $\kappa_b\kappa_c$ plane, over two BZs ($|\kappa_b| \leq \frac{1}{2}$, $|\kappa_c| \lesssim 1$), and for $h\nu = 30, 33$, and 37 eV. The coarse-grained intensity is seen to change significantly over this range of photon energies, and only for 33 eV does it extend over both BZs. This we can partly understand from the $h\nu$ -dependence of κ_a :

For the three photon energies, Eq. (88) yields respectively $\kappa_a(0, 0, h\nu) = 5.9, 6.2$, and 6.5 , which according to the simplest prediction (79) of the κ_c -position of the intensity maximum (seen on the left-hand side of Fig. 16 for $\kappa_a = 6.0$ and 6.8) for the xy beam gives: $\kappa_c = 0.5, 0.2$, and -0.1 , as compared with $0.2, \sim 0$, and -0.6 estimated from the experimental Fig. 19. The latter κ_c -values correspond via Eq. (79) to the somewhat larger κ_a -values: $6.2, 6.4$, and 7.0 , whose intensity distributions can easily be imagined from those for $\kappa_a = 0$ and 6.8 shown on the left-hand side of Fig. 16. These do exhibit the remarkable contraction along κ_c of the experimental intensity distribution seen in Fig. 19 for the highest energy. On top of this comes the narrowing of the beam due the delocalization of the \widehat{xy} WO caused by the downfolding of the valence- and conduction-band orbitals [see Eq. III (93)].

D. CECs in the $\mathbf{b}^*\mathbf{c}^*$ plane

In Fig. 20 we present ARPES results for binding energies, ω , which takes us from the Fermi level to the bottom of the Mo 4d bands so that we also get to see the xz and yz valence bands. The results are shown in the 2D region ($0 \leq \kappa_b \leq \frac{1}{2}$, $0 \leq \kappa_c \lesssim 1$) which with reference to Fig.s 20 (a) and 11 includes the upper half of the BZ centered at $\Gamma_{00} \equiv \Gamma$, plus the lower half of the one centered at $\Gamma_{01} \equiv \Gamma'$. We shall refer to these BZs as respectively the 1st and the 2nd. Together, they form the upper part of the double zone centered at Γ . Here, "upper" and "lower" refer to the orientation which has κ_c pointing upwards.

The right-most panel in Fig. 20 (b) shows ARPES as measured and the left-most panel shows ARPES with the fine-grained (plus some of the coarse-grained) intensity variations symmetrized away by adding the intensities from both sides of the BZ boundary ($\text{CZC}, \kappa_c = \frac{1}{2}$), exploiting the equivalence⁸ of xz and yz . This corresponds to adding the intensities at \mathbf{k} and $\mathbf{k} + \mathbf{c}^*$.

The middle panel shows the CECs from the LDA-TB bands with the common energy of the four xz and yz WOs shifted downwards by 100 meV with respect to the energy of the two xy WOs [see Fig.s 22 (a) and (b)] in order to improve the agreement with the symmetrized ARPES in the right-most panel. This agreement –down to every detail– is astonishing, and so is the straightness of the three sets of lines, even close to where they cross. The theoretical CECs have been colored red, blue, or green according to their respective xy , xz , or yz character, and in order to mimic the spectral-function broadening of the dispersion, the shifted LDA-TB bands were broadened by a Lorentzian with energy-independent width.

The CECs from the *symmetrized* ARPES and the shifted LDA-TB bands behave as described in Paper I, Sect. IV A 4 together with Fig.s 4, 6, 7, and 8. The upper part of the double zone is shown also in Fig. 11 of the present paper.

In Fig. 20 we recognize the CECs of the quasi-1D, degenerate $xy(\mathbf{k})$ and $xy(\mathbf{k} + \mathbf{c}^*)$ bands (red) dispersing in the k_b direction with the distance $2k_b(E)$ between the two sheets increasing like $\sim (2/\pi) \sqrt{(E - B)/|t|}$ with $t \sim -1$ eV [see Sect. IV A Eq. I (23)] and heading towards $\sim \frac{1}{2}$ at the Fermi energy.

The quasi-1D $xz(\mathbf{k})$ (blue) and $yz(\mathbf{k})$ (green) bands dispersing with respectively $k_c - k_b$ and $k_c + k_b$ [see

⁸ Note that whereas the band structure is invariant to the individual mirror operations $k_b \rightarrow -k_b$ and $k_c \rightarrow -k_c$, the eigenfunctions are merely invariant to the inversion $(k_b, k_c) \rightarrow -(k_b, k_c)$. As a consequence, the above-mentioned even/odd symmetries around $k_c = -1, 0, 1$ and $k_c = \frac{1}{2}$ do not hold for the blue and green curves individually, but only for their sums.

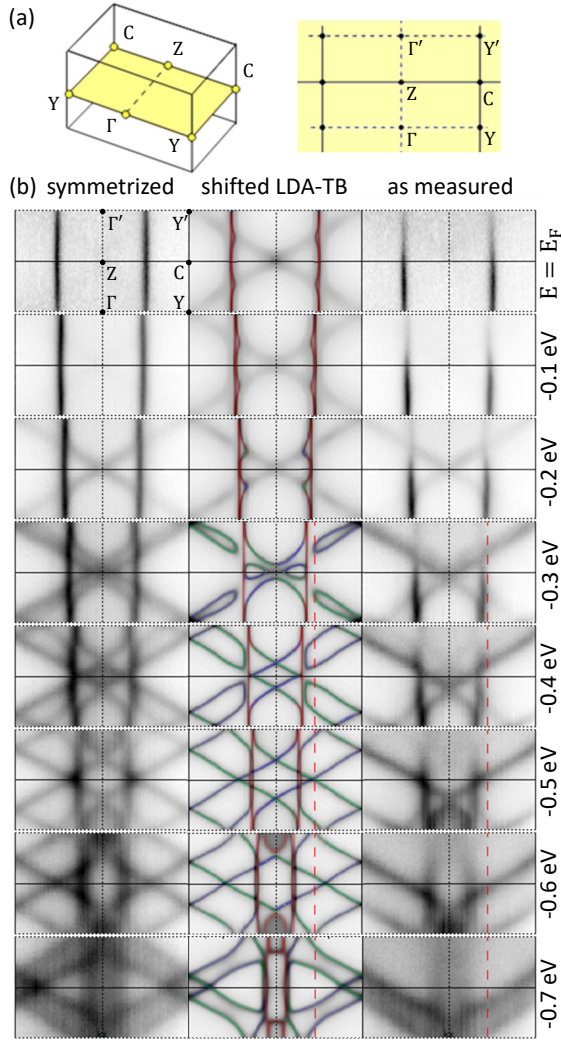


FIG. 20: (a) Orientation in the zone of the $\kappa_b\kappa_c$ -plane with $\kappa_a=6$. The CECs are shown in the upper part of the 1st and the lower part of the 2nd BZ: $|\kappa_b| \leq \frac{1}{2}$, $0 \leq \kappa_c < 1$. See also FIG. 11. (b) Comparison of the CECs computed using the LDA-TB parameters, listed in Eq.s I (43)-(47) including the 100 meV shift, with those measured by ARPES for sample H ($T=6$ K, $h\nu=30$ eV). Red, blue, and green indicate dominating xy , xz , and yz character. The red dashed line ($k_b=0.225$) is the one along which we often show bands, such as the $|\mathbf{k}$ |-projected ones in FIG. 14. The match with the symmetrized ARPES is nearly perfect, and so is the prediction that in ARPES as measured, the xz and yz CECs are extinguished in the respective 2nd zone, i.e. above the respective ZY' line. Indicated on the right are the energies with respect to the Fermi level.

Eq. I(27)], are degenerate at their common bottom at Γ where they are also nearly degenerate- and hybridizes with the two xy bands thus giving rise to CECs which are complicated near Γ . For energies a bit above the common bottom of all three t_{2g} bands, $B \approx E_F - 0.75$ eV, the blue and green pair of CECs are parallel with and lie on either side of respectively the $k_c - k_b = 0$ and

$k_c + k_b = 0$ lines. As the energy increases, so does the distance $\sim (2/\pi) \sqrt{(E - B)/|A_1|}$ between each pair of parallel blue or green CECs. This distance is approximately $\sqrt{t/A_1} \sim 1.8$ times the one between the red xy CECs.

The blue and the green $\mathbf{k} + \mathbf{c}^*$ bands are shifted by $\Delta k_c=1$ and thus behave in the same way as the respective blue and green \mathbf{k} bands. For energies above ~ -0.5 eV, the closest CEC pairs are those on either side of the respective zone boundary, $|k_c + k_b| = \frac{1}{2}$ or $|k_c - k_b| = \frac{1}{2}$, onto which they coalesce when $E \sim E_F - 2|G_1| = E_F - 0.2$ eV. Here, $2G_1$ is the electronic dimerization causing a gap of $\pm 2G_1$ [see Eq. I (29) and Fig. I 6 for $k_b=0.225$].

We are particularly interested in the hybridization of the xy bands inside the gap around E_F . It can be seen in theory by comparison of the light- and the dark red bands in Fig. I 6 and I 7, respectively, or in the middle and bottom parts of Fig. 14 of the present Paper II, and we shall study it in detail in Paper III. Although bands –and not CECs– hybridize, we can see the effect of this hybridization in the LDA-TB part of Fig. 20 at 0.1 and 0.2 eV below E_F as four “notches” pointing inwards, towards Z , and we can follow them as the energy is lowered into the valence bands. The origin of the notches is clearly the energy repulsion between the hybridizing valence-band edge and one of the two degenerate xy bands; the other band is unaffected [see Eq. III (97)]. Since the notch is sharp, it can only come from an edge of a nearby yz or xz band (but not from a far-away yz or xz band) with a weak matrix element, and as long as the notch points towards Z rather than Y , it comes mainly from the edge of the valence (V) rather than from the edge of the conduction (C) band. The corresponding peak is in the upper \widetilde{xy} band (Fig. I 7) and we shall call it a *resonance peak*. (If we take the nearly dispersionless k_a -dimension into account, the peak is a “mountain ridge” extending along \mathbf{a}^*).

According to the *selection rules* derived in Sect. IX B 1 and illustrated in Fig. 14, ARPES *as measured* in Fig. 20 (b) should see the occupied $|\mathbf{k}$ |-projected bands in the 1st physical zone and the occupied $|\mathbf{k} + \mathbf{c}^*$ |-projected bands in the 2nd physical zone. With the blue xz and green yz bands gapped around the Fermi level, these bands should be seen in the 1st physical zone only, and comparison with Fig. 11 shows this to be the case. Specifically, the blue and green bands with $E < E_F - 0.2$ eV are extinguished in their respective 2nd zone. The dimerization distortion of the yz (and xz) intensities for negative κ_c predicted in Fig. 13 for $\kappa_a=6.4$, specifically the intensity enhancement near $\kappa_c=-0.4$ for the upper band was seen in the data; but this is outside the range of positive κ_c shown in Fig. 20 (b).

For the red, metallic xy bands, the Fermi sea inside the outer sheet should be seen in the 1st BZ and the sea inside the inner sheet should be seen in the 2nd BZ, with a switch near the BZ boundary, $k_c=\frac{1}{2}$. This means that the notches should be seen only in the 2nd BZ, but the

drop of intensity for $\kappa_c > 0.5$ in ARPES as measured with $h\nu=30$ eV (Fig. 19) makes this observation difficult. We shall return to it in Sect. III XV.

Herewith, we have arrived at the influence of the yz and xz form factors. In Fig. 20 (b) we see that the intensity as measured for given binding energy (deep inside the valence bands) is slightly stronger for $yz(\mathbf{k})$ than for $xz(\mathbf{k})$ and increases with κ_c in the range $(0|1)$. As may be seen from the theoretical Fig. 16, the former property is consistent with the behavior of $\kappa_a^2 |w_{yz}(\kappa)|^2$ for $\kappa_a \sim 6.4$, but the latter requires $\kappa_a \sim 7$.

E. Energy bands $E_j(k_b, k_c)$

In the preceding section, the CECs *as measured* were shown in the right-hand panel of Fig. 20 (b) and were explained as the fine-grained, double-periodic $|\mathbf{k}|$ -projection of the occupied part of the lower m band in the 1st- and of the upper m band in the 2nd physical zone (see Sect. IX B 1), on the background of the coarse-grained, aperiodic polarization- and WO form factor intensity $\kappa_a^2 |\tilde{w}_m(\kappa)|^2$ (see Sect. IX B 2). Hence, the xz and yz bands were seen only in the respective 1st physical zone, because their upper bands are empty, and so were the metallic xy bands due to the drop of their polarization- and form factor intensity for $h\nu=30$ eV ($\kappa_a=6.3$) in the 2nd BZ.

Fig. 21 (b) now displays the ARPES band structure as measured on the faces of a box with the basal (k_b, k_c) plane extending over the upper half of the double zone, like in Figs. 20 and 11. On the top face, i.e. for $E \sim E_F$, we recognize the 1D xy FS, $(k_b, k_c) \sim (\pm \frac{1}{4}, k_c)$, with its intensity drop in the 2nd BZ. Not only the xy bands are quasi 1D, but so are the xz and the yz bands: Had the box been cut at the top of the valence bands, we would –like in the right-most panel of Fig. 20 (b)– have seen their ridges follow the boundaries of their physical zones (Fig. 11).

The band structures shown in (d)-(e) are obtained by cutting the data along the lines colored in (a). In order to avoid the fine-grained intensity variations, we first show (c) –like in the left-most panel of Fig. 20 (b)– the band structure symmetrized over the 1st and 2nd zones; the benefit of this symmetrization is evident! Had there been no coarse-grained intensity variations, this band structure would have been periodic in the BZ and have the rectangle ΓZCY ($0 \leq k_b \leq \frac{1}{2}, 0 \leq k_c \leq \frac{1}{2}$) as its irreducible part. The symmetrized bands (c) will be compared with the LDA band structure (Fig. 22) in the following Sect. XI and, subsequently, its TB parameters will be fine-tuned to achieve almost perfect agreement with the occupied ARPES bands.

The fine-grained intensity variations, on the other hand, hold the key to resolving the so far elusive splitting and warping of the nearly degenerate quasi-1D xy -like

FS. But let us first test our understanding of the intensity variations, by using it to explain the band structure *as measured* along the lines colored in Fig. 21 (a) and shown in Figs. (b), (d), and (e).

Along $\Gamma Z\Gamma'$ ($k_b=0$) we see the rise of the degenerate $xz(\mathbf{k})$ and $yz(\mathbf{k})$ valence bands from their bottom at $E_F - 0.75$ eV at Γ to their highest point, $E_F - 0.25$ eV, where the blue and green valence-band ridges cross at Z. Here, half their $|\mathbf{k}|$ characters –and hence ARPES intensities– have been lost. On the downturn in the 2nd zones, to Γ' , the $|\mathbf{k} + \mathbf{c}^*|$ characters take over and the intensities drop accordingly. At $E_F - 0.75$ eV we also see the dispersionless bottom of the two degenerate xy bands and expect the intensity to shift from the lower to the upper band as we pass from the 1st to the 2nd BZ. That the measured total xy intensity nevertheless drops, we ascribe to the above-mentioned drop of the form factor in the 2nd BZ.

When going inside the 1st zone from Γ to Y, the other crossing point of the blue xz and green yz valence-band ridges (see Fig. I 8 or II 11), the $xz(\mathbf{k})$ and $yz(\mathbf{k})$ valence bands are seen to rise and lose intensity in a similar same way as they did towards Z, except that there –due to spin-orbit splitting (see Fig. 23)– the maximum was higher. The ΓY -cut in the band structure is also shown on the front face of the box in (b). Intensity is prominently seen from the (lower) xy band rising parabolically from its bottom along ΓZ to the FS along $k_b \approx \frac{1}{4}$. The aforementioned drop of xy intensity in the 2nd BZ is clearly seen on the top face of the box. If we go inside the 2nd zones from Γ' to Y' at the zone boundary, this is the only place where intensity from the valence bands is seen.

Along the green diagonal from Y' to Z, where the gapped $yz(\mathbf{k})$ and $yz(\mathbf{k} + \mathbf{c}^*)$ bands form the valence-band ridge, this ridge is clearly seen; in fact far better than the blue ridge from Y to Z formed by the gapped $xz(\mathbf{k})$ and $xz(\mathbf{k} + \mathbf{c}^*)$ bands. A similar intensity difference between yz and xz was also observed in Fig. 20 and was explained at the end of Sect. XD as due to different form factors. The xz band gives no intensity along the green $Y'Z$ line because it is in the 2nd yz zone, which is empty. Returning now to the blue valence-band ridge along YZ , we see the yz band fall, reach its bottom halfway towards Z, and then rise again to the highest point on the ridge at Z. Here, the yz band not only attains $|\mathbf{k} + \mathbf{c}^*|$ character, but also hybridizes with the xz band via spin-orbit coupling. We also see the parabolic rise of the lower xy band from its bottom at Z towards Y, reaching E_F at half the way. Towards Y' , the xy intensity is reduced by the form factor.

Going along the BZ boundary from Z to C for k_b positive, the nearly degenerate xy bands rise and cross the Fermi level near $(\frac{1}{4}, \frac{1}{2})$ and the xz valence band falls from the highest point on the ridge to its bottom at C. At Z, the green yz band is degenerate with the blue xz valence

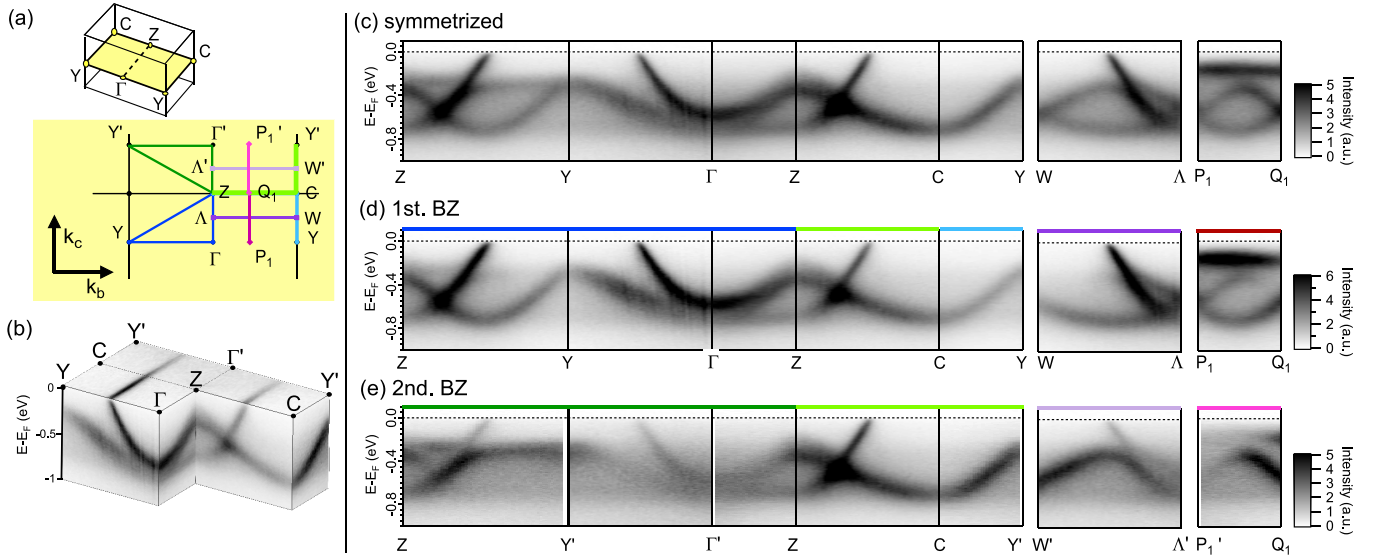


FIG. 21: ARPES band structure. **(a)** Orientation of half the 1st BZ in $\kappa_a\kappa_b\kappa_c$ -space and, in the $\kappa_b\kappa_c$ -plane, half the 1st BZ ($0 \leq \kappa_c \leq \frac{1}{2}$) centered at Γ , and half the 2nd BZ ($\frac{1}{2} \leq \kappa_c \leq 1$) centered at Γ' . The BZ is the physical zone for the xy bands and the physical zones for all three t_{2g} bands were shown in FIG. 11. **(b)** Data as measured from sample H ($T=6$ K, $h\nu=30$ eV) presented in an $E(\kappa_b, \kappa_c)$ -box where from cuts along the κ -paths colored in **(a)** produce the band structures shown in **(c)**-(e). **(d)** Some features can be better seen in the 1st BZ, **(e)** while others are more pronounced in the 2nd BZ, and vice versa. This is so because band selection follows the physical- rather than the Brillouin zone. **(c)** The symmetrized band structure shows all spectral features.

band and has intensity there, which however vanishes after leaving the 1st green zone.

Upon going from C to Y' ($k_b=\frac{1}{2}$) inside the blue xz zone, we see the xz band increase to the blue ridge at Y' . Going instead to Y, we see the other branch of the xz band increase to the blue ridge at Y.

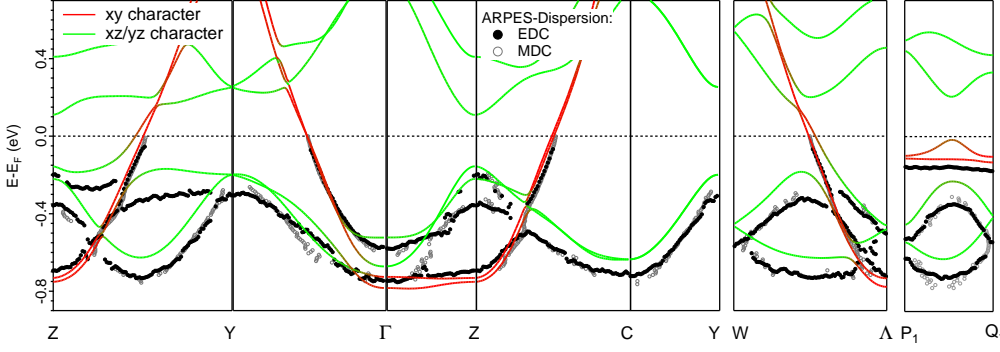
Along ΛW ($k_c=\frac{1}{4}$), the lowest band –with minimum at $(\frac{1}{4}, \frac{1}{4})$ – is the blue $xz(\mathbf{k})$ band. The $yz(\mathbf{k})$ band is degenerate with $xz(\mathbf{k})$ at Λ , but then increases, until at $(\frac{1}{4}, \frac{1}{4})$ it reaches the top of the green ZY ridge where it mixes with the $yz(\mathbf{k} + \mathbf{c}^*)$ band coming from W, and thereby loses its intensity. Going instead from Λ' towards W' ($k_c=\frac{3}{4}$), it is the blue $xz(\mathbf{k} + \mathbf{c}^*)$ band which –with weak intensity– increases until at $(\frac{1}{4}, \frac{3}{4})$ it reaches the top of the blue ZY' ridge where the $|\mathbf{k}\rangle$ character takes over and the $xz(\mathbf{k})$ band continues with full intensity downhill. The lower xy band disperses parabolically upwards from Λ and reaches the Fermi level half the way to W, and the same is seen –with reduced intensity– along $\Lambda'W'$ ($k_c=\frac{3}{4}$) for the higher xy band. The non-vanishing hopping integrals I (46) between an xy WO and an xz or yz WO causes the corresponding bands to repel where they run close. This is the case for the two xy bands and the $yz(\mathbf{k})$ band between Λ and $(\frac{1}{4}, \frac{1}{4})$, and for the two xy bands and the $xz(\mathbf{k})$ band between Λ' and $(\frac{1}{4}, \frac{3}{4})$. It is remarkable that of the three close bands, two repel around the third band, which remains unaffected and thereby ends up as the band of intermediate energy, the lowest of the two xy bands in the present case. This can be seen in Fig. 21 (c)-(e) and will be referred to often in

the following.

The $P_1Q_1P'_1$ -line ($k_b=0.225$) is perpendicular to the ΛW and $\Lambda'W'$ lines and is parallel to, but slightly inside the FS so that the trace of the xy bands is ~ 170 meV below the Fermi level and thereby clearly visible in ARPES –albeit with the usual xy form-factor reduction of the intensity towards P'_1 . Starting from P_1 , we see the blue $xz(\mathbf{k})$ band reaching its bottom midway to Q_1 and –above it, with slightly less intensity,– the green $yz(\mathbf{k})$ band rising towards the top of the green ridge where 50% of its character and intensity are lost and losing even more on the downhill side towards Q_1 . Proceeding from here towards P'_1 in the 2nd green zone, we vaguely see the green yz band –now $|\mathbf{k} + \mathbf{c}^*\rangle$ -like– reach its bottom midway to P'_1 . From Q_1 in the blue 1st zone, we see the blue xz band rise to the ZY' ridge, where it –like the green yz band at the green ridge– has lost half its intensity and thereafter vanishes on the downhill side towards P'_1 . All of this agrees with the $|\mathbf{k}\rangle$ -characters of the four lowest LDA-TB bands shown at the bottom of Fig. 14 and, at the top, with the xy form-factor dropping in the 2nd BZ thus hiding the resonance peak predicted to exist in the upper \widetilde{xy} band.

Before attempting to extract ARPES data beyond the 100 meV scale, we need to assess the degree of agreement between the LDA and the ARPES dispersions.

(a) LDA-TB



(b) LDA-TB shifted

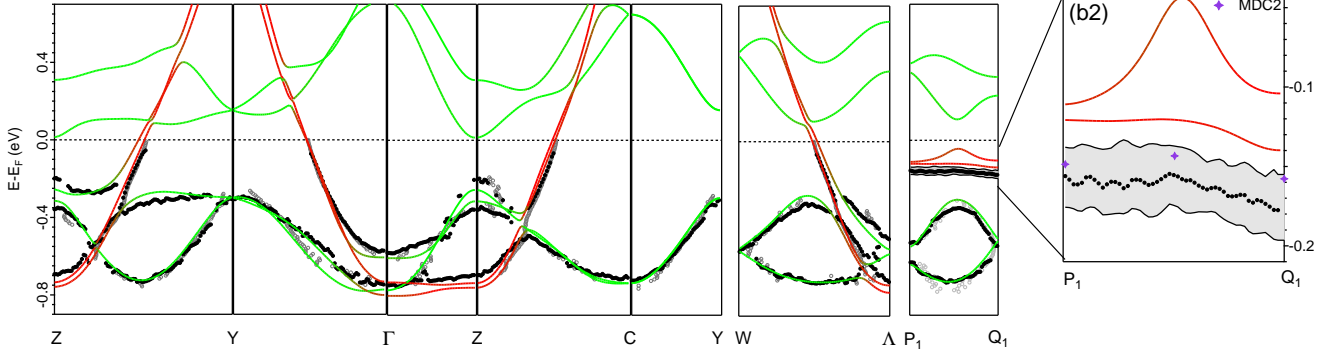


FIG. 22: ARPES (black dots and grey circles) and LDA (xy red and xz/yz green) band structures. The line P_1Q_1 has $k_b=0.225$ and $k_c=0$ to 0.5 , see FIG.s 11, 20, and 21 (a). The experimental bands come from the *symmetrized* ARPES measurements ($T=6K$, $h\nu=30$ eV) on sample H whose metallic bands are 51% filled (see Sect. XVB in Paper III) and displayed in FIG. 21 (c). They were determined by searching the intensity maximum along the direction of either energy (EDC, black dots) or momentum (MDC, grey circles). (a) The LDA bands are the eigenvalues of the six-band TB Hamiltonian defined in Sect. I VI with the parameters listed in Tables I (43)-(47) and (49). (b) As above, but with the energy of the xy WOs shifted 100 meV upwards. The blow-up along P_1Q_1 in (b2) compares the shifted LDA-TB theory with the experimental band (black dots with uncertainty in grey). The diamonds, labeled 'MDC2', indicate the band determined from the maximum along the momentum direction \mathbf{b}^* perpendicular to P_1Q_1 , where the band disperses strongly.

XI. AGREEMENT BETWEEN ARPES AND THE LDA

The band structure derived from the symmetrized ARPES data is shown in Fig. 22 (a) and (b). The points indicated by grey circles were extracted from the peak locations in the momentum distribution curves (MDCs), $I(|\mathbf{k}|)$ in a specified direction, fixed energy E , and the points indicated by black dots were extracted from peak locations in energy distribution curves (EDCs), $I(\text{fixed } \mathbf{k}, E)$. The peak maxima in these curves were found from the zeros in the smoothed first derivative with respect to $|\mathbf{k}|$ for an MDC, or E for an EDC, under the condition that the smoothed second derivative is smaller than zero.

The bands resulting from the first-principles LDA calculation (in the TB representation of the six t_{2g} WOs; see Sect. IV) are shown in (a), with the sum of the xz and yz characters in green and the xy character in red. Note the strong hybridization of the nearly degenerate bottoms of the two xy and the xz and yz valence bands near Γ . Note

also the hybridizations between Z and Y and between W and Λ . Near the middle of the latter line where the two degenerate xy bands in the gap come close to the valence and conduction (V&C) bands, and their repulsion is therefore strong –but in opposite directions– one of the xy states stays unaffected and the other is pushed up or down in energy, depending on whether the repulsion from the valence or the conduction band is stronger. Since this balance tips as we move up through the gap, the hybridization shifts from the upper to the lower xy band and causes the resonance peak to shift from upwards pointing in the upper band, to downwards pointing in the lower band. The fact that the matrix element, $\alpha(\mathbf{k}) + a(\mathbf{k})$, for hybridization of the xy and xz/yz bands decreases with increasing k_b causes the rather strange-looking dispersion of the two xy bands along ΛW . This asymmetry will be explained in Sect. III XIV B; specifically, in connection with Eq. III (97) and with the left-hand sides in the 6th row of Fig. III 26. Along P_1Q_1 , we clearly see the resonance peak in the upper xy band.

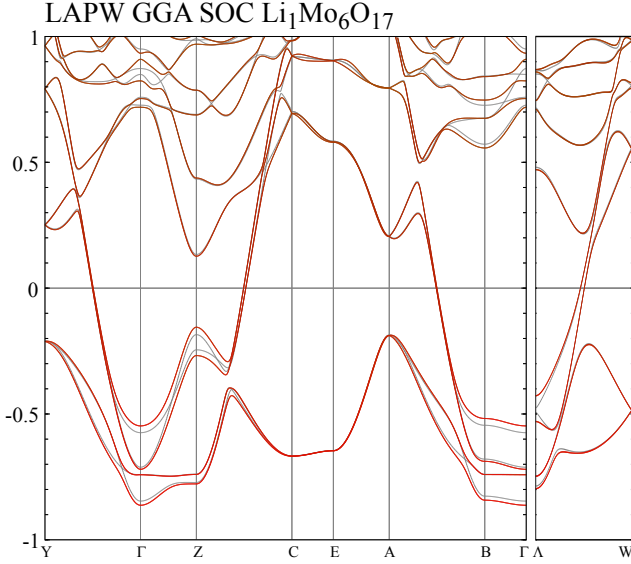


FIG. 23: Relativistic LAPW GGA control calculation of the LiPB band structure along lines in the BZ shown at the top of FIG. 13 whose bottom shows the 336 NMTO LDA band structure. The 6 NMTO TB band structure in the $\Gamma Y Z C$ plane is shown in FIG. I 4. LAPW band energies are in eV with respect to E_F . Red bands are with- and grey bands are without spin-orbit coupling. We see that the crossings between the 3rd and 4th bands along ΓZ and ZC and between the 1st and 2nd bands between ΓY and AB are spin-orbit split by about 80 meV.

A. Shifting the LDA xz and yz bands downwards with respect to the xy bands

Overall in Fig. 22(a), there is good agreement with the occupied ARPES bands, the main discrepancy being that the LDA valence bands lie 100 meV too high with respect to the xy bands and thereby with respect to the Fermi level. This may be partly a surface effect: The xz and yz WOs reach farther into the vacuum and therefore feel a higher LDA potential than the xy WOs which are well inside the staircase. In addition, there is undoubtedly an LDA error; for instance, are LDA bandgaps in semiconductors too small, and FS measurements for bulk $4d$ metals indicate that the accuracy with which the LDA describes the energy separation between inequivalent t_{2g} levels is ~ 50 meV.⁹ For LiPB, we therefore correct the bulk LDA bands by shifting the energy of the green V&C bands downwards by 100 meV [more precisely, we shift the on-site energy, τ_0 , of the xy and XY WOs 100 meV upwards, i.e. from 47 to 147 meV in Table I(43), with respect to the common on-site energy of the $xz, XZ, yz,$

and YZ WOs, and subsequently recalculate the Fermi level]. The result shown in (b) agrees very well with ARPES, as was seen already in Fig. 20(b) for the CECs. An exception is near Z, where the splitting of the valence band is too small and the lowest conduction band nearly touches the Fermi level, thus asking for a fine-adjustment of the TB parameters.

The LDA and ARPES band structures in Figs. 22(a) and (b), are lined up with respect to the Fermi level, which for the LDA calculation for stoichiometric $\text{LiMo}_6\text{O}_{17}$ corresponds to 50% filling of the metallic bands. In the experiment, Li and O vacancies make the filling uncertain and is estimated from the measured $k_F b$ value (Sect. III XV) to be 51 ± 1 %, i.e. to have the effective stoichiometry $\text{Li}_{1.02 \pm 0.02}$. Using the measured Fermi-velocity, this then gives a Fermi level which with respect to the band structure is between 50 and 0 meV above the level for the stoichiometric crystal assumed in the calculation, which means that the metallic ARPES bands could lie 50 to 0 meV below the LDA bands in Fig. 22(b). But this can only account for the ~ 40 meV distance to the lower LDA \tilde{xy} band seen in a direction perpendicular to \mathbf{b}^* , such as along $P_1 Q_1$, in particular in the blow up (b2).

The black dots in (b2) were obtained as the position of the EDC maxima (*one* for each \mathbf{k}) and the grey area indicates the uncertainty of the experiment, as well as the uncertainty in determining the position of the one EDC maximum. The three purple diamonds labeled 'MDC2' are from MDCs along respectively ΓY , ΔW , and ZC , perpendicular to $P_1 Q_1$.

The upper \tilde{xy} band predicted by the LDA, seems to be missing in the symmetrized ARPES data (b2). This, we can understand by going back to the ARPES bands "as-measured" along $P_1 Q_1 P'_1$ in Fig. 21 (d) and (e) where intensity just below the Fermi level was seen in the 1st- but hardly in the 2nd BZ. As illustrated in Fig. 14, the lower xy band is selected in the 1st- and the upper band in the 2nd BZ. Since for $k_b = 0.225$, the xy bands are closer to the valence than to the conduction bands, the repulsion from the former dominates and pushes a resonance peak *up* in the *upper* band. This peak thus has ARPES intensity in the 2nd zone where it gets strongly reduced by the xy form factor. The symmetrization of the $P_1 Q_1$ and $Q_1 P'_1$ ARPES data finally adds to hiding the band in the 2nd BZ behind the one seen in the 1st BZ, and that is the reason why in Fig. 22(b2) only the lower ARPES band is seen. From the ARPES data, we can therefore only uncover the upper \tilde{xy} band if we *avoid* the symmetrization.

B. Fine-tuning the TB Hamiltonian and extracting both quasi-1D bands from ARPES as measured

Our first-principles LDA TB description of the six lowest energy bands given in Sect. I VI has about 40 TB

⁹ For elemental transition metals, 100 meV is the typical size of the s to d energy shift needed to bring the LDA and experimental (dHvA) Fermi surfaces into agreement, see [81].

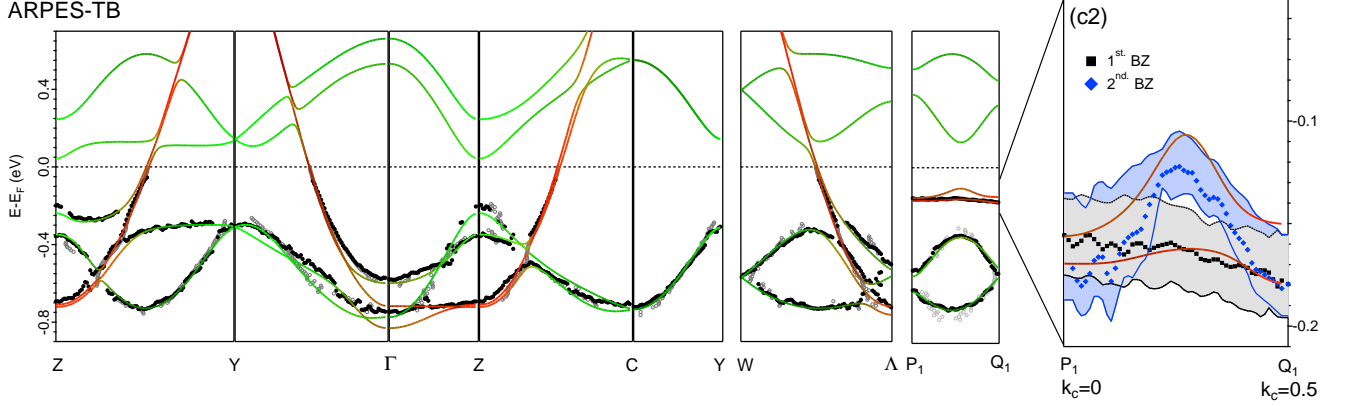


FIG. 24: Band structure obtained as the eigenvalues of the six-band TB Hamiltonian, Eq.s I (35) or I (56), with parameter values fine-tuned to improve the fit to the ARPES bands and given in the square parentheses in Tables I (43)-(47). The Fermi level is ~ 0.1 eV above the center of the gap [see text following Eq. I (49)]. The ARPES data here are those already shown in FIG. 22, except for those in the blow-up (c2) along P_1Q_1 ($k_b=0.225$), which are *non-symmetrized* EDC data from respectively the 1st (black) and 2nd BZ. The latter data is subsequently mirrored around the $k_c=0.5$ zone boundary into the 1st BZ (blue).

parameters (WO energies and hopping integrals). Their LDA values, derived as described in Sect. I II, are given in Tables I (43)-(47) and yield the band structure shown in Fig. 22 (a). As explained above, the improved agreement with ARPES seen in (b) was achieved by merely shifting the value of τ_0 , the energy of the degenerate xy and XY WOs, up with respect to that of the degenerate xz , XZ , yz , and YZ WOs. The latter is the energy at the center of the gap and is taken as the zero of energy in the TB Hamiltonian. Still, the Fermi velocity is too small and the resonance peak along P_1Q_1 is too high. Moreover, the levels near Z , where the V&C bands come closest, remain inaccurate: the splitting of the valence band levels is too small while that of the conduction band levels is too large. This is due to bad convergence and truncation of the xz - yz hybridizations I (40), to our neglect of the spin-orbit coupling in the NMTO –but not in the LAPW (Fig. 23)– calculation, and to the LDA yielding too small a gap.

We therefore refined the parameter values, with the results given in square parentheses in Tables I (43)-(47). Specifically, we found it necessary to modify the values of the intra-ribbon hopping integrals, first of all, between respectively the on-site, 1st-, and 2nd-nearest xy WOs, τ_0 , τ_1 , and τ_2 . This increases the Fermi velocity by about 15%, increases the upward curvature of the bands near half filling, and lowers the half-filling Fermi level to 53 meV above the center of the gap; see Eq.s I (43) and I (48)-(50) in Sect. I VI. Secondly, we refined the values of the xz - yz hopping integrals, m_1 , λ_2 , and λ_3 in Eq. I (47). In addition, the value of the gap parameter, G_1 , originating in the asymmetry (dimerization) between the forwards and backwards hoppings, $xz \leftrightarrow XZ$ ($yx \leftrightarrow YZ$), as explained after Eq. I (27) and given in Eq. I (45), was increased by 10%. The resulting band structure is displayed in Fig. 24 and is seen to agree almost perfectly

with the experiment.

Most importantly, we have succeeded in extracting *both* metallic bands by using the ARPES data *as measured* along $P_1Q_1P'_1$ ($k_b=0.225$) for the EDCs. These ARPES bands are displayed in the blow-up (c2) where the band obtained in the 1st zone from P_1 to Q_1 has been plotted in black squares with the uncertainty in grey, and the band obtained in the 2nd zone from Q_1 to P'_1 has been plotted in reverse order, from Q_1 to P_1 in the 1st zone, and in blue. We now see the resonance peak in the blue upper band, well separated from the grey lower band, while near $k_c = 0, 0.5$, and 1 , the splitting of the two bands is less clear. The reasons for the latter are technical:

1) The extraction was done by assuming only one (possibly broad) maximum per EDC whereby in the zone-boundary (ZB) region ($0.4 < k_c < 0.6$) where both bands have a significant $|\mathbf{k}|$ projection, only one band is found (see red bands in the middle and bottom parts of Fig. 14). In Fig. III 32 we shall see an example of how the one-peak extraction method switches between the two bands when the ZB is crossed.

2) With the ARPES intensity fading away upon approaching $k_c = 1$ (P'_1) smoothening the EDCs before taking the derivative (to locate the maximum) pushes the intensity to increasingly higher binding energies, ω , and thereby causes the band near P'_1 , which is the (blue) upper band, to fall below the one near P_1 , which is the (grey) lower band¹⁰.

Fig. 24 thus demonstrates that the refinement of merely 7 out of the more than 40 TB parameters to fit the ARPES bands, lying more than 0.15 eV below the

¹⁰ The uncertainty of this is not included in the blue uncertainty interval.

Fermi level, achieves nearly perfect agreement *also* for the k_c -dispersion of the quasi-1D bands closer to the Fermi level. This includes agreement with the size and shape of the resonance peak in the upper band, *without* having modified any of the 17 (a, g, α, γ) -parameters I (46) describing hybridization between the xy and the xz and yz bands. This clearly shows the decisive role that resonant coupling to the gapped xz and yz bands plays in determining the splitting and dispersion of the metallic xy bands.

Besides the above-mentioned peculiarities and experimental uncertainties, the agreement between ARPES and the refined TB bands is astonishingly good. In both cases, the peak caused by the resonance with the xz valence band at $(k_b, k_c) = (0.225, 0.725)$ –mirrored around the $k_c = 0.5$ line to the resonance with the yz valence band at $(0.225, 0.275)$ – comes out clearly in the upper \widetilde{xy} band, and so does the *lack* of a visible resonance peak in the *lower* band at $(0.225, 0.275)$.

So it seems justified to use the refined TB model in the following Paper III to describe and seek the origins of the observed k_c -dispersion on the 10 meV-scale and to study the k_c -dispersion as a function of the position of the metallic \widetilde{xy} bands in the gap, i.e. of the k_b -value. This will enable us to study the details of the FS. We shall see that the theoretical splitting between the two metallic bands near the $|k_c| = 0.5$ zone boundary increases as the energy moves away from the valence and towards the conduction band. With the $h\nu = 33$ eV data (see Fig. 19) the zone-selection rule, and the so-called sparrow criterium, we shall be able also with ARPES to separate the two FS sheets.

Considering the good agreement between the widths (0.7 eV) of the occupied part of the metallic 1D xy bands in the ARPES and in the LDA (where this width is independent of our energy shift), we realize that the magnitude of the on-site Coulomb interaction U cannot be large, because the LDA bandwidth should be renormalized by the strength of U . This is fully consistent with the findings of Nuss and Aichhorn [19] for their 4-orbital WO set. They used both dynamical mean field theory and the variational cluster approximation to deduce an upper limit on U in the range of 0.7 to 1.5 eV (depending on the method) in order that the generally good agreement between dispersing ARPES peaks and their LDA bands not be upset. As pointed out already, our final \widetilde{xy} bands are exceedingly delocalized and a consequent reduction in U is expected. Roughly, we expect that a set reduced in size by a factor of n will be n times less localized, with U about n times smaller, implying for our final 2-orbital set relative to the 4-orbital set of Nuss and Aichhorn [19] a reduction by a factor of $2/4 = 1/2$, giving an upper limit on U for our 2-orbital set in the range 0.35 to 0.75 eV. We can infer that yet longer-range repulsions, often denoted as V , will be similarly limited.

XII. SUMMARY AND OUTLOOK

In Sect. IX of this Paper II we derived a one-electron theory of the ARPES intensity variations in LiPB, which was then used in Sect. X to understand and analyze the extensive data presented there.

For the intensity of photoemission with momentum κ and binding energy ω (≥ 0), we used the one-step expression (62) with the least specific choice, plane waves $e^{2\pi i \kappa \cdot \mathbf{r}}$, for the final states, and approximation (63) for the matrix element. As a basis for the initial states, we used the six t_{2g} WOs, $w_m(\mathbf{r})$ and $W_m(\mathbf{r})$, centered on respectively Mo1 and MO1, the most central molybdenums of the lower and the upper strings, $\text{Mo2} \setminus \text{Mo1} / \text{Mo4} \setminus \text{Mo5}$ and $\text{MO5} \setminus \text{MO4} / \text{MO1} \setminus \text{MO2}$, shown in Fig. I 2 (a). Due to the approximate translational equivalence [see Eq.s I (17) and (18)] of $w_m(\mathbf{r})$ and $W_m(\mathbf{r})$, the photoemission intensity is essentially the projection of the initial-state band with energy $E(\mathbf{k}) = E_F - \omega$, onto the *pseudo* Bloch sum, $|w; \mathbf{k}\rangle$ in Eq. I (52) with $\mathbf{k} = \kappa - \mathbf{G}$ in the *double* zone (see Fig.s 11 and Fig. 14 *bottom*). This would have been the initial-state band had the vector distance between Mo1 and MO1 been $\frac{c+b}{2}$, rather than $\frac{c+b}{2} - \mathbf{d}$, and had $W(\mathbf{r})$ been equal to $w(\mathbf{r})$, rather than inverted around $\frac{c+b}{2} - \mathbf{d}$. For a band with dominant m -character, we thus expected that ARPES will see the lower band if κ is in the 1st physical zone, and the upper band if κ is in the 2nd physical zone and the band is occupied. Specifically, that the relative intensity of emission from the $\overset{\text{upper}}{\text{lower}}$ m band is $\frac{1}{2} [1 \pm \cos \phi]$, where $\phi_m(\mathbf{k})$ is given by the m -band structure in Eq. I (60). Taking now the c -axis dimerization into account, we found that this expression is modified to: $\frac{1}{2} [1 \pm \cos(\phi - \eta)]$, where $\eta_m(\kappa) \equiv 2 \arg \tilde{w}_m(\kappa) - 2\pi \kappa \cdot \mathbf{d}$ is the difference between the phase shifts due to the inversion- and displacement dimerizations. These phase shifts were shown in the 1st column of Fig.s 12 and 13 for respectively the xy and yz bands. Whereas the inversion phase shift depends stronger on κ for the yz WO than for the more structurally protected xy WO, the displacement phase shift is independent of m and rather constant. We had therefore expected the selection rule to hold better for the xy bands. However, in both cases and with κ_a (which does not influence the band structure) suitably chosen via the photon energy, the inversion- and displacement phase shifts tend to cancel with the result that the selection rule holds surprisingly well, provided that κ_a is properly chosen. This was seen in the 2nd column of Fig.s 12 and 13.

On top of this fine-grained structure of the photoemission intensity, there is a coarse-grained aperiodic structure given by the WO *form factor* $|\tilde{w}_m(\kappa)|^2$. Since in real space the t_{2g} WO (Fig. I 9) spreads with the same m character onto the 4-5 nearest Mo sites in its plane and on the simple cubic xyz lattice I (12) with 1 Mo per cell, its FT (72) factorizes approximately into a *structure factor*, $\mathcal{S}_m(\kappa)$, times the FT of the "atomic" part of the t_{2g} orbital, factorizing into an angular and a radial part. As explained in Sect. IX B 2, the structure

factors $|\mathcal{S}_{xy}|^2$, $|\mathcal{S}_{yz}|^2$, and $|\mathcal{S}_{xz}|^2$ form 2D square lattices of beams running in respectively the κ_z , κ_x , and κ_y directions in reciprocal space thus giving rise to intensity patterns which are roughly 6 times coarser than the zone-selection patterns. The square lattices formed by the beams from $|\tilde{w}_{xy}(\boldsymbol{\kappa})|^2$ and $|\tilde{w}_{yz}(\boldsymbol{\kappa})|^2$ were shown in column 1 of Fig. 15 and the following columns showed how the angular and radial factors limit the intensities to the extent that only the beams passing through $[\kappa_x, \kappa_y, \kappa_z] = [1, 1, 1]$ should be useful for ARPES investigation of all three WOs. A closer look –and in the crystallographic $(\kappa_a, \kappa_b, \kappa_c)$ space– was given in Fig. 16. The central parts of the three form factors were shown in the *top* part of Fig. 14 along the line $(\kappa_a, \kappa_b) = (6.4, 0.225)$. As seen in the last columns of Figs 12 and 13, the narrowness of the form factors ($\Delta\kappa_c \sim 1$) washes out details of the dimerization distortions of the zone selection, except near the suitably chosen values of κ_a .

Our extensive ARPES data confirmed the LDA-based WO theory of the energy bands and the ARPES intensity variations. Not only was the agreement between the band structures obtained by ARPES and by the LDA very good (Fig. 22), but also leaving little room for an on-site Coulomb repulsion U . Refinement of the LDA-TB parameters to make the fit almost perfect for the large-energy features, automatically improved the results for the small-energy features such as the *resonance peaks* in the upper metallic \tilde{xy} band caused by repulsion from the top of the xz or yz valence bands (Fig. 14 *bottom*), barely detectable by ARPES measured at $h\nu=30$ eV (Fig. 24 (c2)).

The difficulty of detecting the resonance peaks we understood (Sect. XC 2) to stem from the rapid fall-off of the form factor of the \tilde{xy} WO (see Figs 14 *top*, and 16 *left*) when moving away from the centre of the beam given by Eq. (79). The latter depends on κ_a which is controlled by $h\nu$ [Fig. 17 and Eq. (88)] whereby the intensity distribution along the Fermi surface (FS) depends sensitively on the photon energy (Fig. 19).

Our trust in the t_{2g} Hamiltonian with the refined parameter values has thus been strengthened to the extent that in the following Paper III we go on using it together with ARPES data taken at $h\nu=33$ eV to study the splitting and warping of the FS. Such deviations from one-dimensionality, crucial for the physical properties, are tiny and can in Fig. 20 only be seen in the theoretical bands. Moreover, since these deviations are largely induced by the xz and yz bands, as may be realized by comparing the red with the dark-red bands in Fig. 14, they depend sensitively on the Fermi level's distances from these V&C bands and, hence, on the doping.

The resonance peaks are pushed up/down in the upper/lower \tilde{xy} band by the V/C-band edge, whose character is 50% *mixed* $|\mathbf{k}\rangle$ and $|\mathbf{k} + \mathbf{c}^*\rangle$. It was therefore not obvious to what extent the character of the original xy bands (the red ones in the middle panel of Fig. 14) near $k_c=\pm 0.75$ or ± 0.25 are retained in the \tilde{xy} bands, and, hence, how strong the ARPES intensity, proportional to

the $|\mathbf{k}\rangle$ character, should be. We therefore needed to compute the $|\mathbf{k}\rangle$ characters of the \tilde{xy} bands, the dark-red ones in the bottom panel of Fig. 14. This was done using a two-band Hamiltonian obtained by Löwdin downfolding of the V&C blocks of the six-band Hamiltonian I (56) in the $\{\mathbf{k}, \mathbf{k} + \mathbf{c}^*\}$ -representation. The derivation of this two-band Hamiltonian will be our first task in the following Paper III.

Wannier-Orbital theory and ARPES for the quasi-1D conductor $\text{LiMo}_6\text{O}_{17}$.

Part III: The two metallic bands in the gap

L. Dudy

Randall Laboratory, University of Michigan, Ann Arbor, MI 48109, USA
Physikalisches Institut und Röntgen Center for Complex Material Systems,
Universität Würzburg, D-97074 Würzburg, Germany
and
Synchrotron SOLEIL, L'Orme des Merisiers, 91190 Saint-Aubin, France

J.W. Allen

Randall Laboratory, University of Michigan, Ann Arbor, MI 48109, USA

J.D. Denlinger

Advanced Light Source, Lawrence Berkeley National Laboratory, Berkeley, CA 94720, USA

J. He[†]

Department of Physics and Astronomy, Clemson University, Clemson, SC 29534, USA

M. Greenblatt

Department of Chemistry & Chemical Biology, Rutgers University, 123 Bevier Rd. Piscataway, NJ 08854, USA

M.W. Haverkort

Max-Planck-Institut für Festkörperforschung, Heisenbergstrasse 1, D-70569 Stuttgart, Germany
Max-Planck-Institut für Chemische Physik fester Stoffe,
Nöthnitzer Str. 40, D-01187 Dresden, Germany
and
Institut für Theoretische Physik, Universität Heidelberg,
Philosophenweg 16, D-69120 Heidelberg, Germany

Y. Nohara and O.K. Andersen

Max-Planck-Institut für Festkörperforschung, Heisenbergstrasse 1, D-70569 Stuttgart, Germany
(Dated: May 16, 2023)

This is the third paper of a series of three papers presenting a combined study by band theory and angle-resolved photoemission spectroscopy (ARPES) of lithium purple bronze. The first paper laid the foundation for the theory, and the second paper discussed a general comparison between theory and experiment, including deriving an ARPES selection rule. The present paper III focuses in detail on the two metallic, quasi-1D xy -like bands left in the 0.4 eV dimerization gap between the xz and yz valence and conduction (V&C) bands. The hybridizations with the latter change the perpendicular dispersions of –and splitting between– the resulting \widetilde{xy} bands. The edges of the V_C bands, in particular, push resonance peaks up_{down} in the \widetilde{xy} bands which are now described by a two-band Hamiltonian (95) whose two first terms consist of the pure xy -block of the six-band TB Hamiltonian (89), and whose 4 following terms describe the resonant coupling to (i.e., indirect hopping via) the V&C bands. The two-band Hamiltonian extends the selection rule derived in the previous paper to the hybridized \widetilde{xy} bands, which enables, for the first time, extracting the split quasi-1D Fermi surface (FS) from the raw ARPES data. The complex shape of the FS, verified in detail by our ARPES, depends strongly on the Fermi energy position in the gap, implying a great sensitivity to Li stoichiometry of properties dependent on the FS, such as FS nesting or superconductivity. The strong resonances prevent either a two-band TB model or a related real-space ladder picture from giving a valid description of the low-energy electronic structure. Down to a temperature of 6 K, we find no evidence for a theoretically expected downward renormalization of perpendicular single-particle hopping due to LL fluctuations in the quasi-1D chains.

XIII. INTRODUCTION

[†]deceased in 2021.

This last paper in a series of three about ARPES and Wannier orbital (WO) theory of the quasi-1D conductor $\text{LiMo}_6\text{O}_{17}$ deals with the Fermi surface (FS) formed

by the two metallic xy -like bands (the \widetilde{xy} bands) in the gap caused by the c -axis dimerization (Sect. I III A)¹ between the xz - and yz -like valence and conduction (V&C) bands. All six t_{2g} bands, half of them filled in the stoichiometric compound, were studied by band theory in Paper I. In Paper II, we compared the theory with the experiment (by ARPES) for the filled bands. There, also a WO theory of the experimentally found ARPES intensity variations was derived and applied.

As basis for the initial states we used the six t_{2g} WOs, $w_m(\mathbf{r})$ and $W_m(\mathbf{r})$ with $m = xy, xz, yz$, centered on respectively Mo1 and MO1, the most central molybdenums of the lower and the upper strings, $\text{Mo2} \backslash \text{Mo1} / \text{Mo4} \backslash \text{Mo5}$ and $\text{MO5} \backslash \text{MO4} / \text{MO1} \backslash \text{MO2}$, wiggling around the $\mathbf{c} + \mathbf{a}$ direction perpendicular to \mathbf{b} , the direction of the quasi-1D conductivity [see Chart I(15), and Figs 2 and 9]. Due to the approximate translational equivalence of $w_m(\mathbf{r})$ and $W_m(\mathbf{r})$ [see Eq.s I (17) and (18)], the photoemission intensity is essentially the projection of the initial-state band onto the *pseudo* Bloch sum $|\mathbf{k}\rangle$, defined by Eq. I (52). Such a pseudo Bloch sum is a periodic function of \mathbf{k} in the *double* zone (see Fig. I 8), i.e. the zone of the un-dimerized lattice (the one with primitive translations \mathbf{a} , $\frac{\mathbf{c}+\mathbf{b}}{2}$, and $\frac{\mathbf{c}-\mathbf{b}}{2}$, and reciprocal translations \mathbf{a}^* , $\mathbf{c}^*+\mathbf{b}^*$, and $\mathbf{c}^*-\mathbf{b}^*$). The other basis function is simply $|\mathbf{k} + \mathbf{c}^*\rangle$. In the absence of c -axis dimerization, $w_m(\mathbf{r})$ and $W_m(\mathbf{r})$ are identical, apart from a phase factor, and the $|\mathbf{k}\rangle$ and the $|\mathbf{k} + \mathbf{c}^*\rangle$ band structures are each periodic in the double zone and translated by \mathbf{c}^* , i.e. by $\Delta k_c=1$, with respect to each other. In the presence of dimerization, the basis functions become linearly independent and will mix near the crossings of the $|\mathbf{k}\rangle$ and $|\mathbf{k} + \mathbf{c}^*\rangle$ band structures, which will now gap and thereby restore the single-zone periodicity (see Figs I 6 and 7).

This description of the band structure in Paper I, followed by the theory of the ARPES intensity variations in Paper II, explained our comprehensive set of ARPES data for the occupied bands (Figs II 20, 21, 22, and 24), including the observations that the intensity follows the $|\mathbf{k}\rangle$ character (Fig. II 14) and of a surprisingly strong photon-energy dependence of the photoelectron intensity from the FS (Fig. II 19). The former means that the ARPES intensity is enhanced for the lower-energy band in the 1st- and is extinguished in the 2nd physical zone; conversely for the higher-energy band (if occupied)[Sect. II IX B 1 and Fig. 14]. The latter leads us to use $\hbar\nu=33$ eV for the FS studies to be described in the present Paper III Sect. XV.

Fig. II 24 demonstrated that refinement of merely 7 of the over 40 LDA-TB parameters in our six-band t_{2g} Hamiltonian (Sect. I VI) to fit the ARPES bands lying more than 0.15 eV below the Fermi level, achieves nearly perfect agreement *also* for the k_c -dispersion of the quasi-1D bands closer to the Fermi level. This includes agree-

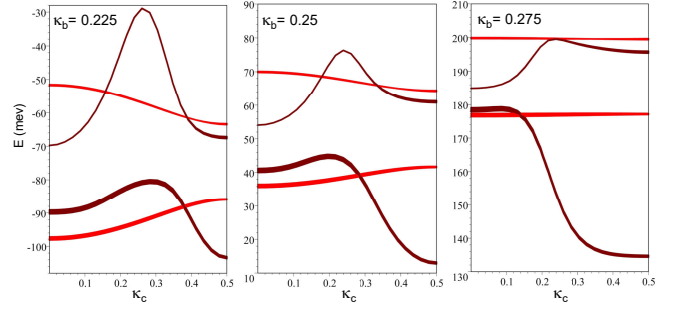


FIG. 25: The two quasi-1D, metallic bands in the gap between the valence (V) and conduction (C) bands as functions of the perpendicular k_c in the irreducible BZ, $0 \leq k_c < 0.5$, and for k_b fixed at 0.225, 0.250, and 0.275. The red bands are the pure xy bands and the dark-red \widetilde{xy} bands include the hybridization with the four V&C bands. The extra fatness (band decoration) is proportional to the $|\mathbf{k}\rangle$ character, which for the dark-red bands was obtained from the two-band Hamiltonian (95). The red and the dark-red fat bands for $k_b=0.225$ were already shown in respectively Figs I 6 and 7, and their $|\mathbf{k}\rangle$ characters in the middle and bottom parts of Fig. II 14. The upper and lower \widetilde{xy} bands as functions of (k_b, k_c) are shown on the left-hand side of Fig. 27. The ARPES-refined TB parameter values I (43)-(46) were used and the xz - yz hybridization was neglected.³ The value of E in the denominators were iteratively adjusted to equal the eigenvalue in question of the two-band Hamiltonian whereby it equals the appropriate eigenvalue of the six-band Hamiltonian with the values I (47) of the xz - yz parameters set to zero. The energy is in meV with respect to the center of the gap. The top of the valence band and the bottom of the conduction band are $\pm 2G_1 = \mp 218$ meV and the ARPES samples had $E_F=75$ meV.

ment with the size and shape of the resonance peak in the upper band –blue in (c2)– *without* having modified any of the 17 (a, g, α, γ) -parameters I (46) describing the hybridization between the xy and the xz and yz V&C bands, parameters which decisively influence the peak structure (Sect.s XIV B 5 and XIV B 6). Our trust in the six-band Hamiltonian has thus been strengthened to the extent that we now go on using it for the ARPES-refined parameter values together with ARPES data taken at $\hbar\nu=33$ eV to study the splitting and warping of the FS.

The resonance peaks are pushed \uparrow in the \widetilde{xy} band by the edges of V_c -bands, whose characters before hybridization with the xy band are 50% *mixed* $|xz; \mathbf{k}\rangle$ and $|xz; \mathbf{k} + \mathbf{c}^*\rangle$, or $|yz; \mathbf{k}\rangle$ and $|yz; \mathbf{k} + \mathbf{c}^*\rangle$. It is therefore not obvious to what extent the character (fatness) of the original xy bands (the red ones in the middle panel of Fig. II 14) near $k_c=\pm 0.75$ or ± 0.25 are retained in the hybridized \widetilde{xy} bands, and, hence, how strong the ARPES intensity, proportional to the $|\mathbf{k}\rangle$ character, should be. We therefore needed to compute the $|\mathbf{k}\rangle$ characters of the \widetilde{xy} bands. This was done using a two-band Hamiltonian obtained by Löwdin downfolding of the V&C blocks of the six-band Hamiltonian I (56) in the $\{\mathbf{k}, \mathbf{k} + \mathbf{c}^*\}$ -representation. The derivation of this Hamiltonian will

¹ I or II refers to sections, figures, and equations in Paper I or II.

be our first task in the theoretical Sect. XIV of the present paper, and the result for $k_b=0.225$ was given as the dark-red fat bands in the bottom panel of Fig. II 14.

The two-band Hamiltonian is also the one from which we can best understand the origin of the splitting and perpendicular dispersion of the two metallic bands shown in Fig. 25, including their development with increasing k_b , which is surprisingly unsymmetric around half-filling, $k_b=0.25$. Having discussed the two bands in great detail in Sect. XIV B and understood that merely the light-red xy –but *not* the dark-red \widetilde{xy} – bands can be described by a 2×2 TB Hamiltonian, we shall in the final theoretical subsection XIV C present and discuss their constant-energy contours (CECs), the FS in particular.

The second part of this paper, starting from Sect. XV, is devoted to the demanding task of using ARPES to determine the FS and its velocities. First, the challenges, issues, and methods are discussed in Sect. XV A. The results of the FS and velocity extraction are then shown in Sect. XV B. They are compared with the TB theory using the ARPES refined parameters and are finally presented in Fig. 32.

In theory, the (fine-grained) ARPES intensity from each band is periodic in the double zone ($|\kappa_c| \leq 1$) with the intensity from the lower band (outer sheet) dominat-

ing in the 1st zone ($|\kappa_c| \leq 0.5$) and the intensity from the upper band (inner sheet) dominating in the 2nd zone ($|\kappa_c| \geq 0.5$). Between zone centers (κ_c integer), the origin of the dominating intensity thus switches from one band (sheet) to the other, with the intensities being equal at the zone boundary. Since the measured spectra of the sheets possess a finite width in momentum, which is much larger than the splitting of the sheets, we can only detect the center of gravity of the sum of intensities from the occupied bands. By taking this into account, the experimentally obtained FS fits perfectly with the theoretical FS. At the zone boundary, we determined an upper bound for the splitting, which is in that sense, in agreement with the theory, that it is larger than the theoretical value. Comparing the experimentally extracted velocities with the theoretical ones, we reach a similar perfect fit as for the FS. Interestingly, the velocities are generally greater than those for pure LDA by about 15%, as we discuss in detail in Sect. XV B 2.

XIV. THEORETICAL SPLITTING AND PERPENDICULAR DISPERSION OF THE TWO METALLIC BANDS IN THE GAP

A. Hamiltonian for the two metallic bands in the $\{\mathbf{k}, \mathbf{k} + \mathbf{c}^*\}$ -representation and of resonance form

We start from the six-band Hamiltonian I (56) in the $\{\mathbf{k}, \mathbf{k} + \mathbf{c}^*\}$ -representation:

H	$ xy; \mathbf{k}\rangle$	$ xy; \mathbf{k} + \mathbf{c}^*\rangle$	$ xz; \mathbf{k}\rangle$	$ xz; \mathbf{k} + \mathbf{c}^*\rangle$	$ yz; \mathbf{k}\rangle$	$ yz; \mathbf{k} + \mathbf{c}^*\rangle$
$\langle xy; \mathbf{k} $	$\tau + t$	iu	$\alpha + a$	$i(\gamma + g)$	$\bar{\alpha} + \bar{a}$	$i(\bar{\gamma} + \bar{g})$
$\langle xy; \mathbf{k} + \mathbf{c}^* $	$-iu$	$\tau - t$	$i(\gamma - g)$	$\alpha - a$	$i(\bar{\gamma} - \bar{g})$	$\bar{\alpha} - \bar{a}$
$\langle xz; \mathbf{k} $	$\alpha + a$	$-i(\gamma - g)$	A	iG	$\lambda + l$	$-i(\mu - m)$
$\langle xz; \mathbf{k} + \mathbf{c}^* $	$-i(\gamma + g)$	$\alpha - a$	$-iG$	$-A$	$-i(\mu + m)$	$\lambda - l$
$\langle yz; \mathbf{k} $	$\bar{\alpha} + \bar{a}$	$-i(\bar{\gamma} - \bar{g})$	$\lambda + l$	$i(\mu + m)$	\bar{A}	$i\bar{G}$
$\langle yz; \mathbf{k} + \mathbf{c}^* $	$-i(\bar{\gamma} + \bar{g})$	$\bar{\alpha} - \bar{a}$	$i(\mu - m)$	$\lambda - l$	$-i\bar{G}$	$-\bar{A}$

(89)

Like in Eq. I (35), the argument, \mathbf{k} , of the Bloch sums of hopping integrals I (36)-(40) is omitted for brevity and an overbar, used when switching from an xz to a yz orbital, indicates the mirror operation $k_b \leftrightarrow -k_b$.

1. Six-band Hamiltonian in the $V\bar{E}C$ subband representation

Since the largest off-diagonal elements I (43)-(47) are \bar{G} and G , which gap the yz bands as in Eq. I (29) and the xz bands in the same way, but with k_b substituted by $-k_b$, we shall now derive a representation in which the xz - xz and yz - yz blocks are diagonal. This mixed representation is the natural one to use for downfolding the xz and yz blocks of the six-band Hamiltonian to a two-band Hamiltonian which describes merely the two \widetilde{xy} bands in the gap and –provided that we neglect the hybridization I (40) between the xz and yz bands– has the simple resonance form (95). This approximation of using the *pure* xz and yz bands (Sect. IV I C), is a good one for $|k_b|$ far away from 0, specifically near the FS, $|k_b| \sim \frac{1}{4}$, and we shall use it from now on.

The eigenvalues, $\pm\sqrt{A^2 + \bar{G}^2}$, of the yz - yz 2×2 diagonal block of the six-band Hamiltonian (89) are the yz conduction (C)- and valence (V)-band energies I (29), and so are $\pm\sqrt{A^2 + G^2}$ for the xz C&V-band energies. The normalized

eigenvectors of this block form the C and V columns of the unitary matrix which gives the xz C&V-band orbitals as:

$$\begin{pmatrix} |xz_C(\mathbf{k})\rangle & |xz_V(\mathbf{k})\rangle \end{pmatrix} = \begin{pmatrix} |xz;\mathbf{k}\rangle & |xz;\mathbf{k}+\mathbf{c}^*\rangle \end{pmatrix} \times \begin{pmatrix} U_C & U_V \\ -isU_V & isU_C \end{pmatrix}, \quad (90)$$

Here, $s(k) \equiv -\text{sgn}\{\sin\pi k\}$ because $G_1 \leq 0$, and

$$U_{\text{v}}^C(\mathbf{k}) \equiv \frac{1}{\sqrt{2}} \sqrt{1 \pm \frac{A(\mathbf{k})}{\sqrt{A(\mathbf{k})^2 + G(\mathbf{k})^2}}}, \quad (91)$$

which are the square roots of the xz C and V-band characters $I(61)$ (before hybridization with the xy bands).

We have chosen $|xz_C(\mathbf{k})\rangle$ and $|xz_V(\mathbf{k})\rangle$ with specific phases –different from those of $|xz_2(\mathbf{k})\rangle$ and $|xz_1(\mathbf{k})\rangle$ in Eq. I (59)– which will simplify the analysis in Sect. XIV B: The coefficients U_C and U_V to $|xz;\mathbf{k}\rangle$ are real, while those to $|xz;\mathbf{k}+\mathbf{c}^*\rangle$ are imaginary. Translation of k by 1 (i.e. \mathbf{k} by \mathbf{c}^*) exchanges U_C and U_V and s and $-s$, whereby the columns of the unitary matrix (90) are exchanged as expected, because they are the eigenvectors for the C&V bands. Exchanging the rows of the matrix of course also corresponds to translating k by 1, but does bring in a phase factor $(is(k))$ which gets passed onto the C&V-band functions: $|xz_C(\mathbf{k}+\mathbf{c}^*)\rangle = \pm |xz_C(\mathbf{k})\rangle is(k)$; and similarly for the orbitals diagonalizing the yz -block of (89), provided that $-k_b$ is substituted by k_b .

With the neglect of hybridization between the xz and yz bands, the unitary 6×6 matrix transforming the Hamiltonian from the reciprocal-lattice representation (89) to the V&C representation merely has three non-zero 2×2 blocks along the diagonal: The xy block is the unit matrix, the xz block is the matrix in Eq. (90), and so is the yz block, but with $k = k_c + k_b$. Hence, the first four rows and columns of the Hamiltonian in the V&C representation become:

H	$ xy;\mathbf{k}\rangle$	$ xy;\mathbf{k}+\mathbf{c}^*\rangle$	$ xz_C(\mathbf{k})\rangle$	$ xz_V(\mathbf{k})\rangle$
$\langle xy;\mathbf{k} $	$\tau + t$	iu	cc	cc
$\langle xy;\mathbf{k}+\mathbf{c}^* $	$-iu$	$\tau - t$	cc	cc
$\langle xz_C(\mathbf{k}) $	$(\alpha + a)U_C + (\gamma + g)sU_V$	$is[(\alpha - a)U_V - (\gamma - g)sU_C]$	$\sqrt{A^2 + G^2}$	0
$\langle xz_V(\mathbf{k}) $	$(\alpha + a)U_V - (\gamma + g)sU_C$	$-is[(\alpha - a)U_C + (\gamma - g)sU_V]$	0	$-\sqrt{A^2 + G^2}$

(92)

The last two (yz_C and yz_V) rows and columns, equal those given above for xz_C and xz_V , but with k_b substituted by $-k_b$ or A and G are substituted by \bar{A} and \bar{G} . For simplicity of notation, we have dropped the argument \mathbf{k} of the matrix elements.

2. Löwdin-downfolded two-band Hamiltonian

The WOs for the two \widetilde{xy} bands in the gap have much longer range than the xy -WOs shown in FIG.s I 5 and I 9, and similarly for the elements in the effective two-band Hamiltonian compared with the range of the Bloch sums in the six-band Hamiltonian. For this reason, we do not perform the downfolding of the xz , XZ , yz , and YZ WOs into the "tails" of the \widetilde{xy} and \widetilde{XY} WOs in real space, but in reciprocal space. Real-space pictures of these downfolded orbitals would be unwieldy and would crucially depend on the position of the energies, E , of the bands in the gap. For the same reason, tables of hopping integrals would be unwieldy and energy dependent. For downfolding from six to two bands, we therefore use analytical Löwdin- rather than numerical (NMT0) downfolding.

With the hybridization between the xz and yz orbitals neglected, the xz and yz downfoldings are additive:

$$(\widetilde{xy}; E, \mathbf{k} \mid \widetilde{xy}; E, \mathbf{k} + \mathbf{c}^*) = (|xy;\mathbf{k}\rangle \mid |xy;\mathbf{k} + \mathbf{c}^*\rangle) + \delta_{xz;E} (|xy;\mathbf{k}\rangle \mid |xy;\mathbf{k} + \mathbf{c}^*\rangle) + \delta_{yz;E} (|xy;\mathbf{k}\rangle \mid |xy;\mathbf{k} + \mathbf{c}^*\rangle). \quad (93)$$

Here, the $\delta_{xz;E}$ and $\delta_{yz;E}$ perturbations involve the Green function for the xz - xz or yz - yz block of the six-band Hamiltonian (89) times the corresponding xz - xy or yz - xy hybridization matrix. The representation chosen for the xz and yz states to be downfolded (integrated out) matters for the formalism –and, hence, for our interpretations,– but *not* for the resulting two-band Hamiltonian. Choosing the V&C representation (92) in which the xz - xz and the yz - yz blocks of the Hamiltonian are diagonal we get:

$$\delta_{xz;E} (|xy;\mathbf{k}\rangle \mid |xy;\mathbf{k} + \mathbf{c}^*\rangle) = \frac{|xz_C\rangle}{E - \sqrt{A^2 + G^2}} (\langle xz_C | H | xy;\mathbf{k}\rangle \langle xz_C | H | xy;\mathbf{k} + \mathbf{c}^*\rangle) + \frac{|xz_V\rangle}{E + \sqrt{A^2 + G^2}} (\langle xz_V | H | xy;\mathbf{k}\rangle \langle xz_V | H | xy;\mathbf{k} + \mathbf{c}^*\rangle), \quad (94)$$

and similarly for $\delta_{yz;E}$. It is by virtue of this choice that the E -dependence of the downfolded orbitals enters solely through the denominators in (94).

In the \widetilde{xy} representation (93), the two-band Hamiltonian is finally seen to be:

$$\begin{aligned} & \left(\begin{array}{cc} \langle \widetilde{xy}; E, \mathbf{k} | H | \widetilde{xy}; E, \mathbf{k} \rangle & \langle \widetilde{xy}; E, \mathbf{k} | H | \widetilde{xy}; E, \mathbf{k} + \mathbf{c}^* \rangle \\ c.c. & \langle \widetilde{xy}; E, \mathbf{k} + \mathbf{c}^* | H | \widetilde{xy}; E, \mathbf{k} + \mathbf{c}^* \rangle \end{array} \right) = \tau(k_b) \begin{pmatrix} 1 & 0 \\ 0 & 1 \end{pmatrix} + \begin{pmatrix} t(\mathbf{k}) & iu(\mathbf{k}) \\ -iu(\mathbf{k}) & -t(\mathbf{k}) \end{pmatrix} \\ & + \frac{\Gamma_C(\mathbf{k})}{E - \sqrt{A^2(\mathbf{k}) + G^2(\mathbf{k})}} + \frac{\Gamma_V(\mathbf{k})}{E + \sqrt{A^2(\mathbf{k}) + G^2(\mathbf{k})}} + \frac{\bar{\Gamma}_C(\mathbf{k})}{E - \sqrt{A^2(\mathbf{k}) + G^2(\mathbf{k})}} + \frac{\bar{\Gamma}_V(\mathbf{k})}{E + \sqrt{A^2(\mathbf{k}) + G^2(\mathbf{k})}}, \end{aligned} \quad (95)$$

with the directly coupled terms on the 1st line and the resonance terms for the coupling via the conduction and valence bands on the 2nd line. The poles at the C&V xz and yz bands, $\pm\sqrt{A^2(\mathbf{k}) + G^2(\mathbf{k})}$ and $\pm\sqrt{A^2(\mathbf{k}) + G^2(\mathbf{k})}$, are numbers while the residues, $\Gamma_C(\mathbf{k})$, $\Gamma_V(\mathbf{k})$, $\bar{\Gamma}_C(\mathbf{k})$, and $\bar{\Gamma}_V(\mathbf{k})$, are 2×2 matrices. The residue for the perturbation by the xz conduction band is:

$$\Gamma_C(\mathbf{k}) = \begin{pmatrix} |\langle xz_C(\mathbf{k}) | H | xy; \mathbf{k} \rangle|^2 & \langle xy; \mathbf{k} | H | xz_C(\mathbf{k}) \rangle \langle xz_C(\mathbf{k}) | H | xy; \mathbf{k} + \mathbf{c}^* \rangle \\ cc & |\langle xz_C(\mathbf{k}) | H | xy; \mathbf{k} + \mathbf{c}^* \rangle|^2 \end{pmatrix} \quad (96)$$

and similarly for the xz valence band. The matrix elements (96) are shown in the 4th row in FIG. 26 and their factors, the matrix elements of the xz - xy hybridization (92), are shown in the 5th row of that figure, to which we shall return in Sect. XIV B. The residues for the perturbations by the yz C&V bands are respectively $\bar{\Gamma}_C(\mathbf{k})$ and $\bar{\Gamma}_V(\mathbf{k})$ with the overbar indicating the mirror operation $k_b \leftrightarrow -k_b$.

E is the energy of the \widetilde{xy} state that we are seeking, i.e. the upper or lower eigenvalue of the two-band Hamiltonian (95), and should therefore be found self-consistently. For states deep inside the gap, we may substitute E by $\tau(k_b)$ from Eq. I (36). Note that E is with respect to the center of the gap and that it enters the two-band Hamiltonian (95) only through the denominators of the four resonance terms. Keeping E as a free parameter therefore provides insight to study how the perpendicular dispersion of the \widetilde{xy} -bands depend on their placement in the gap and on the \mathbf{k} -dependence of the four residues².

B. Origin of the splitting and perpendicular dispersion

Having verified the realism of our LDA-based TB model in Fig. II 24 (c2), and having derived a Hamiltonian (95) for the two metallic \widetilde{xy} bands in the gap (Fig. 25) consisting of TB *plus resonance* terms, we now take up the thread and trace the non-trivial features of the bands back to the Bloch-sums I (36)-(37), $\tau(k_b)$, $t(\mathbf{k})$, and $u(\mathbf{k})$, of the xy - xy hopping integrals, to the

Bloch sums I (38), $A(k_c \mp k_b)$ and $G(k_c \mp k_b)$, of the xz - xz or yz - yz hopping integrals, and to the Bloch sums I (39), $\alpha(\mathbf{k}) + a(\mathbf{k})$ and $\gamma(\mathbf{k}) + g(\mathbf{k})$, of the xy - xz hopping integrals. This is a long route and the essence may be extracted from the synthesis in Sect. XIV B 7.

We start by extending Fig. 25 –like Fig. I 7– from the irreducible ($0 \leq k_c \leq 0.5$) to the double ($-1 < k_c \leq 1$) zone in which all Bloch sums are periodic (the Greek- and Latin-lettered Bloch sums are periodic in respectively the single and the double zone). This is done in Fig. 26 on the top line to the right (the figure to the left will be described in the last paragraph of this subsection), in each of three panels, for $k_b=0.225$, 0.250 and 0.275 , i.e. along the brown, red, and olive dot-dashed lines in Fig. I 8. For clarity, the color of the \widetilde{xy} bands has been changed from dark-red to black in Fig. 26.

Upon increasing k_b from 0.225 to 0.275 , we see the \widetilde{xy} bands develop from having strong upwards-pointing peaks in the upper band near $k_c=\pm 0.75$ and ± 0.25 , plus small downwards bulges in the lower band around $k_c=\pm 0.5$, over having reduced peaks and increased bulges –and thus minimal total width– near midgap, to having large downwards-pointing peaks connected pairwise by large bulges in the lower band, plus reminiscences of the upwards-pointing peaks in the upper band. This development is far from symmetric around the mid-gap energy ($\equiv 0$), despite the fact that the V and C bands on either side of the direct gap have the same character, apart from being respectively xz - XZ (or yz - YZ) bonding and anti-bonding. In the present section we shall show in didactic detail that the origin lies in the complicated bi-products, Eq. (96), forming the residues, $\Gamma(\mathbf{k})$, of the matrix elements for the resonant couplings.

On lines 2-6 in Fig. 26, we identify and analyze the in-

² We could have avoided the U -functions (91) which switch between the V and C bands, had we downfolded the six-band Hamiltonian in the representation (56) instead of in the V&C representation (92). But the price is that we lose the description (94)-(95) in terms of a sum of single resonances, and that E would enter not only the denominators, but also the numerators. The same result is of course obtained by combining in Eq. (95) the C&V terms for xz , as well as those for yz , whereby the U -functions cancel out.

dividual contributions from the direct xy - xy hops (red) and the indirect hops via the xz (blue) and yz (green) V&C bands to the diagonal and off-diagonal elements, $\langle \widetilde{xy}; \mathbf{k} | H | \widetilde{xy}; \mathbf{k} \rangle$ and $\langle \widetilde{xy}; \mathbf{k} | H | \widetilde{xy}; \mathbf{k} + \mathbf{c}^* \rangle$, of the two-band Hamiltonian (95). We end on line 6 which shows $\alpha(\mathbf{k}) + a(\mathbf{k})$ in purple and $\gamma(\mathbf{k}) + g(\mathbf{k})$ in turquoise.

For simplicity in Fig. 26, we have substituted E in the denominators of the resonance terms (95) by $\tau(k_b)$ and shall use a notation in which we drop this argument from e.g. $\langle \widetilde{xy}; \tau(k_b), \mathbf{k} | H | \widetilde{xy}; \tau(k_b), \mathbf{k} + \mathbf{c}^* \rangle$. This approximation slightly enhances the peak features, as may be seen by comparison of Figs 25 and 26.

The bands –but not their $|\mathbf{k}|$ decoration (extra fatness)– have the proper single-zone period 1 in k_c . Where one band is fat and the other not, those bands have respectively pure $|\mathbf{k}|$ and pure $|\mathbf{k} + \mathbf{c}^*|$ character. This is the case for integer values of k_c , whereas for half-integer values, the two bands are of 50% mixed character.

To the left on the 1st line, we show in respectively fat and thin lines the unhybridized $\widetilde{xy}(\mathbf{k})$ and $\widetilde{xy}(\mathbf{k} + \mathbf{c}^*)$ bands. These are the diagonal elements, $\langle \widetilde{xy}; \mathbf{k} | H | \widetilde{xy}; \mathbf{k} \rangle$ and $\langle \widetilde{xy}; \mathbf{k} + \mathbf{c}^* | H | \widetilde{xy}; \mathbf{k} + \mathbf{c}^* \rangle$ of the two-band Hamiltonian (95) and have the double-zone period 2 in k_c .

1. Peak-, bulge-, and contact features

The *primary feature* of the \widetilde{xy} bands in the gap, the *resonance peaks*, originate from either an xz -band edge, which runs along a blue YZY' line in Fig. I 8 (or II 11), or from a yz -band edge, which runs along a green YZY' line in the same figure, and are therefore located at the crossings between such a line and the two red \widetilde{xy} -band CECs seen in the uppermost panels of Fig. II 20 (b). In the CECs, the resonance peaks appear as *notches*. With reference to the bands for fixed values of k_b in Fig. 25, a resonance peak is located where a band edge crosses the appropriate constant k_b -line (dot-dashed in Fig. I 8). The resonance features are therefore well separated in k_c as seen in Fig. 26 on the 1st line to the right.

From the fatnesses of the bands, we see that the resonance peaks have almost pure $|\widetilde{xy}; \mathbf{k}|$ or $|\widetilde{xy}; \mathbf{k} + \mathbf{c}^*|$ character, although the V&C-band edges have $\sim 50\%$ mixed $|xz; \mathbf{k}|$ and $|xz; \mathbf{k} + \mathbf{c}^*|$ (or $|yz; \mathbf{k}|$ and $|yz; \mathbf{k} + \mathbf{c}^*|$) characters, as we saw along ΛW ($k_c = \frac{1}{4}$) and $\Lambda' W'$ ($k_c = \frac{3}{4}$) in Fig. II 21 (d) and (e). The strong $|\mathbf{k}|$ character is what enabled us, in Sect. XI B of Paper II, to detect with ARPES the large peak in the upper \widetilde{xy} band from the resonance with the blue xz valence band at $\mathbf{k} = (0.225, 0.725)$, mirrored ("symmetrized") around $k_c = 0.5$ to $(0.225, 0.275)$. That the lower \widetilde{xy} band merely exhibits a shoulder at $(0.225, 0.725)$ will be explained later, in connection with Eq. (97).

The understanding is quite different for the *secondary feature*, seen around the BZ boundaries ($k_c = \pm 0.5$) on the 1st line in Fig. 26 to the right (but absent to the left). This feature consists of a *bulge* in the lower band and the concomitant filling-in of the valleys between the

neighboring resonance peaks repelled by the xz and yz V or C bands, whichever is closer in energy. These neighboring resonance peaks are therefore in the upper \widetilde{xy} band when $k_b = 0.225$ and 0.250 , and in the lower \widetilde{xy} band when $k_b = 0.275$. The bulge is caused by the hybridization between the $\widetilde{xy}(\mathbf{k})$ and $\widetilde{xy}(\mathbf{k} + \mathbf{c}^*)$ bands – displayed to the left – which cross at $k_c = \pm 0.5$ and split by $\pm |\langle \widetilde{xy}; \mathbf{k} | H | \widetilde{xy}; \mathbf{k} + \mathbf{c}^* \rangle|$. The latter, off-diagonal matrix element of the two-band Hamiltonian (95) is shown in black on the 2nd line to the right. This element is seen to attain its largest absolute value near $k_c = \pm 0.5$ and, here, to have equal contributions from the indirect hops via the xz (blue) and yz (green) bands, and to be amplified by the direct xy - xy (red) contribution. To the left, and in the same colors, are shown the diagonal element, $\langle \widetilde{xy}; \mathbf{k} | H | \widetilde{xy}; \mathbf{k} \rangle$, and its three contributions.

Also the *third characteristic feature* of the \widetilde{xy} bands, the *near contact* between the two bands –and in particular between their CECs [Fig. 27 (d)]– on the ΓY and $\Gamma' Y'$ lines ($k_c = \text{integer}$), is connected with the hybridization between the $\widetilde{xy}(\mathbf{k})$ and $\widetilde{xy}(\mathbf{k} + \mathbf{c}^*)$ bands, albeit with its zero rather than its maximum [Fig. 26, black curve on the second line to the right]. In ARPES [Fig. II 24 (c2)], as well as in previous calculations [25], an apparent crossing on the ΓY line ($k_c = 0$) was noted and a TB description attempted [17]. With our improved resolution, this peculiarity is now seen [Fig. 27 (d)] as a splitting between the two CECs, which along ΓY is anomalously small³ and even decreases with energy. This is in contrast to the relatively large splitting along ZC ($k_c = \frac{1}{2} + \text{integer}$) which is caused by $(\mathbf{k}, \mathbf{k} + \mathbf{c}^*)$ -hybridization and increases with energy. The splitting at integer k_c is even *smaller* than that of the directly-coupled, red bands. This is simple to understand: First of all, the splitting, $2t(\mathbf{k}) = 8(t_1 \cos \pi k_b + t_2 \cos 3\pi k_b)$, of the red bands decreases from 46 meV for $k_b = 0.225$ to 24 meV for $k_b = 0.275$. Secondly, along ΓY ($k_c = 0$) the pure $xy(\mathbf{k})$, $xz(\mathbf{k})$, and $yz(\mathbf{k})$ bands are all bonding between ribbons while the $xy(\mathbf{k} + \mathbf{c}^*)$, $xz(\mathbf{k} + \mathbf{c}^*)$, and $yz(\mathbf{k} + \mathbf{c}^*)$ bands are all anti-bonding [see Fig. I 6]. Since both xy bands in the gap lie above the $xz(\mathbf{k})$ and $yz(\mathbf{k})$ bands, but below the $xz(\mathbf{k} + \mathbf{c}^*)$ and $yz(\mathbf{k} + \mathbf{c}^*)$ bands, the valence bands will push the bonding $xy(\mathbf{k})$ band up, and the conduction bands will push the anti-bonding $xy(\mathbf{k} + \mathbf{c}^*)$ band down in energy. Hence, the hybridization with the xz and yz V&C bands will *diminish* the separation between the xy bands⁴.

It is remarkable that in a region around $k_c = \text{integer}$, the

³ Including the xz - yz hybridization, i.e. the (λ, l, μ, m) hopping integrals, as was done in FIG.s I 24 (c2) and 27 (d), but was neglected in the two-band Hamiltonian and, hence, in FIG.s 26 and 25, decreases the splitting between the \widetilde{xy} bands for integer k_c by a factor ~ 2 .

⁴ The result along $\Gamma' Y'$ ($k_c = \pm 1$) is of course the same although, there, the $|\mathbf{k}|$ bands are anti-bonding and the $|\mathbf{k} + \mathbf{c}^*|$ bands bonding.

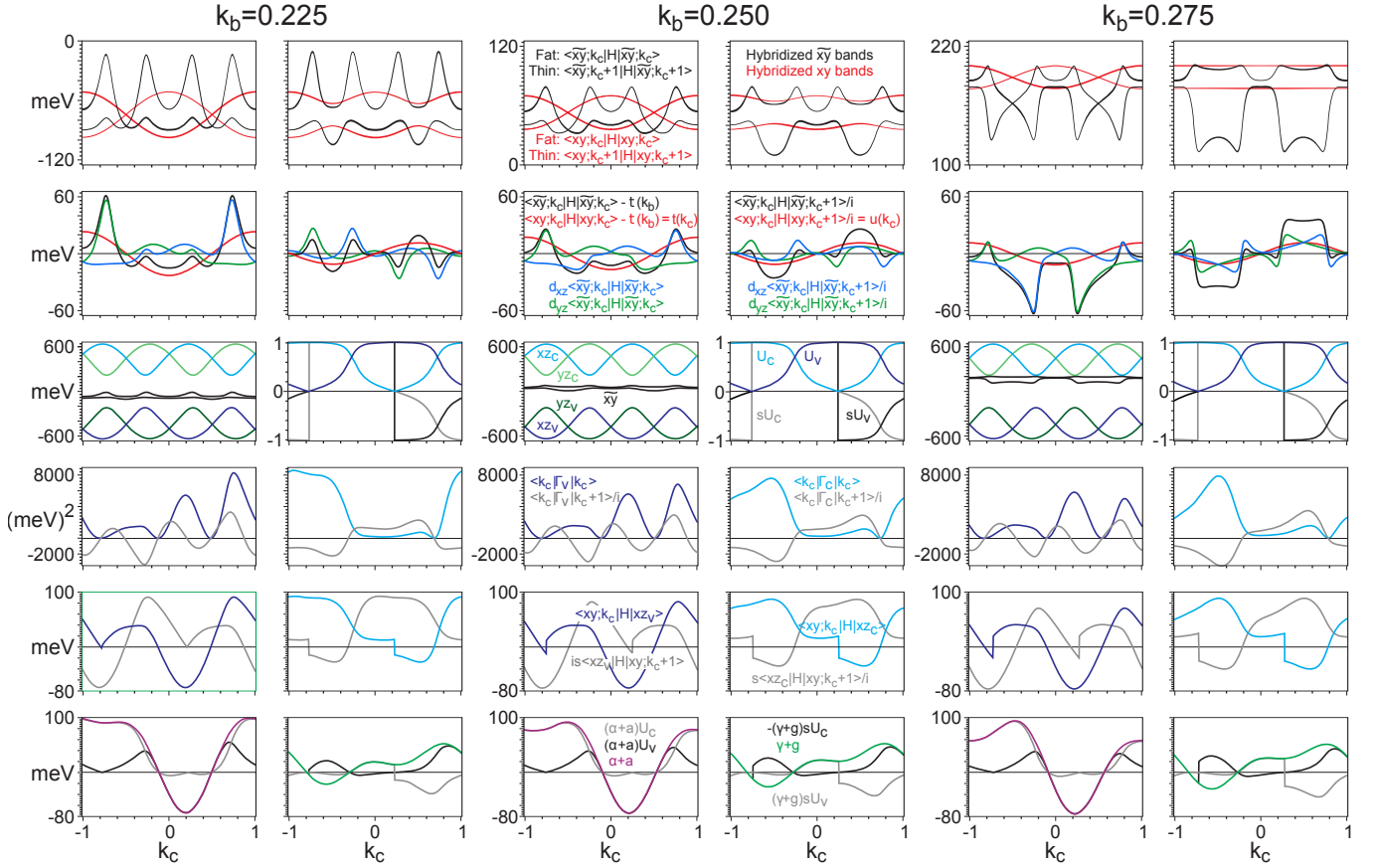


FIG. 26: The following caption is for each of the three k_b -panels: **1st line:** Metallic xy (red) and \widetilde{xy} (black) bands, decorated with their $|\mathbf{k}|$ character, as fct.s of k_c in the double zone. $(\mathbf{k}, \mathbf{k} + \mathbf{c}^*)$ -unhybridized (left) and -hybridized (right). The latter are as in FIG. 25, but extended to the double zone. **2nd line:** Diagonal, $\langle \widetilde{xy}; \mathbf{k} | H | \widetilde{xy}; \mathbf{k} \rangle - \tau(k_b)$ (left), and off-diagonal, $\langle \widetilde{xy}; \mathbf{k} | H | \widetilde{xy}; \mathbf{k} + \mathbf{c}^* \rangle / i$ (right), elements of the two-band Hamiltonian (95). In black, the sum of the contributions from the direct, inter-ribbon xy - XY hops (red) and from the indirect hops via the xz (blue) and yz (green) valence (V) and conduction (C) bands. [Not shown are the $xy(\mathbf{k} + \mathbf{c}^*)$ and $\widetilde{xy}(\mathbf{k} + \mathbf{c}^*)$ bands minus $\tau(k_b)$ in thin black]. **3rd line left:** The black \widetilde{xy} bands in the gap between the blue xz and green yz V (dark) and C (light) bands; the hybridizations of the two latter with the xy bands were neglected, i.e. $\varepsilon_{xz} = \mp \sqrt{A^2 + G^2}$. **3rd line right:** Matrix elements (91) of the unitary transformation (90) between the xz orbitals in the reciprocal-lattice and V&C representations: U_V (dark blue), U_C (light blue), sU_V (black), and sU_C (grey). The probability that at \mathbf{k} the $|xz; \mathbf{k}\rangle$ character is in the V band is U_V^2 , and similarly for U_C^2 . **4th line:** Diagonal, $\langle \mathbf{k} | \Gamma | \mathbf{k} \rangle$ (blue), and off-diagonal, $\langle \mathbf{k} | \Gamma | \mathbf{k} + \mathbf{c}^* \rangle / i$ (grey), matrix elements in meV^2 of the residue for the perturbation of the two-band Hamiltonian via the xz V band (left) or C band [Eq. (96)] (right). **5th line:** The factors $\langle xy; \mathbf{k} | H | xz_V \rangle$ (dark blue) and $\langle xz_V | H | xy; \mathbf{k} + \mathbf{c}^* \rangle / (-is)$ (dark grey) of Γ_V (left) and the factors $\langle xy; \mathbf{k} | H | xz_C \rangle$ (light blue) and $\langle xz_C | H | xy; \mathbf{k} + \mathbf{c}^* \rangle / (is)$ (light grey) of Γ_C (right). See Eq.s (96) and (100). Blue and grey curves are simply related by a \mathbf{c}^* translation. **6th line left:** $\alpha + a$ (purple) and the products, $(\alpha + a)U_V$ (black) and $(\alpha + a)U_C$ (grey), which are the first terms in Eq. (100). **6th line right:** $\gamma + g$ (turquoise) and the products, $-(\gamma + g)sU_C$ (black) and $(\gamma + g)sU_V$ (grey), which are the second terms in Eq. (100). Energies are in meV with respect to the centre of the gap. The ARPES-refined parameter values were used. E in the resonance terms was approximated by $\tau(k_b)$. See Sects. I VI and IIIXIV A.

lower \widetilde{xy} band runs parallel with the red xy band, and that the k_c -region over which this happens, as well as the distance above the xy band, decreases with increasing k_b . We shall return to this at the end of Sect. XIV B 7.

We emphasize that neither of the three characteristic features of the two metallic bands in the gap can be described by a 2×2 TB Hamiltonian alone, but need the resonance terms. The three characteristic features are seen as functions of (k_b, k_c) on the left-hand side of Fig. 27 in Sect. XIV C to which we shall return.

2. Directly coupled terms

We now systematically identify the different terms of the two-band Hamiltonian (95).

Its first term, the energy $\tau(k_b)$ of the two degenerate 1D intra-ribbon xy bands, is included only on the 1st line of Fig. 26, where it is the average of the two red, directly-coupled xy bands, $xy(\mathbf{k})$ and $xy(\mathbf{k} + \mathbf{c}^*)$ to the left or of the $(\mathbf{k}, \mathbf{k} + \mathbf{c}^*)$ -hybridized bands to the right. This average is independent of k_c . On the 2nd line to the

left, $\tau(k_b)$ is neither included in the red, directly-coupled $xy(\mathbf{k})$ band, nor in the black, directly plus indirectly-coupled $\widetilde{xy}(\mathbf{k})$ band.

The second term in Eq. (95) is the xy -block of the six-band Hamiltonian (89) and it gives the perpendicular dispersions and splitting of the red xy bands shown on the 1st line in Fig. 26. The corresponding diagonal and off-diagonal matrix elements, $t(\mathbf{k})$ and $iu(\mathbf{k})$, are the Bloch sums of respectively the average xy - XY hoppings and their dimerizations. They are given in Eq. I(37) and are shown in red on the 2nd line to respectively the left and the right. These Bloch sums of direct hoppings are seen to depend little on k_b in the $\pm 10\%$ interval around k_F .

Also the TB model [17] upon which current TLL theories [5][10] are based, includes 1st- and 2nd-nearest-neighbor terms. But in the attempt to fit the peak, bulk, and band-crossing features of the LDA FS [25] without recognizing their resonant nature, the resulting TB model had an unphysical form (containing e.g. $\sin \pi k_c$ and $\sin 2\pi k_c$ terms) and, as a consequence, its parameter values are incompatible with ours. That the magnitude of its FS warping is several times ours is partly because the stoichiometry was taken to be $\text{Li}_{0.90}$ rather than $\text{Li}_{1.02}$.

3. Symmetries

The red, directly-coupled and the black, directly plus indirectly-coupled $|\mathbf{k}\rangle$ bands shown to the left on the 2nd line are even around $k_c = -1, 0$, and 1 . The red and black matrix elements shown to the right couple each of these bands to itself after a translation of k_c by 1 . These off-diagonal elements, divided by i , are odd around $k_c = -1, 0, 1$ and even around $k_c = \pm 0.5$. The indirect couplings alone, i.e. the perturbations of the \widetilde{xy} -band Hamiltonian by the xz or yz V&C bands, are shown respectively in blue and green. They are related to each other by a sign change^{II 8} of k_b , and those blue and red curves to the left/right are related to each other by a mirror/anti-mirror operation around $k_c = -1, 0, 1$. Moreover, each of the blue and green curves to the right change sign upon k_c -translation by 1 , i.e. they are anti-periodic [see Eq. (99)].

4. Indirectly coupled terms; role of the denominators

The indirect couplings via the xz and yz bands are additive and given by respectively the 3rd&4th and the 5th&6th terms in expression (95), provided that the hybridization between the xz and yz bands is neglected.³ The perturbations via the xz and yz bands have been subdivided into V and C bands whereby each of them takes the form of a single resonance (pole) with the nominator (residue) being a 2×2 matrix with period 2 in k_c —see Eq.s (96) and (92)—and the denominator a period-1 scalar function which is the energy distance between the

\widetilde{xy} band and one of the four xz or yz V or C bands. The energy of the former is $E [\sim \tau(k_b)]$, and that of the latter is given by Eq. I(29), and by the same equation, but with k_b substituted by $-k_b$, for ε_{xz} .

From now on, we shall take advantage of the mirror/anti-mirror symmetries mentioned in the previous Sect. XIV B 3 between the blue xz - and the green yz perturbations of the two-band Hamiltonian to consider merely the blue xz perturbation, which we shall trace back from the 2nd line to the Bloch sums A and G (of respectively the symmetric and asymmetric xz - xz integrals for hopping in- and out-side a bi-ribbon) giving the xz C&V-band energies and character square roots on the 3rd line, and to the Bloch sums α, a, γ , and g of xy - xz hopping integrals on the 6th line.

The most important factor influencing the shapes of the diagonal and off-diagonal matrix elements shown in blue on the 2nd line to the left and the right, and given by the 3rd&4th terms in Eq. (95), is their common energy denominator. This is the distance seen on the 3rd line to the left between the \widetilde{xy} bands in black and the xz V and C bands in respectively dark and light blue. Also shown are the yz V and C bands in respectively dark and light green. The edges, $\mp 2|G_1|$, of the xz bands (blue in Fig. I 8 or II 11) are along $k_c = k_b \mp \frac{1}{2} + 2n$, which for the three chosen values of k_b , and for k_c in the $(-1|1)$ double-zone are at $k_c \sim -0.25$ and 0.75 . This is where the xz -band edges may cause resonance peaks in the \widetilde{xy} bands.

When $k_b = 0.225$, there is a large peak in the unhybridized $\widetilde{xy}(\mathbf{k})$ band on the 1st line to the left near 0.75 and a small one near -0.25 . On the 2nd line, both peaks are blue and point upwards, i.e. are caused by repulsion from the xz valence band. Their sizes decrease strongly as—with k_b increasing—the \widetilde{xy} bands move upwards, away from the valence band. For $k_b = 0.250$, the peaks can still be seen in the unhybridized $\widetilde{xy}(\mathbf{k})$ bands, as well as in the fully hybridized \widetilde{xy} band on the 1st line to the right. But for $k_b = 0.275$, when the upper \widetilde{xy} band is touching the bottom of the C-band edge, only the peak from the xz V-band resonance near 0.75 has survived. The small peak near -0.25 has been overpowered by a large, downwards pointing C-band resonance, shaped like a *canine tooth*. Going back to $k_b = 0.250$, this tooth is reduced to a "hole" on the low- k_c side of the small, blue V-band peak near $k_c = -0.25$.

The contribution from the xz V&C bands to the hybridization between the $\widetilde{xy}(\mathbf{k})$ and $\widetilde{xy}(\mathbf{k} + \mathbf{c}^*)$ bands is shown in blue (and divided by i) on the 2nd line to the right. Whereas the diagonal element of the residue matrix (96) is positive definite, its $(\mathbf{k}, \mathbf{k} + \mathbf{c}^*)$ -mixing off-diagonal elements are purely imaginary and anti-periodic, i.e. they change sign upon translation of k_c by 1 . For $k_b = 0.225$ the blue peak pointing downwards near 0.75 is similar to that of the diagonal element pointing upwards, but its magnitude is reduced by roughly a factor 2 . For k_b increasing, this peak decreases further and it gets superposed by the growing, anti-periodic canine-

tooth structure. At the zone boundaries (ZB), $k_c = \pm 0.5$, the $\widetilde{xy}(\mathbf{k})$ and $\widetilde{xy}(\mathbf{k} + \mathbf{c}^*)$ bands are degenerate, but get split by \pm the numerical value of the off-diagonal element of the two-band Hamiltonian (95), which is seen to increase strongly with k_b . The reason is, as we shall see below, that the contribution from the V band nearly vanishes at the zone boundaries. The uncompensated repulsion from the C band is then what causes the development of the bulge in the lower \widetilde{xy} band.

The V band thus causes peaks in the upper \widetilde{xy} band and the C band causes merging canine teeth plus ZB-centered bulges in the lower \widetilde{xy} band. The peaks and the teeth are resonance features occurring where the FS, $|k_b| \sim \frac{1}{4}$, crosses between the edges, $|k_c \pm k_b| = \frac{1}{2}$, of xz and yz -like V&C bands.

5. Indirectly coupled terms; role of the residues

The residues of the 4 resonance terms in expression (95) are 2×2 matrices whose elements are products of xy - xz and xy - yz hybridization matrix elements (92). For $\Gamma_C(\mathbf{k})$, this is expressed in Eq. (96).

The form (96) with $\langle xy; \mathbf{k} | H | xz_C \rangle$ real and $\langle xz_C | H | xy; \mathbf{k} + \mathbf{c}^* \rangle$ imaginary, causes the two eigenvalues of the $\Gamma_C(\mathbf{k})$ -matrix, $\langle \mathbf{k} | \Gamma_C | \mathbf{k}' \rangle$, to be:

$$\Gamma_1(\mathbf{k}) = \begin{cases} 0 \\ \langle \mathbf{k} | \Gamma | \mathbf{k} \rangle + \langle \mathbf{k} + \mathbf{c}^* | \Gamma | \mathbf{k} + \mathbf{c}^* \rangle \end{cases} \quad (97)$$

Since this holds for any of the 4 residues, subscripts and overbars have been dropped. Obviously, the eigenvalues are periodic in the single zone. With the residue possessing no negative eigenvalue, the sign of the resonance term is that of the denominator, i.e. it is *repulsive*. As a consequence, if the Hamiltonian minus $\tau(k_b)$ is dominated by *one* of the resonance terms, e.g. due to a small denominator, that term will repel *one* of the two xy bands, and leave *the other* band *unperturbed*.

Examples are seen on the 1st line to the right in Fig. 26: Where a resonance peak exists in one of the \widetilde{xy} bands, there is merely a tiny peak or shoulder in the other band. Taking, first, the resonance peak as the one caused by the blue xz valence band near $k_c = 0.75$ for $k_b = 0.225$ or 0.250 , the parts relevant for the blue δ_{xz} -perturbation on the 2nd line to the left, $\frac{\langle \mathbf{k} | \Gamma_V | \mathbf{k} \rangle}{\tau(k_b) + \sqrt{A^2(\mathbf{k}) + G^2(\mathbf{k})}}$ and $\frac{\langle \mathbf{k} + \mathbf{c}^* | \Gamma_V | \mathbf{k} + \mathbf{c}^* \rangle}{\tau(k_b) + \sqrt{A^2(\mathbf{k}) + G^2(\mathbf{k})}}$, are those near $k_c = 0.75$ and -0.25 . The closeness of the black and blue curves confirms that the Hamiltonian is, in fact, dominated by this *one* resonance term. Next, we go to $k_b = 0.275$ where the \widetilde{xy} bands are located just below the bottom of the C bands. The peak in the upper band caused by the repulsion from the V-band edge can still be seen to the right in the top line near $k_c = 0.75$, but the nearby C-band edge repels the lower band much further. In fact, it is now the upper band which is the flatter and has an energy near the upper red xy band. The closeness of the black and blue

curves on the 2nd line to the left confirms that the Hamiltonian is dominated by the xz -band resonances, with a minor, peak-shaped contribution from the V band near $k_c = 0.75$ and a major, contribution with the shape of a canine tooth from the C band near $k_c = -0.25$.

This behavior is also clearly seen in the band structures Figs II 22 and 24) along the ZY and WA lines as was described in Sect. II XI. This could be another reason for the "non-linearity" seen in Fig. 31.

We now return to study the \mathbf{k} -dependence of the matrix elements of the residues $\Gamma(\mathbf{k})$ (96):

Since translation of \mathbf{k} by \mathbf{c}^* yields:

$$\widehat{\mathbf{c}^*} \langle \mathbf{k} | \Gamma | \mathbf{k} \rangle = \langle \mathbf{k} + \mathbf{c}^* | \Gamma | \mathbf{k} + \mathbf{c}^* \rangle, \quad (98)$$

the two diagonal elements with \mathbf{k} in the single zone reduce to *one* real-valued function with \mathbf{k} running over the double zone. For the purely imaginary off-diagonal element:

$$\begin{aligned} \widehat{\mathbf{c}^*} \langle \mathbf{k} | \Gamma | \mathbf{k} + \mathbf{c}^* \rangle &= \langle \mathbf{k} + \mathbf{c}^* | \Gamma | \mathbf{k} \rangle = \\ \langle \mathbf{k} | \Gamma | \mathbf{k} + \mathbf{c}^* \rangle^* &= -\langle \mathbf{k} | \Gamma | \mathbf{k} + \mathbf{c}^* \rangle, \end{aligned} \quad (99)$$

i.e. it is an anti-periodic function of \mathbf{k} .

In Fig. 26 on the 4th line to the right we show the residue matrix $\Gamma_C(\mathbf{k})$ with the diagonal element in light blue and the off-diagonal element in light grey. The former, \mathbf{k} -conserving perturbation of the $xy(\mathbf{k})$ band via the xz C band proceeds mainly through the $|\mathbf{k}\rangle$ character of the latter, and is therefore expected to be strong where this character, U_C^2 [see Eq. (91)] dominates, and weak where the complementary $|\mathbf{k} + \mathbf{c}^*\rangle$ character dominates. The shape of the light blue $\Gamma_C(\mathbf{k})$ curve should therefore correlate with the light blue U_C curve on the 3rd line above it, and also with the k_c -extent of the light-blue xz C band shown to the left on the 3rd line. Remembering (Fig. 16) that the pure $xz(\mathbf{k})$ and $xz(\mathbf{k} + \mathbf{c}^*)$ bands have their *maxima* for respectively odd and even values of $k_c - k_b$, i.e. for k_c near respectively -0.75 and 0.25 , the $|\mathbf{k}\rangle$ character of the xz C band dominates around -0.75 , and the $|\mathbf{k} + \mathbf{c}^*\rangle$ character dominates around 0.25 , both in windows of width 1. This is as expected. However, using the same argument for the shape of the grey, anti-periodic curve showing the matrix element which mixes the $xy(\mathbf{k})$ and $xy(\mathbf{k} + \mathbf{c}^*)$ bands via the xz C band, would make us expect zeroes near -0.75 and 0.25 , which do *not* occur.

This is even worse for $\Gamma_V(\mathbf{k})$, whose diagonal and off-diagonal elements are shown in respectively dark blue and dark grey on the 4th line to the left. Since the k_c -positions of the *minima* of the pure $xz(\mathbf{k})$ and $xz(\mathbf{k} + \mathbf{c}^*)$ bands are shifted by 1 from those of their maxima, we would expect the blue $\Gamma_V(\mathbf{k})$ and $\Gamma_C(\mathbf{k})$ curves to have the same shapes and to be merely shifted by 1. But clearly, $\Gamma_V(\mathbf{k})$ is more complicated; in particular, near $k_c = 0.5$ where the dark-blue U_V curve makes us expect a broad maximum, $\Gamma_V(\mathbf{k})$ has a minimum dropping to zero.

The pitfall in our reasoning is that it has substituted the hybridization elements $\langle xy; \mathbf{k} | H | xz_C(\mathbf{k}) \rangle$ and $\langle xz_C(\mathbf{k}) | H | xy; \mathbf{k} + \mathbf{c}^* \rangle$ in Eq. (96) by overlaps.

We must therefore disentangle the effects of the two xz -to- XZ and XZ -to- xz , i.e. forwards and backwards hopping integrals, whose Bloch-summed average $A(k_c - k_b)$ and difference $G(k_c - k_b)$ are given by Eq. I(38), from those of the many xy - xz and xy - XZ hopping integrals, whose Bloch-summed averages $\alpha(\mathbf{k}) + a(\mathbf{k})$ and differences $\gamma(\mathbf{k}) + g(\mathbf{k})$ are given by Eq.s I(39). Remember, that the averages conserve \mathbf{k} and $\mathbf{k} + \mathbf{c}^*$, while the differences mix them!

The C&V-band eigenfunctions, $|xz_C\rangle$ and $|xz_V\rangle$, are linear combinations of $|xz; \mathbf{k}\rangle$ and $|xz; \mathbf{k} + \mathbf{c}^*\rangle$ specified by a unitary matrix whose elements, given by Eq.s (90)-(91) in terms of A and G , are shown as functions of k_c to the right on the 3rd line of Fig. 26 with U_C and U_V in respectively light and dark blue, and with sU_C and sU_V in respectively light and dark grey. The squares of the blue curves give the probabilities that at \mathbf{k} , the $|xz; \mathbf{k}\rangle$ character is in respectively the light-blue C- or the dark-blue V band, or equivalently, that the C-band character is in respectively the $xz(\mathbf{k})$ or $xz(\mathbf{k} + \mathbf{c}^*)$ band, or equivalently, that the V-band character is in respectively the $xz(\mathbf{k} + \mathbf{c}^*)$ or the $xz(\mathbf{k})$ band. The grey lines are the numerical values, sU_C and sU_V , of the two other elements. Note that where the mixing between $|xz; \mathbf{k}\rangle$ and $|xz; \mathbf{k} + \mathbf{c}^*\rangle$ vanishes, s switches between $+$ and -1 , and where sU_C jumps, U_V vanishes with a kink, and vice versa. As a consequence, $sU_C U_V$ is everywhere smooth.²

The transformation of the six-band Hamiltonian from the $\{|\mathbf{k}\rangle, |\mathbf{k} + \mathbf{c}^*\rangle\}$ - to the V&C representation results in the Hamiltonian (92) whose first two columns contain the expressions needed in Eq. (96) for the hybridization matrix elements in terms of the Bloch sums I(39) of the average hopping integrals, $\alpha + a$, and their dimerizations, $\gamma + g$. These expressions are the only ones from where the xy - xz hoppings enter the two-band Hamiltonian. Our naive expectations for the shapes of the $\Gamma_C(\mathbf{k})$ and $\Gamma_V(\mathbf{k})$ curves on the 4th line were equivalent to the assumption that $\alpha(\mathbf{k}) + a(\mathbf{k})$ is fairly constant and $\gamma(\mathbf{k}) + g(\mathbf{k})$ negligible. On the 5th line of Fig. 26, we now show the correct hybridization elements:

$$\langle xy; \mathbf{k} | H | xz_V \rangle = (\alpha + a) U_C \pm (\gamma + g) sU_V \quad (100)$$

with the upper in light blue to the right and the lower in dark blue to the left. Squaring these curves yields the blue ones directly above on the 4th line. Those latter are the diagonal elements of the residues. Since $sU_C U_V$ is smooth, so are the curves on the 4th line.

The diagonal element, $\langle \mathbf{k} | \Gamma_C | \mathbf{k} \rangle = |\langle xy; \mathbf{k} | H | xz_C \rangle|^2$, of the *conduction*-band residue is reasonably constant in the k_c -interval $(-1.25 | -0.25) = (0.75 | 1.75)$ where U_C dominates, and is small outside. A minor exception is that $\langle \mathbf{k} | \Gamma_C | \mathbf{k} \rangle$ dips to zero near the 0.75-edge due to a zero of $\langle xy; \mathbf{k} | H | xz_C \rangle$ which, itself, is caused by a zero of $(\alpha + a) - (\gamma + g)$ [see Eq. (101) and the purple and

turquoise lines on line 6]. This vanishing of the C-band repulsion is what allows the peak from the V band to be seen on the 1st line, even for $k_b = 0.275$ when the \widetilde{xy} bands are far away from valence band. For k_c increasing inside the U_C window, the light-blue $\langle xy; \mathbf{k} | H | xz_C \rangle$ on the 5th line rises to a broad, 90-meV tall peak, which is near $k_c = -0.5 = 1.5$ when $k_b = 0.275$, and develops into a window-filling plateau when $k_b = 0.225$ and the \widetilde{xy} bands are far away from the C band. We also see the k_c -position of the window shifting with k_b .

In contrast to this simple behavior, the dark-blue *valence*-band residue, $\langle \mathbf{k} | \Gamma_V | \mathbf{k} \rangle = |\langle xy; \mathbf{k} | H | xz_V \rangle|^2$ shown on the 4th line, drops to zero near -0.1 and 0.5 inside the interval $(-0.25 | 0.75)$ where U_V dominates. This was noted before, and the reason is now seen on line 5 to be zeroes of $\langle xy; \mathbf{k} | H | xz_V \rangle$ which are, themselves, caused by zeroes of $\alpha + a$. This is confirmed by the shapes of the $\alpha + a$ and $(\alpha + a)U_V$ curves shown to the left on the bottom line in respectively purple and black. The third zero of $\langle xy; \mathbf{k} | H | xz_V \rangle$ is outside the U_V -window and near $-0.85 (=1.15)$. It is caused by a zero of $\gamma + g$ as shown in turquoise on the bottom line to the right. For k_c decreasing below $-0.85 (=1.15)$, $\langle xy; \mathbf{k} | H | xz_V \rangle$ rises linearly to a sharp, 90 meV high peak at the V-band edge near $-1.25 = 0.75$. It is initially caused by the term $-(\gamma + g)sU_C$ in the lower Eq. (100) shown in black on row 6 to the right, but is subsequently taken over by $(\alpha + a)U_V$ shown to the left.

The peaks due to resonances with the xz bands occur near the xz -band edges. Exactly at the edges, $U_C = U_V$, and the \mathbf{k} -conserving part of the residues therefore takes the values:

$$\langle \mathbf{k} | \Gamma_V | \mathbf{k} \rangle = \frac{1}{2} [(\alpha + a) \pm s(\gamma + g)]^2. \quad (101)$$

The magnitudes and signs of $\alpha + a$ and $\gamma + g$ shown in respectively purple and turquoise on the 6th line, cause the Γ_V coupling at the $k_c = 0.75$ edge (where $s = -1$) and the Γ_C coupling at the $k_c = -0.25$ edge (where $s = 1$) to be much stronger than the two others, i.e. than the Γ_V coupling at -0.25 and the Γ_C coupling at 0.75 , which even has a "hole" here. This is exactly the behavior of the blue peaks seen on the 2nd line to the left.

We finally come to the grey, off-diagonal elements, $\langle \mathbf{k} | \Gamma | \mathbf{k} + \mathbf{c}^* \rangle$, on the 4th line. They are -roughly speaking- anti-periodic (99) versions of the double-periodic blue, diagonal elements. On the 5th line, grey curves are shown to the right for the upper expression (100) and to the left for the lower expression, both with k_c translated by 1. Keeping in mind, that under this translation, Greek lettered functions are invariant (I 41), Latin-lettered functions change sign (I 42), and U_C and U_V are exchanged (91), the grey curves to the right and to the left on the 5th line equal respectively $-is \langle xz_C | H | xy; \mathbf{k} + \mathbf{c}^* \rangle$ and $is \langle xz_V | H | xy; \mathbf{k} + \mathbf{c}^* \rangle$. The grey off-diagonal elements of the residues on the 4th line are therefore simply $\pm is$ times the products of the blue and grey curves shown vertically below on the 5th line.

The reason why on the 4th line the grey $\langle \mathbf{k} | \Gamma_V | \mathbf{k} + \mathbf{c}^* \rangle$ to the left is far more wiggly than the grey $\langle \mathbf{k} | \Gamma_C | \mathbf{k} + \mathbf{c}^* \rangle$ to the right, is that not only does the former possess the two "extra" zeroes from $\alpha + a$ near -0.1 and 0.5 , as well as the one from $\gamma + g$ at -0.85 , but also those translated by 1 , i.e. those near -0.5 , 0.9 , and 0.15 .

These very different k_c -dependencies seen on the 4th line of the blue $\langle \mathbf{k} | \Gamma_C | \mathbf{k} \rangle$ and $\langle \mathbf{k} | \Gamma_V | \mathbf{k} \rangle$ curves, and of the grey $\langle \mathbf{k} | \Gamma_C | \mathbf{k} + \mathbf{c}^* \rangle$ and $\langle \mathbf{k} | \Gamma_V | \mathbf{k} + \mathbf{c}^* \rangle$ curves, i.e. of the conduction- and valence-band residues, are the causes of the strong asymmetry of the perpendicular dispersion and splitting of the metallic bands around the center of the gap.

6. xy - xz and xy - yz hopping integrals

The purple $\alpha + a$ and turquoise $\gamma + g$ Bloch sums I (39) shown on the bottom line are determined by the hopping integrals, a_n , g_n , α_n , and γ_n , computed as matrix elements I (9) of the LDA Hamiltonian between n th-nearest-neighbor xy and xz (or XZ) WOs (see Fig. I 9) with the results given in Table I (46). Specifically, the integrals for hopping between xy and XZ WOs on *different* sublattices are $a_n \pm g_n$. Here, a_1 is the average of- and g_1 half the difference between the integrals for hopping from xy at the origin to XZ on the neighboring ribbon, inside or outside the same bi-ribbon, i.e. to XZ at respectively $-0.012\mathbf{a} - 0.5\mathbf{b} + 0.467\mathbf{c}$ and $-(0.012\mathbf{a} - 0.5\mathbf{b} + 0.533\mathbf{c})$; similarly for a'_1 and g'_1 , except that the XZ orbital is translated by \mathbf{b} . For a_2 and g_2 , the XZ WO is translated by $-2\mathbf{b}$, and for a'_2 and g'_2 , by $2\mathbf{b}$. For the Greek-lettered hopping integrals, the two orbitals are on the *same* sublattice. Specifically, the integrals for hopping from xy at the origin to xz at $\pm\mathbf{b}$ are $\alpha_1 \pm \gamma_1$, to xz at $\pm\mathbf{c}$ are $\alpha_2 \pm \gamma_2$, to xz at $\pm(\mathbf{c} + \mathbf{b})$ are $\alpha_3 \pm \gamma_3$, and to xz at $\pm(\mathbf{c} - \mathbf{b})$ are $\alpha'_3 \pm \gamma'_3$. Calling γ an electronic dimerization is really a misnomer, because the reason for its existence is simply the difference of relative orientation of the two orbitals. Finally, α_0 is the xy - xz on-site (crystal-field) term.

The parameters dominating the behavior of the $\alpha + a$ Bloch sum are: the integral for hopping between the xy and XZ nearest-neighbor WOs, $a_1 = -49$ meV, and the crystal-field term, $\alpha_0 = 31$ meV. Had the former been the only non-vanishing parameter in the $\alpha + a$ Bloch sum, the corresponding term, $2a_1 \cos \pi(k_c - k_b)$, would have killed the peak from the valence-band resonance at $|k_c - k_b| = \frac{1}{2}$. So, clearly, this peak –convincingly observed with ARPES– is sensitive to the value of the crystal-field term caused by the ribbon-inversion (see Sect. I III A) and to the details of the xy - XZ and xy - xz hoppings. Note that none of these parameter values were adjusted to fit the ARPES.

7. Synthesis

From the bottom four lines in Fig. 26 we have seen that the k_c -dependencies of the A , G , $\alpha + a$, and $\gamma + g$ Bloch sums of the xz - xz and xy - xz hopping integrals change relatively little for k_b in the $\pm 10\%$ range around $k_F = \frac{1}{4}$.

By far the strongest k_b -variation of the black \widetilde{xy} bands displayed on the top two lines is the one coming from the denominators of the four resonance terms via $E \approx \tau(k_b)$, to be seen on the 3rd line to the left, in combination with the very different shapes of the V- and C-band residues seen on the 4th line to respectively the left and the right.

What makes the blue resonance peak caused by the edge of the xz V band –seen on the 2nd line to the left near $k_c = 0.75$ – differ in shape from the (unhybridized) blue canine-tooth resonance near $k_c = -0.25$ caused by the edge of the xz C band, is the zero of the purple $\alpha + a$ near $k_c = 0.5$ seen on the bottom line. This zero is a bit inside the frame of the U_V window ($-0.25|0.75$) and therefore "cuts a hole" in Γ_V on the low- k_c side of the resonance, which is thereby sharpened up (see the blue curves to the left on the 4th line). Nothing like this happens for Γ_C near $k_c = -0.25$, because the zero of $\alpha + a$ near -0.1 is outside the U_C window ($-1.25|-0.25$). Hence, it is the shape of the canine tooth which is the simpler!

On the other hand, as seen for $k_b = 0.275$ on the 1st line to the left, the backside of the tooth at $k_c = -0.25$ reaches across the ZB at -0.5 , where it is crossed symmetrically by the backside of the $\widetilde{xy}(\mathbf{k} + \mathbf{c}^*)$ -band tooth caused by the resonance with the yz C band at -0.75 . To the right and in black, we now see that strong $(\mathbf{k}, \mathbf{k} + \mathbf{c}^*)$ -hybridization around -0.5 merges the canine teeth in the lower band at -0.75 and -0.25 , thus resulting in a 60-meV splitting of the two \widetilde{xy} bands.

We can go back and compare with what happens for $k_b = 0.225$. Here, we see on the 2nd line to the left that the blue resonance peak at 0.75 is so sharp, that it hardly reaches the ZB at 0.5 and therefore hardly overlaps the peak at 0.25 in the $\widetilde{xy}(\mathbf{k} + \mathbf{c}^*)$ band (seen above on the 1st line) from the yz valence band. Moreover, the hybridization at the zone boundary ZB is much weaker than for $k_b = 0.275$ (black curves to the right on the 2nd line) so that it merely leads to the formation of a bulge in the lower band, 35 meV below the minimum in the upper band between its resonance peaks (1st line to the right).

The zero of the purple $\alpha + a$ near $k_c = 0.5$ which sharpens the peaks from the V bands, also makes the V bands (dark blue and dark green on line 3) contribute nothing to the $(\mathbf{k}, \mathbf{k} + \mathbf{c}^*)$ -hybridization at the ZB. The hybridization, therefore, comes exclusively from the C bands and from the dimerization, u , of the direct, perpendicular hops (red curves to the right on the 2nd line). The blue and the green –equally large– contributions each have a residue given by the value at $k_c = 0.5$ of the grey curve to the right on line 4. For k_b increasing from 0.255 to 0.275 , this value increases from 2500 to 3500 meV² and thereby enhances the dominating effect of the decreasing denominator. Since from Eq.s (95), (96),

and the upper (100): $\Gamma_C(k_b, 0.5) = -\Gamma_C(k_b, -0.5) = (\alpha + a)_{-0.5}(\gamma - g)_{-0.5} = (\alpha + a)_{-0.5}(\gamma + g)_{0.5}$, the increase comes from $\gamma + g$.

Finally, we shall explain why around $k_c=0$ the *lower* band is so flat, more than the upper band, and why with increasing k_b this flatness increases and its range decreases.

But first, we will explain why the repulsion of the *upper* \widetilde{xy} band by the C band increases far less with k_b than expected from the decrease of the denominators (3rd line, left). The reason is found on lines 4 and 6: For the upper band near $k_c=0$ –which is the $\widetilde{xy}(\mathbf{k} + \mathbf{c}^*)$ band and, hence, the $\widetilde{xy}(\mathbf{k})$ band near ± 1 – the light-blue C-band residue, $\Gamma_C(k_b, k_c \sim \pm 1)$, decreases by a factor 4 for k_b increasing from 0.225 to 0.275, mainly because [see Eq. (100)] the purple $\alpha + a$ decreases by almost a factor 2. This trend is furthermore enhanced by a non-vanishing repulsion from the V band whose dark-blue residue near $k_c=\pm 1$ hardly changes with k_b and thus becomes more important when $\Gamma_C(k_b, \pm 1)$ is small.

The reason why around $k_c=0$ the black lower \widetilde{xy} band runs parallel to the red xy band is (see line 2 to the left) that the repulsions from the blue xz and the green yz V bands disperse in opposite directions away from $k_c=0$, whereby their effects on the dispersion cancel. The reason why the distance of the black band above the red band as well as the k_c -extent of its flat part decreases with increasing k_b , is the same as the reason why the blue resonance peak near $k_c=-0.25$ is much smaller than the one near 0.75, namely: that for the dark-blue V-band residues on the 4th line $\Gamma_V(k_b, -0.25)$ is much less than $\Gamma_V(k_b, 0.75)$, and this –in itself– is because the zero of $\alpha + a$ at $k_c=-0.1$ is closer to -0.25 than the zero at 0.5 is to 0.75 (purple curves on line 6). As we now –with k_b increasing– move up in the metallic bands, the V-band perturbation decreases due to the increasing energy denominator and –as the C band is approached– canine teeth growing near $k_c=-0.25$ and 0.25 limit the region over which the lower band is flat.

We conclude that the remarkable asymmetry between the contributions from the V&C bands to the k_c -dispersion and splitting of the \widetilde{xy} bands in the gap, is mainly due to the difference between the positions of the V&C bands with respect to the structure in the \mathbf{k} -conserving $\alpha + a$ Bloch sum of the xy - xz hopping integrals. Specifically, the zero of $\alpha + a$ near $k_c=0.5$ is inside the region where the V band is formed by the $xz(\mathbf{k})$ band –and the C band by the $xz(\mathbf{k} + \mathbf{c}^*)$ band [see see dark- and light-blue curves in the figures to the right on line 3]– and not the other way around.

C. Constant energy contours

On the left-hand side of Fig. 27, we show the upper (a), the lower (b), and both (c) metallic \widetilde{xy} bands in the gap, which extends from -218 meV to $+218$ meV, as functions of (k_b, k_c) in the stripe $0.225 \leq k_b \leq 0.275$

and $0 \leq k_c \leq 1$. From the description at the beginning of Sect. XIV B, we recognize the development of the bands –for k_b increasing– from having strong, upwards-pointing resonance peaks near $k_c=0.75$ and 0.25 in the upper band (a), plus a small downwards bulge around $k_c=0.5$ in the lower band (b), over having reduced peaks plus a wider and deeper bulge –and minimal width– near midgap, to having strong, downwards-pointing resonance peaks (canine teeth) connected by a large bulge in the lower band, plus reminiscences of the upwards-pointing resonance peaks in the upper band. The splitting between the two bands (c) is smallest at $k_c=\text{integer}$ where the $|\mathbf{k})$ and $|\mathbf{k} + \mathbf{c}^*)$ characters cannot mix and where the direct and indirect hoppings work in opposite directions.

In (d), we show the constant energy contours (CECs) for k_b positive and energies ranging from 100 meV below– to 100 meV above the Fermi level which is, itself, 75 meV above the center of the gap. For $E - E_F = -100$ meV, we recognize from the LDA-TB part of Fig. II 20, two notches pointing towards Z in the inner sheet and, in the outer sheet, a bulge centered at the ZB, $k_c=0.5$. As the energy increases, so does the distance between the bulge and the inner sheet, the notches shrink, and new notches develop in the outer sheet, on either side of the bulge, and pointing towards Y and Y'. It is obviously the resonance peaks pointing ^{upwards} in the ^{upper} band which give rise to the notches pointing towards _{Y&Y'} in the _{inner} sheets. Along ΓY ($k_c=\text{integer}$), the two sheets are in near contact.

Since the quasi-1D bands disperse far more along k_b than along k_c , the shape of two CECs in (d) resembles that of the two energy bands in Fig. 25 or in Fig. 26 on the 1st line, to the right. The $E \leftrightarrow k_b$ scaling is approximately: $dE = -\tau'(k_b) dk_b$, with $\tau'(k_b)$ being the dominating part of the Fermi velocity (I 48). This resemblance is less good close to the edge of the C- or the V-band where the hybridization with the edge makes the two bands and the two CECs behave differently: Whereas one band remains undistorted, the other gets repelled [see Eq. (97)] and, eventually, fuses with the CECs of the edge [see Fig. II 20].

If we interpret a CEC as a doped FS, an energy increase of 50 meV corresponds to a 4% increase of the electron doping, and the undoped FS is the CEC whose k_b averaged over k_c equals $\frac{1}{4}$.

We shall now analyze the ARPES data for energies closer to the Fermi level than the 0.15 eV studied in Paper II and identify further features of the theory discussed above.

XV. EXPERIMENTAL FS AND VELOCITIES AND COMPARISON WITH THEORY

In this section we describe our analysis of the ARPES data taken from the intensity cube $I(E, \kappa_b, \kappa_c)$. Fig. 28 shows the FS obtained from sample H at $T=6$ K measured at the two photon energies $h\nu=30$ eV and 33eV,

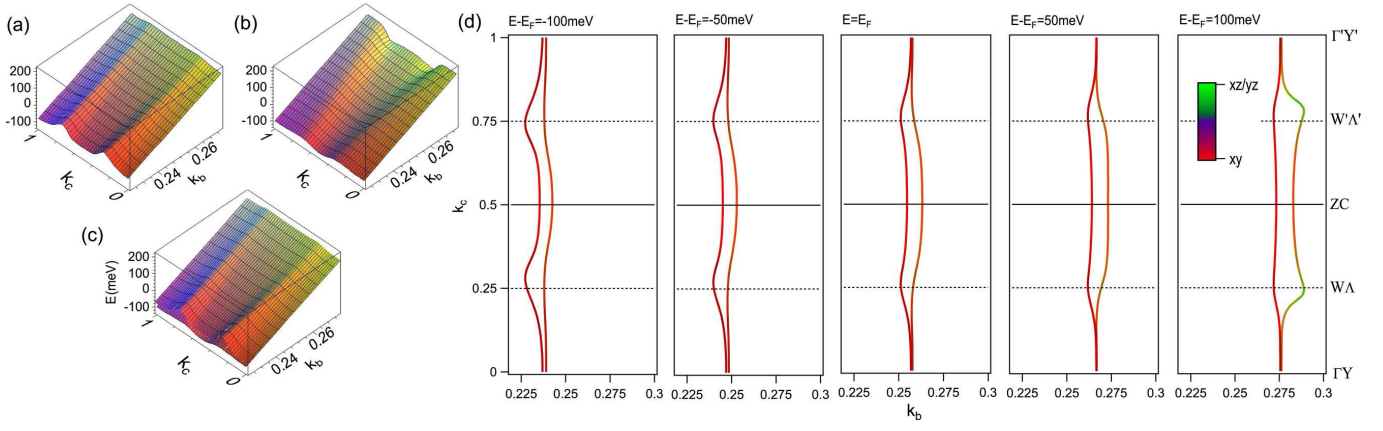


FIG. 27: **(a)-(c)**: The two quasi-1D bands in the gap for the six-band Hamiltonian (56) with the ARPES-refined parameter values I (43)-(47). The \mathbf{k} -space region considered is the stripe $\pm 10\%$ around k_{Fb} in the upper half of the 1st and the lower half of the 2nd BZ, $0 \leq k_c \leq 1$. The energies of the upper **(a)**, the lower **(b)**, and both metallic bands **(c)**, relative to the center of the gap, defined as 0. $E_F = 75$ meV above the center. **(d)**: CECs calculated by tracing the roots of the secular determinant $|H(k_a, k_b) - E|$. The colors indicate the orbital characters of the bands. The notches in the inner sheet point to Z and those in the outer sheet to Y and Y' (see FIG.s 11 and 20 in Paper II). The CECs have been *compressed* by a factor 3.3 along k_c in order to make their warping visible. The ratio between the warping $\delta k_{i_{Fb}}$ of each (inner or outer) FS sheet and $k_{Fb} \sim 0.25$ is ~ 0.02 . This is ~ 5 times more than without the resonant coupling to the V&C bands (see red bands for $k_b = 0.25$ in FIG.s 25 and 26).

which correspond to $\kappa_a = 6.3$ and 6.6 , respectively, and from sample G with $h\nu = 30$ eV, $\kappa_a = 6.3$. A FS consists of the four values (left and right, inner and outer sheets) of the Fermi-momentum κ_{Fb} as a function of κ_c when the dispersion with κ_a is neglected. Also, the κ_b -projected Fermi-velocity will be extracted as a function of κ_c . Before presenting and discussing the data in relation to our theory, we discuss the challenges and issues we are facing and explain the method we are using.

A. Challenges, issues, and methods used for the Fermi-surface determination

1. LiPB-specific issues

As explained in detail in Sect. II IX, the ARPES intensities from the six t_{2g} ($m = yz, xz, xy$) bands in LiPB display fine- and coarse-grained variations.

While the two subbands of a given m are periodic in the single zone, the fine-grained intensity modulation considered in Sect. II IX B 1 follows the $|\mathbf{k}|$ -character, apart from the nearly canceling phase shifts from the inversion and displacement dimerizations. It is therefore almost periodic in the double zone (FIG.s II 11, 12, and 13), as if the ribbons had been translationally equivalent (Sect. I III A) with the intensity from the lower m -band in the 1st zone and the intensity from the upper m -band in the 2nd zone. Due to the dimerization of the ribbons, the m -band is gapped at the physical zone boundary and the shift from one subband to the other of the dominating $|\mathbf{k}|$ -character takes place over a *region* around this boundary. This was illustrated in the bottom part of

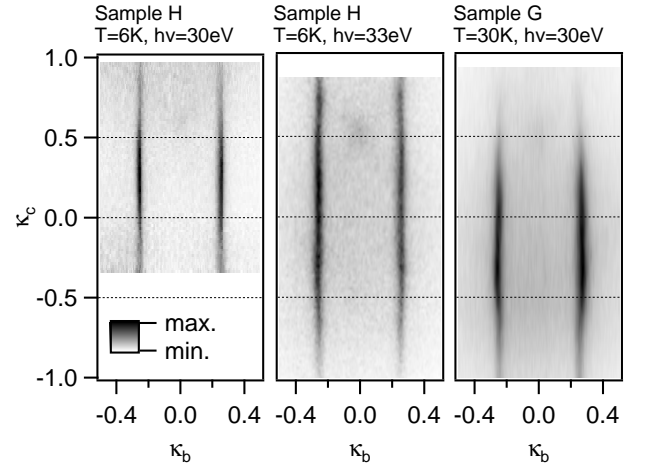


FIG. 28: Three Fermi-surfaces out of the data which we use in the following analysis. The two first (similar to FIG. II 19) are from a sample H at $T = 6$ K measured at two photon energies $h\nu = 30$ eV and 33 eV, corresponding to $\kappa_a = 6.3$ and 6.6 , respectively. The last is from a sample G with $h\nu = 30$ eV, $\kappa_a = 6.3$. The figures have been *stretched* along κ_c by a factor 1.7; compare with FIG.s II 11 and 20 (b), which are to scale.

Fig. II 14 for $k_b = 0.225$ and we now repeat this in Fig. 29, but only for $k_b = 0.245$ and the two \tilde{xy} -bands, i.e. those with energies less than ~ 100 meV below E_F . The tilde and the dark-red color indicate that these xy -like bands are hybridized with the valence(V)- and conduction(C)- xz - and yz -bands which give rise to the peak-, bulge-, and near-contact features first mentioned in Sect. XIV B 1. The 2nd zone extends from $k_c = -1$ to -0.5 and from 0.5

to 1, with the 1st zone inserted between them, from -0.5 to 0.5 . Only near the zone-boundaries, $k_c = \pm 0.5$, does ARPES see both bands of which the lower has a large bulge whose minimum is split from the upper minimum by as much as 50 meV. The near contact between the two bands [sheets in Fig. 27 (d)] at k_c integer is not directly seen in ARPES, because here, one of the bands (sheets) is extinguished, the upper band (inner sheet) at even k_c and the lower band (outer sheet) at odd k_c . The resonance peaks in the upper band are clearly seen at $|k_c| = 0.76$.

Since without the fine-grained ARPES intensity modulation, each band is periodic in the single zone (see Figs 25 and 26 top line to the right), symmetrization of the ARPES bands around the zone boundaries enabled us in Paper II to reconstruct the dispersions continuously (Figs II 20 and II 21). However, with $\hbar\nu = 30$ eV, the coarse-grained intensity of the \tilde{xy} -bands falls off rapidly for $\kappa_c > 0.5$, and this made it difficult, but –thanks to the fine-grained modulations– not impossible to detect the resonance peaks in the upper band [see Fig. II 24(c2)]. Later, we realized that the spread of the Wannier orbital onto several molybdenums makes the coarse-grained intensity sensitive to the photon energy, which can therefore be chosen to yield good visibility over a sufficiently wide range of κ_c and to produce cancellation between the inversion- and displacement phase shifts.

The ARPES intensity from the inner and outer sheets of the FS behaves like the intensity for respectively the upper and lower \tilde{xy} -bands, as we shall see in Fig. 32. For extracting the FS, our present method to be described below, however fails near the zone boundaries because we have no good symmetrization scheme unlike for the bands. We can merely *estimate* the splitting at the boundary from the so-called Sparrow criterion used in astronomy [82]

To set the scale, we first recall from the theoretical FS in Fig. 27 (d) that even at $k_c = 0.5$, the k_b -splitting between the inner and outer sheets amounts to merely $0.01b^*$, i.e. to 2% of the distance between the left and right-hand FS sheets. The experimental Fig. 28 shows both left- and right-hand sheets and, here, the inner and outer sheets cannot be distinguished because the momentum-distribution widths of the two spectral functions of the bands are larger than their splitting (see Sect. II XC 2). However, already in the data, we see a slight wrinkle at $\kappa_c = \pm 0.5$ caused by the shift of intensity from one band to the other.

There is a second issue specific to LiPB; it is a quasi-1D material and, at high enough temperatures, manifests a TL-like spectral function with a broad spinon edge feature and a somewhat sharper holon peak feature [3, 18, 78]. For the data here, the momentum integrated EDCs around k_{Fb} gave a power-law like line-shape. Although the LiPB ARPES lineshape is well described by the TL spectral function at high temperature, the spectra do not sharpen as much as expected in the theory [78]

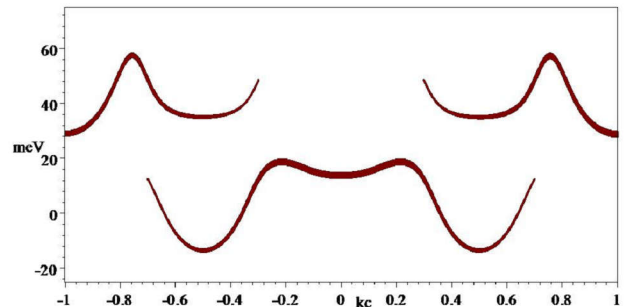


FIG. 29: The \tilde{xy} bands in the double zone for the two-band Hamiltonian (95) with ARPES-refined TB parameters, like in the bottom panel of Fig. II 14, but only for the dark-red \tilde{xy} bands, for $k_b = 0.245$, and on an extended energy scale with the upper frame at the Fermi level (75 meV). The fatness is proportional to the fine-grained band-factor ARPES intensity because for our particular case of $\kappa_a = 6.6$, the dimerization phase shift, η II (70), is negligible in the k_c -region of interest (see Fig. II 12).

at low temperature⁵. Therefore our specific procedure, described below, follows a route in which no theoretical spectral function is forced onto the experimental data.

2. General issues

Note that the change of momentum in κ_b , visible in Fig. 28, is small - we will see that it is in the range of 0.01 which translates to the experimentally very demanding range of 0.012\AA^{-1} using the solid-state definition (ssd) of reciprocal space (see Sect. III of Paper I). For our measurements, that is about the size of two detector pixels. We will see that it is very well possible to extract such a *relative* change from the ARPES data by our method. Nevertheless, one has to care about the *absolute* values of the extracted momentum in order to determine the FS filling. Measuring the electrons' energy and momentum requires electro-optical lenses, slits, and a perfect potential landscape of the electrical field around the individual sample. As a result, for the experimental data, there are always distortions in momentum and energy⁶. In order to remove the distortions, after correction of the

⁵ It might be important here to remind again that, in the TL model, the Fermi momentum k_F remains well defined.

⁶ Restricting to momentum-space distortions and not distortions in the energy direction as well as only for distortions related to electro-optical lenses and slits, the distortions are larger for hemispherical analyzers and less for a momentum microscope, see Ref. 83. However, this is only true for perfect flat samples with perfect potential-landscape of the electrical field and not with cleaved samples.

energy distortion by the slit and conversion from angular space to \mathbf{k} -space with the canonical formulas (see, e.g., Ref. 79), we had to apply image corrections using for two energies⁷ the symmetry that the maximum of the occupied yz -band is along $\kappa_c + \kappa_b$ and maximum of the xz -band is along $\kappa_c - \kappa_b$, see Sect. I IV, Fig. I 8, and Fig. II 20. Fine corrections around the absolute momentum space were then done by the BZ-periodicity of the xz/yz bands. There is a limit to the extent to which our criteria above can be used to correct all distortions⁸. From our data, the error of having the yz and xz bands at 120° is about 0.5 degree (2 pixels in κ_b on the full length of $\Delta\kappa_c=2$). The determination of the absolute value of the Fermi-momentum and the filling is limited to a systematic error of about 1 % .

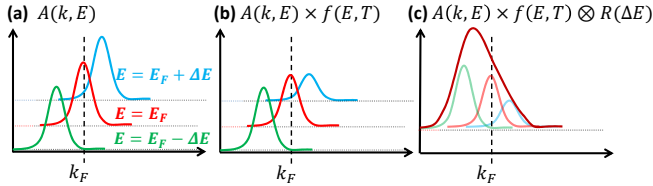


FIG. 30: Sketch to explain a masking effect hindering the Fermi-momentum determination when only considering the maximum of the MDC at E_F . (a) Shown are three MDC's for different energies as indicated around E_F . In (a), the spectral function give perfectly symmetric and Lorentzian-like MDC's. The combined effect of (b) the distribution function $f(E)$, and (c) convolution with the energy resolution $R(\Delta E)$ results in an asymmetric line-shape for the MDC at E_F (dark red in (c)).

In order to obtain the value of the Fermi-momentum, one may think that it suffices to determine the peak maximum of the MDC at E_F . In reality, the *exact* determination of the Fermi-momentum is an important issue warranting discussions to be found in e.g. Refs. 84–88. There are many intrinsic and extrinsic reasons not to determine the correct k_{Fb} . Particularly important for us is a masking effect in extracting the Fermi momentum which occurs rather generally and does not depend much on whether the sample is a Fermi-liquid, marginal Fermi-

liquid, or a TL-liquid. This effect is sketched in Fig. 30: Even if (a) the ARPES spectral function is perfectly symmetric and Lorentzian-like in the momentum direction, the combined effects of the distribution function (e.g. the Fermi function) (b) and the convolution with the experimental energy resolution (c), results in an asymmetric line-shape for MDC's for energies near $E_F \pm \Delta E$. Here, ΔE represents the experimental energy resolution, which for $h\nu=30$ eV is 16 meV (Sect. X C 2). Hence, the asymmetry causes the peak momentum to be *inside* the FS.

3. Method

With these considerations in mind, we now explain our methods. It is important to mention again that theory dictates that we cannot distinguish the two bands but obtain an average dispersion weighted by the ARPES band-factor intensity, the $|\mathbf{k}|$ -character shown in Fig. 29. This means that for $|\kappa_c| < 0.35$, we are mainly extracting the outer FS sheet (lower band) while for $0.65 < |\kappa_c|$, we mainly extract the inner sheet (upper band). Thus, like for the bands, the selection rule allows us to distinguish the two FS sheets, except near the zone-boundary, $|\kappa_c|=0.5$, where the intensity shifts from one band to the other. We first discuss, in Sect. XV A 3 a, what can be deduced for the zone-boundary situation, using the Sparrow criterion [82] to analyze the MDC widths. This exercise will bring out the fact that the experimental MDC widths greatly exceed the splitting that we wish to determine and thereby make clear the crucial role of the selection rule, which we exploit in Sect. XV A 3 b, using a so-called dispersion analysis, to determine the Fermi momentum as well as the Fermi velocity of separate branches.

a. Sparrow MDC peak-width analysis At the zone boundaries, $|\kappa_c|=0.5$, although we have no way to separate the inner and outer FS sheets, we can nonetheless estimate their possible splitting, as we now describe. As follows from the fine-grained intensity modulation of the two \widetilde{xy} -bands discussed in Sect. II IX B 1 and displayed in Fig. 29, the MDC at E_F for $\kappa_c=0.5$ (or -0.5) is an equally weighted combination of the Lorentzian-like⁹ MDC's of both sheets and, as the combination, has the measured total width $\Gamma_{MDC}^{\kappa_c=0.5}$. With this, we can use the so-called Sparrow criterion [82], which states that two identical, separated Lorentzians of the same width $\Gamma_{MDC}^{j=1} = \Gamma_{MDC}^{j=2}$ are indistinguishable if they add up to give a flat top with zero slope and curvature at their center of mass. These conditions allow computing a splitting ($\Delta\kappa_b$) as well as the width of the two Lorentzians ($\Gamma_{MDC}^{1/2}$) from the measured total width ($\Gamma_{MDC}^{\kappa_c=0.5}$). In fact, it will be an upper limit for the splitting and reads: $\Delta\kappa_b^{\kappa_c=0.5} = \Gamma_{MDC}^{\kappa_c=0.5} / \sqrt{3}$. The two Lorentzian have a

⁷ It has to be done at different energies in order to correct possible distortions in the (E, κ_b) - and (E, κ_c) - plane. In a hemispherical analyzer, these distortions are mainly dependent on the curve of the entrance slit but also on the positioning of the beam on the sample relative to the axis of the lens.

⁸ We will notice in Fig. 32 a remnant of trapezoidal distortion in the (κ_b, κ_c) -plane. This flaw could have been corrected by symmetry arguments, but careful thought shows that it does not help with the absolute determination of the Fermi-momentum to infinite exactness. We need a data set of equal BZ-zone size with a lower photon energy to have a better momentum resolution or a data set over more BZs. Also, the coarse-grain modulation would have to be absent.

⁹ Here, we use the standard definition of the Lorentzian with $I = \frac{A}{\pi} \frac{\Gamma/2}{(\kappa - \kappa_F)^2 + (\Gamma/2)^2}$.

width of: $\Gamma_{MDC}^j = \Gamma_{MDC}^{\kappa_c=0.5} \sqrt{3}/(1 + \sqrt{3})$. The results of this Sparrow analysis are given in Tab. I and also indicated by the diamonds in Fig. 32. From the table, by seeing that the measured MDC-widths at zone-boundary ($\Gamma_{MDC}^{\kappa_c=\pm 0.5}$) and zone-center ($\Gamma_{MDC}^{\kappa_c=0}$) are almost the same, we can already see that there is a limit to the determination of the splitting. The MDC's are obviously broad. This broadening is much more than the momentum resolution of the apparatus ($\Delta\kappa_b \approx 0.005$, see Sect. II X A). The broadening can be for different reasons. There is an *intrinsic* component by the spectral function of the corresponding electron liquid. In the case of a Luttinger-liquid, it is well known (see, e.g., Ref. 89) that the MDC's are typically sharper, and the EDC's are broader (when compared to a Fermi-liquid). However, there can also be an *extrinsic* component –by an experimental momentum resolution which is not produced by the apparatus alone but, for example, can be caused by the quality of the samples-surface and the so-called k_z -broadening [90, 91] that arises from the limited probing depth of the photoelectron. In general, it is hard and requires multiple experiments to distinguish the intrinsic and extrinsic components with full certainty. Looking at the widths for different samples, displayed in Tab. I, we can believe that there is a larger intrinsic component but also some extrinsic component.

We reiterate that the resulting separation estimate by the Sparrow criterion is an upper limit and the actual splitting has to be below the smallest splitting listed in Tab. I, resulting in $\Delta\kappa_b^{\kappa_c=0.5} < 0.017$. By taking advantage of the selection rule, we will see that this is indeed the case, and we note now that even this upper limit is considerably less than the magnitude of the experimental MDC width at $\kappa_c = 0$, where the selection rule applies and only one branch contributes.

Sample		$\Gamma_{MDC}^{\kappa_c=0.5}$	Γ_{MDC}^j	$\Gamma_{MDC}^{\kappa_c=0}$	$\Delta\kappa_b^{\kappa_c=0.5}$
H 6K,30 eV	+	0.030	0.0191	0.031	0.017
H 6K,33 eV	+	0.047	0.030	0.051	0.028
	-	0.044	0.028	0.051	0.025
G 30K,30 eV	+	0.060	0.038	0.052	0.035
	-	0.051	0.033	0.052	0.030

TABLE I: Result of the MDC peak-width analysis (compare also with Fig. 28). The 1st column gives the individual dataset, the 2nd indicates whether $\kappa_c=+0.5$ or $\kappa_c=-0.5$ was measured. Column 3 gives the Lorentzian-width Γ obtained by a line-fit and is averaged over both branches, at positive and negative κ_b . Column 4 gives the width of the two Lorentzian (Γ_{MDC}^j) at $\kappa_c=\pm 0.5$ according to the Sparrow criterion. The 5th is the Lorentzian-width at $\kappa_c=0$. The last column, finally, shows the upper limit for the separation in κ_b momentum ($\Delta\kappa_b^{\kappa_c=0.5}$) according to the Sparrow-criterion.

b. Dispersion Analysis The method used to extract the Fermi-momentum κ_{Fb} as a function of κ_c is basically to extrapolate the metallic ARPES band along κ_b for fixed κ_c to the Fermi level (Fig. II 21). The details are

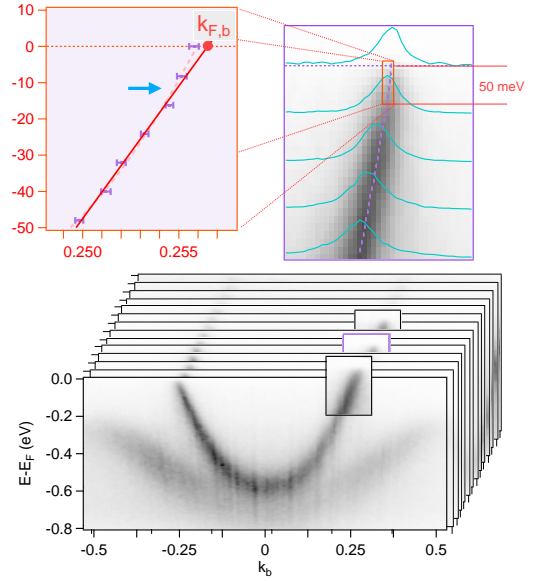


FIG. 31: Method used for the extraction of the Fermi-momentum. The experimental data set is sliced along the κ_c -direction (bottom). Each κ_c -slice can then be viewed as containing multiple so-called MDC's. The MDC's are intensity curves at fixed energy, dependent only on κ_b (see the magenta curves in the upper right as examples). Then, a line fit with a Lorentzian for all the MDC's between $E_F - 50$ meV and E_F was performed. The maximum of the Lorentzian defines the dispersion $E(\kappa_b, \kappa_c = \text{const.})$ (upper left). The Fermi-momentum κ_{Fb} is found by linear extrapolation in this interval between $E_F - 50$ meV and E_F (see red extrapolation line and red circle at k_{Fb} in upper left).

Sample	used κ_c -range	k_{Fb}^{avg}	Li-stoichiometry
H 6K,30 eV	0 ; 0.995	0.255 ± 0.006	1.02 ± 0.02
H 6K,33 eV	-0.785 ; 0.905	0.254 ± 0.005	1.02 ± 0.02
G 30K,30 eV	-0.824 ; 0.777	0.255 ± 0.008	1.02 ± 0.02
Average		0.255 ± 0.006	1.02 ± 0.02

TABLE II: Extracted absolute average Fermi-momentum k_{Fb}^{avg} (3rd column) and the Li-stoichiometry from the electron filling (last column). The 1st column identifies the dataset used, the 2nd column the span of κ_c over which the average was taken (cf. Fig. 32). The error given here is the error of determining the average and does not include the variation of $k_{Fb}(\kappa_c)$ with κ_c . The last column gives the Li-stoichiometry from the Luttinger count of the FS, including its error in determination.

sketched in Fig. 31. The experimental data set is sliced along the κ_c -direction; see the slices on the lower part of the figure. Each slice can be seen as a set of so-called momentum distribution curves (MDC's). An MDC (see also Sect. XI in Paper II) is the photoelectron-intensity at fixed energy, here only dependent on κ_b (see the magenta curves in the upper right of Fig. 31 as examples for MDC's). For the analysis, we choose now to use all

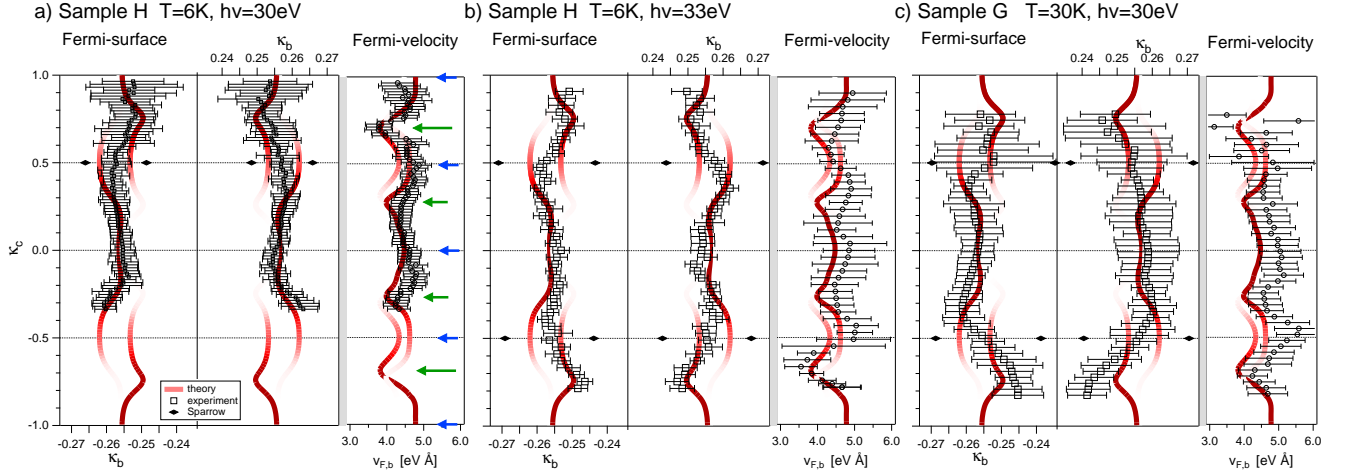


FIG. 32: Results of the Fermi-momentum extraction (black points with error bars, see Sect. XV A 3 b) in the double zone and for each individual dataset, as indicated. For each set, the larger panel shows the four FS sheets (left and right, outer and inner), while the smaller panel shows the k_b -projected velocity (102) averaged using the left and right k_b -projected velocity. Underlaid in dark red with an intensity proportional to the $|\mathbf{k}|$ -character [Eq. II (71) with $\eta=0$, i.e. Eq. I (61)] are the theoretical FS [Fig. 27 (d)] and its k_b -projected Fermi-velocity. Also included in the graphs for the FS are the results (Tab. I) of the Sparrow analysis for the maximum splitting at the zone boundary. $\kappa_a=6.3, 6.6, 6.3$ in respectively a), b) and c). Each theoretical and experimental FS has been compressed by a factor 11 along κ_c .

MDC's with energies between E_F-50 meV and E_F (the separation ΔE was typically 5 meV). We then fit each MDC (on each dispersion branch) with a Lorentzian. The maximum position of the Lorentzians defines the dispersion (indicated by the purple lines in the upper left of Fig. 31). We interpolated the Fermi-momentum (κ_{Fb}) by a line-fit with the linear function $\kappa_b = (E - E_F)/v_F + \kappa_{Fb}$ (see red line in upper left of Fig. 31). By this line-fit we remove the error arising from the masking-effect discussed above (see Fig. 30) which appears as a "kink" near the value of the energy resolution¹⁰. In accordance with the energy resolution of about 16 meV, the kink sets in at (see blue arrow) $E - E_F \approx 13$ meV in Fig. 31.

This method also gives naturally an estimate of the κ_c -dependence of the Fermi velocities projected onto the κ_b -direction,

$$\mathbf{v}_{Fj}(k_c) \cdot \mathbf{b}^*/b^* \equiv \partial E_j(k_b, k_c) / (\partial k_b b^*)|_{E_F}. \quad (102)$$

The result of this extraction method is displayed in Fig. 32 and Tab. II.

¹⁰ This "kink" should not be confused with the "kink" resulting from an interaction of a bosonic mode (for an example see, e.g. Ref. 92). Such a bosonic "kink", for energies lower than the energy of the bosonic mode, is bending to the momentum on the unoccupied side- because the Fermi-velocity is re-normalized to smaller values.

B. Results of the Fermi-surface determination and Comparison with Theory

1. Fermi-surface

The result of the Fermi-momentum extraction is displayed in Fig. 32. It compares the experimental FS (black points with error bars) with the theoretical FS (dark-red) calculated using the two-band Hamiltonian (95) with the ARPES-refined parameter values and drawn with the fine-grained intensity proportional to the $|\mathbf{k}|$ -character I (61) because for $\kappa_a=6.3$ and 6.6 the dimerization phase shift $\eta(\kappa)$ is negligible (see Sect. II IX B 1 Eq. (71) and Fig. 12).

We see that the Fermi-momentum extracted from ARPES fits beautifully with the theoretical FS sheet of dominating intensity: In all three measurements, it aligns with the outer sheet for $|\kappa_c| < 0.35$ and with the inner sheet for $|\kappa_c| > 0.65$. Near the zone-boundaries, $|\kappa_c|=0.5$, where the dominating intensity shifts from one sheet to the other, so does the experimentally extracted κ_{Fb} . Also, the general shape of the experimental FS fits nicely with the prediction by theory. This is, on the one hand, not astonishing as we use ARPES-refined parameter values, but on the other hand, the refinement was done for features well away from the Fermi energy, and yet, all details of the theoretical FS (seen in Fig. 27 (d) and described in Sect. XIV C) are seen in the experiment, with the exception of the near contact between the inner and outer sheets, which does require interpolation of the former to $k_c=0$ or extrapolation of the latter to $k_c=1$. Later on, we will discuss this also for the Fermi-

velocities.

The experimental upper bound given by the Sparrow criterion on the splitting between the inner and outer sheets at the ZB, $|\kappa_c|=0.5$, is indicated by the black diamonds. It is consistent with, but considerably larger than, the theoretical splitting.

As can be seen from Tab. II, for all three samples, k_{Fb} averaged over k_c gives a Luttinger volume which corresponds to an effective $\text{Li}_{1.02\pm0.02}$ stoichiometry, i.e. an electron filling of 0.51 ± 0.01 . This places the Fermi level 75 meV above the center of the gap in the calculation.

Finally, we note that the procedure of refining the values of the TB parameters to fit the ARPES dispersions for energies more than 0.15 eV below E_F in one sample does well in describing the dispersions for energies closer to E_F than 0.15 eV in all three samples. This is a testimonial, both to the reproducibility of our findings for samples from different sources and to the essential role that resonant coupling to the higher-energy gapped xz and yz bands plays in determining the dispersion and splitting of the metallic \widetilde{xy} bands.

2. Fermi-velocity

To the right of each FS in Fig. 32, we show the k_c -dependence of the k_b -projected Fermi-velocity (102): in black, as extracted from ARPES and in red, as calculated with the two-band Hamiltonian¹¹.

Overall, we see a good qualitative correspondence between the theoretical and the experimentally extracted values. For those k_c values where the k_b direction is normal to the FS, the velocity projection (102) has extrema. At the zone centers ($k_c=\text{integer}$) and zone boundaries ($|\kappa_c|=0.5$) –indicated by blue arrows in Fig. 32– these extrema are flat maxima. For the inner-sheet (upper-band) notches (green long arrows at $|\kappa_c|\approx0.75$), the extrema are deep *minima*. Also the outer sheet (lower band) has velocity minima (green short arrows at $|\kappa_c|\approx0.30$). Their origins are the weak resonance peaks at $|\kappa_c|\approx0.25$ (see Fig. 29 and Eq. (101)), combined with the increase of $|\mathbf{k} - |\mathbf{k} + \mathbf{c}^*)$ hybridization and the concomitant formation of bulges as the zone boundaries at $|\kappa_c|=0.5$ are approached.

The velocity of the outer sheet (lower band) decreases from 4.5 eV Å at the zone center ($k_c=0$) to the 4.0 eV Å deep minima near $|\kappa_c|=0.30$, and rises again to the 4.6 eV Å maxima at the centers of the bulges, $|\kappa_c|=0.5$. For the inner sheet (outer band), the velocity decreases from 4.7 eV Å at the zone centers ($|\kappa_c|=1$), to 3.9 eV Å deep minima near the notches, and rises again to 4.3 eV Å maxima at the zone boundaries. These sheet- and k_c -dependent values may be compared with the dominat-

ing value 4.6 eV Å of $b\tau'(k_b)$ in Eq.s I (50) and (48) from the direct hopping along the ribbon. Due to the indirect hops via the valence and conduction bands giving rise to the resonance terms in Eq. (95), the band- and k_c average of the velocity projections is smaller than $b\tau'(k_b)$. The velocities extracted from the ARPES data (black) clearly show both the qualitative behavior and the general magnitude implied by the theory (dark-red). To a small extent, this is expected since, as explained in Sect. I XI and specified in Tables I 43 and 45, a few of the many LDA TB parameters were refined to make the bands agree with the large- but not the small-energy features of the ARPES bands.

It is also interesting for the many-body physics of LiPB to compare the experimental velocities to those for the TB bands based on the LDA parameters. The LDA dominant velocity value is¹² 4.0 eV Å. The experimental velocities (and those for the ARPES-refined TB) are generally greater than those for the LDA¹³ by about 15%.

There are two points to be made. First, for a 3D quasi-particle material the increase of the experimental velocity relative to the LDA value would seem surprising since the usual effect [81], arising from an energy-dependent single-particle self-energy, e.g., caused by $e-e$ or $e-ph$ interactions, is an *increase* of the Fermi-mass, i.e. a decrease of the Fermi velocity¹⁴. Indeed such was found in the single-site DMFT quasi-particle treatment of LiPB [19]. However, LiPB is a quasi-1D material whose ARPES k -averaged lineshapes show TL-model properties, i.e. quasi-particle suppression and spin-charge separation. Specifically, the holon-peak and spinon-edge features disperse with different velocities, v_ρ and v_σ , respectively [14, 89, 95]. Our model-independent ARPES analysis procedure, if performed on a TL-lineshape, would yield a dispersion intermediate between v_ρ and v_σ , but tending mostly to that of the holon peak. Within 1D theory, v_ρ and v_σ can just as well be either larger or smaller than the underlying v_F of a non-interacting system, as can be seen, for example from formulas within the framework of the “g-ology” formulation [89, 96]. So if we identify the LDA value of $v_F=4.0$ eV Å as “non-interacting,” which ignores the difficulty of disentangling any many-body contribution already present in LDA, and

¹² Calculated from $b\tau'(k_b)$ and also given in Eq. (50) of Paper I.

¹³ The band- and k_c -resolved velocities which result from using the shifted and the straight LDA parameters (see FIG. 22) have averages more than 15% below that of the experimental velocities in FIG. 32, and they have much larger variations: Near $k_c=0$ and 0.5 the LDA velocities do lie around the 15% lower LDA value, 4.0 eVÅ, but for intermediate values of k_c , they vary much more, reaching minima at 3.4 and 3.0 eVÅ for respectively the upper and lower bands (inner and outer sheets) in the shifted LDA and, in the straight LDA, minima at 2.5 eVÅ and 3.3 eVÅ with the deeper minimum now for the upper band.

¹⁴ For quasi-particles, one would invoke a very strong k -dependence of the self-energy to understand a decrease of the mass, as discussed, e.g., in Ref.93 and Ref.94.

¹¹ The velocity projections of Eq.(102) were calculated as differences between the bands for $k_b=0.2505$ and 0.2495 .

think of our ARPES lineshape in a TL context, it is well within general theoretical expectations that our experimental velocity is larger than the LDA value. In this view, it may well be that our ARPES-refined TB description is modifying the entire k_b dispersion somewhat in order to reproduce the experimental low-energy scale velocity near E_F .

Second, combining our results with a previous ARPES lineshape analysis [97], we can be somewhat more precise about the velocity renormalizations for LiPB. At high temperatures, where the LiPB ARPES lineshapes are well described by TL lineshape theory [95] for nonzero T , the best TL description [97] for the Γ -Y ($k_c=0$) ARPES lineshapes was achieved for $v_\rho/v_\sigma=2$. At that time no definitive LDA value of v_F was available. If we now think of our ARPES velocity as being nearly that of v_ρ , and take our LDA velocity as an underlying “non-interacting” v_F , then –at least for Γ Y– we conclude that v_ρ is roughly $1.15v_F$, and that v_σ is roughly $0.6v_F$ ¹⁵. A 1D Hubbard-model analysis [17] estimated $v_\sigma/v_F \approx J/2\tau$ with $J \approx 0.2$ eV being an effective super-exchange interaction, and $\tau \approx 0.8$ eV being the primary k_b hopping, implying $v_\sigma/v_F \approx 1/8$.

3. Connecting to the TL critical exponent α

As already written in the introduction of Paper I, LiPB displays Luttinger liquid properties. Most remarkably, although the FS is well defined and could be extracted above, the lineshapes are better described by a TL spectral function. Nevertheless, there are also substantial T -dependent departures from the TL model. The ARPES line shapes at temperatures 250K to 300K are well described by the TL spectral function, showing both spinon and holon features (broadened by temperature and experimental resolution). With decreasing T the exponent varies with T , from $\alpha = 0.9$ at 250K to 0.6 at 50K, and also, the ARPES lineshape no longer agrees with the TL lineshape, although it does continue to display quantum critical scaling, a characteristic 1D property [18]. The spectra for k -integration along the quasi-1D direction, for temperatures $T=4$ K and 30 K and resolution 5 meV, are well described by a power law with $\alpha = 0.7$ [3].

In the following, we repeat the analysis of Ref. 3 with our recent data sets used to determine the FS above.

¹⁵ We take cognizance that the previous high- T , Γ -Y, TL lineshape analysis [97] found $v_\rho = 4.0$ eV \AA , coincidentally, we think, the same as our LDA value. That our present value of roughly 4.6 eV \AA along Γ -Y ($k_c=0$) is somewhat larger could perhaps be due to the considerable temperature difference (250K vs. 6K), the considerable difference in the analyzer angle resolutions along k_b (0.016 \AA^{-1} in the early work vs. 0.006 \AA^{-1} in the present work), or perhaps some small sample dependence. In any case the ratio $v_\rho/v_\sigma \approx 2$ is essentially the same for the present lineshapes and the text conclusion that v_ρ is nontrivially larger than v_F is unaltered.

However, in the course of the present study, we found that (i) all previous TB ladder models are very unrealistic, and (ii) the detectable bands of ARPES vary with fine-grained intensity proportional to the $|\mathbf{k}\rangle$ -character. In principle, these findings should inform the choice of a particular TL model. For the phenomenological extraction of the α value, however, we still use the same procedure as in Ref. 3 to obtain its value. As before, we use the κ -integrated spectral weight of a one-band, spin-rotational invariant TL-model [95] with $v_\rho/v_\sigma=2$. The theoretical spectrum was broadened by the experimental energy resolution of 16 meV.

The data displayed in Fig. 33 are integrated over κ_b and κ_c (cf. Fig.28). For the κ_c -direction, the data are integrated over two intervals, according to whether the dominant character is $|\mathbf{k}\rangle$ or $|\mathbf{k} + \mathbf{c}^*\rangle$. As visible in Fig. 33, sample G ($T=30$ K) shows a typical value of $\alpha = 0.70$ for both intervals. The data for sample H ($T=6$ K) vary a bit more on the two intervals but are still within the error range, yielding in average $\alpha = 0.58$. Connecting to the study of Ref. [18], despite a considerable difference in the determined α -values for samples G and H, these values are within the α -ranges of former studies. To shed light on more details, temperature-dependent measurements in the full range of relevant momenta would be required as well as the usage of a more realistic TL model than the one-band, spin-rotational invariant TL-model for the line-fit.

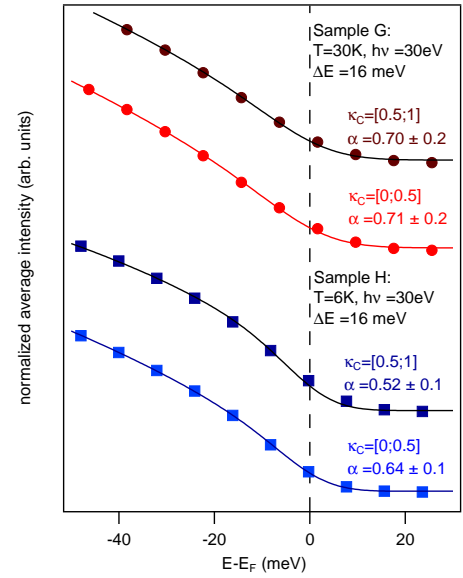


FIG. 33: Analysis of the TL-exponent of the data for sample G ($T=30$ K) and H ($T=6$ K). The FS’s were presented in Fig. 28. Here the data is momentum-integrated over two intervals, where the dominating band character is either $|\mathbf{k}\rangle$ or $|\mathbf{k} + \mathbf{c}^*\rangle$.

XVI. CONCLUSION AND IMPLICATIONS

In conclusion, we have presented in great detail the electronic structure of $\text{LiMo}_6\text{O}_{17}$ that is experimentally obtainable using ARPES, emphasizing the degree of one-dimensional behavior of the bands in the vicinity of E_F and the excellent overall agreement with the LDA band structure. With the aim of fully describing and understanding the metallic bands found in the ARPES experiment, especially the details of FS splitting and warping, the LDA electronic structure was downfolded to a tight-binding description with the three Mo1-centered t_{2g} Wannier orbitals (WOs) per formula unit (Sect. I VI) using the newly developed full-potential version of the NMTO method (Sect. I II). This description is based on analyzing the LiPB crystal structure as built from corner-sharing MoO_6 octahedra forming a staircase running along **c** of bi-ribbons extending along **b** (Sect. I III).

The six t_{2g} WOs per primitive cell accurately describe not only the four bands seen by ARPES, but all six bands in the 1 eV neighborhood of E_F . This band structure (Sect. I IV and Fig. I 4) is basically 2D and formed by the xy , xz , and yz WOs (Fig. I 9) giving rise to three 1D bands running along respectively **b**, **c**+**b**, and **c**-**b**, i.e. at a 120° angle to the two other bands (Figs I 8 and II 20). The dimerization from $c/2$ to c of the ribbons into bi-ribbons gaps the xz and yz bands and leaves the xy band metallic in the gap, but resonantly coupled to its edges and, hence, to the **c**+**b** and **c**-**b** directions. Inclusion of the xz and yz bands are indispensable in describing the strong indirect contributions to the k_c -dispersion and splitting of the metallic xy bands. These are most prominent (see Figs I 8, II 20, and III 32) at the crossing of the xy -band CECs running parallel to the $P_1Q_1P'_1$ -line ($k_b=0.225$) in reciprocal space with those of the xz and yz V&C-band edges along respectively ZY' and ZY . All the ARPES-measured dispersions, as well as the FS, indeed confirm the resonant indirect couplings and thus the essential need for the six-band picture. The TB bands are very well described by an analytic 6×6 Hamiltonian I (35) or (56) with parameters optimized to match the ARPES data for energies more than 0.15 eV below E_F . Finally, the mix of direct and resonant indirect couplings along the **c**-direction can be explicitly displayed by further analytical downfolding to the effective 2×2 Hamiltonian III (95). This and direct observation by ARPES is compelling evidence for the existence of pronounced resonance structures near E_F in LiPB.

Our results have four important implications for general questions posed in the Introduction in Paper I. These implications follow directly from the central content of the paper, our new knowledge, and understanding of the size of the splitting and perpendicular dispersions of the quasi-1D bands in the gap (Figs III 25 and 26), especially the indirect resonance contributions. They have been stated already in the flow of the presentation, and we merely summarize them here.

First, the reality of the resonance contributions casts

serious doubts on theoretical descriptions based on TB bands which are featureless like the red ones in Figs 25 and 26, i.e. casts doubt on all previous TB and TL models. Further, in constructing an appropriate many-body Hamiltonian, it should be taken into serious consideration that with ARPES, we have now been able to follow the resonance peak induced by the valence band to energies nearly 150 meV below the Fermi level (Fig. II 20) and, there, find the peak to have a magnitude of about 50 meV, as predicted by the LDA, cf. Fig. II 24 (c2).

Second, the general magnitude of the t_\perp -hoppings would suggest that 1D to 3D crossover should occur for T as high as at least 150 K, unless thwarted by the theoretically expected strong downward low- T renormalization due to LL fluctuations on the chains, as pointed out in the Introduction. However, the good agreement between LDA and ARPES data at $T=6$ K implies that this renormalization does not take place. This circumstance is not only puzzling, given the evidence for LL effects on the chains at high T , but eliminates one very attractive explanation for the exceptional stability of quasi-1D behavior in this material. Our new quantitative knowledge of the t_\perp -hoppings further emphasizes this puzzle.

Third, the coupling of the quasi-1D bands to the V&C bands causes the details of the FS splitting and warping (Figs 27 and 32) to depend strongly on the position of E_F which in turn depends on the Li concentration. This implies that any property sensitive to the details of the FS will be very sensitive to the stoichiometry. One can then speculate that this FS sensitivity is connected to the sample dependence of the SC, especially if the SC is the product of the quasi-1D nature of the FS. We have already noted that the actual position of E_F in LiPB is such as to maximize the quasi-1D nature of the FS. This could be an important addition to the various previous theories of the SC [6, 7, 9, 20, 21].

Fourth, the spatial dependence of the t_\perp -hoppings argues strongly against coupled ladder models of the chains. At the simplest level, the magnitude of the direct terms for hoppings within and between bi-ribbons (Sect. I IV) differ by less than a factor of two, respectively, $t_{\perp,1} \equiv -(t_1 + u_1) = 14$ meV and $t_{\perp,2} \equiv -(t_1 - u_1) = 8$ meV¹⁶. Just this would leave the ladders not very well defined as separable objects. But, much more importantly,

¹⁶ Since our TB model is considerably more detailed than those previously published [25][26][4][17], we have been forced to change notation. The relation between ours and the earlier notation is: $\tau = t$, $t_1 + u_1 = t_\perp$, and $t_1 - u_1 = t'_\perp$. Note that τ in Sect. IV Eq.s (23) and (25) is the coefficient to $\cos \pi n k_b$ whereas τ_n in the Appendix Eq. (37) are the coefficients to $\cos 2\pi n k_b$. As a result, $\tau \sim 2\tau_1$. Greek and Latin letters denote hops respectively inside the same sublattice, xy - xy and XY - XY , and between sublattices, xy - XY , i.e. essentially intra- and inter-ribbon hops. Subscripts denote the hopping distance. Without subscript, Greek and Latin letters denote Bloch sums of hopping integrals, i.e. functions of $\mathbf{k} = (k_b, k_c)$ which upon translation by \mathbf{c}^* are respectively invariant or change sign. See Eq.s I (37)-(40).

the range of the indirect contributions is at least an *order of magnitude* longer and even depends crucially on the position of the \widetilde{xy} bands in the gap (Sect. III XIV). We conclude that modeling the chains as separable, weakly coupled ladders is very unrealistic.

In Paper II, we have also remarked on the likely smallness of Coulomb interactions, such as a local repulsion U . Drawing on calculated results from Nuss and Aichhorn [19], we estimated for our final \widetilde{xy} bands an upper limit on U in the range 0.35 to 0.75 eV. Without serious calculations of the Coulomb interactions and their range, calculations that have not yet been made, but should be, this is, of course, an indirect inference from our results. But we emphasize that there is no evidence from our detailed comparison of ARPES and theory for the 1D \widetilde{xy} bands near and at E_F that the Coulomb interactions are able to disrupt the strong covalent bonding that leads to the distinctive FS features that we have elucidated.

Indeed, it took only small refinements of the parameter values to bring our TB Hamiltonian into complete agreement with the ARPES bands up to 0.15 eV below the Fermi level, so we know that the Coulomb correlation effects on the energy bands must be quantitatively small. We can infer that yet longer-range repulsions, often denoted as V , will be similarly limited.

To conclude, our results offer both a strong motivation and a concrete framework for a serious reappraisal of the extent to which the various past many-body models capture the actual measured one-electron electronic structure of LiPB sufficiently well to be trusted for rationalizing its fascinating quasi-1D, many-body, coupled-chain physics. The efforts to understand the resulting behavior are still ongoing, and we hope that our new knowledge and highly portable description of the one-electron electronic structure will contribute to this effort.

-
- [1] M. Greenblatt, W. McCarroll, R. Neifeld, M. Croft, and J. Waszczak, Solid State Communications **51**, 671 (1984), ISSN 0038-1098, URL <http://www.sciencedirect.com/science/article/pii/003810988490944X>.
 - [2] M. Onoda, K. Toriumi, Y. Matsuda, and M. Sato, Journal of Solid State Chemistry **66**, 163 (1987), ISSN 0022-4596, URL <http://www.sciencedirect.com/science/article/pii/0022459687902313>.
 - [3] L. Dudy, J. D. Denlinger, J. W. Allen, F. Wang, J. He, D. Hitchcock, A. Sekiyama, and S. Suga, Journal of Physics: Condensed Matter **25**, 014007 (2013), URL <http://stacks.iop.org/0953-8984/25/i=1/a=014007>.
 - [4] J. Merino and R. H. McKenzie, Phys. Rev. B **85**, 235128 (2012), URL <http://link.aps.org/doi/10.1103/PhysRevB.85.235128>.
 - [5] J. Merino and J. V. Alvarez, Phys. Rev. B **91**, 035135 (2015), URL <https://link.aps.org/doi/10.1103/PhysRevB.91.035135>.
 - [6] W. Cho, C. Platt, R. H. McKenzie, and S. Raghu, Phys. Rev. B **92**, 134514 (2015), URL <https://link.aps.org/doi/10.1103/PhysRevB.92.134514>.
 - [7] N. Lera and J. V. Alvarez, Phys. Rev. B **92**, 174523 (2015), URL <https://link.aps.org/doi/10.1103/PhysRevB.92.174523>.
 - [8] G. Wu, X.-s. Ye, X. Zeng, B. Wu, and W. Clark, Scientific Reports **6** (2016), URL www.nature.com/articles/srep20721.
 - [9] C. Platt, W. Cho, R. H. McKenzie, R. Thomale, and S. Raghu, Phys. Rev. B **93**, 214515 (2016), URL <https://link.aps.org/doi/10.1103/PhysRevB.93.214515>.
 - [10] P. Chudziński, The European Physical Journal B **90**, 148 (2017), ISSN 1434-6036, URL <https://doi.org/10.1140/epjb/e2017-70733-4>.
 - [11] J. Lu, X. Xu, M. Greenblatt, R. Jin, P. Tinnemans, S. Licciardello, M. R. van Delft, J. Buhot, P. Chudzinski, and N. E. Hussey, Science Advances **5**, eaar8027 (2019), <https://www.science.org/doi/pdf/10.1126/sciadv.aar8027>, URL <https://www.science.org/doi/abs/10.1126/sciadv.aar8027>.
 - [12] S.-i. Tomonaga, Progress of Theoretical Physics **5**, 544 (1950), ISSN 0033-068X, <https://academic.oup.com/ptp/article-pdf/5/4/544/5430161/5-4-544.pdf>, URL <https://doi.org/10.1143/ptp/5.4.544>.
 - [13] J. M. Luttinger, Journal of Mathematical Physics **4**, 1154 (1963), <https://doi.org/10.1063/1.1704046>, URL <https://doi.org/10.1063/1.1704046>.
 - [14] T. Giamarchi, Quantum physics in one dimension (Oxford university press, 2004), URL www.global.oup.com/academic/product/quantum-physics-in-one-dimension-9780198525004.
 - [15] J. Hager, R. Matzdorf, J. He, R. Jin, D. Mandrus, M. A. Cazalilla, and E. W. Plummer, Phys. Rev. Lett. **95**, 186402 (2005), URL <http://link.aps.org/doi/10.1103/PhysRevLett.95.186402>.
 - [16] D. Orgad, S. A. Kivelson, E. W. Carlson, V. J. Emery, X. J. Zhou, and Z. X. Shen, Phys. Rev. Lett. **86**, 4362 (2001), URL <https://link.aps.org/doi/10.1103/PhysRevLett.86.4362>.
 - [17] P. Chudzinski, T. Jarlborg, and T. Giamarchi, Phys. Rev. B **86**, 075147 (2012), URL <http://link.aps.org/doi/10.1103/PhysRevB.86.075147>.
 - [18] F. Wang, J. V. Alvarez, S.-K. Mo, J. W. Allen, G.-H. Gweon, J. He, R. Jin, D. Mandrus, and H. Höchst, Phys. Rev. Lett. **96**, 196403 (2006), URL <http://link.aps.org/doi/10.1103/PhysRevLett.96.196403>.
 - [19] M. Nuss and M. Aichhorn, Phys. Rev. B **89**, 045125 (2014), URL <https://link.aps.org/doi/10.1103/PhysRevB.89.045125>.
 - [20] O. Sepper and A. G. Lebed, Phys. Rev. B **88**, 094520 (2013), URL <https://link.aps.org/doi/10.1103/PhysRevB.88.094520>.
 - [21] A. G. Lebed and O. Sepper, Phys. Rev. B **87**, 100511 (2013), URL <https://link.aps.org/doi/10.1103/PhysRevB.87.100511>.
 - [22] X. Xu, A. F. Bangura, J. G. Analytis, J. D. Fletcher, M. M. J. French, N. Shannon, J. He, S. Zhang, D. Mandrus, R. Jin, et al., Phys. Rev. Lett. **102**, 206602 (2009), URL <https://link.aps.org/doi/10.1103/PhysRevLett.102.206602>.

- 1103/PhysRevLett.102.206602.
- [23] N. Wakeham, A. F. Bangura, X. Xu, J.-F. Mercure, M. Greenblatt, and N. E. Hussey, *Nature communications* **2**, 396 (2011), URL www.nature.com/articles/ncomms1406.
 - [24] M. H. Whangbo and E. Canadell, *Journal of the American Chemical Society* **110**, 358 (1988).
 - [25] Z. S. Popovic and S. Satpathy, *Phys. Rev. B* **74**, 045117 (2006), URL <http://link.aps.org/doi/10.1103/PhysRevB.74.045117>.
 - [26] T. Jarlborg, P. Chudzynski, and T. Giamarchi, *Phys. Rev. B* **85**, 235108 (2012), URL <https://link.aps.org/doi/10.1103/PhysRevB.85.235108>.
 - [27] J. A. M. Haverkort, in *International workshop on Strong correlations and angle-resolved photoemission spectroscopy* (2013), URL <http://corpes13.xfel.eu/>.
 - [28] Y. Nohara and O. K. Andersen, *Phys. Rev. B* **94**, 085148 (2016), URL <https://link.aps.org/doi/10.1103/PhysRevB.94.085148>.
 - [29] J. P. Pouget, B. Hennion, C. Escribe-Filippini, and M. Sato, *Phys. Rev. B* **43**, 8421 (1991), URL <https://link.aps.org/doi/10.1103/PhysRevB.43.8421>.
 - [30] M.-H. Whangbo, E. Canadell, P. Foury, and J.-P. Pouget, *Science* **252**, 96 (1991).
 - [31] J. D. Denlinger, G.-H. Gweon, J. W. Allen, C. G. Olson, J. Marcus, C. Schlenker, and L.-S. Hsu, *Phys. Rev. Lett.* **82**, 2540 (1999), URL <http://link.aps.org/doi/10.1103/PhysRevLett.82.2540>.
 - [32] K. Breuer, D. M. Goldberg, K. E. Smith, M. Greenblatt, and W. McCarroll, *Solid State Communications* **94**, 601 (1995), ISSN 0038-1098, URL <http://www.sciencedirect.com/science/article/pii/0038109895001433>.
 - [33] U. von Barth and L. Hedin, *Journal of Physics C: Solid State Physics* **5**, 1629 (1972), URL <http://stacks.iop.org/0022-3719/5/i=13/a=012>.
 - [34] O. K. Andersen and T. Saha-Dasgupta, *Phys. Rev. B* **62**, R16219 (2000), URL <https://link.aps.org/doi/10.1103/PhysRevB.62.R16219>.
 - [35] R. Tank and C. Arcangeli, *physica status solidi (b)* **217**, 89 (2000), ISSN 1521-3951, URL [http://dx.doi.org/10.1002/\(SICI\)1521-3951\(200001\)217:1<89::AID-PSSB89>3.0.CO;2-C](http://dx.doi.org/10.1002/(SICI)1521-3951(200001)217:1<89::AID-PSSB89>3.0.CO;2-C).
 - [36] O. Andersen, T. Saha-Dasgupta, R. Tank, C. Arcangeli, O. Jepsen, and G. Krier, *Electronic Structure and Physical Properties of Solids. The Uses of the LMTO Method* (Springer, 2000), URL <https://link.springer.com/book/10.1007/3-540-46437-9>.
 - [37] O. K. Andersen, *Phys. Rev. B* **12**, 3060 (1975), URL <https://link.aps.org/doi/10.1103/PhysRevB.12.3060>.
 - [38] O. K. Andersen and O. Jepsen, *Phys. Rev. Lett.* **53**, 2571 (1984), URL <https://link.aps.org/doi/10.1103/PhysRevLett.53.2571>.
 - [39] E. Pavarini, A. Yamasaki, J. Nuss, and O. K. Andersen, *New Journal of Physics* **7**, 188 (2005), URL <http://stacks.iop.org/1367-2630/7/i=1/a=188>.
 - [40] E. Zurek, O. Jepsen, and O. Andersen, *ChemPhysChem* **6**, 1934 (2005), ISSN 1439-7641, URL <http://dx.doi.org/10.1002/cphc.200500133>.
 - [41] A. Yamasaki, M. Feldbacher, Y.-F. Yang, O. K. Andersen, and K. Held, *Phys. Rev. Lett.* **96**, 166401 (2006), URL <https://link.aps.org/doi/10.1103/PhysRevLett.96.166401>.
 - [42] F. Lechermann, A. Georges, A. Poteryaev, S. Biermann, M. Posternak, A. Yamasaki, and O. K. Andersen, *Phys. Rev. B* **74**, 125120 (2006), URL <https://link.aps.org/doi/10.1103/PhysRevB.74.125120>.
 - [43] L. Boeri, G. B. Bachelet, M. Giantomassi, and O. K. Andersen, *Phys. Rev. B* **76**, 064510 (2007), URL <https://link.aps.org/doi/10.1103/PhysRevB.76.064510>.
 - [44] G.-Q. Liu, V. N. Antonov, O. Jepsen, and O. K. Andersen, *Phys. Rev. Lett.* **101**, 026408 (2008), URL <https://link.aps.org/doi/10.1103/PhysRevLett.101.026408>.
 - [45] P. R. C. Kent, T. Saha-Dasgupta, O. Jepsen, O. K. Andersen, A. Macridin, T. A. Maier, M. Jarrell, and T. C. Schulthess, *Phys. Rev. B* **78**, 035132 (2008), URL <https://link.aps.org/doi/10.1103/PhysRevB.78.035132>.
 - [46] T. Saha-Dasgupta, O. Andersen, J. Nuss, A. Poteryaev, A. Georges, and A. Lichtenstein, *arXiv preprint arXiv:0907.2841* (2009).
 - [47] E. Zurek, O. Jepsen, and O. K. Andersen, *Inorganic Chemistry* **49**, 1384 (2010), pMID: 20067284, <https://doi.org/10.1021/ic9014515>, URL <https://doi.org/10.1021/ic9014515>.
 - [48] O. K. Andersen and L. Boeri, *Annalen der Physik* **523**, 8 (2011).
 - [49] M. W. Haverkort, M. Zwierzycki, and O. K. Andersen, *Phys. Rev. B* **85**, 165113 (2012), URL <https://link.aps.org/doi/10.1103/PhysRevB.85.165113>.
 - [50] N. Marzari, A. A. Mostofi, J. R. Yates, I. Souza, and D. Vanderbilt, *Rev. Mod. Phys.* **84**, 1419 (2012), URL <https://link.aps.org/doi/10.1103/RevModPhys.84.1419>.
 - [51] O. Andersen, *NMTOs and their Wannier functions, Correlated Electrons: from Models to Materials: Lecture Notes of the Autumn School Correlated Electrons 2012* (Forschungszentrum Jülich, 2012), vol. 2 of *Schriften des Forschungszentrums Jülich: Reihe Modeling and Simulation*, ISBN 978-3-89336-796-2, URL <http://hdl.handle.net/2128/4611>.
 - [52] M. Zwierzycki and O. Andersen, *Acta Physica Polonica A* **1**, 64 (2009), URL <http://yadda.icm.edu.pl/przyrbwn/element/bwmeta1.element.bwnjournal-article-appv115n1010kz?q=bwmeta1.element.bwnjournal-number-appola-2009-115-1;10&qt=CHILDREN-STATELESS>.
 - [53] M. Methfessel, M. v. Schilfgaarde, and C. R. A., *Electronic Structure and Physical Properties of Solids. The Uses of the LMTO Method* (Springer, 2000), URL <https://link.springer.com/book/10.1007/3-540-46437-9>.
 - [54] J. M. Wills, O. Eriksson, M. Alouani, and P. D. L., *Electronic Structure and Physical Properties of Solids. The Uses of the LMTO Method* (Springer, 2000), URL <https://link.springer.com/book/10.1007/3-540-46437-9>.
 - [55] J. M. Wills, M. Alouani, P. Andersson, A. Delin, O. Eriksson, and O. Grechnev, *Full-Potential Electronic Structure Method: energy and force calculations with density functional and dynamical mean field theory*, vol. 167 (Springer Science & Business Media, 2010).
 - [56] K. Lejaeghere, G. Bihlmayer, T. Björkman, P. Blaha, S. Blügel, V. Blum, D. Caliste, I. E. Castelli, S. J. Clark, A. Dal Corso, et al., *Science* **351** (2016), ISSN 0036-8075, <https://science.sciencemag.org/content/351/6280/aad3000.full.pdf>, URL <https://science.sciencemag.org/content/351/6280/aad3000>.
 - [57] O. Andersen, O. Jepsen, and G. Krier, *Lectures in Methods of Electronic Structure Calculations* (Worl

- Scientific, 1995), ISBN 978-981-4503-77-8, URL <http://www.worldscientific.com/worldscibooks/10.1142/2103#t=aboutBook>.
- [58] L. Vitos, *Computational quantum mechanics for materials engineers: the EMTO method and applications* (Springer Science & Business Media, 2007).
- [59] W. R. L. Lambrecht and O. K. Andersen, Phys. Rev. B **34**, 2439 (1986), URL <https://link.aps.org/doi/10.1103/PhysRevB.34.2439>.
- [60] E. Zurek, J. Autschbach, and O. K. Andersen, AIP Conference Proceedings **963**, 1421 (2007), <https://aip.scitation.org/doi/pdf/10.1063/1.2836021>, URL <https://aip.scitation.org/doi/abs/10.1063/1.2836021>.
- [61] S. Satpathy and Z. Pawlowska, physica status solidi (b) **145**, 555 (1988), <https://onlinelibrary.wiley.com/doi/pdf/10.1002/pssb.2221450221>, URL <https://onlinelibrary.wiley.com/doi/abs/10.1002/pssb.2221450221>.
- [62] W. Ku, H. Rosner, W. E. Pickett, and R. T. Scalettar, Phys. Rev. Lett. **89**, 167204 (2002), URL <https://link.aps.org/doi/10.1103/PhysRevLett.89.167204>.
- [63] Y. Nohara and O. K. Andersen, to be submitted.
- [64] P. Foury and J. Pouget, International Journal of Modern Physics B **7**, 3973 (1993).
- [65] M. I. Aroyo, D. Orobengoa, G. de la Flor, E. S. Tasci, J. M. Perez-Mato, and H. Wondratschek, Acta Crystallographica Section A **70**, 126 (2014), URL <http://dx.doi.org/10.1107/S205327331303091X>.
- [66] P. Kopietz, V. Meden, and K. Schönhammer, Phys. Rev. Lett. **74**, 2997 (1995), URL <http://link.aps.org/doi/10.1103/PhysRevLett.74.2997>.
- [67] E. L. Shirley, L. J. Terminello, A. Santoni, and F. J. Himpsel, Phys. Rev. B **51**, 13614 (1995), URL <http://link.aps.org/doi/10.1103/PhysRevB.51.13614>.
- [68] S. Moser, Journal of Electron Spectroscopy and Related Phenomena **214**, 29 (2017), ISSN 0368-2048, URL <http://www.sciencedirect.com/science/article/pii/S0368204816301724>.
- [69] F. Matsui, T. Matsushita, and H. Daimon, Journal of Electron Spectroscopy and Related Phenomena **195**, 347 (2014), ISSN 0368-2048, URL <http://www.sciencedirect.com/science/article/pii/S0368204814000668>.
- [70] H. Daimon, S. Imada, H. Nishimoto, and S. Suga, Journal of Electron Spectroscopy and Related Phenomena **76**, 487 (1995), proceedings of the Sixth International Conference on Electron Spectroscopy.
- [71] H. Nishimoto, T. Nakatani, T. Matsushita, S. Imada, H. Daimon, and S. Suga, Journal of Physics: Condensed Matter **8**, 2715 (1996), URL <http://stacks.iop.org/0953-8984/8/i=15/a=020>.
- [72] W. McCarroll and M. Greenblatt, Journal of Solid State Chemistry **54**, 282 (1984), ISSN 0022-4596, URL <http://www.sciencedirect.com/science/article/pii/0022459684901579>.
- [73] M. L. Knotek and P. J. Feibelman, Phys. Rev. Lett. **40**, 964 (1978), URL <http://link.aps.org/doi/10.1103/PhysRevLett.40.964>.
- [74] J. Denlinger, G.-H. Gweon, J. Allen, J. Marcus, and C. Schlenker, Journal of Electron Spectroscopy and Related Phenomena **101-103**, 805 (1999), ISSN 0368-2048.
- [75] S. Moser, L. Moreschini, J. Jaćimović, O. S. Barišić, H. Berger, A. Magrez, Y. J. Chang, K. S. Kim, A. Bostwick, E. Rotenberg, et al., Phys. Rev. Lett. **110**, 196403 (2013).
- [76] S. M. Walker, F. Y. Bruno, Z. Wang, A. de la Torre, S. Ricco, A. Tamai, T. K. Kim, M. Hoesch, M. Shi, M. S. Bahramy, et al., Advanced Materials **27**, 3894 (2015), ISSN 1521-4095.
- [77] L. Dudy, M. Sing, P. Scheiderer, J. D. Denlinger, P. Schütz, J. Gabel, M. Buchwald, C. Schlueter, T.-L. Lee, and R. Claessen, Advanced Materials **28**, 7443 (2016).
- [78] F. Wang, J. V. Alvarez, J. W. Allen, S.-K. Mo, J. He, R. Jin, D. Mandrus, and H. Höchst, Phys. Rev. Lett. **103**, 136401 (2009), URL <https://link.aps.org/doi/10.1103/PhysRevLett.103.136401>.
- [79] S. Hüfner, *Photoelectron spectroscopy: principles and applications* (Springer Science & Business Media, 2013).
- [80] A. Damascelli, Physica Scripta **T109**, 61 (2004), URL <https://doi.org/10.1238/2Physica.topical.109a00061>.
- [81] A. Mackintosh and O. Andersen, *The electronic structure of transition metals* (Cambridge University Press, Cambridge, 1980), chap. Electrons at the Fermi surface, pp. 149–224.
- [82] A. Jones, J. Bland-Hawthorn, and P. Shopbell, in *Astronomical Data Analysis Software and Systems IV* (1995), vol. 77, p. 503, URL www.adsabs.harvard.edu/full/1995ASPC...77..503J.
- [83] C. Tusche, A. Krasnyuk, and J. Kirschner, Ultramicroscopy **159**, 520 (2015), ISSN 0304-3991, special Issue: LEEM-PEEM 9, URL <https://www.sciencedirect.com/science/article/pii/S0304399115000698>.
- [84] M. Lindroos and A. Bansil, Physical review letters **77**, 2985 (1996).
- [85] V. N. Strocov, R. Claessen, G. Nicolay, S. Hüfner, A. Kimura, A. Harasawa, S. Shin, A. Kakizaki, P. Nilsson, H. Starnberg, et al., Physical review letters **81**, 4943 (1998).
- [86] L. Kipp, K. Roßnagel, C. Solterbeck, T. Strasser, W. Schattke, and M. Skibowski, Phys. Rev. Lett. **83**, 5551 (1999), URL <https://link.aps.org/doi/10.1103/PhysRevLett.83.5551>.
- [87] A. Kaminski and H. M. Fretwell, New Journal of Physics **7**, 98 (2005), URL <http://stacks.iop.org/1367-2630/7/i=1/a=098>.
- [88] V. Brouet, A. Nicolaou, M. Zacchigna, A. Taleb-Ibrahimi, P. Le Fevre, and F. Bertran, Journal of Electron Spectroscopy and Related Phenomena **185**, 146 (2012), ISSN 0368-2048, URL <https://www.sciencedirect.com/science/article/pii/S0368204812000436>.
- [89] J. Voit, Journal of Physics: Condensed Matter **5**, 8305 (1993), URL <http://stacks.iop.org/0953-8984/5/i=44/a=020>.
- [90] T. Grandke, L. Ley, and M. Cardona, Phys. Rev. B **18**, 3847 (1978), URL <https://link.aps.org/doi/10.1103/PhysRevB.18.3847>.
- [91] V. Strocov, Journal of Electron Spectroscopy and Related Phenomena **130**, 65 (2003), ISSN 0368-2048, URL <https://www.sciencedirect.com/science/article/pii/S0368204803000549>.
- [92] A. Lanzara, P. Bogdanov, X. Zhou, S. Kellar, D. Feng, E. Lu, T. Yoshida, H. Eisaki, A. Fujimori, K. Kishio, et al., Nature **412**, 510 (2001).
- [93] T. Miyake, C. Martins, R. Sakuma, and F. Aryasetiawan,

- Phys. Rev. B **87**, 115110 (2013), URL <https://link.aps.org/doi/10.1103/PhysRevB.87.115110>.
- [94] C. H. P. Wen, H. C. Xu, Q. Yao, R. Peng, X. H. Niu, Q. Y. Chen, Z. T. Liu, D. W. Shen, Q. Song, X. Lou, et al., Phys. Rev. Lett. **121**, 117002 (2018), URL <https://link.aps.org/doi/10.1103/PhysRevLett.121.117002>.
- [95] D. Orgad, Philosophical Magazine B **81**, 377 (2001), <https://doi.org/10.1080/13642810108226410>, URL <https://doi.org/10.1080/13642810108226410>.
- [96] J. Solyom, Advances in Physics **28**, 201 (1979), <https://doi.org/10.1080/00018737900101375>, URL <https://doi.org/10.1080/00018737900101375>.
- [97] G.-H. Gweon, J. W. Allen, and J. D. Denlinger, Phys. Rev. B **68**, 195117 (2003), URL <https://link.aps.org/doi/10.1103/PhysRevB.68.195117>.